In situ site- and time-resolved analysis of local corrosion and inhibition of aerospace alloys

Mopon, M.

DOI
10.4233/uuid:d0581ac0-402a-4e2e-a2e9-4f1e4e0a5538

Publication date
2026

Document Version
Final published version

Citation (APA)
Mopon, M. (2026). *In situ site- and time-resolved analysis of local corrosion and inhibition of aerospace alloys*. [Dissertation (TU Delft), Delft University of Technology]. https://doi.org/10.4233/uuid:d0581ac0-402a-4e2e-a2e9-4f1e4e0a5538

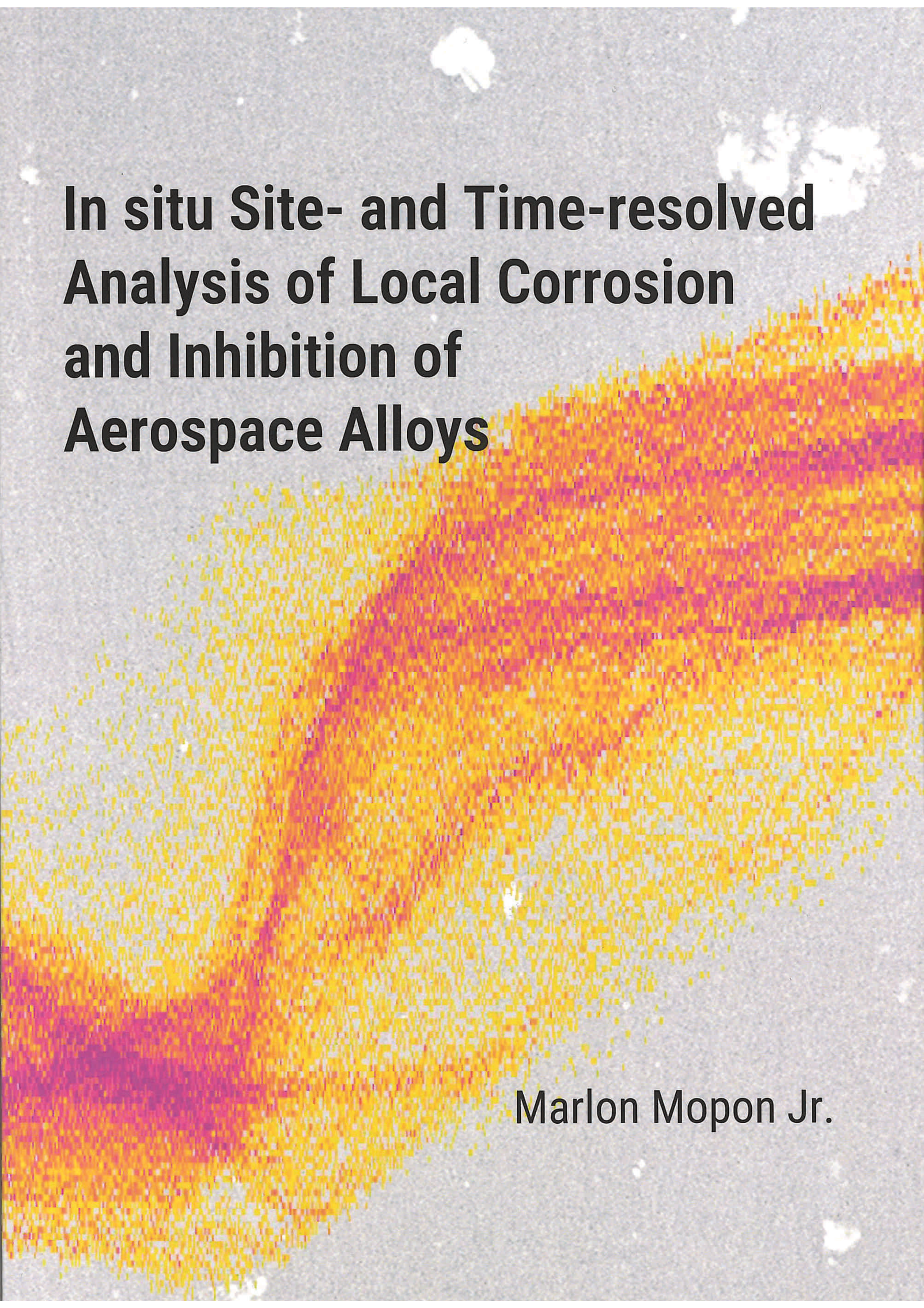

In situ Site- and Time-resolved Analysis of Local Corrosion and Inhibition of Aerospace Alloys

Marlon Mopon Jr.

In situ Site- and Time-resolved Analysis of Local Corrosion and Inhibition of Aerospace Alloys

Dissertation

for the purpose of obtaining the degree of doctor
at Delft University of Technology
by the authority of the Rector Magnificus, Prof.dr.ir. T.H.J.J. van der Hagen
chair of the Board for Doctorates
to be defended publicly on
Tuesday 06 January 2026 at 3:00 o'clock

by

Marlon MOPON Jr

Master of Science in Chemical Engineering
University of the Philippines Diliman, Quezon City, Philippines
born in Cavite, Philippines

This dissertation has been approved by the promotors.

Composition of the doctoral committee:

Rector magnificus	Chairperson
Dr. S.J. Garcia Espallargas	Delft University of Technology, promotor
Prof.dr.ir. J.M.C Mol	Delft University of Technology, promotor

Independent members:

Prof.dr.ir. R. Benedictus	Delft University of Technology
Dr.ir. T.C. Bor	University of Twente
Dr.ir. A.M. Homborg	Netherlands Defence Academy
Dr.ir. J. Ustarroz	Université Libre de Bruxelles
Dr. V. Shikirskiy	Université Paris Cité

Keywords: Local corrosion, corrosion inhibition, in situ optics, electrochemical noise, galvanic couple, AA2024-T3, AA7075-T6
Printed by: Ipskamp Printing B.V.
Cover: A full 8-bit pixel activity level distribution of an intermetallic particle overlayed on an SEM image of aluminum alloy.

ISBN 978-94-6473-988-6
An electronic version of this dissertation is available at
https://repository.tudelft.nl/

Summary

The main objective of this dissertation is to advance the understanding of local corrosion and inhibition in aerospace aluminium alloys by applying in situ reflected light microscopy, integrated with electrochemical measurements, to systematically analyse the behaviour of a large number of intermetallic particles and other local corrosion sites. This technique generates site-resolved datasets with high spatial and temporal resolution, capturing the diverse and dynamic nature of local corrosion phenomena. To fully harness this information, new developments in data processing and analysis were implemented, enabling the extraction of time-dependent parameters and robust classification of local corrosion and inhibition behaviours. These advances helped uncover new mechanistic insights into how corrosion and inhibition processes initiate, evolve, and interact across varying microstructures at the alloy surface under different environments. Crucially, this approach moves beyond isolated observations of individual sites, allowing for a broader and more representative understanding of local behaviour across the material. This broader perspective provides insights that can enable the development of more targeted and efficient active corrosion protection strategies.

Chapter 1 introduces the two aerospace aluminium alloys studied in this work, AA2024-T3 and AA7075-T6, and outlines the role of corrosion inhibitors in their active protection. It also reviews current local characterization techniques used to study corrosion and inhibition in these alloys. These techniques are systematically evaluated based on key performance metrics: spatial resolution, morphological and chemical information depth, and area measurement time. This comparative analysis reveals the specific strengths and trade-offs of each method, highlighting how no single technique excels in all categories. Notably, reflected light microscopy emerges as uniquely capable of delivering good area measurement time and sufficient spatial resolution to resolve changes in individual sites, though it does so with limited information depth. Strategies for mitigating this limitation, such as integration with complementary techniques are briefly discussed. The chapter concludes by presenting the objective of this work, emphasizing the role of reflected light microscopy in meeting these objectives, and providing the outline of the succeeding chapters.

*Section 1 (***Chapter 2** and **Chapter 3**) focuses on *local corrosion inhibition* in AA2024-T3. Local corrosion of AA2024-T3 has been studied in great detail. The same can be said about its inhibition behaviour in the presence of a wide variety of corrosion inhibitors. However, how changes in inhibitor availability affect local corrosion and inhibition over time is a less-explored avenue. This section explores this aspect of inhibition by using $Ce(NO_3)_3$, also referred to as Ce(III), as a model inhibitor and analysing how its time-dependent availability impacts local surface changes.

Chapter 2 analyses how time-dependent Ce(III) availability during the initial stages *of exposure* to a corrosive environment affects the corrosion inhibition at intermetallic particles (IMPs) of varying compositions. Specifically, this chapter examines how the effectiveness of inhibition is affected when the Ce(III) supply is delayed, allowing IMP dealloying and trench formation to develop before the inhibitor is introduced into the system. Samples were immersed in 0.05 M NaCl, and Ce(III) was introduced at controlled delays of 0, 30, 60, and 180 seconds to estimate the maximum tolerable delay in inhibitor supply without compromising protection. The final inhibitor concentration after inhibitor introduction was 0.001 M. In situ reflected light microscopy was used to monitor real-time surface changes, while SEM-EDX and confocal laser microscopy confirmed the extent of particle degradation and local Ce(III) deposition. Image subtraction was used to determine pixel-by-pixel changes (i.e., pixel activity level). A new quantification approach based on the simplified pixel activity level distribution (sPAD) was implemented to analyse time-dependent changes of pixels on the surface of the IMP and on its adjacent matrix. The sPAD graphically presents the activity level distribution as a function of time and is built from the maximum (maxAL), median (midAL), and minimum (minAL) pixel activity level at each time point. The midAL is the primary focus of the sPAD analysis, while the maxAL and minAL serve as supporting indicators, especially during times when midAL is less responsive to surface changes. Supported by post-immersion SEM and confocal microscopy data, a correlation was established between the IMP midAL at the end of immersion and the extent of Ce(III) precipitation. Furthermore, analysis of the median end-of-immersion midAL across a large number of IMPs showed that longer delays in Ce(III) supply led to greater Ce(III) precipitation. Moreover, even with delayed inhibitor availability, the time when precipitation-associated surface changes slow down (i.e., t_{sp}) and the end-of-immersion midAL values remained lower than those of uninhibited IMPs. This indicates that inhibition of local corrosion still occurred even with supply delays. Criteria based on the median midAL and t_{sp} are developed to determine if the delay duration is tolerable. The criteria require that the median midAL and median t_{sp} at a given delay condition be lower than the median midAL and median t_{sp} of a corresponding uninhibited system. Applying the criteria for the Ce(III)-based system at hand led to an estimated maximum tolerable delay of around 60 s. The findings presented in this chapter suggest that immediate inhibitor availability is not necessary to achieve sufficiently protective inhibition of AA2024.

Chapter 3 extends the analysis of time-dependent Ce(III) availability by examining how corrosion inhibition at the IMP level evolves after initial immersion in a Ce(III)-containing environment, followed by re-immersion in a Ce(III)-free environment. This sequential exposure (i.e., immersion followed by re-immersion) approximates what happens on an exposed AA2024 surface when inhibitor reservoirs in the corrosion protection system are depleted and the system can no longer provide continuous inhibitor supply. Under ideal corrosion protection scenarios, the inhibition layer formed during immersion should remain stable even after the supply is cut off, ensuring sustained protection despite the absence of additional inhibitor. To evaluate the stability of the inhibiting layer, this chapter analyses how local activity across IMP sites develops during the immersion and re-immersion sequence. The findings highlighted that local corrosion behaviour during re-immersion is more varied than the relatively uniform activation observed in IMPs immediately exposed to Ce(III)-free electrolyte. Site-level behaviour was grouped into four categories based on whether localized activity was low or high during immersion (with inhibitor) and re-immersion (without inhibitor): low during both stages (Low/Low), low during immersion but high during re-immersion (Low/High), high during immersion but low during re-immersion (High/Low), and high during both stages (High/High). Mechanisms underlying these categories were proposed by examining the compositional and morphological characteristics of individual IMPs and their surrounding environment. Despite the observed variability, a clear trend emerged: most sites with high-level activity during re-immersion have minimal Ce(III) precipitation during immersion. The impact of exposure duration and inhibitor supply delay during the initial immersion period was subsequently explored. The results show that prolonging the initial immersion duration (e.g., up to 72 h) or slightly delaying inhibitor supply (e.g., 30 seconds) can both lead to fewer active sites during re-immersion, likely due to enhanced local Ce deposition. These findings suggest that active corrosion protection systems could attain better inhibiting layer stability during re-immersion through strategies that promote stronger inhibitor interaction, subject to limits that do not compromise inhibitor effectiveness, such as the tolerable delay criteria proposed in Chapter 2.

*Section 2 (***Chapter 4** and **Chapter 5**) focuses on local corrosion in AA7075-T6, and later, in a galvanically coupled system of AA7075-T6 and AA2024-T3. Despite being a widely used aerospace alloy, AA7075-T6 has been studied less extensively than AA2024-T3. The section begins with a detailed investigation of AA7075-T6's local corrosion behaviour, with particular emphasis on its susceptibility to streaking corrosion. This in-depth analysis provides a foundation for understanding the more complex corrosion behaviour that arises when the two alloys are combined in a multi-metal assembly.

Chapter 4 investigates the initiation and propagation of streaking corrosion in AA7075-T6 using in situ reflected light microscopy and open-circuit potential (OCP) measurements. Streaking corrosion is a lesser-known local corrosion process characterized by rapidly propagating dissolution streaks on the metal surface associated with the attack of an altered surface layer (ASL). Through in situ observation of the AA7075 surface during immersion in 0.05 M NaCl, streaking corrosion is revealed to initiate preferentially at microscale intermetallic particles and, in some cases, at defects. Previous studies have suggested the initiation of ASL dissolution is due to nanoscale structural features present in the surface layer. The simplified pixel activity level distribution approach first introduced in Chapter 2 is used to track changes over time at intermetallic particle sites affected by streaking corrosion. The analysis revealed a temporary suppression of activity increase on the IMP surface when a propagating streak links with the IMP. This is indicative of a previously unreported microgalvanic coupling process between two distinct local corrosion events. Furthermore, electrochemical monitoring identified an OCP transient sequence clearly caused by streaking characterized by an initial drop marking ASL breakdown, followed by high-frequency fluctuations during propagation, and a rapid rise as streaking terminates. This is the first time an OCP transient sequence has been directly attributed to a specific local corrosion event, demonstrating a clear cause-and-effect relationship rather than mere correlation. The findings presented in this chapter demonstrate how site- and time-resolved analysis uncovers interactions between local corrosion events and enhances the interpretation of global electrochemical measurements such as OCP by reconciling its features with specific local events.

Chapter 5 combines the findings from Chapter 4 with the existing understanding of AA2024-T3 local corrosion to explore the influence of macroscale galvanic coupling between AA2024-T3 and AA7075-T6 on their localized corrosion behaviour. This was achieved through in situ reflected light microscopy combined with galvanic current and potential measurements via a zero-resistance ammeter. This integrated approach enabled simultaneous visualization and quantification of microscale corrosion events across both alloys. The findings reveal that galvanic coupling drives electron flow from AA2024 to AA7075, enhancing cathodic activity at IMPs in AA2024 and intensifying local corrosion. This increased cathodic activity leads to corrosion that extends beyond the trenches and seems to affect the overall pH of the AA2024 surface, which apparently reduced the deposition of corrosion products. These changes are observed despite the two alloys not constituting a conventional strong galvanic pair. Based on qualitative analysis of the activity maps, distinct stages of local corrosion for galvanically-coupled AA2024 and AA7075 were identified, namely: (stage 1) dealloying-dominated stage, (stage 2) trenching-dominated stage, and (stage 3) beyond-trench (BT) activity dominated stage. While initial IMP dealloying and trench initiation in stage 1 remain largely unaffected by galvanic coupling, trench propagation in stage 2 is accelerated, contributing to early particle detachment and copper redeposition. This likely triggers the extensive BT activity on the AA2024 side observed in stage 3. On the AA7075 side, the development of extensive streaking corrosion appears to affect the galvanic current density and potential of the couple. This manifests as transients in galvanic current and potential. It is also accompanied by a brief slowdown of stage 2 trench propagation on the AA2024 side and an apparent decrease in the overall extent of trenching on the AA7075 side. The findings of this chapter highlight the impact of macroscale galvanic interactions in altering localized corrosion processes and emphasize that even weak galvanic coupling can still have a substantial effect on corrosion behaviour. This chapter also underscores that complex interactions can only be fully understood through site- and time-resolved analysis. By directly linking localized surface events to global electrochemical responses, the combined use of optical and electrochemical techniques reveals mechanisms that would otherwise remain hidden, highlighting the power of this integrated approach for studying corrosion in multi-material systems.

In summary, this dissertation shows that a simple hyphenated optical-electrochemical system, combined with a robust and sensitive optical activity quantification protocol, can enable effective site- and time-resolved analysis of local corrosion and inhibition in aerospace aluminium alloys. This approach proves to be a powerful tool for characterizing the diverse local behaviours of corrosion and inhibition, identifying interactions between local processes - both within individual alloys and across dissimilar materials - and directly linking specific surface processes to their electrochemical responses. The key conclusions drawn from this work are as follows:

- The extent of inhibitor precipitation correlates strongly with optically measured activity levels, establishing optical analysis as a reliable tool for tracking local inhibition behaviour (**Chapter 2**).
- Introducing Ce(III) after slight dealloying of AA2024 intermetallic particles (IMPs) significantly increases inhibitor precipitation. Despite the slight corrosion, effective inhibition can still occur, as long as precipitation-associated surface activity stabilizes more quickly than corrosion-associated surface activity of corresponding uninhibited systems (**Chapter 2**).
- Re-immersion behaviour is highly variable, but most unstable IMPs are those showing low activity levels during the initial immersion in the inhibitor-containing solution. Enhancing immersion activity, through increased Ce(III) precipitation, can improve re-immersion stability of the inhibiting layers (**Chapter 3**).
- Initiation of the dissolution of altered or deformed surface layers (i.e., streaking corrosion) in AA7075-T6 is predominantly triggered by intermetallic particles. Streaking corrosion propagation also leads to optically-detectable microgalvanic interactions with intermetallic particles linked to it (**Chapter 4**).
- Time-aligned in situ reflected microscopy and open-circuit potential measurements allows identification of local corrosion events that cause specific OCP transient sequences (**Chapter 4**).
- Macroscale galvanic coupling between dissimilar aluminium alloys leads to aggravation of local corrosion processes. Site- and time-resolved analysis of local corrosion in this multi-material systems can thus provide more distinct insights than just a global comparison of the degree of corrosion (**Chapter 5**).

Several opportunities for further investigation have also been identified based on the findings of this work. These are divided into technique-based and materials-based opportunities. Technique-based opportunities are research paths that can help further advance the current approach for site- and time-resolved analysis. Materials-based opportunities pertain to lines of inquiry that might benefit from the site- and time-resolved approach. The opportunities identified are listed below. The first four opportunities are technique-based while the last two are materials-based.

- **Combined brightfield and darkfield illumination**: The in situ imaging used in this work mainly relies on brightfield illumination, which captures light that is directly reflected from the sample surface. In contrast, darkfield illumination captures only the scattered light, highlighting surface features such as pit walls or roughness. Brightfield images can be used to relate optical signals to microstructural features (e.g., deposition thickness), but doing so often requires detailed knowledge of the system and additional ex situ tests. By capturing both brightfield and darkfield images during in situ analysis, it becomes possible to gather complementary data that can help identify and characterize surface features without relying as much on ex situ characterization. Many commercially available digital microscopes already support both illumination modes. However, switching between them can reduce temporal resolution, since it takes time to alternate between brightfield and darkfield imaging. Integrating the two types of images to obtain sensible quantitative data is also a hurdle that needs to be addressed.

- **Electrochemical transient analysis**: OCP measurements in Chapter 4 and galvanic current and potential measurements in Chapter 5 highlight how local corrosion processes like streaking corrosion can have distinct transient sequences. The current work provided potential explanations for the rise of these transients. Nonetheless, a more detailed quantitative analysis of these transients alongside a closer look at the optics-based kinetics of streaking corrosion propagation, can further unravel the nature of these transients. Furthermore, given that the propagation of streaking corrosion is matched by the duration of high frequency transients, it might be possible to estimate the fraction of the surface affected by streaking corrosion just from electrochemical data.
- **From optics to mechanical:** The site- and time-resolved approach used in this work focuses on observing local corrosion and inhibition through optical methods. However, the ultimate goal of corrosion control is to preserve the mechanical integrity of aerospace aluminium alloys. To make this optical approach more relevant for industry, the observations should be connected to mechanical performance. By analysing optical data from many sites and relating it to mechanical behaviour, we can identify how much surface activity is acceptable before mechanical properties are compromised. This can help assess whether a system with active corrosion protection remains structurally sound.
- **Modelling optically-observed changes**: Although it is difficult to directly convert optical activity from reflected light microscopy into exact reaction rates, the time-dependent evolution of this activity provides insight into how surface changes develop. Time-based optical parameters such as the onset of dealloying or the point when

trenching becomes dominant can thus help improve physics-based models of local corrosion and inhibition in aluminium alloys.

- **Inhibiting layer build-up**: The inhibitor exposure conditions in this study are based on a single, continuous immersion period. In contrast, real-world environments often involve intermittent exposure, where the metal surface undergoes repeated wet–dry cycles. During drying, the inhibitor may be washed away with the electrolyte or left behind as a residue due to evaporation. In the subsequent wet cycle, inhibitor levels can be replenished, for example, by leaching from embedded reservoirs in organic coatings. Understanding how these cyclic exposure conditions affect the local formation and stability of inhibiting layers is key to explaining the long-term corrosion protection performance observed in systems subjected to wet–dry cycling in the literature.
- **Inhibition of galvanically-coupled dissimilar alloys**: Local corrosion analysis of galvanically coupled AA2024-T3 and AA7075-T6 showed changes in their local corrosion behaviour relative to metals corroding on their own under open-circuit conditions. Understanding how the galvanic coupling impacts the performance of corrosion inhibitors such as Ce(III) can provide further insights on how to mitigate corrosion in such multi-material systems.

Samenvatting

Het hoofddoel van dit proefschrift is het verdiepen van het begrip van lokale corrosie en inhibitie in aluminium vliegtuiglegeringen door het toepassen van in situ gereflecteerde lichtmicroscopie, geïntegreerd met elektrochemische metingen, om systematisch het gedrag van een groot aantal intermetallische deeltjes en andere lokale corrosieplaatsen te analyseren. Deze techniek levert locatie-specifieke datasets met een hoge ruimtelijke en temporele resolutie, waarmee de diverse en dynamische aard van lokale corrosieverschijnselen kan worden vastgelegd. Om deze informatie ten volle te benutten, zijn nieuwe ontwikkelingen op het gebied van gegevensverwerking en -analyse geïmplementeerd, waarmee tijdsafhankelijke parameters konden worden geëxtraheerd en lokale corrosie- en inhibitiegedragingen op robuuste wijze konden worden geclassificeerd. Deze vooruitgang heeft geleid tot nieuwe mechanistische inzichten in hoe corrosie- en inhibitieprocessen initiëren, zich ontwikkelen en met elkaar interageren binnen verschillende microstructuren aan het legeringsoppervlak onder uiteenlopende omgevingscondities. Cruciaal is dat deze benadering verder gaat dan geïsoleerde waarnemingen van individuele locaties, waardoor een breder en representatiever inzicht in het lokale gedrag over het gehele materiaal wordt verkregen. Dit bredere perspectief biedt inzichten die kunnen bijdragen aan de ontwikkeling van meer gerichte en efficiënte strategieën voor actieve corrosiebescherming.

Hoofdstuk 1 introduceert de twee vliegtuiglegeringen die in dit werk zijn bestudeerd, AA2024-T3 en AA7075-T6, en beschrijft de rol van corrosie-inhibitoren in hun actieve bescherming. Daarnaast wordt een overzicht gegeven van de huidige lokale karakteriseringstechnieken die worden gebruikt om corrosie en inhibitie in deze legeringen te bestuderen. Deze technieken worden systematisch geëvalueerd op basis van belangrijke prestatiecriteria: ruimtelijke resolutie, mate van morfologische en chemische informatie, en de tijd die nodig is om een oppervlak te meten. Deze vergelijkende analyse brengt de specifieke sterke punten en afwegingen van elke methode in kaart en toont aan dat geen enkele techniek op alle vlakken uitblinkt. Met name blijkt dat gereflecteerde lichtmicroscopie uniek is in het combineren van een goede meettijd voor grotere oppervlakken met voldoende ruimtelijke resolutie om veranderingen op individuele locaties waar te nemen, zij het met een beperkte

informatiediepte. Strategieën om deze beperking te ondervangen, zoals integratie met complementaire technieken, worden kort besproken. Het hoofdstuk wordt afgesloten met de formulering van de doelstelling van dit werk, waarbij de rol van gereflecteerde lichtmicroscopie in het realiseren van deze doelstelling wordt benadrukt, en een overzicht wordt gegeven van de opbouw van de volgende hoofdstukken.

Sectie 1 (**Hoofdstuk 2** en **Hoofdstuk 3**) richt zich op lokale corrosie-inhibitie van AA2024-T3. Lokale corrosie van AA2024-T3 is al uitgebreid onderzocht, evenals het inhibitiegedrag in aanwezigheid van een breed scala aan corrosive-inhibitoren. Minder aandacht is echter besteed aan de vraag hoe veranderingen in de beschikbaarheid van de remmer de lokale corrosie en inhibitie in de tijd beïnvloeden. Deze sectie onderzoekt dit aspect van inhibitie aan de hand van $Ce(NO_3)_3$, ook wel Ce(III) genoemd, als modelremmer, en analyseert hoe de tijdsafhankelijke beschikbaarheid ervan invloed heeft op lokale oppervlakteveranderingen.

Hoofdstuk 2 analyseert hoe de tijdsafhankelijke beschikbaarheid van Ce(III) tijdens de beginfase van blootstelling aan een corrosieve omgeving de corrosie-inhibitie bij intermetallische deeltjes (IMPs) van verschillende samenstellingen beïnvloedt. In het bijzonder onderzoekt dit hoofdstuk hoe de effectiviteit van inhibitie wordt beïnvloed wanneer de toevoer van Ce(III) wordt vertraagd, waardoor IMP-ontlegering en vorming van omringende sleuven (trenching) kunnen optreden voordat de inhibitor in het systeem wordt gebracht. Monsters werden ondergedompeld in 0.05 M NaCl en Ce(III) werd toegevoegd met gecontroleerde vertragingen van 0, 30, 60 en 180 seconden om de maximale toelaatbare vertraging in de inhibitortoevoer zonder verlies aan bescherming te bepalen. De uiteindelijke inhibitorconcentratie na toevoeging bedroeg 0.001 M. In situ gereflecteerde lichtmicroscopie werd gebruikt om realtime oppervlakteveranderingen te volgen, terwijl SEM-EDX en confocale lasermicroscopie de mate van deeltjesdegradatie en lokale Ce(III)-neerslag bevestigden. Beeldsubtractie werd toegepast om pixel-voor-pixel veranderingen (de zogeheten pixelactiviteitsniveaus) te bepalen. Een nieuwe kwantificatiemethode op basis van de vereenvoudigde verdeling van pixelactiviteitsniveaus (sPAD) werd geïmplementeerd om tijdsafhankelijke veranderingen van pixels op het oppervlak van het IMP en op de aangrenzende matrix te analyseren. De sPAD geeft grafisch de verdeling van het activiteitsniveau weer als functie van de tijd en wordt opgebouwd uit het maximale (maxAL), mediane (midAL) en minimale (minAL) pixelactiviteitsniveau op elk tijdstip. De midAL vormt de kern van de sPAD-analyse, terwijl maxAL en minAL fungeren als ondersteunende indicatoren, vooral in perioden waarin de midAL minder gevoelig is voor veranderingen aan het oppervlak. Met ondersteuning van post-immersie SEM- en confocale data werd een correlatie vastgesteld tussen de IMP midAL aan het einde van de immersie en de mate van Ce(III)-precipitatie. Bovendien toonde de analyse van de mediane eind-midAL over een groot aantal IMPs aan dat langere vertragingen in Ce(III)-toevoer tot meer Ce(III)-precipitatie leidden. Ondanks de vertraagde beschikbaarheid van de inhibitor bleven de tijd waarop de door precipitatie-gerelateerde oppervlakteveranderingen vertraagden (t_{sp}) en de midAL-waarden aan het einde van de onderdompeling lager dan die van IMP's zonder inhibitor. Dit geeft aan dat inhibitie van lokale corrosie nog steeds plaatsvond, zelfs bij vertraagde toevoer. Er werden criteria ontwikkeld op basis van de mediane midAL en t_{sp} om te bepalen of een bepaalde vertraging nog toelaatbaar is. De criteria vereisen dat zowel de mediane midAL als de mediane t_{sp} bij een bepaalde vertraging lager zijn dan die van een overeenkomstig systeem zonder inhibitor. Toepassing van deze criteria voor het onderzochte Ce(III)-systeem leidde tot een geschatte maximale toelaatbare vertraging van ongeveer 60 seconden. De bevindingen in dit hoofdstuk suggereren dat onmiddellijke beschikbaarheid van de inhibitor niet noodzakelijk is om voldoende bescherming tegen corrosie in AA2024 te bereiken.

Hoofdstuk 3 breidt de analyse van de tijdsafhankelijke beschikbaarheid van Ce(III) uit door te onderzoeken hoe corrosie-inhibitie op het niveau van intermetallische deeltjes (IMPs) zich ontwikkelt na een initiële onderdompeling in een Ce(III)-bevattende omgeving, gevolgd door een heronderdompeling in een omgeving zonder Ce(III). Deze sequentiële blootstelling (d.w.z. onderdompeling gevolgd door heronderdompeling) benadert wat er gebeurt op een blootgesteld AA2024-oppervlak wanneer de inhibitorreservoirs in het corrosiebeschermingssysteem zijn uitgeput en het systeem geen continue inhibitortoevoer meer kan bieden. In een ideaal scenario voor corrosiebescherming zou de inhibitie-laag die tijdens de initiële onderdompeling is gevormd, stabiel moeten blijven nadat de toevoer wordt stopgezet, zodat de bescherming behouden blijft ondanks de afwezigheid van extra inhibitor. Om de stabiliteit van deze inhibitie-laag te evalueren, analyseert dit hoofdstuk hoe de lokale activiteit op IMP-locaties zich ontwikkelt tijdens de onderdompelings- en heronderdompelingsequentie. De resultaten laten zien dat het lokale corrosiegedrag tijdens heronderdompeling veel gevarieerder is dan de relatief uniforme activatie die werd waargenomen bij IMPs die direct werden blootgesteld aan een Ce(III)-vrije elektrolyt. Het gedrag op deeltjesniveau werd ingedeeld in vier categorieën, afhankelijk van of de lokale activiteit laag of hoog was tijdens de onderdompeling (met inhibitor) en heronderdompeling (zonder inhibitor): laag in beide fasen (Laag/Laag), laag tijdens onderdompeling maar hoog tijdens heronderdompeling (Laag/Hoog), hoog tijdens onderdompeling maar laag tijdens heronderdompeling (Hoog/Laag), en hoog in beide fasen (Hoog/Hoog). De onderliggende mechanismen van deze categorieën werden verklaard door de samenstelling en morfologie van individuele IMPs en hun directe omgeving te bestuderen. Ondanks de waargenomen variatie kwam een duidelijke trend naar voren: de meeste locaties met hoge activiteit tijdens heronderdompeling vertoonden minimale Ce(III)-precipitatie tijdens de initiële onderdompeling. Vervolgens werd het effect onderzocht van zowel de blootstellingsduur als de vertraging in inhibitortoevoer tijdens de initiële onderdompeling. De resultaten tonen aan dat het verlengen van de initiële onderdompeling (bijvoorbeeld tot 72 uur) of een lichte vertraging van de inhibitortoevoer (bijvoorbeeld 30 seconden) beide kunnen leiden tot minder actieve locaties tijdens heronderdompeling, waarschijnlijk als gevolg van verbeterde lokale Ce-afzetting. Deze bevindingen suggereren dat actieve corrosiebeschermingssystemen een betere stabiliteit van de inhibitie-laag tijdens heronderdompeling kunnen bereiken via strategieën die sterkere interactie met de inhibitor bevorderen, mits binnen grenzen die de effectiviteit van de inhibitor niet ondermijnen, zoals de toelaatbare vertraging die in Hoofdstuk 2 werd voorgesteld.

Sectie 2 (**Hoofdstuk 4** en **Hoofdstuk 5**) richt zich op lokale corrosie in AA7075-T6, en later op een galvanisch gekoppeld systeem van AA7075-T6 en AA2024-T3. Ondanks het feit dat AA7075-T6 een veelgebruikte legering is in de luchtvaart, is deze minder uitgebreid bestudeerd dan AA2024-T3. De sectie begint met een gedetailleerd onderzoek naar het lokale corrosiegedrag van AA7075-T6, met bijzondere aandacht voor de gevoeligheid voor streaking corrosion. Deze diepgaande analyse vormt de basis voor het begrijpen van het meer complexe corrosiegedrag dat ontstaat wanneer beide legeringen worden gecombineerd in een multi-metaalsamenstelling.

Hoofdstuk 4 onderzoekt de initiatie en voortplanting van streaking corrosion in AA7075-T6 met behulp van in situ gereflecteerde lichtmicroscopie en metingen van het open-circuit potentiaal (OCP). Streaking corrosion is een minder bekend lokaal corrosieproces dat wordt gekenmerkt door snel voortplantende oplossingsstrepen op het metaaloppervlak, geassocieerd met de aantasting van een gewijzigde oppervlaktelaag (ASL). Door in situ observatie van het AA7075-oppervlak tijdens onderdompeling in 0,05 M NaCl blijkt dat streaking corrosion bij voorkeur initieert aan microschaal intermetallische deeltjes, en in sommige gevallen aan defecten. Eerdere studies suggereerden dat de initiatie van ASL-oplossing wordt veroorzaakt door nanostructurele kenmerken in de oppervlaktelaag. De vereenvoudigde verdeling van pixelactiviteitsniveaus (zoals geïntroduceerd in Hoofdstuk 2) wordt gebruikt om veranderingen in de tijd te volgen op intermetallische deeltjes die zijn beïnvloed door streaking corrosion. De analyse toonde een tijdelijke onderdrukking van activiteitsverhoging op het IMP-oppervlak wanneer een voortschrijdende streep met het deeltje in contact komt. Dit wijst op een eerder niet gerapporteerd microgalvanisch koppelingsproces tussen twee verschillende lokale corrosieprocessen. Bovendien identificeerde elektrochemische monitoring een specifieke OCP-transientreeks die duidelijk werd veroorzaakt door streaking corrosion. Deze wordt gekenmerkt door een initiële spanningsval bij het afbreken van de ASL, gevolgd door hoge-frequentiefluctuaties tijdens de voortschrijdende, en een snelle stijging bij beëindiging van de streaking. Het is de eerste keer dat een OCP-transientsequentie direct is toegeschreven aan een specifiek lokaal corrosieverschijnsel, waarmee een duidelijke oorzaak-gevolgrelatie wordt aangetoond in plaats van slechts een correlatie. De bevindingen in dit hoofdstuk tonen aan hoe site- en tijdsresolutieanalyse interacties tussen lokale corrosieprocessen aan het licht brengt en de interpretatie van globale elektrochemische metingen zoals OCP verbetert, door kenmerken ervan direct te koppelen aan specifieke lokale gebeurtenissen.

Hoofdstuk 5 combineert de bevindingen uit Hoofdstuk 4 met bestaande inzichten in lokale corrosie van AA2024-T3 om de invloed te onderzoeken van macroschaal galvanische koppeling tussen AA2024-T3 en AA7075-T6 op hun lokale corrosiegedrag. Dit werd gerealiseerd door in situ gereflecteerde lichtmicroscopie te combineren met metingen van galvanische stroom en potentiaal via een nulweerstandsammeter. Deze geïntegreerde benadering maakte het mogelijk om gelijktijdig microschaal corrosieprocessen op beide legeringen zowel visueel waar te nemen als kwantitatief te analyseren. De resultaten tonen aan dat galvanische koppeling een elektronenstroom van AA2024 naar AA7075 induceert, wat leidt tot verhoogde kathodische activiteit op de IMP’s in AA2024 en een intensivering van lokale corrosie. Deze verhoogde kathodische activiteit leidt tot corrosie die zich uitbreidt voorbij de trenchgebieden en blijkbaar het pH-niveau aan het AA2024-oppervlak beïnvloedt, wat op zijn beurt de afzetting van corrosieproducten lijkt te verminderen. Deze veranderingen worden waargenomen ondanks het feit dat de twee legeringen geen klassiek sterk galvanisch paar vormen. Op basis van kwalitatieve analyse van lateraal geresolveerde activiteit konden drie duidelijke fasen van lokale corrosie voor galvanisch gekoppeld AA2024 en AA7075 worden geïdentificeerd, namelijk: (fase 1) ontlegering-gedomineerde fase, (fase 2) trenching-gedomineerde fase, en (fase 3) fase met activiteit voorbij de trench (beyond-trench, BT). Terwijl de initiële ontlegering en trenchinitiatie van IMP’s in fase 1 grotendeels onaangetast blijven door galvanische koppeling, wordt trenchpropagatie in fase 2 versneld, wat bijdraagt aan vroegtijdige ondergraving van deeltjes en koperherafzetting. Dit lijkt de intensieve BT-activiteit op het AA2024-oppervlak in fase 3 te veroorzaken. Aan de kant van AA7075 blijkt de ontwikkeling van uitgebreide streaking corrosion invloed te hebben op de galvanische stroomdichtheid en potentiaal van het koppel. Dit komt tot uiting in transiënten in galvanische stroom en potentiaal. Het gaat ook gepaard met een tijdelijke vertraging van de trenchpropagatie in fase 2 op het AA2024-oppervlak en een zichtbare afname van de trenchomvang aan de AA7075-zijde. De bevindingen in dit hoofdstuk benadrukken dat macroschaal galvanische interacties lokale corrosieprocessen aanzienlijk kunnen beïnvloeden, zelfs wanneer de galvanische koppeling relatief zwak is. Daarnaast onderstreept dit hoofdstuk dat dergelijke complexe interacties alleen volledig begrepen kunnen worden via site- en tijdsopgeloste analyse. Door lokale oppervlaktestructuurveranderingen direct te koppelen aan globale elektrochemische respons, onthult de gecombineerde inzet van optische en elektrochemische technieken mechanismen die anders verborgen zouden blijven, wat het krachtige potentieel van deze geïntegreerde aanpak voor het bestuderen van corrosie in multimateriële systemen aantoont.

Samenvattend laat dit proefschrift zien dat een eenvoudig gekoppeld optisch-elektrochemisch systeem, gecombineerd met een robuust en gevoelig protocol voor optische activiteitskwantificatie, effectieve site- en tijdsopgeloste analyse van lokale corrosie en inhibitie aluminium vliegtuiglegeringen mogelijk maakt. Deze benadering blijkt een krachtig instrument te zijn voor het karakteriseren van de diverse lokale uitingen van corrosie en inhibitie, het identificeren van interacties tussen lokale processen, zowel binnen individuele legeringen als tussen verschillende materialen, en het direct koppelen van specifieke oppervlakteveranderingen aan hun elektrochemische respons. De belangrijkste conclusies van dit werk zijn als volgt:

- De mate van inhibitorprecipitatie correleert sterk met optisch gemeten activiteitsniveaus, waarmee optische analyse wordt vastgesteld als een betrouwbare methode voor het volgen van lokaal inhibitiegedrag (**Hoofdstuk 2**).
- Het toevoegen van Ce(III) na lichte onlegering van intermetallische deeltjes (IMPs) in AA2024 leidt tot een aanzienlijke toename van inhibitorprecipitatie. Ondanks de lichte corrosie kan er nog steeds effectieve inhibitie optreden, zolang de door precipitatie-gerelateerde oppervlakteactiviteit sneller stabiliseert dan de corrosie-gerelateerde oppervlakteactiviteit van overeenkomstige niet-geïnhibeerde systemen (**Hoofdstuk 2**).

- Het heronderdompelingsgedrag is sterk variabel, maar de meeste instabiele IMPs vertonen lage activiteitsniveaus tijdens de initiële onderdompeling in de inhibitorhoudende oplossing. Verhoging van de activiteit tijdens onderdompeling, bijvoorbeeld via toegenomen Ce(III)-precipitatie, kan de stabiliteit van de inhibitie-laag tijdens heronderdompeling verbeteren (**Hoofdstuk 3**).
- De initiatie van de oplossing van gewijzigde of gedeformeerde oppervlaktelagen (i.e., *streaking corrosion*) in AA7075-T6 wordt voornamelijk veroorzaakt door intermetallische deeltjes. De voortplanting van streaking corrosion leidt bovendien tot optisch detecteerbare microgalvanische interacties met intermetallische deeltjes waaraan de streep gekoppeld is (**Hoofdstuk 4**).
- Tijdgecoördineerde in situ gereflecteerde microscopie en open-circuit potentiaalmetingen maken het mogelijk om lokale corrosieprocessen te identificeren die specifieke OCP-transiëntsequenties veroorzaken (**Hoofdstuk 4**).
- Macroschaal galvanische koppeling tussen verschillende aluminiumlegeringen leidt tot verergering van lokale corrosieprocessen. Site- en tijdgeresolveerde analyse van lokale corrosie in dergelijke multimateriële systemen biedt daarom meer onderscheidende inzichten dan een louter globale vergelijking van de mate van corrosie (**Hoofdstuk 5**).

Op basis van de bevindingen in dit werk zijn ook verschillende mogelijkheden voor vervolgonderzoek geïdentificeerd. Deze zijn onderverdeeld in techniekgerichte en materiaalgerichte onderzoekskansen. Techniekgerichte kansen betreffen onderzoekspaden die kunnen bijdragen aan de verdere ontwikkeling van de huidige methode voor site- en tijdsopgeloste analyse. Materiaalgerichte kansen hebben betrekking op onderzoeksvragen waarbij de site- en tijdsopgeloste aanpak mogelijk nieuwe inzichten kan opleveren. De geïdentificeerde onderzoekskansen worden hieronder opgesomd. De eerste vier zijn techniekgericht, de laatste twee zijn materiaalgericht.

- **Gecombineerde helder- en donkerveld-verlichting**: De in situ beeldvorming die in dit werk is gebruikt, maakt voornamelijk gebruik van helderveld-verlichting, waarbij licht wordt vastgelegd dat direct wordt gereflecteerd door het monsteroppervlak. Donkerveld-verlichting daarentegen registreert alleen verstrooid licht en benadrukt oppervlaktekenmerken zoals putwanden of ruwheid. Helderveld-beelden kunnen worden gebruikt om optische signalen te relateren aan microstructurele kenmerken (zoals afzetdikte), maar dit vereist vaak gedetailleerde kennis van het systeem en aanvullende ex situ tests. Door zowel helderveld- als donkerveld-beelden vast te leggen tijdens in situ analyse, kan aanvullende informatie worden verkregen die helpt bij het identificeren en karakteriseren van oppervlaktekenmerken, zonder al te veel afhankelijkheid van ex situ karakterisatie. Veel commercieel verkrijgbare digitale microscopen ondersteunen beide verlichtingsmodi al. Het schakelen tussen de modi kan echter de temporele resolutie verlagen, omdat het tijd kost om tussen helderveld en donkerveld te wisselen. Ook vormt het integreren van beide beeldtypes tot zinvolle kwantitatieve data een uitdaging die nog moet worden opgelost.

- **Analyse van elektrochemische transiënten**: De OCP-metingen in Hoofdstuk 4 en de galvanische stroom- en potentiaalmetingen in Hoofdstuk 5 tonen aan dat lokale corrosieprocessen, zoals streaking corrosion, duidelijke transiëntsequenties kunnen veroorzaken. In dit werk zijn mogelijke verklaringen gegeven voor het ontstaan van deze transiënten. Niettemin kan een meer gedetailleerde kwantitatieve analyse van deze transiënten, in combinatie met een diepere kijk op de optisch gebaseerde kinetiek van streaking corrosion-voortschrijding, verdere inzichten bieden in de aard van deze signalen. Aangezien de propagatie van streaking corrosion lijkt samen te vallen met de duur van hoge-frequentie transiënten, zou het mogelijk zijn om het oppervlakpercentage dat wordt beïnvloed door streaking uitsluitend op basis van elektrochemische gegevens te schatten.
- **Van optisch naar mechanisch:** De in dit werk gebruikte site- en tijdgeresolveerde benadering richt zich op het observeren van lokale corrosie en inhibitie via optische methoden. Het uiteindelijke doel van corrosiebestrijding is echter het behoud van de mechanische integriteit van aluminium vliegtuiglegeringen. Om deze optische benadering relevanter te maken voor industriële toepassingen, moeten de waarnemingen worden gekoppeld aan mechanische prestaties. Door optische gegevens van een groot aantal locaties te analyseren en te relateren aan mechanisch gedrag, kan worden bepaald hoeveel oppervlakteactiviteit nog toelaatbaar is voordat de mechanische eigenschappen in het gedrang komen. Dit kan helpen om te beoordelen of een systeem met actieve corrosiebescherming structureel betrouwbaar blijft.
- **Modelleren van optisch waargenomen veranderingen:** Hoewel het moeilijk is om optische activiteit uit gereflecteerde-lichtmicroscopie direct om te zetten in exacte reactiesnelheden, biedt de tijdsafhankelijke evolutie van deze activiteit inzicht in hoe veranderingen aan het oppervlak zich ontwikkelen. Tijdgebaseerde optische parameters, zoals het begin van de ontlegering of het moment waarop trenchvorming

dominant wordt, kunnen daarom helpen bij het verbeteren van fysische modellen van lokale corrosie en inhibitie in aluminiumlegeringen.

- **Opbouw van de inhibitie-laag**: De inhibitorblootstellingsomstandigheden in deze studie zijn gebaseerd op een enkele, continue onderdompelingsperiode. In werkelijkheid zijn blootstellingen vaak intermitterend en ondergaat het metaaloppervlak herhaalde nat-droog cycli. Tijdens de droogfase kan de inhibitor samen met het elektrolyt worden weggespoeld of als residu achterblijven door verdamping. In de daaropvolgende natte cyclus kan het inhibitorgehalte worden aangevuld, bijvoorbeeld door uitloging uit ingebedde reservoirs in organische coatings. Begrijpen hoe deze cyclische blootstellingsomstandigheden de lokale vorming en stabiliteit van inhibitie-lagen beïnvloeden is essentieel om de langetermijnprestaties van corrosiebescherming te verklaren die in literatuur zijn waargenomen onder nat-droog omstandigheden.
- **Inhibitie van galvanisch gekoppelde ongelijksoortige legeringen**: De analyse van lokale corrosie in galvanisch gekoppeld AA2024-T3 en AA7075-T6 toonde veranderingen aan in hun corrosiegedrag ten opzichte van de toestand waarin de legeringen afzonderlijk corroderen onder open-circuitcondities. Begrijpen hoe galvanische koppeling de werking van corrosieinhibitoren zoals Ce(III) beïnvloedt, kan extra inzichten opleveren voor het tegengaan van corrosie in dergelijke multi-materiële systemen.

Paglalagom

Ang pangunahing layunin ng disertasyong ito ay palalimin ang pag-unawa sa lokal na proseso ng pangangalawang at inhibisyon nito sa mga aluminyong haluang-metal na ginagamit sa industriyang panghimpapawid. Ito ay inaral sa pamamagitan ng *in situ reflected light microscopy* katambal ang iba't ibang uri ng elektrokemikal na pagsusukat upang sistematikong masuri ang lokal na pagbabago ng malaking koleksyon ng mga intermetalikong partikel at iba pang lokasyon ng pangangalawang. Ang pamamaraang ito ay nagbunga ng mga datos na base sa maraming lokasyon at nagtataglay ng mataas na resolusyong espasyo at resolusyong oras. Ang mga datos na ito ay nakapagtatala ng iba-ibang katangian ng mga penomenang kaugnay ng lokal na pangangalawang. Upang lubos na magamit ang mga nakolektang datos, ang proseso ng kanilang pagsusuri ay pinagtibay. Ang panibagong proseso ng pagsusuri ay nagbigay-daan sa pagkamit ng mga parametrong base sa oras at komprehensibong klasipikasyon ng iba't ibang proseso ng lokal na pangangalawang at inhibisyon. Ang mga pagbabagong ito ay nagbunga ng mga panibagong mekanistikong pananaw ukol sa pagsisimula at pag-progreso ng lokal na pangangalawang at inbisyon, maging sa kung paano nila inaapektuhan ang bawat isa. Ang proseso ng pagsusuri na sentro sa disertasyong ito ay nagbigay-daan din sa mas malawak at mas representatibong pag-unawa sa mga lokal na pagbabago sa kabuuan ng materyal. Ito ay dahil tinitingnan ng naturang proseso ang koleksyon ng datos mula sa iba't ibang lokasyon sa halip na ang iilan-ilang indibidwal na obserbasyon. Sa huli, ang kaalamang nakamit mula sa pag-aaral na ito ay maaaring magamit sa pagbuo ng mas tiyak at mas mabisang mga estratehiya para sa aktibong pagkontra ng pangangalawang.

Ipinakikilala sa **Kabanata 1** ang dalawang aluminyong haluang-metal na inaral sa disertasyong ito, ang AA2024-T3 at AA7075-T6. Inilalarawan rin dito ang papel ng mga inhibitor, mga kemikal na ginagamit para sa inhibisyon ng pangangalawang, sa aktibong pagprotekta ng mga naturang metal. Tinatalakay rin dito ang mga kasalukuyang lokal na teknik sa karakterisasyon na ginagamit upang pag-aralan ang pangangalawang at inhibisyon nito. Ang mga teknik na ito ay sistematikong pinaghambing batay sa mga pangunahing kategorya ng perpormans: resolusyong espasyo, lalim ng impormasyong morpolohikal at kemikal, at oras ng pagsukat ng partikular na lugar. Ipinapakita ng paghahambing na ito ang mga kalakasan at kahinaan ng

bawat pamamaraan. Binibigyang-diin din ng paghahambing na walang iisang teknik na nangingibabaw sa lahat ng kategorya. Sa kabila nito, ang *reflected light microscopy* (RLM) ay nagpakita ng interesanteng potensyal dahil sa kakayahan nitong sukatin ng mabilis ang iba't ibang lugar kasabay ng pagbibigay ng mataas na resolusyong espasyo. Dahil dito, maaaring gamitin ang teknik upang epektibong maobserbahan ang mabilis na pagbabago sa mga lokal na lokasyon ng pangangalawang. Sa kabilang banda, limitado ang lalim ng impormasyong naibibigay ng teknik na ito kaya't maikli ring tinalakay ang mga estratehiya para mabawasan ang limitasyong ito. Isang halimbawa ay ang pagtatambal nito sa mga teknik na nagbibigay ng komplementaryong impormasyon. Nagtatapos ang kabanata sa pagpapahayag ng layunin ng disertasyong ito kasabay ng pagbibigay diin sa papel ng RLM sa pagtamo ng mga nasabing layunin at paglalahad ng balangkas ng mga susunod na kabanata.

Nakatuon ang **Seksyon 1 (Kabanata 2** at **Kabanata 3)** sa lokal na inhibisyon ng pangangalawang ng AA2024-T3. Ang lokal na pangangalawang ng AA2024-T3 sa ilalim ng impluwensiya ng iba't ibang uri ng inhibitor ay masusi nang pinag-aralan ng mga dalubhasa. Gayunpaman, ang epekto sa lokal na pangangalawang ng pagbabago ng konsentrasyon o presensya depende sa oras ng mga inhibitor ay hindi pa lubusang nasusuri. Ang aspetong ito ay binusisi gamit ang $Ce(NO_3)_3$, o Ce(III), bilang modelong inhibitor.

Sinusuri sa **Kabanata 2** kung paano naaapektuhan ng presensya ng Ce(III) na nakadepende sa oras ang inhibisyon ng mga intermetalikong partikel (IMPs) na may iba't ibang komposisyon. Binibigyang pansin sa kabanatang ito kung paano bumababa ang bisa ng inhibisyon kapag inantala ang pagdagdag ng Ce(III) sa sistema sa mga unang sandali ng pangangalawang. Ang mga sampol ng AA2024-T3 ay inilubog sa 0.05 M NaCl kasunod ang pagdadagdag ng Ce(III) matapos ang 0, 30, 60, at 180 segundo. Ang pag-antala ay nagsilbing basehan upang matantiya kung gaano katagal maaaring payagang mangalawang ang metal bago ito ilantad sa inhibitor nang hindi kinokompromiso ang proteksiyon. Ang total na konsentrasyon ng inhibitor pagkatapos ng pagdagdag ay 0.001 M. Ginamit ang *in situ* RLM (iRLM) para masubaybayan ang pagbabago ng mga sampol. Ginamit din ang scanning electron microscopy katambal ang energy dispersive X-ray spectroscopy (SEM-EDX) at confocal laser microscopy (CLM) upang makumpirma ang antas ng lokal na pangangalawang at lokal na deposisyon ng Ce(III). Ang pagbabago sa bawat piksel (pixel activity level) sa mga imaheng nakuha mula sa iRLM ay nasukat gamit ang proseso ng pagmemenos ng mga larawan. Pinatupad ang bagong paraan ng pagsusukat na nakasentro sa konsepto ng simplified pixel activity level distribution (sPAD) upang masuri ang mga pagbabagong nakadepende sa oras ng mga piksel ng IMP at ng pumapaligid na *matrix*. Ang sPAD ay maaaring butingtingin sa anyo ng grap na naglalarawan ng distribusyon ng antas ng aktibidad depende sa oras. Ang grap ay binuo mula sa pinakamataas (maxAL), panggitna (midAL), at pinakamababang (minAL) antas ng aktibidad sa bawat punto ng pagsusukat. Ang midAL ang pangunahing pokus ng sPAD, habang ang maxAL at minAL ay mga pantulong na indikasyon, lalo na kung mababa ang sensitibidad ng midAL sa mga pagbabagong dulot ng pangangalawang. Batay sa mga datos mula sa SEM-EDX at CLM na nakuha matapos ang paglulubog, natukoy ang ugnayan ng midAL ng IMP sa pagtatapos ng paglubog at ng antas ng pagdedeposito ng Ce(III). Napag-alaman din na kahit may pagkaantala sa pagdadagdag ng inhibitor, nananatiling mas maiksi ang oras kung kailan bumabagal ang mga pagbabagong kaugnay ng pagdedeposito (t_{sp}) at mas mababa ang midAL sa dulo ng paglulubog kumpara sa sistemang walang inhibitor. Ipinapahiwatig nito na maaari pa ring maganap ang epektibong inhibisyon ng lokal na pangangalawang kahit na may pagkaantala sa pagdadagdag ng inhibitor. Dagdag pa dito, bumuo rin ng pamantayang batay sa *median* ng mga midAL at t_{sp} upang matukoy kung katanggap-tanggap ang haba ng pagkaantala. Ipinakita ng aplikasyon ng pamantayan sa kasalukuyang sistema ng Ce(III) na ang tinatayang pinakamahabang katanggap-tanggap na pagkaantala ay humigit-kumulang 60 segundo. Ipinapahiwatig ng mga obserbasyon sa kabanatang ito na hindi kinakailangan ang agarang pagdagdag ng inhibitor upang makamit ang sapat na proteksiyon laban sa lokal na pangangalawang ng AA2024.

Pinapalawig sa **Kabanata 3** ang pagsusuri ng epekto ng presensya ng Ce(III) na nakadepende sa oras sa pamamagitan ng pag-aaral kung paano nagbabago ang lokal na inhibisyon matapos ang paunang paglubog sa isang kapaligirang may Ce(III) na sinundan ng muling paglubog sa kapaligirang walang Ce(III). Ang ganitong pagkakasunod-sunod ng mga pangyayari ay inaaproksima ang kaganapan sa isang sistema ng aktibong proteksyon para sa AA2024 kung saan naubos na ang nakaimbak na inhibitor. Sa ideyal na senaryo ng proteksiyon, dapat manatiling matatag ang deposito ng inhibitor na nabuo sa unang paglubog kahit na wala nang suplay ng inhibitor sa muling paglubog. Ito ay upang masiguro na patuloy ang proteksiyon. Sinusuri sa kabanatang ito kung paano nagbabago ang lokal na aktibidad sa mga lokasyon ng mga IMP kung may magkasunod na paunang paglubog at muling paglubog. Naipakita dito na mas maraming iba-ibang proseso ng lokal na pangangalawang ang naoobserbahan sa muling paglubog kumpara sa sistemang direktang inilubog sa solusyong walang Ce(III). Hinati sa apat na kategorya ang mga IMP batay sa kung mababa o mataas ang aktibidad sa paunang paglubog (may inhibitor) at sa muling paglubog (walang inhibitor): mababa/mababa (Low/Low), mababa/mataas (Low/High), mataas/mababa (High/Low), at mataas/mataas (High/High).

Sinuri ang mga posibleng mekanismo sa likod ng mga kategoryang ito gamit ang impormasyon ukol sa komposisyon at morpolohiya ng mga IMP at ng kanilang paligid. Karamihan sa mga may mataas na aktibidad sa muling paglubog ay yaong may kaunting deposito ng Ce(III) sa paunang paglubog. Natukoy din na ang pagpapahaba ng paunang paglubog (hanggang 72 oras) o sandaling pagkaantala (30 segundo) sa pagdadagdag ng inhibitor ay parehong nagdudulot ng mas kaunting aktibong lugar sa muling paglubog. Ito ay marahil sa mas mataas na antas ng lokal na deposisyon ng Ce. Ipinapahiwatig nito na ang mga sistema para sa aktibong proteksyon laban sa pangangalawang ay maaaring magkaroon ng mas matatag na deposito ng inhibitor sa muling paglubog kung gagamit ng mga estratehiyang nagpapalakas ng interaksyon ng inhibitor sa metal, basta't hindi lalampas sa mga limitasyon gaya ng katanggap-tanggap na pagkakaantala na binanggit sa Kabanata 2.

Ang **Seksyon 2 (Kabanata 4 at Kabanata 5)** ay nakatuon sa lokal na pangangalawang sa AA7075-T6 at, sa huli, sa sistemang may galbanikong tambalan ng AA7075-T6 at AA2024-T3. Bagaman isa sa mga pinaka-ginagamit na haluang metal sa industriyang panghimpapawid, mas kaunti ang masusing pag-aaral sa AA7075-T6 kumpara sa AA2024-T3. Nagsisimula ang seksyon sa detalyadong pagsusuri ng lokal na pangangalawang ng AA7075-T6, partikular na sa proseso ng gumuguhit na pangangalawang. Ang masusing pagsusuring ito ay nagsisilbing pundasyon para maunawaan ang mas komplikadong anyo ng pangangalawang na lumilitaw kapag pinagkabit ang dalawang metal.

Ang **Kabanata 4** ay sumusuri sa pagsisimula at paglaganap ng gumuguhit na pangangalawang sa AA7075-T6 gamit ang iRLM at ang pagsusukat ng boltahe ng bukas na sirkit (OCP). Ang gumuguhit na pangangalawang ay isang hindi gaanong kakilalang proseso ng lokal na pangangalawang. Ito ay naoobserbahan bilang mabilis na pagkalat ng mga guhit sa ibabaw ng metal na nauugnay sa pag-atake sa isang altered surface layer (ASL). Sa pamamagitan ng pagmamasid ng ibabaw ng AA7075 habang nakalubog ito sa 0.05 M NaCl, natuklasan na ang gumuguhit na pangangalawang ay kadalasang nagsisimula sa mga mikroskopikong IMP o, sa mangilan-ngilang kaso, sa mga depekto kahit na batay sa mga dating pag-aaral, ang pag-atake ng ASL ay dulot ng istruktura nito. Ginamit ang sPAD na unang ipinakilala sa Kabanata 2 upang subaybayan ang pagbabago sa mga IMP na apektado ng gumuguhit na pangangalawang. Ipinakita ng pagsusuri na may pansamantalang pagtigil ng aktibidad sa ng IMP kapag nakakonekta ito sa isang pangangalawang na kasalukuyang gumuguhit. Ito ay indikasyon ng isang hindi pa naiuulat na mikrogalbanikong interaksyon sa pagitan ng lokal na pangangalawang ng IMP at ng gumuguhit na pangangalawang, dalawang magkaibang lokal na proseso ng pangangalawang. Dagdag pa dito, natukoy ng elektrokemikong pagsusukat ang isang katangi-tanging pagbabago ng OCP na dulot ng gumuguhit na pangangalawang. Ang pagbabago ay nagsisimula sa paunang pagbagsak ng OCP na hudyat ng pag-atake ng ASL. Sinundan ito ng mabilis ng taas-baba ng habang nagpapatuloy ang propagasyon ng pangangalawang. Natapos ito sa mabilis na pagtaas ng OCP sabay sa pagtigil ng gumuguhit na pangangalawang. Ito ang unang beses na ang pagbabago ng OCP direktang naiugnay sa isang partikular na kaganapang ng lokal na pangangalawang. Ipinapakita ng mga natuklasan sa kabanatang ito na ang pagsusuring batay sa iba't ibang lokasyon at batay sa oras ay nakakatuong sa pagkilala ng mga interaksyon sa pagitan ng mga lokal na proseso ng pangangalawang at nagbibigay-linaw sa interpretasyon ng mga global na elektro-kemikong pagsusukat tulad ng OCP.

Ang **Kabanata 5** ay ang pagsasama ng mga natuklasan sa Kabanata 4 at ng mga kasalukuyang kaalaman ukol sa pangangalawang ng AA2024-T3 para higit pang maintindihan ang epekto ng pagtatambal ng AA2024-T3 at AA7075-T6 sa kani-kanilang lokal na proseso ng pangangalawang. Ginamit dito ang pinagsamang iRLM at pagsusukat ng galbanikong kuryent at boltahe sa pamamagitan ng zero-resistance ammeter. Nagbigay-daan ang paraang ito sa sabayang pagtingin at pagsusukat ng mga mikroskopikong pangangalawang sa parehong metal. Lumabas na ang galbanikong tambalan ng dalawang haluang-metal ay nagdudulot ng pagdaloy ng mga elektron mula sa AA2024 papunta sa AA7075. Ito ay nagpapataas ng katodikong aktibidad ng mga IMP sa AA2024 na siyang nagpapalala sa lokal na pangangalawang. Nagbubunga ito ng pangangalawang na lampas pa sa hangganan ng mga trench at tila nakakaapekto sa kabuuang pH sa ibabaw ng AA2024. Ang pagbabago ng pH ay isa sa maaaring dahilan ng pagbaba ng antas ng deposisyon ng mga produkto ng pangangalawang. Naitala ang mga pagbabagong ito kahit na ang dalawang haluang-metal ay hindi itinuturing na malakas na galbanikong pares. Batay sa pagsusuri ng mga mapa ng aktibidad, natukoy ang tatlong yugto ng lokal na pangangalawang sa pinagtambal na AA2024 at AA7075: (1) yugtong nangigibabaw ang dealloying, (2) yugtong nangingibabaw ang trenching, at (3) yugtong nangigibabaw ang aktibidad dulot ng pagbabago na lampas sa hangganan ng mga trench (BT activity). Habang ang dealloying at pagsisimula ng trenching sa unang yugto ay hindi gaanong naaapektuhan ng pagtatambal, ang paglaki ng mga trench sa pangalawang yugto ay bumilis na siyang nagreresulta sa mas maagang redeposisyon ng tanso. Malamang na ito ang sanhi ng malawakang BT activity sa AA2024 na nakita sa pangatlong yugto. Sa banda ng AA7075, lumitaw na ang pag-usbong ng malawakang gumuguhit na pangangalawang ay nakakaapekto sa galbanikong kuryente at boltahe. Kalakip nito ay bahagyang pagpabagal ng paglaki ng mga trench sa AA2024 at tila pagbaba ng antas ng trenching sa AA7075. Binibigyang-diin ng mga natuklasan na kahit ang mahinang galbanikong pares ay may malaking epekto pa rin sa lokal na pangangalawang. Ang ganitong kumplikadong interaksyon ay mas epektibong napag-aaralan sa pamamagitan ng pagsusuring batay sa iba't ibang lokasyon at sa oras.

Sa kabuuan, ipinapakita ng disertasyong ito na ang simpleng pinagsamang optikal at elektrokemikal na sistema, kasama ng matatag at sensitibong protokol para sa pagsukat ng optikal na aktibidad, ay maaaring magbigay-daan sa epektibong pag-aaral ng lokal na pangangalawang at inhibisyon nito sa mga aluminyong haluang-metal. Ang paraang ito ay naipakitang isang epektibong kasangkapan para sa paglalarawan ng iba't ibang lokal na proseso ng pangangalawang at inhibisyon, para pagtukoy ng interaksyon sa pagitan ng mga lokal na proseso, sa loob man ng iisang haluang-metal o sa pagitan ng magkaibang materyales, at para sa direktang pag-uugnay ng mga partikular na proseso ng pangangalawang at ng kanilang kaukulang elektrokemikal na signal. Ang mga pangunahing konklusyon mula sa gawaing ito ay ang mga sumusunod:

- Malaki ang ugnayan ng antas ng deposisyon ng inhibitor sa mga optikal na sukat ng antas ng aktibidad. Ito ay nagpapatunay na isang maaasahang teknik ang optikal na pagsusuri para sa pagsubaybay sa lokal na inhibisyon (**Kabanata 2**).
- Ang pagdadagdag ng Ce(III) matapos ang bahagyang dealloying ng mga IMP sa AA2024 ay nagpapataas ng antas ng deposisyon ng inhibitor. Kahit na ang pagtaas na ito ay may kaakibat na pangangalawang, epektibo pa rin ang inhibisyon kung mas mabilis ang pagpanatag ng kaukulang aktibidad kaysa sa aktibidad na makikita sa sistemang walang inhibitor (**Kabanata 2**).
- Iba-iba ang paraan ng pangangalawang ng mga IMP sa muling paglubog ngunit karamihan sa mga IMP na may hindi matatag na inhibisyon ay ang mga may mababang antas ang aktibidad sa paunang paglubog. Ang pagpapataas ng aktibidad sa paunang paglubog sa pamamagitan ng pagpapalakas ng deposisyon ng Ce(III) ay nagpapabuti sa stabilidad ng deposisyon sa muling paglubog (**Kabanata 3**).
- Ang pagsisimula ng gumuguhit na pangangalawang sa AA7075-T6 ay kadalasang nangyayari sa ibabaw ng mga IMP. Bukod pa dito, ang propagasyon nito ay may kaakibat na mikrogalbanikong interaksyon sa mga konektadong IMP na maaaring maobserbahan gamit ang optikal na teknik (**Kabanata 4**).

- Ang sabayang in situ reflected microscopy at pagsusukat ng OCP ay nagbibigay-daan sa pagtukoy ng mga partikular na pangyayari ng lokal na pangangalawang na nagdudulot ng partikular na pagbabago sa OCP (**Kabanata 4**).
- Ang galbanikong tambalan ng magkaibang aluminyong haluang-metal ay nagpapalala sa mga proseso ng lokal na pangangalawang. Ang pagsusuri ng mga sistemang ito nang batay sa iba't ibang lokasyon at sa oras ay nagbibigay ng mas malinaw na pananaw kaysa sa simpleng global na paghahambing ng antas ng kaagnasan (**Kabanata 5**).

Mayroon ding ilang oportunidad para sa karagdagang pananaliksik batay sa mga natuklasan sa gawaing ito. Ang mga ito ay nahahati sa mga oportunidad na nakabase sa teknik at nakabase sa materyales. Ang mga oportunidad na nakabase sa teknik ay mga landas ng pananaliksik na makatutulong sa karagdagang pagpapaunlad ng kasalukuyang pamamaraan ng pagsusuring batay sa iba't ibang lokasyon at sa oras. Ang mga oportunidad na nakabase sa materyales ay tumutukoy naman sa mga linya ng pananaliksik na maaaring makinabang sa kasalukuyang pamamaraan. Nakalista sa ibaba ang mga oportunidad na ito. Ang unang apat ay nakabase sa teknik habang ang huling dalawa ay nakabase sa materyales.

- **Pagsasama ng iluminasyong brightfield at darkfield**: Ang in situng proseso ng pagkuha ng mga image na ginamit sa disertasyong ito ay nakabatay sa iluminasyong brightfield. Ang iluminasyong ito ay bumubuo ng imahe mula sa nareplektang liwanag ng materyal kapag ito ay inilawan sa direksyong perpendikular dito. Sa kabilang banda, ang iluminasyong darkfield ay bumubuo ng imahe mula sa kumalat na liwanag kapag ito ay inilawan nang may maliit na anggulo. Ang iluminasyong ito ay nagpapatingkad sa mga tampok ng ibabaw gaya ng dingding ng pit o kagaspangan. Maaaring gamitin ang mga imaheng brightfield upang iugnay ang mga optikal na signal sa mga katangiang mikrostruktural (halimbawa: kapal ng deposito), ngunit kadalasan ay nangangailangan ito ng mas detalyadong kaalaman sa sistema at karagdagang ex situ na pagsusuri. Sa pamamagitan ng sabay na pagkuha ng mga imaheng brightfield at imaheng darkfield habang nakalubog ang materyal, maaaring makalikom ng komplementaryong datos na makatutulong sa pagtukoy at pagkarakterisa ng mga tampok sa ibabaw nang hindi gaanong umaasa sa ex situng pagsusuri. Marami nang mikroskopya ang sumusuporta sa parehong uri ng iluminasyon. Gayunpaman, ang paglipat sa pagitan ng mga iluminasyong ito ay maaaring magpababa ng resolusyong temporal dahil kailangan ng oras upang maipatupad ang pagpapalit. Ang pagsasama ng dalawang uri ng imahe upang makakuha ng makabuluhang datos ay isa ring hamon na kailangang tugunan.

- **Pag-aaral ng elektrokemikal na signal**: Ang mga pagsusukat ng OCP sa Kabanata 4 at ng galbanikong kuryent at boltahe sa Kabanata 5 ay nagpapakita kung paanong ang mga lokal na proseso tulad ng gumuguhit na pangangalawang ay maaaring magkaroon ng natatanging elektrokemikal na signal. Nagbigay ang kasalukuyang disertasyon ng mga posibleng paliwanag para sa paglitaw ng mga signal na ito. Gayunpaman, ang mas detalyadong kuwantitatibong pagsusuri sa mga signal na ito kasabay ng mas malalim na pagtingin sa bilis ng pagbabagong nakabatay sa optiks ay makatutulong upang higit na maunawaan ang kalikasan ng mga ito. Bukod pa dito, dahil ang propagasyon ng gumuguhit na pangangalawang ay tumutugma sa haba ng panahon ng mga bahagi ng signal na may mabilis na taas-baba, maaaring tantiyahin ang sukat ng bahaging apektado ng gumuguhit na pangangalawang gamit lamang ang datos na elektrokemikal.
- **Mula optiks patungong mekanikal**: Ang pagsusuri na ginamit sa disertasyong ito ay nakatuon sa pagmamasid ng lokal na pangangalawang at inhibisyon sa pamamagitan ng mga optikal na pamamaraan. Gayunpaman, ang panghuling layunin ng pagkontrol sa pangangalawang ay mapanatili ang mekanikal na integridad ng mga istrukturang gumagamit ng haluang-metal. Upang mas maging kapaki-pakinabang ang paraang ito sa industriya, ang mga obserbasyon ay dapat iugnay sa mekanikal na kaganapan. Sa pamamagitan ng pagsusuri ng optikal na datos mula sa maraming lugar at pag-uugnay nito sa mekanikal na katangian, maaaring matukoy kung gaano karaming aktibidad sa ibabaw ang katanggap-tanggap bago maapektuhan ang mga katangiang mekanikal. Makakatulong ito upang masabi kung ang isang sistema na may aktibong proteksyon laban sa pangangalawang ay nananatiling matatag.
- **Pagmomodelo ng pagbabagong optikal**: Bagama't mahirap direktang alamin ang kaakibat na bilis ng mga kemikal na reaksyong nagdudulot ng optikal na aktibidad mula sa reflected light microscopy, ang pag-usbong ng mga aktibidad na ito depende sa oras ay nagbibigay ng kaalaman kung paano umuusad ang mga pagbabago sa mga haluang-metal. Ang mga parametrong optikal na nakabase sa oras tulad ng pagsisimula ng dealloying o ang punto kung kailan nangingibabaw ang trenching ay maaaring makatulong sa pagpapabuti ng mga modelong pangpisika para sa lokal na pangangalawang at inhibisyon ng mga aluminyong haluang-metal.
- **Pagbuo ng deposito ng inhibitor**: Ang kondisyon ng inhibisyon sa pag-aaral na ito ay nakabatay sa iisang tuloy-tuloy na yugto ng paglubog. Sa mga industriyal o komersyal na sistema, kadalasang pahinto-hinto ang paglubog dahil sa paulit-ulit na nababasa at natutuyo ang ibabaw ng metal. Sa panahon ng pagpapatuyo, maaaring mawala ang

inhibitor kasama ng elektrolito o maiwan bilang labi dahil sa pagsingaw ng tubig. Sa susunod na yugto ng pagkabasa, maaaring mapunan muli ang inhibitor, halimbawa sa pamamagitan ng *leaching* mula sa mga imbakan ng inhibitor na nasa loob ng organikong sapin na ginagamit sa aktibong proteksyon laban sa pangangalawang. Ang pag-unawa sa kung paano naaapektuhan ng ganitong pahinto-hintong paglubog ang lokal na pagbuo at katatagan ng mga deposito ng inhibitor ay mahalaga upang maipaliwanag ang pangmatagalang bisa ng proteksiyon laban sa pangangalawang.

- **Inhibisyon ng pinagtambal na aluminyong haluang-metal**: Ang pagsusuri sa lokal na pangangalawang ng pinagtambal na AA2024-T3 at AA7075-T6 ay nagpakita ng mga pagbabago sa kanilang lokal na proseso kumpara sa mga metal na nangangalawang nang magkahiwalay. Ang pag-unawa sa kung paano naaapektuhan ng tambalan ang bisa ng mga inhibitor gaya ng Ce(III) ay maaaring magbigay pa ng karagdagang kaalaman kung paano mababawasan ang pangangalawang sa mga sistemang may iba-ibang materyal na tulad nito.

Contents

Summary i
Samenvatting ix
Paglalagom xix
Contents xxix
Nomenclature xxxiii

Chapter 1. Introduction

1.1. Aluminium alloys in the aerospace industry 1
1.2. Local corrosion initiation and progression in AA2024-T3 and AA7075-T6 3
1.3. Local corrosion inhibition 7
1.4. Capturing the distribution of local corrosion and inhibition behaviour 9
1.5. Quantification of optics-based measurements Through image analysis 17
1.6. Research outline 21
1.7. References 24

Chapter 2. Local corrosion and inhibition behaviour of AA2024-T3 intermetallics under delayed Ce(III) supply: an in situ optical study

2.1. Introduction 34
2.2. Experimental 37
  2.2.1. Materials 37
  2.2.2. Experimental protocols 37
  2.2.3. Image analysis 38
2.3. Results 42
  2.3.1. Local behaviour of S-phase IMPs at different Ce(III) supply times 42
  2.3.2. Local behaviour of θ-phase IMPs at different Ce(III) supply times 45
  2.3.3. Local behaviour of secondary IMPs at different Ce(III) supply times 48
  2.3.4. Activity levels and extent of inhibitor deposition 50

2.4. Discussion 52
2.4.1. Quantifying optical changes with simplified pixel activity distribution (sPAD) plots 52
2.4.2. Using reflected light microscopy to estimate the tolerable delay limit for Ce(III) supply 56
2.4.3. Ce(III) precipitation at different supply times 57
2.5. Conclusion 60
2.6. References 61
2.7. Supporting Information 65
2.7.1. Preparation of epoxy-embedded samples 65
2.7.2. Electrolyte and inhibitor injection protocol 66
2.7.3. Global activity maps (GAMs) of samples 68
2.7.4. Image analysis protocol 73
2.7.5. Post-immersion SEM-EDX of selected IMPs 75
2.7.6. Quantification of activity onset for uninhibited IMPs 78
2.7.7. Protocol for analysis of simplified pixel activity distribution plots 79
2.7.8. Parameters extracted from simplified pixel activity distribution plots 80

Chapter 3. Local re-immersion behaviour of Ce-based inhibiting layers on AA2024-T3 intermetallics: Enhanced stability through partial dealloying and prolonged exposure

3.1. Introduction 82
3.2. Experimental 85
3.2.1. Materials 85
3.2.2. Experimental protocols 85
3.2.3. Image analysis 86
3.3. Results and Discussion 89
3.3.1. Evolution of IMP surface activity during re-immersion 89
3.3.2. Immersion/re-immersion behaviour subtypes and proposed mechanisms 96
3.3.3. Effect of inhibiting layer formation conditions on inhibiting layer stability during re-immersion 104
3.4. Conclusion 112
3.5. References 113

3.6. Movies 117
3.7. Supporting Information 120
  3.7.1. Potential atmospheric corrosion prior to immersion or re-immersion 120
  3.7.2. EDX spectra of selected intermetallic particles 121
  3.7.3. Local activity evolution of selected IMPs 123
  3.7.4. Identification of immersion/re-immersion behaviour subtypes 124
  3.7.5. Replicates of tests at varying immersion conditions 126

Chapter 4. Intermetallic particles trigger streaking corrosion in AA7075-T6

4.1. Introduction 132
4.2. Experimental 134
4.3. Results 136
  4.3.1. Streaking corrosion initiation 136
  4.3.2. Surface activation of IMPs that initiate and do not initiate streaks 144
  4.3.3. Intermetallic particle activity and streak propagation 147
  4.3.4. Correlation between OCP transients and streaking corrosion 149
4.4. Discussion 151
4.5. Conclusion 155
4.6. References 156
4.7. Movies 159
4.8. Supporting Information 160
  4.8.1. Supplementary figures 160
  4.8.2. Supplementary discussion 168

Chapter 5. Galvanic coupling between AA7075-T6 and AA2024-T3 intensifies local corrosion

5.1. Introduction 180
5.2. Experimental 183
  5.2.1. Materials 183
  5.2.2. Sample preparation 183
  5.2.3. In situ optical-electrochemical corrosion testing 183
  5.2.4. Image analysis 185
5.3. Results and Discussion 186
  5.3.1. Local corrosion progression of disconnected AA2024 and AA7075 186
  5.3.2. Impact of galvanic-coupling on local corrosion of AA2024 and AA7075 189

- 5.3.3. Local corrosion progression of galvanically-coupled AA2024 and AA7075 194
- 5.3.4. Kinetics of local corrosion processes in AA2024-AA7075 couple 197
- 5.3.5. Galvanic current density and potential of AA2024-AA7075 couple 200
- 5.3.6. Mechanism of local corrosion in AA2024-AA7075 couple 205

5.4. Conclusion 209

5.5. References 210

5.6. Movies 214

5.7. Supporting Information 216

- 5.7.1. Validation of direction of electron flow 216
- 5.7.2. Regions of interest used for local analysis 217
- 5.7.3. Kinetic parameters estimated from optics 221

List of Publications 223

Acknowledgements 225

About the Author 227

Nomenclature

AMT	Area measurement time
AMX	Adjacent matrix (with respect to an intermetallic particle)
ASL	Altered surface layer (produced in AA7075-T6 by mechanical polishing)
BP	Bottom plane
BT	Beyond-trench
CID	Chemical information depth
DSxx	Immersed in inhibitor-containing solution for xx hours with 30-s supply delay
E_{gal}	Galvanic potential
EI	Electrically-isolated test
EMS	Embedded metal samples
FP	Facing plane
GAM	Global activity map
GC	Galvanically-couple tests
GND	Ground electrode
H/H	High activity in immersion and high activity in re-immersion
H/L	High activity in immersion and low activity in re-immersion
IMP	Intermetallic particle
j_{gal}	Galvanic current density
LAM	Local activity map
L/L	Low activity in immersion and low activity in re-immersion
L/H	Low activity in immersion and high activity in re-immersion
LM	Light microscopy
LTH	Lower threshold
maxAL	Maximum activity level based on the pixel activity level distribution
MID	Morphological information depth
midAL	Median activity level based on the pixel activity level distribution
minAL	Minimum activity level based on the pixel activity level distribution
OCP	Open-circuit potential

ORR	Oxygen reduction reaction
RE	Reference electrode
Reim	Re-immersion
RLM (or RM)	Reflected light microscopy
ROI	Region of interest
RROI	Rectangular region of interest (for isolating a particle and its adjacent matrix)
SC	Streaking corrosion
SEM-EDX	Scanning electron microscopy – energy dispersive X-ray spectroscopy
SLCM	Scanning laser confocal microscopy
sPAD	Simplified pixel activity level distribution
SR	Spatial resolution
TMAZ	Thermomechanically affected zone
TP	Top plane
TSxx	Inhibitor supplied after xx seconds of immersion (for delayed inhibitor supply)
t_{fwt}	Trench full-width time
t_{onset}	Onset time (in the context of dealloying)
t_{reim}	Re-immersion time
t_{sp}	Onset of slow period (based on the sPAD)
t_{tp}	Dealloying-to-trenching transition point time
t_{supply}	Inhibitor supply time
UDxx	Immersed in inhibitor-containing solution for xx hours without supply delay
WE	Working electrode
ZRA	Zero-resistance ammeter

1

Introduction

1.1. Aluminium alloys in the aerospace industry

Aluminium alloys such as AA2024-T3 and AA7075-T6 are widely used in the aerospace industry due to their high strength-to-weight ratio [1–4]. These materials enable the construction of lightweight yet mechanically durable structures, which is essential for improving fuel efficiency and payload capacity in aircraft. AA2024-T3 (Al-Cu-Mg) is part of the 2xxx series of Al alloys which have Cu as the main alloying element. It is generally used in fuselage skins and wing surfaces which require high strength, good workability, and good damage tolerance [2–4]. AA7075-T6 (Al-Mg-Zn-Cu) is part of the 7xxx series whose main alloying element is Zn. This series is known for alloys with ultrahigh-strength [1]. AA7075-T6 is used in more heavily loaded parts such as wing spars, landing gear, and joints, where even higher strength is required [1]. Table 1.1 shows nominal compositions of AA2024 and AA7075.

The T3 and T6 suffixes of the two alloys pertain to their temper designation. In temper nomenclature, the letter indicates basic treatment condition while the subsequent digit indicates the secondary treatment used to influence properties [4]. Essentially, these suffixes summarize the heat treatment and mechanical processing applied to the alloy to obtain target characteristics. The T3 in AA2024-T3 indicates that it underwent a sequence of solution heat treatment, cold working, and natural ageing [2,4]. The T6 in AA7075-T6 indicates that it underwent a sequence of solution heat treatment and artificial ageing [2,4].

Table 1.1. Typical compositions of AA2024-T3 and AA7075-T6 expressed in terms of weight percentages of the alloying elements and the balance being aluminium [1,4].

	Zn	**Mg**	**Cu**	**Mn**	**Cr**	**Fe**	**Si**	**Ti**
AA2024	-	1.5	4.4	0.6 – 1.5	0.1	≤ 0.5	≤ 0.5	0.15
AA7075	5.1 – 6.1	2.1 – 2.9	1.2 – 2.0	0.3	0.18 – 0.28	0.4 – 0.5	0.4	0.2

Despite their mechanical advantages, these AA2024-T3 and AA7075-T6 are highly susceptible to localized corrosion when exposed to chloride-containing environments. Such environments can develop on the surface of the alloys due to exposure to marine air, de-icing chemicals, or atmospheric pollution. The susceptibility stems from the capability of chloride ions to attack the passive oxide layer that forms on the surface of aluminium alloys. This can lead to different forms of corrosion attack which can compromise the performance of the alloys. AA2024-T3 and AA7075-T6 are particularly vulnerable to localized corrosion. This is a form of corrosion that occurs in specific, concentrated areas of the metal surface as opposed to uniform corrosion (or general corrosion) which affects the entire metal surface. Localized corrosion is often harder to detect and can result in intense damage in the attack sites. The intense damage stems from chemical and electrochemical activity being focused on a small attack site which leads to the development of more aggressive environments. The susceptibility of AA2024-T3 and AA7075-T6 to local corrosion is due to the presence of intermetallic particles (IMPs) that are formed during their thermomechanical processing [5–11]. These particles differ in composition and electrochemical potential from the surrounding aluminium matrix and often serve as the initiation sites for local corrosion. Table 1.2 summarizes reported compositions of IMPs observed in the two alloys. While the distribution of each IMP composition can vary from surface to surface, Hughes et al. [11] reported that IMP compositional domains containing Al, Cu, Fe, Mn, and Si are usually most abundant for AA2024-T3. These domains are closely followed by S-phases and θ-phases. For AA7075-T6, Zhu et al. [12] reported that, among the IMPs in the 10 μm-scale, $Al_7Fe_2Cu(Mn)$ and Mg_2Si are likely the most abundant.

Table 1.2. Compositions reported for intermetallic particles observed in AA2024-T3 and AA7075-T6.

AA2024-T3		**AA7075-T6**	
Particle Type	*Ref.*	*Particle Type*	*Ref.*
AlCuFeMnSiMg	[8,10]	$Al_7Cu_2Fe(Mn)$	[12,15,16]
AlCuFeMn-low Si	[10,13]	$(Al,Cu)_6(Fe,Cu)$	[15,16]
AlCuFeMn-high Si	[8,14]	Al_6Fe	[15]
$Al_6(Cu,Fe,Mn)$	[11,13,14]	Mg_2Si	[12,15–17]
Al_7Cu_2Fe	[8,10,11,13,14]	α-$Al_{12}Fe_3Si$	[15]
Al_2CuMg (S-phase)	[10,11,13]	SiO_2	[15]
AlCu (θ-phase)		Al_2CuMg (S-phase)	[12,18]
		MgZnCu (nm-scale)	[12]
		$MgZn_2$ (η-phase)	[19]

1.2. Local corrosion initiation and progression in AA2024 and AA7075

The initiation and progression of localized corrosion around IMPs in AA2024 have been extensively studied [14,20–31]. When exposed to chloride-containing environments, corrosion typically initiates with the breakdown of the native passive layer, particularly at or near the IMP-matrix interface. This breakdown allows for electrolyte ingress and initiates a sequence of corrosion events, as schematically illustrated in Figure 1.1.

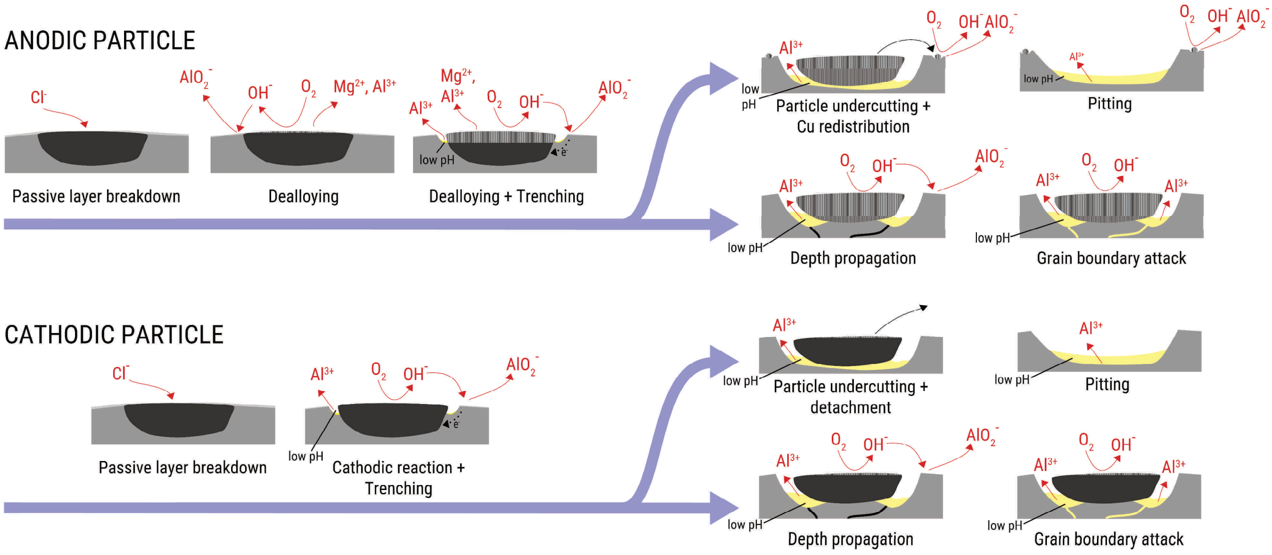

Figure 1.1. Simplified representation of the initiation and progression of local corrosion in AA2024-T3 for anodic and cathodic IMPs. The process begins with passive layer breakdown over the IMP followed by varying degrees of dealloying and trenching. At advanced stages, this can lead to particle undercutting, Cu redistribution, particle detachment, and pit formation [25,26]. It can also lead to sub-surface grain boundary attack and cooperative corrosion [28,29].

The corrosion of the IMP begins with the selective dissolution of less noble elements within the IMP, such as magnesium and aluminium (i.e., dealloying). This is more pronounced in anodic particles and limited in cathodic ones. In anodic particles, dealloying alters the composition, typically enriching the particle in copper. This makes it more cathodic relative to the surrounding aluminium matrix, creating a local microgalvanic couple that enables matrix dissolution. For cathodic particles, microgalvanic coupling can already be established without the need for ennoblement. The cathodic reactions supported on the particle surface (i.e., oxygen reduction reaction, ORR) raise the local pH, which in turn destabilizes the natural passive film on the adjacent matrix. This leads to anodic dissolution of the matrix, resulting in the formation of a trench around the IMP (i.e., trenching). As dissolution progresses, the environment within the trench becomes increasingly acidic due to the hydrolysis of dissolved metal ions. This acidification further undermines passivity and accelerates matrix dissolution, allowing the trench to propagate deeper into the substrate. The extent and rate of both dealloying and trenching can vary significantly depending on the composition of the particle [32,33], the local microstructure [25,26], and the presence and proximity of neighbouring particles [29], all of which influence local electrochemical interactions and chemical gradients.

As dealloying and trenching reach an advanced stage, the local corrosion process can evolve in multiple directions. In some cases, dealloying may progress to completion, further enhancing the particle's cathodic nature and driving continued matrix attack. Trench progression can also eventually lead to undercutting (i.e., the particle becomes physically detached from the matrix due to localized material loss beneath it). The detached particle may fall off or dissolve, leaving behind a localized pit at the original corrosion site [25,26]. Alternatively, the trench may extend into subsurface grain boundaries, initiating or accelerating grain boundary attack, particularly in microstructural regions such as precipitate-free zones or Cu-decorated boundaries [28,29,34]. In these cases, the subsurface anodic dissolution can be further sustained through cooperative corrosion, where nearby cathodic particles support oxygen reduction and intensify the local galvanic environment. This interaction can promote a broader zone of attack that couples adjacent corrosion sites and leads to features such as corrosion rings.

Due to the generally similar intermetallic compositions (see Table 1.2), the local corrosion behaviour of AA7075 intermetallics follows the same overall mechanism as in AA2024. Dealloying of less noble intermetallic phases is still observed, typically followed by trenching. AA7075 also contains a high fraction of Fe-rich particles (e.g., Al_7Cu_2Fe, $(Al,Cu)_6(Fe,Cu)$) [15], which are typically cathodic [35]. Consequently, some intermetallics in AA7075 show preferential dissolution at the particle–matrix boundary even before extensive surface dealloying occurs. In more advanced stages, AA7075 may also exhibit intergranular and exfoliation corrosion [36–39]. The latter results from corrosion product buildup along near-surface grain boundaries, which generates internal stresses that lift and delaminate surface grains, producing a layered, flake-like morphology [39]. In addition, AA7075 is prone to streaking corrosion, a form of surface-localized attack associated with the rapidly propagating lateral dissolution of a surface layer generated by high strains during mechanical treatment of the alloy [40–42].

The time-dependence of the local corrosion events in AA2024 and AA7075 is also a critical aspect for understanding and effectively controlling these processes. Under open-circuit exposure to chloride-containing electrolytes, IMP dealloying has been consistently shown to start early and progress rapidly (i.e., from seconds to a few minutes) [27,32]. The trenching development follows shortly after and progresses over the next few hours [21,27]. Depending on the local conditions, intergranular corrosion can progress on similar time scales as trenching [28,43]. Other local events such as streaking corrosion in AA7075 can also propagate across the surface in a matter of seconds (i.e., linear propagation rates ranging from 2 to around 8 $\mu m\ s^{-1}$ during open-circuit exposure to NaCl solutions) [41].

The temporal dynamics, combined with local microstructural and electrochemical variability, lead to a wide range of localized corrosion outcomes in both AA2024 and AA7075. The same general mechanism occurs at intermetallic sites in both alloys, beginning with passive film breakdown and followed by dealloying, trenching, and sometimes subsurface attack. However, the timing, rate, and severity of these processes can vary. The variation is influenced by local microstructural features and electrochemical conditions. As a result, the corrosion behaviour of the two alloys is best understood as *a distribution of individual events* that follow a common sequence but diverge in how they develop over time and space. This variability is illustrated in Figure 1.2, which shows the corroded surface of AA2024 and AA7075 simultaneously immersed in 0.05 M NaCl. The image is a representative example of data acquired through in situ microscopy, a technique extensively employed throughout this work. Multiple intermetallic sites exhibit distinct corrosion responses, ranging from limited activity to severe dissolution, despite being exposed to similar environmental conditions. Local activity not limited to intermetallic particles (i.e., streaking corrosion) is also observed particularly on the AA7075 surface.

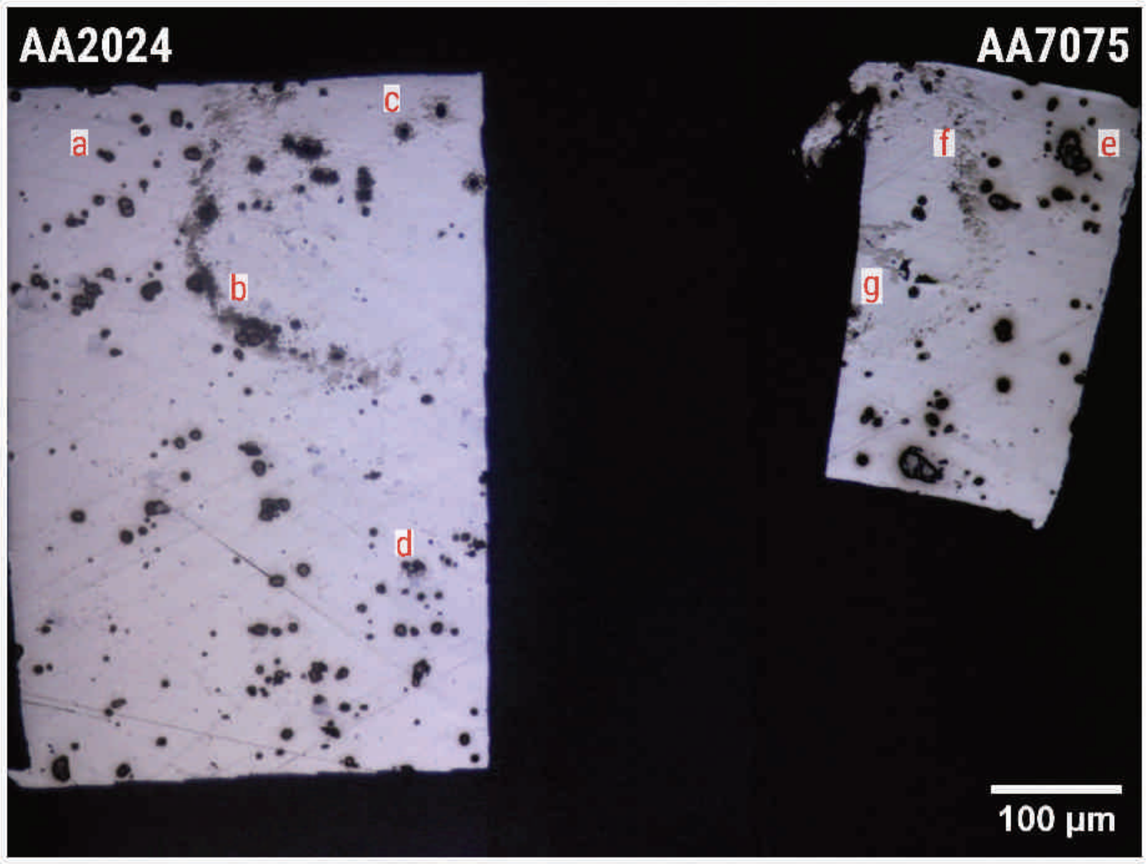

Figure 1.2. Local corrosion events that develop on the surface of AA2024-T3 and AA7075-T6 after immersion in 0.05 M NaCl for 50 minutes observed through a reflected light microscope. The AA2024 local events include **(a)** IMP dealloying and trenching, **(b)** IMP dealloying and trenching with corrosion product deposition, **(c)** corrosion product ring around a zone of inactive particles, and **(d)** partial IMP dealloying and trenching of a particle. The AA7075 local events include **(e)** IMP dealloying and trenching, **(f)** corrosion product ring around a zone with limited local activity, and **(g)** apparent corrosion filaments.

1.3. Local corrosion inhibition

Given the high susceptibility of AA2024 and AA7075 to localized corrosion, effective protection strategies are essential to ensure their long-term performance in industrial applications, aerospace or otherwise. Traditional barrier coatings are often insufficient in completely preventing localized attack around intermetallic particles. As a result, there has been growing interest in corrosion inhibitors, which are chemical species that reduce the rate of corrosion by interfering with electrochemical reactions at vulnerable sites. Corrosion inhibitors are especially valuable because they provide active protection, helping to suppress localized corrosion even after coating damage or electrolyte ingress.

In the past, the most effective corrosion inhibitors for aluminium alloys were chromate-based compounds, especially those containing hexavalent chromium [44,45]. These inhibitors offered excellent performance by forming adherent, self-healing passive films that suppressed both anodic and cathodic reactions. Because of this, chromates became a key component in many aerospace corrosion protection systems, including conversion coatings, primers, and sealants. However, hexavalent chromates are both toxic and carcinogenic, raising serious health and environmental concerns [45,46]. Increasing regulatory restrictions, such as those under the European Union's REACH regulation [47], have accelerated the transition away from chromate-based systems. This shift has driven extensive research into safer and more sustainable alternatives that can provide comparable levels of corrosion protection.

Several promising alternatives have been developed. These include rare earth salts such as cerium compounds [48–51], lithium compounds [52–54], molybdates [55–57], silicates [57–60], and phosphates [57,61,62], and a wide variety of organic inhibitors [57,63–66]. These inhibitors operate through different mechanisms, including surface film formation, adsorption onto active sites, or the precipitation of protective compounds. They are commonly applied in corrosion protection systems through incorporation in protective coatings and surface treatments. If the coating or surface treatment gets damaged and exposes the substrate to a corrosive environment (e.g., chloride-rich solution), the inhibitors are designed to leach out at the damaged spot to protect the metal [67–69]. The incorporation of the inhibitors thus turns the initial *passive* barrier protection provided by the coatings and surface treatments into an *active* corrosion protection scheme. The protection system becomes capable of responding to loss of barrier protection, similar to that provided by chromate-based systems. Active anticorrosion coatings fall under a diverse group of “smart” coatings which aim at prolonging the service life of protected metal substrates [70].

The effectiveness of corrosion inhibition varies depending on the alloy’s composition, microstructure, and surrounding chemical environment. Nonetheless, because localized corrosion in aluminium alloys occurs as a distribution of individual events, localized corrosion inhibition is also expected, to a certain extent, to exhibit a distribution of behaviours. Inhibition is therefore not uniform across the surface but depends on local conditions at each site. This underscores the need for corrosion protection strategies that embrace spatial (and temporal) variability, targeting the most vulnerable regions to achieve robust and comprehensive surface protection.

1.4. Capturing the distribution of local corrosion and inhibition behaviour

Understanding the range of behaviours of localized corrosion and inhibition events is essential for accurately assessing the performance and reliability of corrosion protection strategies in aerospace alloys like AA2024 and AA7075. Because these events evolve over time and vary in both onset and progression, effective analysis requires techniques that not only resolve individual sites and capture enough of the surface to reveal the spatial distribution of events, but also possess sufficient temporal resolution to track their development. This section reviews current analytical approaches for local corrosion and inhibition, highlighting the techniques most suitable for site- and time-resolved analysis.

Techniques for analysing local corrosion and inhibition can be compared in terms of four attributes: (1) spatial resolution, (2) morphological information depth, (3) chemical information depth, and (4) coverage time. Notably, there is a distinction being made for point measurements and area measurements. Point measurements are made at one particular location, while area measurements pertain to a set of point measurements over a geometric boundary. Definitions of the attributes are as follows:

- **Spatial resolution (SR):** The minimum lateral distance that the technique can clearly detect for each point measurement. High SR is important for studying fine details like corrosion around intermetallic particles.
- **Morphological Information depth (MID):** The extent of morphological or topological data a technique provides. Techniques with higher MID can provide almost 3D-resolved information.
- **Chemical information depth (CID):** The richness of chemical or electrochemical information that the technique provides. Techniques with higher CID can provide direct insight into local corrosion reaction rates.
- **Area measurement time (AMT):** This refers to how quickly a technique can analyse a given surface area. For probing techniques, AMT is determined by the time required to collect data at each point and the time needed to move between points. Techniques with slow point acquisition inherently result in longer scan durations, making them less practical for large-area analysis due to the extended time needed. In contrast, for global techniques (i.e., those that assess the surface in bulk), the total measurement time is the primary factor influencing AMT, as the entire area is captured simultaneously. High AMTs are a limitation when investigating time-sensitive surface changes, as the system may evolve before the

measurement is completed. For probing techniques, AMT also increases with finer spatial resolution, since more measurement points are required to cover the same area. In this comparison, AMT is estimated based on the expected time needed to analyse an area of approximately 1 mm^2. For probing techniques, a spatial resolution of 20 μm (i.e., measurements taken at 20 μm intervals) is used as an additional basis. This resolution was selected based on values available in the literature for local electrochemical techniques. A spatial resolution is not needed for estimating the AMT of global techniques.

In an ideal world, there is one analytical technique that will have high scores on all attributes. However, inherent trade-offs in technique design, such as physical constraints, operating principles, or instrumentation limitations lead to techniques scoring low on some factors. The scoring system (i.e., 1 to 5 with 5 being high) for evaluating existing analytical techniques is presented in Table 1.3. The levels for SR were defined from length scales typically encountered for corrosion research [13,71]. High SR score corresponds to better capacity to observe small scales. It is noted that the techniques with microscale resolution can get either a 3 or a 4. The higher score is designated for techniques capable of delivering submicron resolutions. MID is scored based on how close the information is to being 3D-resolved. Techniques that give 3D information about the internal structure of the material, not just the surface, receive higher scores. CID is scored based on the relevance of the information to estimating local corrosion reaction rates. Techniques that provide material surface compositions are scored lower while techniques that provide data relevant to estimation of reaction rates (e.g., surface electrochemistry, solution composition) are scored higher. The highest CID score is given for techniques which can give compositional information for both the solution and the surface. AMT is scored based on the estimated measurement time of the technique. Those with low measurement time (i.e., fast techniques) have a higher AMT rating. Using this evaluation framework, a selection of commonly used techniques for analysing local corrosion and inhibition processes was reviewed. Table 1.4 presents the selected techniques as well as a general description of their operating mechanism and relevant works used to estimate attribute scores.

Figure 1.3 visualizes the attribute scores of the selected techniques typically used for analysing local corrosion and inhibition in aerospace aluminium alloys. Global electrochemical techniques (e.g., open-circuit potential measurements, chrono methods, electrochemical impedance spectroscopy, polarization) can provide data directly related to corrosion rates with fast area measurement time. The score has a range though as open-circuit potential measurements and chrono methods (e.g., chronoamperometry, chronopotentiometry) can measure at sub-second intervals but techniques like EIS can take close to an hour, depending on the frequencies being measured. Furthermore, even though global electrochemical techniques have a high AMT score, this is balanced by its low spatial resolution score which is due to it being a global technique. It is typically not site-resolved as each measurement is the net effect of activity from all sites on the sample surface.

Table 1.3. Scoring system for comparison of existing experimental techniques for analysing local corrosion and inhibition in aerospace alloys.

Score	Spatial resolution	Morphological information depth	Chemical information depth	Area measurement time
1	≥ 1 mm (macroscale)	No morphological information	No chemical information	Not practical for the area specified
2	100 µm - 1 mm (mesoscale)	Low contrast 2D morphology	Surface elemental/chemical composition	More than 1 hour
3	1 µm – 100 µm (microscale, individual IMPs)	High contrast 2D morphology	Surface electrochemical data *or* solution (electro)chemical data	Several minutes to ~ 1 hour
4	100 nm ≤ 1 µm (microscale, individual IMPs)	3D morphology	Surface electrochemical data *and* solution (electro)chemical data	Tens of seconds to ~ 1 minute
5	≤ 100 nm (nanoscale)	3D morphology with depth (subsurface) information	Surface chemical data *and* solution (electro)chemical data	Sub-seconds to seconds

Table 1.4. Selection of analytical techniques relevant for the analysis of local corrosion and inhibition.

Technique	Overview	Ref.
Global Electrochemical Techniques (Global Echem)	This is a class of techniques which includes conventional electrochemical methods such as electrochemical impedance spectroscopy (EIS), polarization techniques (e.g., potentiodynamic polarization, linear polarization), and electrochemical noise techniques. These techniques essentially measure the current or potential response of the system when subjected to different conditions (e.g., open-circuit, polarized) and different environments.	[66,72–74]
Scanning Vibrating Electrode Technique (SVET)	This is a surface scanning technique that measures ionic current density (i.e., current density due to ion flow) over a corroding surface which enables determination of local anodic and cathodic sites.	[74–83]
Local Electrochemical Impedance Spectroscopy (LEIS)	This is a local version of EIS implemented through the use of a probe-based setup that collects frequency-dependent electrochemical data at specific points on the sample surface.	[79–82,84–86]
Scanning Electrochemical Microscopy (SECM)	This is a local electrochemical technique used to probe surface reactivity, corrosion activity, and chemical fluxes near the surface by using a microelectrode tip to measure faradaic currents associated with presence of electroactive species.	[78–82,87–90]
Scanning Kelvin Probe (SKP) and Scanning Kelvin Probe Force Microscopy (SKPFM)	This is a local electrochemical technique that measures the surface potential difference (i.e., Volta potential) between a sample and a vibrating metallic probe. The technique can be implemented with the tip of an atomic force microscopy (AFM) to achieve better spatial resolution.	[74,79–82,89,91]

Table 1.4. Selection of analytical techniques relevant for the analysis of local corrosion and inhibition. (continued)

Technique	Overview	Ref.
Scanning Ion-selective Electrode Technique (SIET)	This is a local electrochemical technique that measures the concentration of specific ions (e.g., H^+) over a particular site.	[75,79–82,92,93]
Scanning Droplet Cells (SDC)	This is a localized electrochemical technique that applies electrochemical measurements (e.g., EIS, polarization) on a portion of the sample surface covered by a droplet supported by a capillary or microcell.	[79,82,94]
Scanning Electron Microscopy (SEM)	This is an electron microscopy technique that scans the surface with a focused electron beam to obtain surface morphology images. It can be combined with Energy-Dispersive X-ray Spectroscopy (EDX) or Electron Backscatter Diffraction (EBSD) to obtain further information about elemental composition or grain orientation, respectively.	[20,95,96]
Atomic Force Microscopy (AFM)	This is a high-resolution technique that uses a scanning probe to map the surface topography of the material.	[31,82,97,98]
Transmission Electron Microscopy (TEM)	This is an advanced electron microscopy technique that allows visualization of the internal structure of ultrathin samples at ultrahigh resolutions. It can also be combined with EDX.	[25,26,35,95,99,100]
Light Microscopy (LM)	This is a class of techniques that uses visible light and lenses for widefield and high resolution observation of the surface or structure of a sample.	[32,72,101–105]
Confocal Microscopy (CM)	This is an optical imaging technique that uses focused laser light and a spatial pinhole to produce high resolution, depth-resolved images of a sample.	[20,21]

Table 1.4. Selection of analytical techniques relevant for the analysis of local corrosion and inhibition. (continued)

Technique	Overview	Ref.
Raman Microscopy (RmM)	This technique is a combination of optical microscopy and Raman spectroscopy that provides information about chemical composition and molecular structure of the sample at specific locations.	[31,102, 106]
Time-of-Flight Secondary Ion Mass Spectroscopy (ToF-SIMS)	This is a surface analysis technique that provides detailed chemical composition information regarding the outermost layers of the sample by detecting ions ejected following sample bombardment with an ion beam.	[107,108]

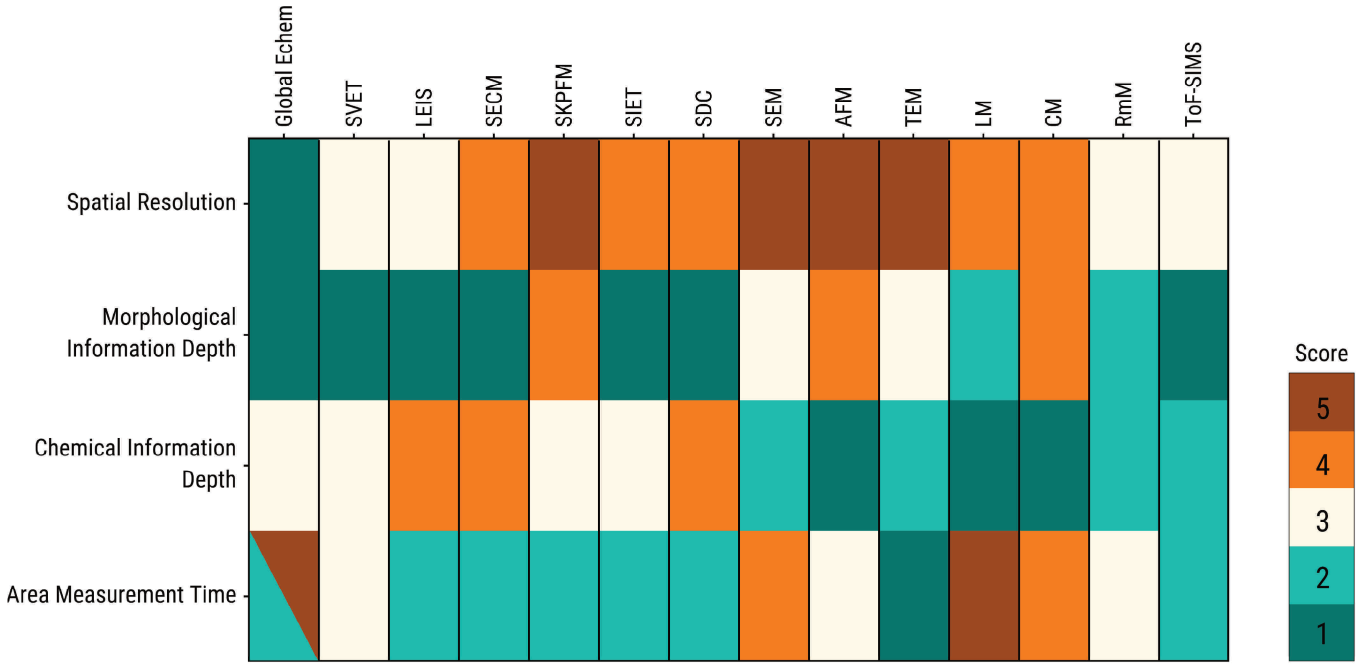

Figure 1.3. Comparison of different techniques used for analysing local corrosion and inhibition in aerospace aluminium alloys based on the attributes presented in Table 1.3. Triangular notations indicate the range of score for the technique or family of techniques.

Most local electrochemical techniques (e.g., SVET, LEIS, SECM, SKPFM, SIET, SDC) already offer good spatial resolution with scores ranging from 3 to 5. These techniques are well suited for site-resolved analysis of local corrosion and inhibition around IMP sites. They also provide in-depth chemical or electrochemical data for either the material surface or the solution at each site. Most of them generate minimal morphological data except for SKPFM. A clear downside of these techniques is their low AMT score which ranged from 2 to 3. Being techniques tailored for local analysis, they operate by scanning several points across the surface. As such, they need time to move across the sample surface, which significantly increases their time needed to measure a surface [79,82]. It is possible to compensate for the long measurement time at the expense of the number of points analysed which effectively reduces its spatial resolution.

High-resolution microscopy techniques (e.g., SEM, AFM, TEM), especially when combined with methods such as EDX or EBSD, can provide detailed information about morphology and composition. SEM can be effectively used for the analysis of multiple sites as reflected by its high AMT score. AFM can also be used for multi-site analysis albeit it would require longer duration to measure an area. TEM on the other hand is not compatible with the analysis of a large area as its field of view per measurement is considerably small. Notably, these techniques are often used for ex situ analysis. As such, when these techniques are used to study the time-dependence of local corrosion and inhibition over multiple sites, the data is generally quasi in situ, with time intervals in the range of minutes to hours [20,25,99]. It is possible to implement in situ analysis using specialized containment cells [26,31]. This approach can achieve temporal resolution in the range of minutes, though this often reduces area that can be covered primarily due to limitations on the size of the sample that can be accommodated.

Variants of optical microscopy (e.g., LM, CM) mainly provide morphology-related data. These techniques can effectively capture micron scale to sub-micron scale features, although not at the same level of detail as high-resolution microscopy techniques. It is possible to obtain chemical data from optical microscopy but this typically requires the use of chemical labels (e.g., pH indicators [109,110], fluorescent markers [104]). Nonetheless, these methods offer much higher temporal resolution and comparable spatial resolution when compared to local electrochemical techniques or the quasi in situ and in situ variants of high-resolution microscopy. This is particularly important when studying fast processes that change rapidly over time. Other techniques, such as Raman microscopy [102,106] and ToF-SIMS [107], provide in-depth information on local composition, with spatial and temporal resolution comparable to that of local electrochemical techniques.

Comparison of the technique scores shows that LM methods offer the most effective spatial resolution for analysing local corrosion and inhibition at individual IMP sites. They also allow fast area measurement, enabling simultaneous observation of multiple sites across the surface with high temporal resolution. However, the main limitation of LM methods is their reduced informational depth relative to local electrochemical techniques or high-resolution microscopy techniques. Nonetheless, LM variants that take advantage of light interference to generate 3D measurements are available [100,111] and can help improve the LM methods' low MID score. Moreover, apart from the use of chemical labels, the CID limitation can also be addressed by combining LM data with complementary techniques that provide electrochemical or compositional insights.

Due to their simplicity and flexibility, LM methods are well suited for integration with other techniques [101,112]. Practical combinations include global electrochemical measurements or ex situ methods such as SEM, which together provide morphological, compositional, and electrochemical information. Global electrochemical methods coupled with LM methods also provide the possibility of synchronized time-dependent data since these two family of methods can deliver fast area measurement times. Deeper analysis of the time-dependent behaviour can also yield quantitative parameters that can supplement the lower informational depth of LM. Notably, LM methods can also be coupled with local electrochemical techniques to offer a more comprehensive view of site-specific corrosion and inhibition behaviours. Such combination can also take advantage of the intuitive and easy-to-interpret image data typically obtained from LM methods to make sense of the local electrochemical data.

One of the most accessible and practical implementations of LM methods is through USB digital microscopes (DMs). These commercially available tools offer advantages in terms of simplicity, versatility, and affordability. Depending on the model, many DMs also deliver high frame rates, making them well-suited for capturing rapid surface changes linked to local corrosion. When paired with proper lighting and stable setups, DM-based systems are capable of detecting submicron-scale changes, capabilities that will be demonstrated in the following chapters of this work.

1.5. Quantification of optics-based measurements through image analysis

Denissen et al. [72,105,113] laid the path currently being followed for systematic analysis of local corrosion and inhibition in aluminium alloys using integrated optical and electrochemical methods. Olgiati et al. [32] further extended this framework to enable site-specific analysis of corrosion initiation in AA2024 through the extraction of optics-based kinetic parameters for IMPs of known compositions. Extracting kinetic parameters marks a significant step forward as it transforms image data from a purely qualitative tool into a source of meaningful, quantitative insight. Their approach to the quantification of the optics-based data is simple and can be summarized in three general steps: (1) image acquisition and pre-processing, (2) segmentation, and (3) quantitative analysis.

The first step covers the image acquisition during in situ optical experiments, conversion of the raw images to 8-bit grayscale images, and their subsequent alignment. Image alignment is achieved using the stack registration (StackReg) plugin of ImageJ [114,115]. It is necessary for ensuring accurate placement and determination of the location of surface changes especially when there is some movement of the sample during the experiment. If the surface is completely stable during the experiment, then the use of image alignment is not necessary.

Denissen et al. [72,105,113] and Olgiati et al. [32] mainly used reflected light microscopy with a USB digital microscope operated in brightfield mode. These USB digital microscopes can be considered low-cost and typically operates with non-coherent white light. Brightfield mode involves the use of axial illumination (i.e., light source is perpendicular to the surface of the sample) to light the sample. The photodetector is on the same location as the light source. If the surface is flat and reflective, majority of the incident light is reflected back to the detector leading to the observance of a bright surface. Local surface changes induced by local corrosion and inhibition can lead to changes in morphology [116] or local refractive indexes [72,101] which impact the amount of light reflected to the detector. These changes in reflected light intensity manifest as variations in image brightness, which are later quantified as optical activity during the quantitative analysis step. Figure 1.4 schematically illustrates how different surface conditions can lead to such optical changes. The conditions presented are the ones considered relevant to systems that use non-coherent white light. In the base case (Figure 1.4a), a flat surface produces strong specular reflection and therefore appears bright. It is emphasized that a perfectly flat surface is not necessary as the advantage of the technique is in its capacity to detect and analyse the changes. When the surface undergoes morphological changes which result in features with dimensions larger than the wavelength of the incident light (Figure 1.4b-d), geometric scattering reduces the amount of light reflected back into the microscope, leading to local darkening. On the other hand, when the surface composition changes or when subwavelength features such as nanoscale porosity (Figure 1.4e-f), the local refractive index is altered, potentially lowering the effective reflectance. In real systems, the observed optical contrast usually arises from a combination of these cases. For example, corrosion product deposition involves, at least, material buildup and refractive index changes. Because optical images alone cannot unambiguously identify which specific processes are responsible for the observed intensity changes, reflected light microscopy must be complemented with additional analytical techniques to verify the underlying physical and chemical transformations occurring at the surface.

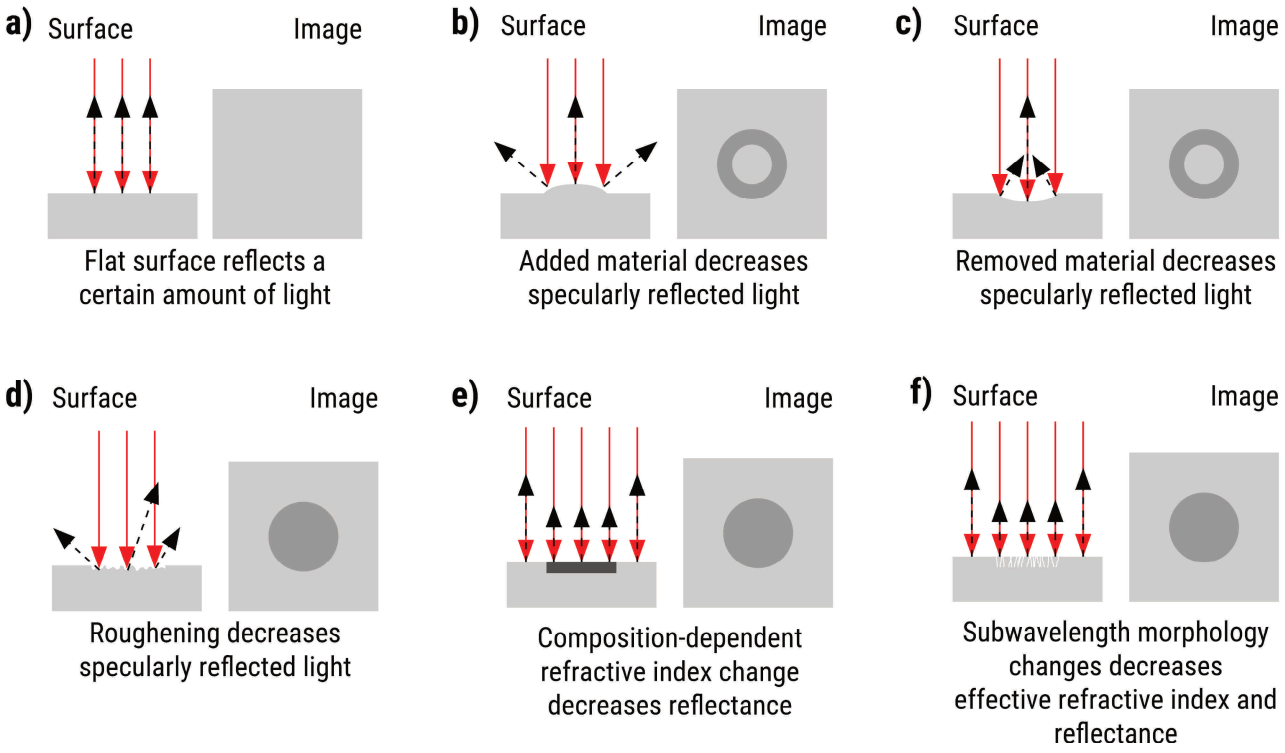

Figure 1.4. Schematic illustration of how different surface conditions influence the darkening observed in reflected light microscope. **(a)** Flat surface shows strong specular reflection (base case). Reduced reflection caused by **(b)** material buildup, **(c)** material loss, or **(d)** surface roughening. The morphological features in (b–d) are larger than the wavelength of light. **(e)** Local compositional changes alter the refractive index, lowering the effective reflectance. **(f)** Subwavelength-scale features modify the effective refractive index in a similar way, also decreasing the reflectance. Red arrows represent incident light. Black arrows represent reflected light.

Segmentation is the step of the analysis where boundaries are defined. This analysis boundary is often referred to as region of interest (ROI). As shown in the previous section, light microscopy techniques have good spatial resolution and coverage time which makes it capable of doing effective widefield and localized measurements simultaneously [101]. Defining an ROI that covers the entire surface gives the subsequent quantification a global context. The corrosion or inhibition behaviour that is being analysed is that of the entire alloy. Meanwhile, ROIs that focus more on microstructural features (e.g., IMPs) give the quantification a more local context. The corrosion or inhibition behaviour that is being analysed is that of the microstructural feature. It is noted that segmentation is a well-established image analysis procedure. Image segmentation protocols have been heavily developed for instance in the analysis of living cells [117]. Unlike cells though which have very dynamic structures, the structures of alloys are generally fixed. As such, ROIs can be established through ex situ analysis or even from the microscopy images themselves.

Quantification is the step wherein numerical values are extracted from the images. Since corrosion and inhibition are the processes being analysed, the key aspect that can be quantified with the image data is the extent of surface changes. With the aligned images of the metal surface as input, it is possible to determine where changes occurred by getting the difference between a reference 8-bit image and a subsequent time-series of 8-bit images. The reference 8-bit image is typically the image at the start of the analysis. The image difference is calculated by getting the absolute value of the change in pixel-by-pixel intensity between the reference image and any image in the time series. Majority of the image calculations in this work are implemented with ImageJ [114]. It is noted that there are other calculations that can be performed on images (i.e., image subtraction) which is presented in further detail in the succeeding chapters. After applying the image difference calculation for the entire set of images, the evolution of the pixel-by-pixel intensity change with time is obtained. This intensity change is referred to as *activity* and the numerical value of the intensity change is referred to as the *activity level*. Furthermore, the images that resulted from the differencing is also referred to as *activity maps*. Since the images used are 8-bit, the activity levels have a value range of 0 to 255 (i.e., 256 levels). The ROIs defined during the segmentation part determines which parts of the activity maps will be analysed. Essentially, the ROIs dictate which pixels will be considered part of a set. Their use limits the activities being considered which is useful when correlating the surface change with specific microstructures or compositions.

Pixel measurement is the aspect of quantification that involves summarizing the activity of a set of selected pixels within the activity maps. The simplest pixel measurement approach is to calculate the average intensity of the pixels in the ROI [118]. Another approach is to apply a threshold and count the number of pixels in the ROI with activity above it. Denissen et al. [72,105] used this approach and arrived at parameters that indicate what fraction of the surface is affected by corrosion (i.e., degraded area percentage, changed surface area percentage) [72,105]. Both the average intensity and the affected area fraction can be plotted against time to have a clearer picture of the temporal dependence of the surface changes.

This PhD dissertation builds on the works of Denissen et al. [72,105,113] and Olgiati et al. [32] and applies in situ optical microscopy (i.e., reflected light microscopy) integrated with electrochemical measurements and ex situ analysis to investigate the distribution of local corrosion and inhibition behaviours across aerospace aluminium alloys. This work focuses on the systematic study of a large number of intermetallic particles and other local corrosion sites, enabling identification of how site-specific responses vary under different exposure conditions. Extraction of time-dependent parameters are also explored to supplement the decreased informational depth of reflected light microscopy. The novelty of this work is in its site- and time-resolved approach to characterizing local corrosion inhibition. This enables the identification and classification of a wide range of site-specific behaviours across many particles and locations, which is essential for two main reasons. First, from a mechanistic standpoint, mapping the distribution of these behaviours provides a more complete understanding of how local corrosion and inhibition processes initiate, evolve, and interact within complex alloy microstructures. This moves beyond isolated case studies and allows trends and patterns to emerge at the population level. Second, from a corrosion protection standpoint, identifying the diversity of local behaviours reveals the limitations of existing inhibitor systems and supports the development of more targeted and robust active protection strategies. In effect, this study bridges the gap between localized site behaviour and broader material performance, contributing both to fundamental understanding and practical advancements in corrosion mitigation. Additionally, this work introduces new approaches for quantitative analysis and interpretation of activity levels, enhancing their value as a tool for analysis of time-dependent local corrosion and inhibition behaviour.

1.6. Research outline

Chapter 2 builds on the work of Olgiati et al. [32] by examining how the effectiveness of corrosion inhibition is influenced by the time-dependent activation (i.e., dealloying and trenching) of intermetallic particles with varying compositions in AA2024-T3. $Ce(NO_3)_3$, also referred to as Ce(III), is used as model inhibitor. A key objective is to determine how delayed can the inhibitor be supplied after the exposure of the alloy to a corrosive solution without compromising the resulting corrosion protection. The changes in the time-dependent local activity evolution across IMP sites were analysed to determine the impact of the inhibitor supply delay. A new approach for quantitative analysis of the activity levels of the set of pixels in the IMP ROI is also presented. The findings presented in the chapter highlight how delayed supply of the inhibitor can cause significant changes in the precipitation behaviour of the inhibitor (i.e., more pronounced precipitation with longer supply delay). Potential implications of the observed changes on active corrosion protection strategies for AA2024 are also discussed in this chapter.

Chapter 3 continues the investigation of corrosion inhibition in AA2024-T3 with Ce(III). However, it shifts the focus from inhibition behaviour following introduction of Ce(III) to when the inhibitor is no longer supplied to the system. In ideal conditions, the inhibiting layer initially formed when Ce(III) is supplied to the system should remain stable even when the supply is not available anymore. This chapter explores this stability by analysing how local corrosion across IMP sites develops when the sample is first immersed in corrosive solution containing Ce(III) and then re-immersed in an inhibitor-free corrosive solution. This exposure sequence approximates what happens in active corrosion protection systems when the inhibitor supply is depleted and there is no more steady supply of inhibitor to the IMP sites. This chapter reveals that local corrosion behaviour under inhibitor-depleted conditions is more diverse than the relatively uniform initiation observed in uninhibited systems. Site-level behaviour was categorized into four general cases based on low or high activity during both immersion (inhibitor present) and re-immersion (inhibitor absent). Mechanisms underlying these categories were proposed by examining the compositional and morphological characteristics of individual IMPs and their surrounding environment. Additionally, the chapter also explores the impact of the exposure duration to Ce(III) and the delay in Ce(III) supply on inhibition stability during re-immersion. The implications of the results on ways to improve re-immersion stability of active corrosion protection strategies are also identified.

Chapter 4 shifts focus to AA7075-T6, another commonly used aluminium alloy in aerospace applications, and investigates the initiation and propagation of streaking corrosion using in situ reflected light microscopy and concurrent electrochemical measurements. Unlike dealloying and trenching around intermetallic particles, streaking corrosion is a less known local corrosion process characterized by rapidly propagating dissolution streaks on the metal surface due to attack of an altered surface layer (ASL). This chapter provides insights on the nature of streaking corrosion, specifically on how its initiation is actually closely related to the processes happening on IMPs. This chapter also presents ways of correlating activity of multiple regions of interest which allowed identification of previously unreported galvanic interaction between propagating streaks and corroding IMPs. Furthermore, synchronized optical and electrochemical measurements also enabled exact determination of the surface events that cause specific open-circuit potential transient sequences. The findings presented in this chapter demonstrate how site- and time-resolved analysis uncovers interactions between local corrosion events and enhances the interpretation of global electrochemical measurements.

Chapter 5 brings the analysis of local corrosion closer to real life systems wherein the alloys are typically part of a multi-material system. This chapter examines the influence of macroscale galvanic coupling between AA2024-T3 and AA7075-T6 on localized corrosion behaviour using in situ reflected light microscopy combined with galvanic current and potential measurements via a zero-resistance ammeter. This integrated approach enabled simultaneous visualization and quantification of microscale corrosion events across both alloys. The findings reveal that galvanic coupling results in electron flow from AA2024 to AA7075, and visible local corrosion intensification on AA2024 IMPs. The intensification is attributed to the galvanic current enhancing cathodic activity at IMPs in AA2024. This increased cathodic activity leads to corrosion that extends beyond the trenches and seems to affect the overall pH of the AA2024 surface, which may reduce the deposition of corrosion products. Based on qualitative analysis of the optical activity maps, distinct stages of local corrosion were identified. Kinetic parameters estimated from the simplified pixel activity level distribution of the local corrosion sites were used to estimate the boundaries of each stage. Comparison of these kinetic parameters between sites from galvanically-coupled and open-circuit tests further enabled determination of the impact of the macroscale galvanic coupling on local corrosion. Furthermore, by linking these parameters to galvanic current and potential data, the study connects the progression of local corrosion to changes in the overall electrochemical response over time. On the AA7075 side, the development of streaking corrosion is shown to impact the electrochemical interaction between the alloys. This manifests as transients in galvanic current and potential and is also accompanied by changes in trench propagation on both sides of the couple. Altogether, the findings in this chapter highlight the role of macroscale galvanic interactions in altering localized corrosion processes and demonstrate the value of combining optical and electrochemical techniques to better understand corrosion behaviour in multi-material systems.

1.7. References

[1] S. Li, X. Yue, Q. Li, H. Peng, B. Dong, T. Liu, H. Yang, J. Fan, S. Shu, F. Qiu, Q. Jiang, Development and applications of aluminum alloys for aerospace industry, *J. Mater. Res. Technol.* 27 (2023) 944–983. doi:10.1016/j.jmrt.2023.09.274.

[2] P. Rambabu, N. Eswara Prasad, V.V. Kutumbarao, R.J.H. Wanhill, Aluminium Alloys for Aerospace Applications, (2017) 29–52. doi:10.1007/978-981-10-2134-3_2.

[3] A. Heinz, A. Haszler, C. Keidel, S. Moldenhauer, R. Benedictus, W.S. Miller, Recent development in aluminium alloys for aerospace applications, *Mater. Sci. Eng. A* 280 (2000) 102–107. doi:10.1016/s0921-5093(99)00674-7.

[4] E.A. Starke, J.T. Staley, Application of modern aluminum alloys to aircraft, *Prog. Aerosp. Sci.* 32 (1996) 131–172. doi:10.1016/0376-0421(95)00004-6.

[5] L. Paussa, F. Andreatta, D. De Felicis, E. Bemporad, L. Fedrizzi, Investigation of AA2024-T3 surfaces modified by cerium compounds: A localized approach, *Corros. Sci.* 78 (2014) 215–222. doi:10.1016/j.corsci.2013.10.001.

[6] F.F. Chen, I. Cole, A.E. Hughes, A.M. Glenn, E. Sapper, J. Osborne, Microstructure characterisation and reconstruction of intermetallic particles, *Mater. Corros.* 65 (2014) 664–669. doi:10.1002/maco.201307345.

[7] A.E. Hughes, R. Parvizi, M. Forsyth, Microstructure and corrosion of AA2024, *Corros. Rev.* 33 (2015) 1–30. doi:10.1515/corrrev-2014-0039.

[8] J.V. de Sousa Araujo, I. Costa, X. Zhou, Comparison of Constituent Intermetallic Particles in Different Aluminium Alloys, *Metallogr. Microstruct. Anal.* 14 (2025) 106–119. doi:10.1007/ s13632-025-01170-w.

[9] A.S. Hammad, H. Lu, M.M. El-Sayed Seleman, R.Q. Dzakyprasetyo, A. Anawati, Corrosion Behaviour of Aluminum Alloy AA7075-T651, *IOP Conf. Ser. Mater. Sci. Eng.* 541 (2019) 012006. doi:10.1088/1757-899x/541/1/012006.

[10] A.E. Hughes, A.M. Glenn, N. Wilson, A. Moffatt, A.J. Morton, R.G. Buchheit, A consistent description of intermetallic particle composition: An analysis of ten batches of AA2024-T3, *Surf. Interface Anal.* 45 (2013) 1558–1563. doi:10.1002/sia.5207.

[11] A.E. Hughes, C. MacRae, N. Wilson, A. Torpy, T.H. Muster, A.M. Glenn, Sheet AA2024?T3: a new investigation of microstructure and composition, *Surf. Interface Anal.* 42 (2010) 334–338. doi:10.1002/sia.3163.

[12] Y. Zhu, K. Sun, G.S. Frankel, Intermetallic Phases in Aluminum Alloys and Their Roles in Localized Corrosion, *J. Electrochem. Soc.* 165 (2018) C807–C820. doi:10.1149/2.0931811jes.

[13] A. Boag, A.E. Hughes, N.C. Wilson, A. Torpy, C.M. MacRae, A.M. Glenn, T.H. Muster, How complex is the microstructure of AA2024-T3?, *Corros. Sci.* 51 (2009) 1565–1568. doi:10.1016/j.corsci.2009.05.001.

[14] R.G. Buchheit, R.P. Grant, P.F. Hlava, B. Mckenzie, G.L. Zender, Local Dissolution Phenomena Associated with S Phase (Al_2CuMg) Particles in Aluminum Alloy 2024?T3, *J. Electrochem. Soc.* 144 (1997) 2621–2628. doi:10.1149/1.1837874.

[15] R. Ayer, J.Y. Koo, J.W. Steeds, B.K. Park, Microanalytical study of the heterogeneous phases in commercial Al-Zn-Mg-Cu alloys, *Metall. Mater. Trans. A* 16 (1985) 1925–1936. doi:10.1007/ bf02662393.

[16] F. Andreatta, H. Terryn, J.H.W. de Wit, Effect of solution heat treatment on galvanic coupling between intermetallics and matrix in AA7075-T6, *Corros. Sci.* 45 (2003) 1733–1746. doi:10.1016/s0010-938x(03)00004-0.

[17] S.Y. Chen, C.Y. Huang, C.S. Lin, Microstructure inhomogeneity of the constituent particles of 7075-T6 aluminum alloy after alkaline cleaning and desmutting, *Corros. Sci.* 184 (2021) 109354. doi:10.1016/j.corsci.2021.109354.

[18] Q. Yan, H. Zhang, C. Man, K. Pang, X. Wang, Z. Cui, H. Cui, The Effect of Intermetallic Compounds on Corrosion and Tribocorrosion Behavior of 7075 Aluminum Alloy, *J Mater Eng Perform* 33 (2024) 11494–11509. doi:10.1007/s11665-023-08771-y.

[19] N. Birbilis, M.K. Cavanaugh, R.G. Buchheit, Electrochemical behavior and localized corrosion associated with Al7Cu2Fe particles in aluminum alloy 7075-T651, *Corros. Sci.* 48 (2006) 4202–4215. doi:10.1016/j.corsci.2006.02.007.

[20] G.O. Ilevbare, O. Schneider, R.G. Kelly, J.R. Scully, In Situ Confocal Laser Scanning Microscopy of AA 2024-T3 Corrosion Metrology: I. Localized Corrosion of Particles, *J. Electrochem. Soc.* 151 (2004) B453. doi:10.1149/1.1764780.

[21] O. Schneider, G.O. Ilevbare, J.R. Scully, R.G. Kelly, In Situ Confocal Laser Scanning Microscopy of AA 2024-T3 Corrosion Metrology: II. Trench Formation around Particles To, *J. Electrochem. Soc.* 151 (2004) B465. doi:10.1149/1.1764781.

[22] T. Hashimoto, X. Zhang, X. Zhou, P. Skeldon, S.J. Haigh, G.E. Thompson, Investigation of dealloying of S phase (Al2CuMg) in AA 2024-T3 aluminium alloy using high resolution 2D and 3D electron imaging, *Corros. Sci.* 103 (2016) 157–164. doi:10.1016/j.corsci.2015.11.013.

[23] D. Li, Y. Hu, B. Guo, Study on the evaluation of localized corrosion of 2024T3 aluminum alloy with EIS, *Mater. Sci. Eng. A* 280 (2000) 173–176. doi:10.1016/s0921-5093(99)00686-3.

[24] M. Buchler, J. Kerimo, F. Guillaume, W.H. Smyrl, Fluorescence and Near-Field Scanning Optical Microscopy for Investigating Initiation of Localized Corrosion of Al 2024, *J. Electrochem. Soc.* 147 (2000) 3691. doi:10.1149/1.1393960.

[25] A. Kosari, F. Tichelaar, P. Visser, H. Zandbergen, H. Terryn, J.M.C. Mol, Dealloying-driven local corrosion by intermetallic constituent particles and dispersoids in aerospace aluminium alloys, *Corros. Sci.* 177 (2020) 108947. doi:10.1016/j.corsci.2020.108947.

[26] A. Kosari, H. Zandbergen, F. Tichelaar, P. Visser, P. Taheri, H. Terryn, J.M.C. Mol, In-situ nanoscopic observations of dealloying-driven local corrosion from surface initiation to in-depth propagation, *Corros. Sci.* 177 (2020) 108912. doi:10.1016/j.corsci.2020.108912.

[27] A. Boag, A.E. Hughes, A.M. Glenn, T.H. Muster, D. McCulloch, Corrosion of AA2024-T3 Part I: Localised corrosion of isolated IM particles, *Corros. Sci.* 53 (2011) 17–26. doi:10.1016/j.corsci.2010.09.009.

[28] A.M. Glenn, T.H. Muster, C. Luo, X. Zhou, G.E. Thompson, A. Boag, A.E. Hughes, Corrosion of AA2024-T3 Part III: Propagation, *Corros. Sci.* 53 (2011) 40–50. doi:10.1016/j.corsci.2010.09.035.

[29] A.E. Hughes, A. Boag, A.M. Glenn, D. McCulloch, T.H. Muster, C. Ryan, C. Luo, X. Zhou, G.E. Thompson, Corrosion of AA2024-T3 Part II: Co-operative corrosion, *Corros. Sci.* 53 (2011) 27–39. doi:10.1016/j.corsci.2010.09.030.

[30] S.R.K. Malladi, Q. Xu, F.D. Tichelaar, H.W. Zandbergen, F. Hannour, J.M.C. Mol, H. Terryn, Early stages during localized corrosion of AA2024 TEM specimens in chloride environment, *Surf. Interface Anal.* 45 (2013) 1619–1625. doi:10.1002/sia.5193.

[31] A. Kreta, M. Rodošek, L. Slemenik Perše, B. Orel, M. Gaberšcek, A. Šurca Vuk, In situ electrochemical AFM, ex situ IR reflection–absorption and confocal Raman studies of corrosion processes of AA 2024-T3, *Corros. Sci.* 104 (2016) 290–309. doi:10.1016/j.corsci.2015.12.023.

[32] M. Olgiati, P.J. Denissen, S.J. Garcia, When all intermetallics dealloy in AA2024-T3: quantifying early stage intermetallic corrosion kinetics under immersion, *Corros. Sci.* (2021) 109836. doi:10.1016/j.corsci.2021.109836.

[33] J. Li, N. Birbilis, R.G. Buchheit, Electrochemical assessment of interfacial characteristics of intermetallic phases present in aluminium alloy 2024-T3, *Corros. Sci.* 101 (2015) 155–164. doi:10.1016/j.corsci.2015.09.012.

[34] S.P. Knight, M. Salagaras, A.R. Trueman, The study of intergranular corrosion in aircraft aluminium alloys using X-ray tomography, *Corros. Sci.* 53 (2011) 727–734. doi:10.1016/j.corsci.2010.11.005.

[35] R.P. Wei, C.M. Liao, M. Gao, A transmission electron microscopy study of constituent-particle-induced corrosion in 7075-T6 and 2024-T3 aluminum alloys, *Metall Mater Trans A Phys Metall Mater Sci* 29 (1998) 1153–1160. doi:10.1007/s11661-998-0241-8.

[36] G. Özer, A. Karaaslan, Effects of RRA heat treatment on the exfoliation corrosion (EXCO), intergranular corrosion (IGC), and electrical conductivity of AA7075 alloy, *Mater. Corros.* 70 (2019) 549–557. doi:10.1002/maco.201810436.

[37] S. Niverty, C. Kale, K.N. Solanki, N. Chawla, Multiscale investigation of corrosion damage initiation and propagation in AA7075-T651 alloy using correlative microscopy, *Corros. Sci.* 185 (2021) 109429. doi:10.1016/j.corsci.2021.109429.

[38] T.S. Huang, G.S. Frankel, Influence of grain structure on anisotropic localised corrosion kinetics of AA7XXX-T6 alloys, *Corros. Eng. Sci. Technol.* 41 (2006) 192–199. doi:10.1179/174327 806x120739.

[39] F.H. Cao, Z. Zhang, J.F. Li, Y.L. Cheng, J.Q. Zhang, C.N. Cao, Exfoliation corrosion of aluminum alloy AA7075 examined by electrochemical impedance spectroscopy, *Mater. Corros.* 55 (2004) 18–23. doi:10.1002/maco.200303691.

[40] Z. Zhao, G.S. Frankel, On the first breakdown in AA7075-T6, *Corros. Sci.* 49 (2007) 3064–3088. doi:10.1016/j.corsci.2007.02.001.

[41] R.S. Huang, C.J. Lin, H.S. Isaacs, Measuring streaking rates of an Al–Zn alloy using a difference imaging technique, *Corros. Sci.* 48 (2006) 1867–1873. doi:10.1016/j.corsci.2006.05.039.

[42] R.S. Huang, C.J. Lin, H.S. Isaacs, A Difference-Imaging Technique Used to Study Streaking Corrosion of Aluminum Alloys AA7075 and AA8006 in Chloride Solution, *Electrochemical and Solid-State Letters* 9 (2006) B11–B14. doi:10.1149/1.2140503.

[43] W. Zhang, G.S. Frankel, Transitions between pitting and intergranular corrosion in AA2024, *Electrochim. Acta* 48 (2003) 1193–1210. doi:10.1016/s0013-4686(02)00828-9.

[44] E. Eichinger, J. Osborne, T. Van Cleave, Hexavalent chromium elimination: An aerospace industry progress report, *Met. Finish.* 95 (1997) 36–41. doi:10.1016/s0026-0576(97)86771-2.

[45] R.L. Twite, G.P. Bierwagen, Review of alternatives to chromate for corrosion protection of aluminum aerospace alloys, *Prog. Org. Coat.* 33 (1998) 91–100. doi:10.1016/s0300-9440(98)00015-0.

[46] C.C. Alvarez, M.E. Bravo Gómez, A. Hernández Zavala, Hexavalent chromium: Regulation and health effects, *J. Trace Elem. Med. Biol.* 65 (2021) 126729. doi:10.1016/j.jtemb.2021.126729.

[47] R. Marx, A. Rouw, Risk Reduction Potential of REACH Authorisation, *Eur. J. Risk Regul.* 9 (2018) 154–161. doi:10.1017/err.2017.80.

[48] K.A. Yasakau, M.L. Zheludkevich, S.V. Lamaka, M.G.S. Ferreira, Mechanism of Corrosion Inhibition of AA2024 by Rare-Earth Compounds, *J. Phys. Chem. B* 110 (2006) 5515–5528. doi:10.1021/jp0560664.

[49] J.A.C. Mendez, Y.M. Vong, J. de J.P. Bueno, Cerium and Other Rare Earth Salts as Corrosion Inhibitors—A Review, *Prot. Met. Phys. Chem. Surf.* 58 (2022) 801–810. doi:10.1134/s207020 5122040141.

[50] M. Bethencourt, F.J. Botana, J.J. Calvino, M. Marcos, M.A. Rodríguez-Chacón, Lanthanide compounds as environmentally-friendly corrosion inhibitors of aluminium alloys: a review, *Corros. Sci.* 40 (1998) 1803–1819. doi:10.1016/s0010-938x(98)00077-8.

[51] T.H. Muster, H. Sullivan, D. Lau, D.L.J. Alexander, N. Sherman, S.J. Garcia, T.G. Harvey, T.A. Markley, A.E. Hughes, P.A. Corrigan, A.M. Glenn, P.A. White, S.G. Hardin, J. Mardel, J.M.C. Mol, A combinatorial matrix of rare earth chloride mixtures as corrosion inhibitors of AA2024-T3: Optimisation using potentiodynamic polarisation and EIS, *Electrochim. Acta* 67 (2012) 95–103. doi:10.1016/j.electacta.2012.02.004.

[52] P. Visser, Y. Liu, H. Terryn, J.M.C. Mol, Lithium salts as leachable corrosion inhibitors and potential replacement for hexavalent chromium in organic coatings for the protection of aluminum alloys, *J. Coat. Technol. Res.* 13 (2016) 557–566. doi:10.1007/s11998-016-9784-6.

[53] E. Michailidou, P. Visser, J.M.C. Mol, A. Kosari, H. Terryn, K. Baert, Y. Gonzalez-Garcia, The effect of pH on the corrosion protection of aluminum alloys in lithium-carbonate-containing NaCl solutions, *Corros. Sci.* 210 (2023) 110851. doi:10.1016/j.corsci.2022.110851.

[54] Z. Li, A. Homborg, Y. Gonzalez-Garcia, A. Kosari, P. Visser, A. Mol, Evaluation of the formation and protectiveness of a lithium-based conversion layer using electrochemical noise, *Electrochim. Acta* 426 (2022) 140733. doi:10.1016/j.electacta.2022.140733.

[55] M.S. Vukasovich, J.P.G. Farr, Molybdate in corrosion inhibition—A review, *Polyhedron* 5 (1986) 551–559. doi:10.1016/s0277-5387(00)84963-3.

[56] P. Rodic, I. Milošev, Corrosion Inhibition of Pure Aluminium and Alloys AA2024-T3 and AA7075-T6 by Cerium(III) and Cerium(IV) Salts, *J. Electrochem. Soc.* 163 (2016) C85–C93. doi:10.1149/2.0431603jes.

[57] I.A.W. Ma, S. Ammar, S.S.A. Kumar, K. Ramesh, S. Ramesh, A concise review on corrosion inhibitors: types, mechanisms and electrochemical evaluation studies, *Journal of Coatings Technology and Research 2021 19:1* 19 (2021) 241–268. doi:10.1007/s11998-021-00547-0.

[58] O. Lopez-Garrity, G.S. Frankel, Corrosion Inhibition of AA2024-T3 By Sodium Silicate, *Electrochim Acta* 130 (2014) 9–21. doi:10.1016/j.electacta.2014.02.117.

[59] T. Zheng, L. Wang, J. Liu, J. Wang, G. Jia, The corrosion inhibition effect of sodium silicate and Triton X-100 on 2024-T3 aluminum alloy in NaOH medium: Experimental and theoretical research, *Colloids Surf A Physicochem Eng Asp* 610 (2021) 125723. doi:10.1016/j.colsurfa.2020.125723.

[60] M. Kazemi, I. Danaee, D. Zaarei, Deposition and corrosion behavior of silicate conversion coatings on aluminum alloy 2024, *Mater. Werkst.* 45 (2014) 574–581. doi:10.1002/mawe.201400212.

[61] R. Naderi, M.M. Attar, Electrochemical assessing corrosion inhibiting effects of zinc aluminum polyphosphate (ZAPP) as a modified zinc phosphate pigment, *Electrochim. Acta* 53 (2008) 5692–5696. doi:10.1016/j.electacta.2008.03.029.

[62] A.F. Cantor, D. Denig-Chakroff, R.R. Vela, M.G. Pfeinik, D.L. Lynch, Use of polyphosphate in corrosion control, *J. Am. Water Works Assoc.* 92 (2000) 95–102. doi:10.1002/j.1551-8833.2000.tb08820.x.

[63] K. Xhanari, M. Finšgar, Organic corrosion inhibitors for aluminum and its alloys in chloride and alkaline solutions: A review, *Arab. J. Chem.* 12 (2019) 4646–4663. doi:10.1016/j.arabjc.2016.08.009.

[64] T.G. Harvey, S.G. Hardin, A.E. Hughes, T.H. Muster, P.A. White, T.A. Markley, P.A. Corrigan, J. Mardel, S.J. Garcia, J.M.C. Mol, A.M. Glenn, The effect of inhibitor structure on the corrosion of AA2024 and AA7075, *Corros. Sci.* 53 (2011) 2184–2190. doi:10.1016/j.corsci.2011.02.040.

[65] S.V. Lamaka, M.L. Zheludkevich, K.A. Yasakau, M.F. Montemor, M.G.S. Ferreira, High effective organic corrosion inhibitors for 2024 aluminium alloy, *Electrochim. Acta* 52 (2007) 7231–7247. doi:10.1016/j.electacta.2007.05.058.

[66] C. Özkan, L. Sahlmann, C. Feiler, M. Zheludkevich, S. Lamaka, P. Sewlikar, A. Kooijman, P. Taheri, A. Mol, Laying the experimental foundation for corrosion inhibitor discovery through machine learning, *npj Mater. Degrad.* 8:21 (2024). doi:10.1038/s41529-024-00435-z.

[67] M.L. Zheludkevich, J. Tedim, M.G.S. Ferreira, "Smart" coatings for active corrosion protection based on multi-functional micro and nanocontainers, *Electrochim. Acta* 82 (2012) 314–323. doi:10.1016/j.electacta.2012.04.095.

[68] F. Peltier, D. Thierry, Review of Cr-Free Coatings for the Corrosion Protection of Aluminum Aerospace Alloys, *Coatings* 12 (2022) 518. doi:10.3390/coatings12040518.

[69] B. Shri Prakash, J.N. Balaraju, Chromate (Cr^{6+})-free surface treatments for active corrosion protection of aluminum alloys: a review, *J. Coat. Technol. Res.* 21 (2024) 105–135. doi:10.1007/s11998-023-00831-1.

[70] I.I. Udoh, H. Shi, E.F. Daniel, J. Li, S. Gu, F. Liu, E.-H. Han, Active anticorrosion and self-healing coatings: A review with focus on multi-action smart coating strategies, *J. Mater. Sci. Technol.* 116 (2022) 224–237. doi:10.1016/j.jmst.2021.11.042.

[71] D.R. Gunasegaram, M.S. Venkatraman, I.S. Cole, Towards multiscale modelling of localised corrosion, *Int. Mater. Rev.* 59 (2014) 84–114. doi:10.1179/1743280413y.0000000024.

[72] P.J. Denissen, S.J. Garcia, Reducing subjectivity in EIS interpretation of corrosion and corrosion inhibition processes by in-situ optical analysis, *Electrochim. Acta* 293 (2019) 514–524. doi:10.1016/j.electacta.2018.10.018.

[73] A.M. Homborg, R.A. Cottis, J.M.C. Mol, An integrated approach in the time, frequency and time-frequency domain for the identification of corrosion using electrochemical noise, *Electrochim. Acta* 222 (2016) 627–640. doi:10.1016/j.electacta.2016.11.018.

[74] J.A. Moreto, C.E.B. Marino, W.W. Bose Filho, L.A. Rocha, J.C.S. Fernandes, SVET, SKP and EIS study of the corrosion behaviour of high strength Al and Al–Li alloys used in aircraft fabrication, *Corros. Sci.* 84 (2014) 30–41. doi:10.1016/j.corsci.2014.03.001.

[75] L.B. Coelho, M. Taryba, M. Alves, M.F. Montemor, M.G. Olivier, Unveiling the effect of the electrodes area on the corrosion mechanism of a graphite - AA2024-T3 galvanic couple by localised electrochemistry, *Electrochim. Acta* 277 (2018) 9–19. doi:10.1016/j.electacta. 2018.04.187.

[76] J. Tedim, A.C. Bastos, S. Kallip, M.L. Zheludkevich, M.G.S. Ferreira, Corrosion protection of AA2024-T3 by LDH conversion films. Analysis of SVET results, *Electrochim Acta* 210 (2016) 215–224. doi:10.1016/j.electacta.2016.05.134.

[77] T. Hu, H. Shi, D. Hou, T. Wei, S. Fan, F. Liu, E.H. Han, A localized approach to study corrosion inhibition of intermetallic phases of AA 2024-T3 by cerium malate, *Appl. Surf. Sci.* 467–468 (2019) 1011–1032. doi:10.1016/j.apsusc.2018.10.243.

[78] R. Parvizi, A.E. Hughes, M. Forsyth, M.Y. Tan, Probing Localised Corrosion Inhibition of AA2024-T3 by Integrating Electrode Array, SVET, SECM, and SEM-EDS Techniques, Metals 2023, Vol. 13, *Page 1703* 13 (2023) 1703. doi:10.3390/met13101703.

[79] N. Jadhav, V.J. Gelling, Review—The Use of Localized Electrochemical Techniques for Corrosion Studies, *J. Electrochem. Soc.* 166 (2019) C3461–C3476. doi:10.1149/2.0541911jes.

[80] M.C.L. de Oliveira, R.M.P. da Silva, R.M. Souto, R.A. Antunes, Investigating local corrosion processes of magnesium alloys with scanning probe electrochemical techniques: A review, *J. Magnes. Alloys* 10 (2022) 2997–3030. doi:10.1016/j.jma.2022.09.024.

[81] W. Chang, H. Qian, Z. Li, A. Mol, D. Zhang, Application and prospect of localized electrochemical techniques for microbiologically influenced corrosion: A review, *Corros. Sci.* 236 (2024) 112246. doi:10.1016/j.corsci.2024.112246.

[82] Z. Lai, D. Li, S. Cai, M. Liu, F. Huang, G. Zhang, X. Wu, Y. Jin, Small-Area Techniques for Micro- and Nanoelectrochemical Characterization: A Review, *Anal. Chem.* 95 (2023) 357–373. doi:10.1021/acs.analchem.2c04551.

[83] A.C. Bastos, M.C. Quevedo, O.V. Karavai, M.G.S. Ferreira, Review—On the Application of the Scanning Vibrating Electrode Technique (SVET) to Corrosion Research, *J. Electrochem. Soc.* 164 (2017) C973–C990. doi:10.1149/2.0431714jes.

[84] P.J. Denissen, V. Shkirskiy, P. Volovitch, S.J. Garcia, Corrosion Inhibition at Scribed Locations in Coated AA2024-T3 by Cerium- and DMTD-Loaded Natural Silica Microparticles under Continuous Immersion and Wet/Dry Cyclic Exposure, *ACS Appl. Mater. Interfaces* 12 (2020) 23417–23431. doi:10.1021/acsami.0c03368.

[85] G. Acosta, L. Veleva, D. de la Fuente, Mapping the initial corrosion activity of aluminium alloy 2024?T3 in diluted substitute ocean water by localized electrochemical impedance spectroscopy, *Mater. Corros.* 69 (2018) 1368–1374. doi:10.1002/maco.201810109.

[86] S. Marcelin, N. Pébère, Synergistic effect between 8-hydroxyquinoline and benzotriazole for the corrosion protection of 2024 aluminium alloy: A local electrochemical impedance approach, *Corros. Sci.* 101 (2015) 66–74. doi:10.1016/j.corsci.2015.09.002.

[87] J.C. Seegmiller, D.A. Buttry, A SECM Study of Heterogeneous Redox Activity at AA2024 Surfaces, *J. Electrochem. Soc.* 150 (2003) B413. doi:10.1149/1.1593041.

[88] Z. Li, G. Li, P. Visser, A. Homborg, Y. Gonzalez-Garcia, A. Mol, Local scanning electrochemical microscopy analysis of a lithium-based conversion layer on AA2024-T3 at progressive stages of formation, *Electrochim. Acta* 469 (2023) 143270. doi:10.1016/j.electacta.2023.143270.

[89] A. Maljusch, C. Senöz, M. Rohwerder, W. Schuhmann, Combined high resolution Scanning Kelvin probe—Scanning electrochemical microscopy investigations for the visualization of local corrosion processes, *Electrochim. Acta* 82 (2012) 339–348. doi:10.1016/j.electacta. 2012.05.134.

[90] Z. Lai, M. Liu, P. Bi, F. Huang, Y. Jin, Perspectives on Corrosion Studies Using Scanning Electrochemical Cell Microscopy: Challenges and Opportunities, *Anal. Chem.* 95 (2023) 15833–15850. doi:10.1021/acs.analchem.3c02423.

[91] H. Sheng, C. Dong, K. Xiao, X. Li, L. Lu, Anodic dissolution of a crack tip at AA2024-T351 in 3.5wt% NaCl solution, International Journal of Minerals, Metallurgy, *and Materials* 19 (2012) 939–944. doi:10.1007/s12613-012-0651-x.

[92] L.B. Coelho, M. Taryba, M. Alves, X. Noirfalise, M.F. Montemor, M.G. Olivier, The corrosion inhibition mechanisms of Ce(III) ions and triethanolamine on graphite—AA2024-T3 galvanic couples revealed by localised electrochemical techniques, *Corros. Sci.* 150 (2019) 207–217. doi:10.1016/j.corsci.2019.02.007.

[93] S.V. Lamaka, M. Taryba, M.F. Montemor, H.S. Isaacs, M.G.S. Ferreira, Quasi-simultaneous measurements of ionic currents by vibrating probe and pH distribution by ion-selective microelectrode, *Electrochem. Commun.* 13 (2011) 20–23. doi:10.1016/j.elecom.2010.11.002.

[94] F. Andreatta, L. Fedrizzi, The use of the electrochemical micro-cell for the investigation of corrosion phenomena, *Electrochim. Acta* 203 (2016) 337–349. doi:10.1016/j.electacta. 2016.01.099.

[95] R. Parvizi, A.E. Hughes, A.M. Glenn, P. Cizek, M.Y. Tan, M. Forsyth, Role of microstructure in corrosion initiation of a highly-deformed AA2024 wire, *Corros. Sci.* 144 (2018) 184–197. doi:10.1016/j.corsci.2018.08.052.

[96] X. Zhou, C. Luo, T. Hashimoto, A.E. Hughes, G.E. Thompson, Study of localized corrosion in AA2024 aluminium alloy using electron tomography, *Corros. Sci.* 58 (2012) 299–306. doi:10.1016/j.corsci.2012.02.001.

[97] P. Schmutz, G.S. Frankel, Corrosion Study of AA2024?T3 by Scanning Kelvin Probe Force Microscopy and In Situ Atomic Force Microscopy Scratching, *J. Electrochem. Soc.* 145 (1998) 2295–2306. doi:10.1149/1.1838634.

[98] E.O. Fanijo, J.G. Thomas, Y. Zhu, W. Cai, A.S. Brand, Surface Characterization Techniques: A Systematic Review of their Principles, Applications, and Perspectives in Corrosion Studies, *J. Electrochem. Soc.* 169 (2022) 111502. doi:10.1149/1945-7111/ac9b9b.

[99] A. Kosari, M. Ahmadi, F. Tichelaar, P. Visser, Y. Gonzalez-Garcia, H. Zandbergen, H. Terryn, J.M.C. Mol, Editors' Choice—Dealloying-Driven Cerium Precipitation on Intermetallic Particles in Aerospace Aluminium Alloys, *J. Electrochem. Soc.* 168 (2021) 041505. doi:10.1149/1945-7111/abf50d.

[100] F.M. Queiroz, M. Magnani, I. Costa, H.G. de Melo, Investigation of the corrosion behaviour of AA 2024-T3 in low concentrated chloride media, *Corros. Sci.* 50 (2008) 2646–2657. doi:10.1016/j.corsci.2008.06.041.

[101] V. Shkirskiy, F. Kanoufi, Reflective microscopy for mechanistic insights in corrosion research, *Curr. Opin. Electrochem.* 39 (2023) 101259. doi:10.1016/j.coelec.2023.101259.

[102] J. Zhao, A. Santoso, S.J. Garcia, Small concentrations of NaCl help building stable inhibiting layers from 2, 5-dimercapto-1, 3, 4-thiadiazole (DMTD) on AA2024-T3, *Corros. Sci.* 225 (2023) 111562. doi:10.1016/j.corsci.2023.111562.

[103] F. Raffin, A. Makogon, F. Kanoufi, J. Echouard, V. Shkirskiy, P. Volovitch, Initial cathodic reactivity of intermetallic particles in 7175 aluminum alloy buried under 6 µm thick anodized oxide layer revealed by in-situ reflective microscopy, *Electrochim. Acta* 492 (2024) 144155. doi:10.1016/j.electacta.2024.144155.

[104] L. Godeffroy, A. Makogon, S. Gam Derouich, F. Kanoufi, V. Shkirskiy, Imaging and Quantifying the Chemical Communication between Single Particles in Metal Alloys, *Anal. Chem.* 95 (2023) 9999–10007. doi:10.1021/acs.analchem.3c01258.

[105] P. Denissen, In-situ Visual Quantification of Corrosion and Corrosion Protection, (2020). doi:10.4233/uuid:64f8f06e-5cc6-40cd-8c8d-722da6304b06.

[106] J.D. Ramsey, R.L. McCreery, Raman microscopy of chromate interactions with corroding aluminum alloy 2024-T3, *Corros. Sci.* 46 (2004) 1729–1739. doi:10.1016/j.corsci.2003.10.010.

[107] M. Li, A. Seyeux, F. Wiame, P. Marcus, J. Swiatowska, Localized corrosion induced surface modifications of Al-Cu-Li alloy studied by ToF-SIMS 3D imaging, *npj Mater. Degrad. 2021 5:1* 5 (2021) 1–8. doi:10.1038/s41529-021-00170-9.

[108] M. Li, A. Seyeux, F. Wiame, P. Marcus, J. Swiatowska, Insights on the Al-Cu-Fe-Mn intermetallic particles induced pitting corrosion of Al-Cu-Li alloy, *Corros. Sci.* 176 (2020) 109040. doi:10.1016/j.corsci.2020.109040.

[109] H.S. Isaacs, G. Adzic, C.S. Jeffcoate, 2000 W.R. Whitney Award Lecture: Visualizing Corrosion, *Corrosion* 56 (2000) 971–978. doi:10.5006/1.3294386.

[110] H.S. Isaacs, C. Scheffey, R. Huang, The Location of Events Producing Potential Transients During Pitting of Freely Corroding Al and Its Alloys, *ECS Trans.* 11 (2008) 1–12. doi:10.1149/1.2925257.

[111] J.P.H. Sukamto, W.H. Smyrl, N. Casillas, M. Al-Odan, P. James, W. Jin, L. Douglas, Microvisualization of corrosion, *Mater. Sci. Eng. A* 198 (1995) 177–196. doi:10.1016/0921-5093(95)80073-4.

[112] J.-F. Lemineur, H. Wang, W. Wang, F. Kanoufi, Emerging Optical Microscopy Techniques for Electrochemistry, *Annu. Rev. Anal. Chem.* 15 (2022) 57–82. doi:10.1146/annurev-anchem-061020-015943.

[113] P.J. Denissen, A.M. Homborg, S.J. Garcia, Interpreting Electrochemical Noise and Monitoring Local Corrosion by Means of Highly Resolved Spatiotemporal Real-Time Optics, *J. Electrochem. Soc.* 166 (2019) C3275–C3283. doi:10.1149/2.0341911jes.

[114] C.A. Schneider, W.S. Rasband, K.W. Eliceiri, NIH Image to ImageJ: 25 years of image analysis, *Nat. Methods* 9 (2012) 671–675. doi:10.1038/nmeth.2089.

[115] P. Thévenaz, U.E. Ruttimann, M. Unser, A pyramid approach to subpixel registration based on intensity, *IEEE Trans. Image Process.* 7 (1998) 27–41. doi:10.1109/83.650848.

[116] P.M.F. Forte, P.E.R. Felgueiras, F.P. Ferreira, M.A. Sousa, E.J. Nunes-Pereira, B.P.J. Bret, M.S. Belsley, Exploring combined dark and bright field illumination to improve the detection of defects on specular surfaces, *Opt. Lasers Eng.* 88 (2017) 120–128. doi:10.1016/j.optlaseng. 2016.08.002.

[117] E.T. Arena, C.T. Rueden, M.C. Hiner, S. Wang, M. Yuan, K.W. Eliceiri, Quantitating the cell: turning images into numbers with ImageJ, *WIREs Dev. Biol.* 6 (2017) e260. doi:10.1002/wdev.260.

[118] S. Lee, J. Kim, P. Bae, S. Lee, H. Kim, Intensity Histogram-Based Reliable Image Analysis Method for Bead-Based Fluorescence Immunoassay, *Biochip J.* 18 (2024) 137–145. doi:10.1007/s13206-023-00137-9.

2

Local corrosion and inhibition behaviour of AA2024-T3 intermetallics under delayed Ce(III) supply: An in situ optical study

Understanding how late an inhibitor can be released once corrosion initiated without compromising corrosion protection may help in developing more efficient anticorrosion coatings. We explored this idea through time-controlled $Ce(NO_3)_3$ availability to AA2024-T3 immersed in 0.05 M NaCl. $Ce(NO_3)_3$ was supplied at 0, 30, 60, and 180 s from the start of immersion to get a concentration of 0.001 M. Detailed visualization of surface changes at the intermetallic particle level was obtained using in situ reflected microscopy. SEM-EDX and confocal laser microscopy confirmed the extent of intermetallic degradation and local inhibitor deposition corresponding to operando changes. When the inhibitor is supplied within 60 s of immersion, the surface changes slowdown earlier and are visually less extensive than in uninhibited systems. Furthermore, our results highlight the potential of reflected microscopy for local corrosion inhibition studies and underscore the importance of understanding the interaction between inhibitor release timing and corrosion protection.

This chapter has been published as:

M. Mopon, A. Mol, S. J. Garcia, Effect of delayed inhibitor supply on AA2024-T3 intermetallic activity: A local in situ analysis with reflected microscopy, *Corros. Sci.* 230 (2024) 111910. doi: 10.1016/j.corsci.2024.111910.

2.1. Introduction

AA2024-T3 is widely used in the aerospace industry due to its excellent strength-to-weight ratio. However, intermetallic particles (IMPs) formed during thermomechanical processing make it susceptible to local corrosion [1–3]. Coatings are typically used to reduce this corrosion susceptibility by providing barrier protection against corrosive environments. However, the protection provided by coatings is passive and is typically lost when there is mechanical damage that exposes the underlying metal. More reliable protection can be achieved by incorporation of active corrosion inhibition strategies [4–6]. This is typically accomplished by adding corrosion inhibitors [7–10] in the coatings. When the coating is damaged, the inhibitors are released to interact with the exposed metal surface, thereby constraining the extent of local corrosion.

Local corrosion at AA2024-T3 IMPs begins with the dealloying of IMPs [11–13]. This is characterized by the removal of less noble elements (e.g., Mg, Al) and subsequent enrichment of more noble components (e.g., Cu). In a recent study by Olgiati et al. [14], in situ reflected optical microscopy with kinetic analysis of image changes revealed that the surface activity at the IMP surface consistent with dealloying initiated within the first two minutes of exposure to 0.05 M NaCl (i.e., 23 ± 11 s for S-phase, 86 ± 12 s for AlCuFeMn, 79 ± 18 s for $(Al,Cu)_x(Fe,Mn)_ySi$). After a transition time (i.e., 68 ± 23 s for S-phase, 195 ± 48 s for AlCuFeMn, 224 ± 142 s for $(Al,Cu)_x(Fe,Mn)_ySi$), surface activity eventually develops at the adjacent matrix of the IMPs. This activity is attributed to Al dissolution (i.e., trenching) driven by galvanic coupling with the ennobled IMP. Given the rapid initiation of these local corrosion processes, it is crucial to have corrosion inhibitors readily available to minimize the extent of local corrosion. This has led to the development of active corrosion protection strategies that emphasize fast release [15–18] ideally followed by sustained supply of the inhibitor [19,20]. However, fast release and sustained supply are two competing aspects of inhibitor release since prioritising the former may affect the latter, which can then compromise the long-term reliability of the corrosion protection system [21].

Numerous strategies have been explored to prevent early inhibitor depletion in active corrosion protection systems. One effective approach involves using carriers with higher local inhibitor storage capacity [15,22,23] to enhance long-term availability of inhibitors. The higher inhibitor reserves, in principle, compensate for the initial fast release rates. Sacrificing some of these initial fast release capabilities is also a potential strategy to retain the inhibitors within the system for an extended period. This is a minimally studied approach given that slower release rates would entail a certain degree of local corrosion. Nonetheless, this might be viable for precipitation-type inhibitors like cerium salts, which rely on local corrosion (i.e., dealloying) to deposit on the surface of IMPs [24–26].

Cerium deposition is influenced by the local alkalinity from the oxygen reduction reaction (ORR) occurring at the dealloying IMPs. The mechanistic interplay of dealloying-generated cathodic activity and cerium precipitation has been the subject of several studies. Li et al. [27] reported that depletion of Mg and Al due to dealloying in S-phase (i.e., Al_2CuMg) particles is needed for thick cerium deposits to form. On the other hand, Paussa et al. [28] found that fast magnesium dissolution during S-phase dealloying enables cathodic activity on nearby sites and accounts for the thick cerium deposits observed in S-phases. More recently, Kosari et al. [25] reported that the anodic and cathodic processes can occur simultaneously on IMPs from the onset of exposure, regardless of their composition. They identified dealloying as the primary factor in generating Cu-rich sites which facilitate cathodic reactions through nanogalvanic coupling with less noble regions of the IMP [11,12,25]. They emphasized the pivotal role of dealloying in determining the extent of cerium precipitation.

Based on the dealloying-driven mechanism of cerium precipitation coupled and the reported dealloying initiation times of AA2024-T3 IMPs, it can be argued that the cerium concentration does not necessarily need to be at a critical level at the very start of exposure to a corrosive solution for it to be protective. Thus, the initial inhibitor release from inhibition systems can be slowed down to a certain degree. This can lead to longer retention of Ce(III) within the system which allows for a more sustained release. A slower initial release effectively translates to delaying the availability of critical inhibitor concentrations to the surface of the IMPs. The delay in inhibitor availability, however, cannot be indefinite as this will result in significant local corrosion progression. Therefore, it seems necessary to determine a tolerable delay limit which can be used to extend inhibitor availability without compromising corrosion protection. We explored this idea in this work.

Here, an in situ reflected microscopy technique was used to analyse local surface changes when the availability of the inhibitor was intentionally delayed for a model system (i.e., electrolyte volume, electrolyte concentration, and inhibitor concentration are fixed). The microscopy technique previously enabled unprecedented visualization of intermetallic particle corrosion [14] and is thus promising for observing local inhibitor deposition and inhibitor layer growth.

The technique allows surface observations at 1-second intervals of all IMPs within a field of view of approximately 800 x 600 microns (resolution: ~10 pixel μm^{-2}). This allows for the analysis of the concurrent behaviour of more IMPs, a limitation encountered in higher resolution in situ methods like SKPFM [29,30] or EC-AFM [31,32]. $Ce(NO_3)_3$, further denoted as Ce(III), was used as the inhibitor for the system. Pre-immersion scanning electron microscopy with energy dispersive X-ray spectroscopy (SEM-EDX) was used to identify IMP composition which was then related to the surface changes observed. We quantified the extent and kinetics of these changes through a pixel subtraction-based image analysis protocol. The extent and kinetics were used to identify a tolerable delay limit specific to the model system conditions. Furthermore, we proposed mechanisms to elucidate why the inhibition behaviour varies at different Ce(III) supply times.

2.2. Experimental

2.2.1. Materials

Commercial grade bare AA2024-T3 (Kaiser Aluminium, rolled thickness = 2 mm) was used for the corrosion tests. Epoxy-embedded metal samples (EMS) with an exposed metal surface area of approximately 500 x 500 μm^2 were prepared from the metal sheets using a procedure described in earlier works [14,33]. Additional details on the preparation of the EMS are also provided in Supporting Information 2.7.1. A 0.05 M NaCl aqueous solution (>98% purity NaCl in “Millipore Elix 3 UV” treated water) was used as the corrosive solution while a 0.045 M $Ce(NO_3)_3$ + 0.05 M NaCl aqueous solution was used for adjusting the inhibitor concentration.

2.2.2. Experimental Protocols

The experimental protocols used were adopted from earlier works [14,33]. The EMS surface was ground with SiC sandpaper from 320 to 4000 grit. They were then polished with 3 and 1 µm diamond paste. The location and spot composition of IMPs (i.e., around 100 – 200 particles per EMS) on the polished sample surface were determined using SEM-EDX (JEOL JSM-7500F field emission scanning electron microscope coupled with energy dispersive X-ray spectroscopy). Back-scattered electron images were collected at a 15 kV accelerating voltage and a 10 µA emission current. The mapped EMS were quickly repolished (~10 s) with 1 µm diamond paste and washed in an ultrasonic bath containing ethanol before the immersion tests to remove contaminants from the SEM-EDX analysis. The EMS were placed in reflected microscopy setup (Figure 2.1a) which involves a digital microscope (Dinolite AM7515MT4A, ~10 pixel μm^{-2}) operating in brightfield mode for in situ acquisition of images of the surface during immersion [14]. The setup can also be used for electrochemical potential noise measurements during immersion, but this aspect of the experiment will be covered elsewhere. For the systems with non-delayed Ce(III) supply (t_{supply} = 0 s), a syringe was used to add 4.5 mL of 0.05 M NaCl + 0.001 M $Ce(NO_3)_3$ solution to the electrochemical cell. The electrolyte volume was dictated by the volume of our corrosion cell while the electrolyte solution was based on our previous work [14]. The time at which the EMS surface was fully exposed to the NaCl solution is t = 0. For the systems with delayed Ce(III) supply, a syringe was used to add 4.4 mL of the 0.05 M NaCl solution into the electrochemical cell. Corresponding volume of a 0.045 M $Ce(NO_3)_3$ solution was added using another syringe (27 gauge needle) at the delayed inhibitor supply times (t_{supply} = 30, 60, 180 s with respect to t = 0) to obtain a Ce^{3+} concentration of 0.001

M. Additional details about our electrolyte injection protocol are provided in Supporting Information 2.7.2. The t_{supply} values used were based on the t_{onset} and transition times reported by Olgiati et al. for IMPs in AA2024-T3 exposed to 0.05 M NaCl [14]. At the t_{supply} values selected, the IMP types identified are at different stages of dealloying and trenching: *(i)* at t_{supply} = 0 s (TS0), all the IMP types are inactive; *(ii)* at t_{supply} = 30 s (TS30), the S-phase IMPs are starting to dealloy; *(iii)* at t_{supply} = 60 s (TS60), S-phases have dealloyed considerably while the secondary particles (i.e., AlCuFeMn, $(Al,Cu)_x(Fe,Mn)_ySi)$) are just starting; *(iv)* at t_{supply} = 180 s (TS180), all IMP types are generally exhibiting an advanced state of dealloying with signs of trenching. Immersion test in 0.05 M NaCl was also conducted to serve as control and to establish uninhibited behaviour of θ-phase. Duplicates of the delayed supply immersion tests were also implemented to confirm reproducibility (Supporting Information 0). After the 3-h immersion, the EMS were removed from the corrosive environment, washed with deionized water, and dried in ambient conditions. Post-immersion analysis of the EMS was performed with a scanning laser confocal microscopy (SLCM) and SEM-EDX.

2.2.3. Image Analysis

Surface changes were identified through a pixel-based analysis of the optical images based on our previously reported protocol [14]. Additional details about our protocol are provided in Supporting Information 2.7.4. In a first step, the processing involved conversion of the images to grayscale, recursive repositioning to align images, and subtraction of images (i.e., image @ 0 s – image @ *x* s) to identify the pixels that changed (i.e., darkened). These steps were implemented in ImageJ. The output of these steps is a grayscale image showing changed pixels for the entire EMS thereby providing the global activity map (GAM). A built-in ImageJ look-up table (i.e., Jet) was used to recolour the GAMs to enable easier visualisation of the magnitude of the changes (i.e., activity level).

The succeeding step involved local activity analysis of the IMPs with known composition using MatLab (MathWorks). IMP limits were set using the pre-immersion SEM-EDX data and superimposed on the GAMs using a method we reported previously [14]. Based on the EDX-derived composition, the IMPs were grouped into S-phases (Al_2CuMg), the θ-phases (Al_2Cu), and the secondary particles (AlCuFeMn or $(Al,Cu)_x(Fe,Mn)_ySi)$). It is emphasized that classification of the IMPs into compositional groups is based on the relative amounts of elements measured. Rectangular regions of interest (RROI) that surround the particles were set to isolate pixels specific to each intermetallic particle. The sides of the RROIs have a 4-pixel margin with respect to the left-, right-, top-, and bottom-most pixels of the particle border. The margin set was based on the affected area of selected particles after 600 s of exposure to 0.05 M NaCl. Ultimately, activity will likely extend beyond the RROI beyond 600 s but the changes that can be attributed to the intermetallic particles are presumed to be sufficiently captured. The RROIs are then superimposed on the GAM (Figure 2.1b) to extract each IMP's local activity map (LAM). Around 100 to 200 LAMs were analysed per EMS.

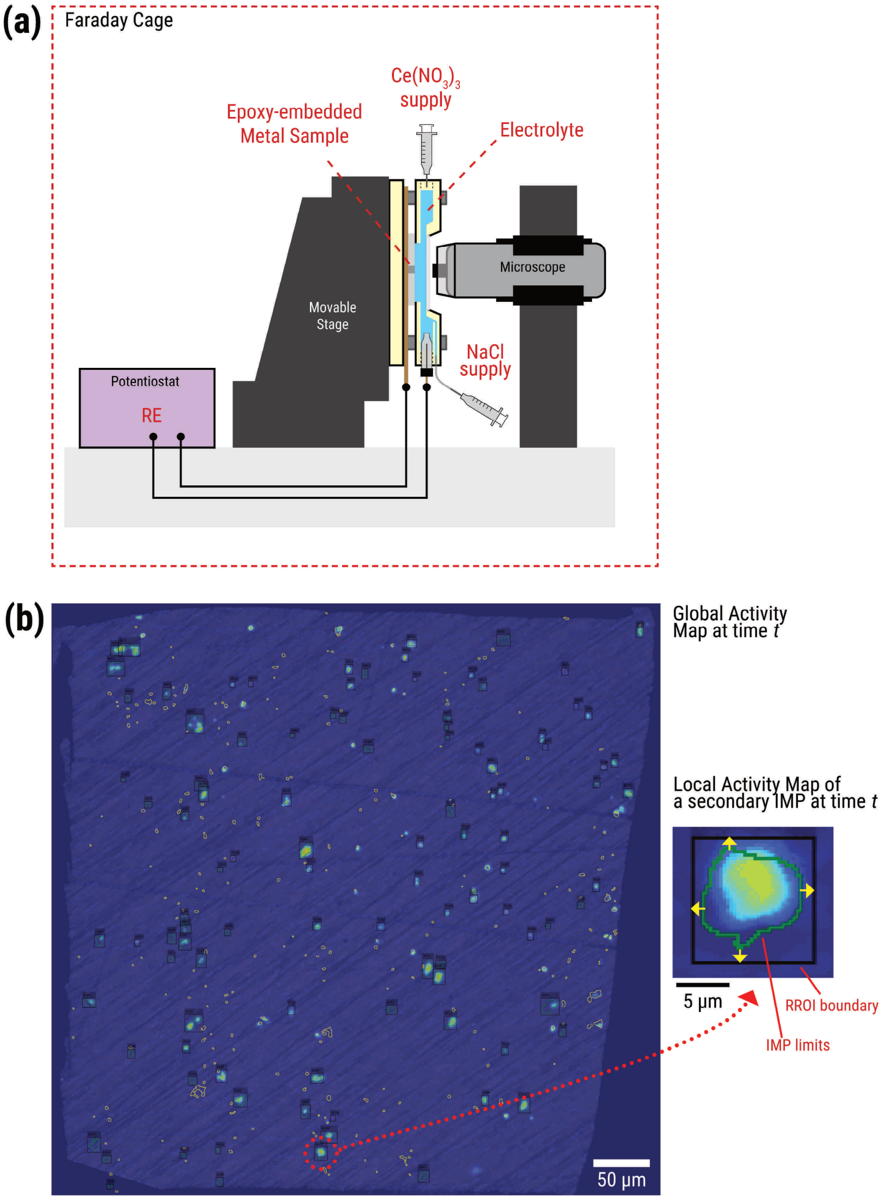

Figure 2.1. (a) in situ reflected microscopy setup (with electrochemical measurement capabilities) used to observe local surface changes during exposure to the electrolyte, and **(b)** a global activity map of an epoxy-embedded sample with IMP outlines and rectangular region of interest (RROI) boundaries used to establish the local activity maps. The global activity map is superimposed on an optical image (background) to highlight the position of the IMPs in the actual sample. The local activity map shows the degree of change of pixels at time t with respect to its initial condition (i.e., activity level) and the spatial distribution of the change.

Local activity depicted in the LAMs is quantified in terms of the pixel activity level. This is equivalent to the pixel gray-level which ranges from 0 to 255, with 0 indicating no detected change with respect to the initial condition. The distribution of activity levels of the pixels in the LAMs and its kinetics is our primary means for quantitative analysis of the surface changes in this work. At a specific time *t*, the pixel activity level distribution of a given LAM can be represented in terms of a histogram generated using MatLab's built-in *imhist* function. The distribution can be extracted for both the IMP pixels (Figure 2.2a) and the adjacent matrix (AMX) pixels (Figure 2.2b). The separate distributions are used to distinguish changes likely related to IMP processes (e.g., dealloying, inhibitor/oxide deposition) or to matrix processes (e.g., trenching, inhibitor/oxide deposition). For simpler analysis, the maximum (maxAL), minimum (minAL), and median activity levels (midAL) of the histograms are extracted. The midAL was favoured as the measure of central tendency because it is less sensitive to outliers. These three parameters are used to establish a simplified pixel activity level distribution for the IMP pixels ($sPAD_{IMP}$) and for the adjacent matrix pixels ($sPAD_{AMX}$). Measuring the sPAD at different times produces the time-series $sPAD_{IMP}(t)$ (Figure 2.2b) and $sPAD_{AMX}(t)$ which enables analysis of the time-dependent trends of the surface changes. Compared to our previous method which focuses on measuring percentage of pixels that changed ($S_{changed}$ %) based on a lower bin threshold (LTH), using the sPAD allows observation of changes even when *all* pixels in the LAM have activity levels greater the LTH (i.e., $S_{changed}$ = 100 %). This is especially useful for assessing local inhibitor effect at the end of immersion.

It should be noted that analysis of the LAMs and the sPADs was focused on active IMPs (i.e., IMPs which exhibited detectable change). These IMPs were prioritised because we cannot be completely certain if inactivity in the presence of the inhibitor is due to the interaction with the inhibitor or due to the inherent stability of the IMPs during the immersion period investigated. Supporting Information 2.7.4 provides additional details on how active IMPs were distinguished from inactive IMPs.

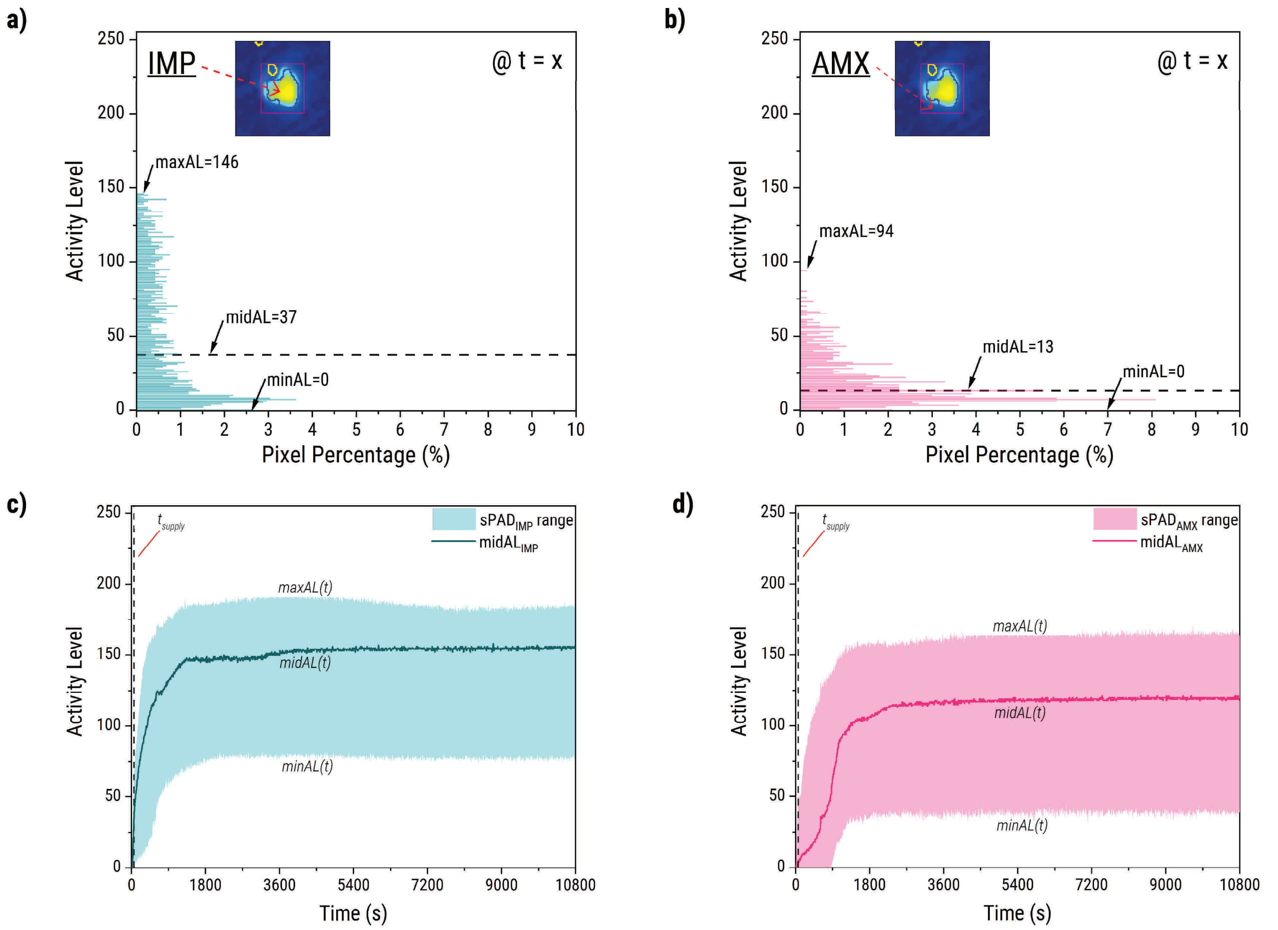

Figure 2.2. Maximum, minimum, and median values are extracted from the **(a)** IMP, and **(b)** adjacent matrix (AMX) pixel activity level distribution at time t. These were then used to build the simplified pixel activity distribution vs time plots for the **(c)** intermetallic particle pixels ($sPAD_{IMP}(t)$), and for the **(d)** adjacent matrix pixels ($sPAD_{AMX}(t)$). The resulting plots are used to assess the region involved with specific optical activity.

2.3. Results

2.3.1. Local behaviour of S-phase IMPs at different Ce(III) supply times

Figure 2.3a shows LAMs of the representative S-phase IMP when Ce(III) is not present in the system. Distinct low-level activity (i.e., light blue pixels) at the IMP was observed within 35 s. This was followed by increase of the activity level of the IMP pixels and activation of adjacent matrix (AMX) pixels (i.e., appearance of light blue pixels in AMX). At 1800 s, the activity of the AMX pixels closest to the IMP boundary is higher than that of the IMP pixels. Further pixel activity increase was concentrated among these AMX pixels. Activation of new AMX pixels on the areas far from the IMP also progressed slowly from 1800 s as evident from minimal changes in the LAMs. The post-immersion SEM image shows that the IMP pixel activity is consistent with the IMP degradation (i.e., dealloying) while the high-level activity among the AMX pixels is consistent with trenching. Furthermore, the lower AMX activity on the pixels beyond the trench coincides with presence of scattered dark spots. Previous works attributed this to corrosion induced by redistributed Cu particles released by the degraded S-phase particle [11,24,34].

Figure 2.3b shows there is a significant reduction in surface changes for the representative S-phase IMP at TS0 when compared to the uninhibited S-phase particle. Activity comparable to the initial changes of the uninhibited S-phase (i.e., activity at 35 s) were not observed until 1800 s. In spite of this activity during immersion, no signs of dealloying or trenching are visible in the post-immersion SEM image. However, spot composition approximated from the EDX spectra for the IMP surface indicated trace amounts of Ce (Atomic %: Ce ~ 0.3; Supporting Information 2.7.5 - Figure S2.11a). While this is not an accurate quantification, this suggests that the optical activity observed can be correlated to Ce deposition. Post-immersion SLCM analysis of another set of TS0 S-phase particles (Figure 2.4a) with similar activity level (Figure 2.4b) was used to estimate the scale of the corresponding Ce deposition. The SLCM images (Figure 2.4c) of these particles show that there is indeed a height difference between the S-phase particles (point 1 and point 2) and the rest of the metal surface. In contrast, other particles within the region which have minimal optical activity (point 3) registered minimal height difference from the rest of the surface. The corresponding line profile through the S-phase IMPs (Figure 2.4d) further indicates that the height difference is submicron (~ 0.1 μm). This coupled with the detected Ce in SEM/EDX points to submicron Ce deposition after three hours of immersion when the inhibitor is supplied at 0 s.

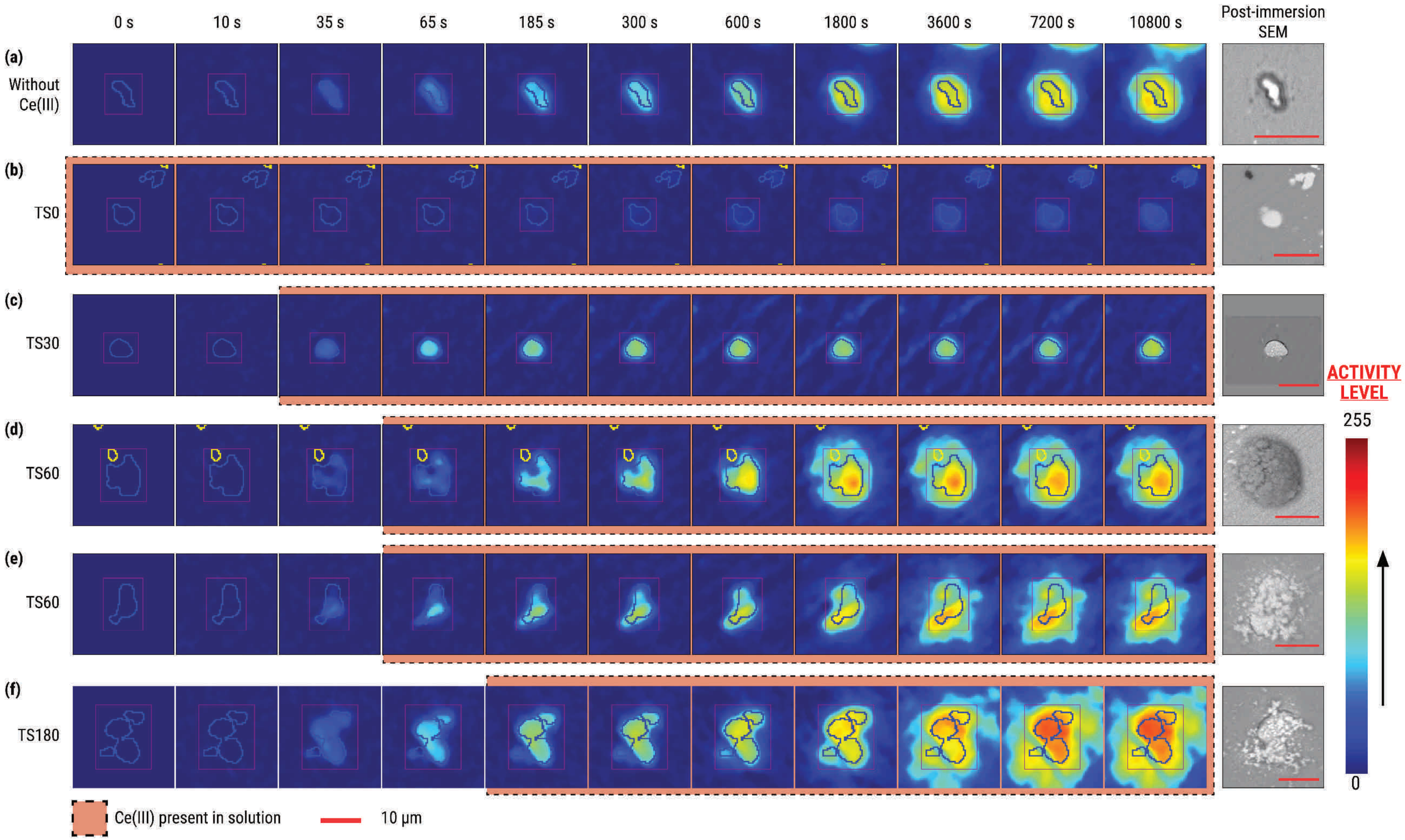

Figure 2.3. Local activity maps (LAMs) of representative S-phase (Al_2CuMg) IMPs show evolution of the surface with time during exposure to **(a)** 0.05 M NaCl and with Ce(III) supplied at **(b)** 0, **(c)** 30, **(d)** 60 (visible corrosion product deposition), **(e)** 60 (visible Ce precipitation), and **(f)** 180 s from the start of immersion. The map colours represent the pixel activity level (i.e., change of the pixel gray-level with respect to its initial condition) at time *t*. The blue outline and the magenta rectangle overlaid on the map marks the IMP and RROI boundary, respectively. The LAMs highlight where the changes are happening in the context of the IMP and how extensive are the changes. The corresponding post-immersion back-scattered SEM images allude to the nature of the surface changes observed in the LAMs.

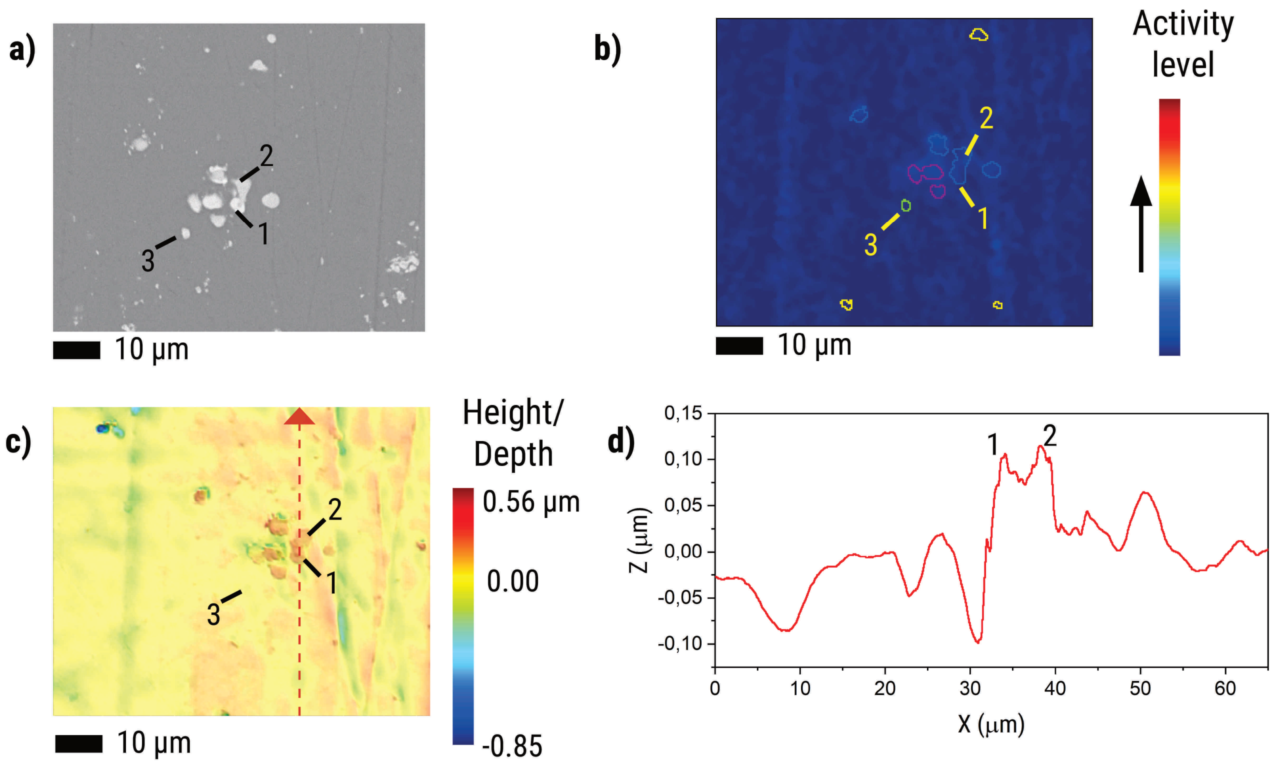

Figure 2.4. (a) Pre-immersion SEM image of S-phase particles, and their **(b)** activity after three hours of exposure to 0.05 M NaCl and 0.001 M Ce(III) supplied at 0 s. The **(c)** SLCM images and corresponding **(d)** line profile for the particles indicate that low-level activity observed corresponds to submicron changes which we associate with Ce deposition.

Higher activity levels were generally observed for the TS30 S-phase IMP compared to the TS0 S-phase (Figure 2.3c). The onset of low-level activity of the TS30 S-phase IMP is similar though to the uninhibited S-phase particle. After Ce(III) addition, there is a rapid increase of pixel activity which lasted until around 300 s at the IMP. This was accompanied by minimal activation of the AMX pixels. It should be noted that the slight reduction in activity between 7200 s and 10800 s is due to changes in the microscope lighting. The post-immersion back-scattered SEM image shows that the high IMP activity is associated with the formation of bright globular deposits which contain Ce (Atomic %: Ce ~ 4.8; Supporting Information 2.7.5 - Figure S2.11b). This further supports the correspondence between optically measurable activity and Ce(III) deposition and layer growth. Meanwhile, the lower AMX pixel activity is attributed to minimal changes on the adjacent matrix. Matrix activity outside the RROI was also

Figure 2.3d and Figure 2.3e show behaviour of two representative TS60 S-phase IMPs. The progression of their surface changes is generally comparable but the compositions of their deposited layer at the end of exposure have some interesting variation. Their initial activity is comparable with the uninhibited S-phase. After the addition of Ce(III), the changes became more similar to TS30. High activity spots were visible at the IMP surface of particles at around

65 s. These spots are likely preferential sites for Ce(III) deposition. The presence of these spots suggests compositional heterogeneity or differences in dealloying activity within the IMP. Unlike TS30, further deposition was observed for both particles, leading to increased AMX pixel involvement between 600 s and 1800 s. The changes appear to slow down after 1800 s which suggest minimal or no further deposition. Post-immersion back-scattered SEM image of the first TS60 S-phase (Figure 2.3d) shows that the outline of thick dark deposited layer coincides with the active pixels in the LAMs. Based on EDX, the deposit contained Ce precipitates mixed with corrosion products (Atomic %: Ce ~ 0.8, Al ~ 27.5, O ~ 71.2; Supporting Information 2.7.5 - Figure S2.11c). Meanwhile, post-immersion back-scattered SEM image of the second TS60 S-phase (Figure 2.3d) shows a bright deposit similar to the Ce-rich deposit observed for the TS30 S-phase. The higher amount of corrosion products on the deposited layer of the first TS60 S-phase is potentially due to a rupture of the initial Ce deposits. This could have enabled release and deposition of corrosion products on top of the Ce layer resulting in the dark colour observed.

S-phase behaviour at TS180 (Figure 2.3e) is comparable to the behaviour in TS60. However, the TS180 particle exhibited continued surface changes for a longer duration (i.e., until around 7200 s) which points to sustained progression of the local processes that contribute to deposition. Post-immersion SEM shows narrow trenching around the IMP and irregular deposition on top of it. The deposit is comparable to the second TS60 S-phase (Figure 2.3d). Based on EDX analysis of the IMP, the deposit contained Ce precipitates mixed with corrosion products (Atomic%: Ce ~ 8.0, Al ~ 11.2 , O ~ 71.9; Supporting Information 2.7.5 - Figure S2.11d).

2.3.2. Local behaviour of θ-phase IMPs at different Ce(III) supply times

Figure 2.5a shows that the onset of surface changes (i.e., appearance of light blue pixels on IMP) for uninhibited θ-phase particles is likely within the first minute of immersion, close to the onset of changes of uninhibited S-phase particles. A sample of 12 particles placed the mean activity onset for θ-phase particles at 43 ± 42 s. The high standard deviation is attributed to the Mg content (0 – 2 At%) [35] of the particles as well as the potential heterogeneity within the particle [3]. Supporting Information 2.7.6 shows how the activity onset was quantified for the θ-phase IMPs. After the onset of activity, the subsequent increase of IMP and AMX pixel activity due to dealloying and trenching followed the same course as the uninhibited S-phase IMP.

Matrix dissolution due to Cu redistribution is also observed as dark spots beyond the main trench.

Figure 2.5b shows that the surface changes of the representative TS0 θ-phase IMP were also considerably reduced compared to the uninhibited θ-phase. Its behaviour during immersion is generally similar to the TS0 S-phase albeit with much lower activity levels. The optically detected changes are also attributed to submicron Ce deposition based on comparable activity and cerium detected on the IMP via EDX (Atomic %: Ce ~ 0.4; Supporting Information 2.7.5 - Figure S2.12a).

Distinct low-level activity for TS30 θ-phase (Figure 2.5c) was observed at a spot on the IMP much earlier than the uninhibited θ-phase. The activation of this spot is comparable to that of the TS30 S-phase which suggests that it is also a preferential deposition site for Ce(III). This highly localized activity is attributed to higher concentration of less noble elements (e.g., Mg) on the region. This is typically encountered when an S-phase is embedded in a θ-phase IMP [36]. Activation of rest of the IMP and some of the AMX pixels due to further deposition was eventually observed. There were minimal changes though after 600 s. SEM-EDX analysis of the first active spot showed *visible* bright globular Ce-containing deposits (Atomic %: Ce ~ 2.3; Supporting Information 2.7.5 - Figure S2.12b). There were also some signs of dealloying in this region (dark spots in point 1 of Figure 2.5c), but trenching was not apparent. Ce was also detected in the IMP region which activated much later but at a lower amount (Atomic %: Ce ~ 1.1; Supporting Information 2.7.5 - Figure S2.12c).

Figure 2.5d shows that TS60 θ-phase IMP activity was not detectable until around 185 s, with similar mode to the region of the TS30 θ-phase IMP which activated much later. The surface changes of the IMP were also observed after the addition of Ce(III) to the solution indicating that it is deposition-related. The activity was concentrated at the IMP but increased activation of AMX pixels was also observed after 600 s. Surface changes were minimal after 3600 s. The post-immersion SEM image shows a narrow trench around the particle and more prominent deposition compared to the TS30 θ-phase IMP.

The initiation and progression of surface changes of the TS180 θ-phase (Figure 2.5e) are generally similar to the TS60 θ-phase IMP. Activity associated with dealloying of the IMP surface was initially seen at around 65 s as expected for this type of IMP in 0.05 M NaCl solution. Once Ce(III) was added, simultaneous IMP pixel activity increase and AMX pixel activation

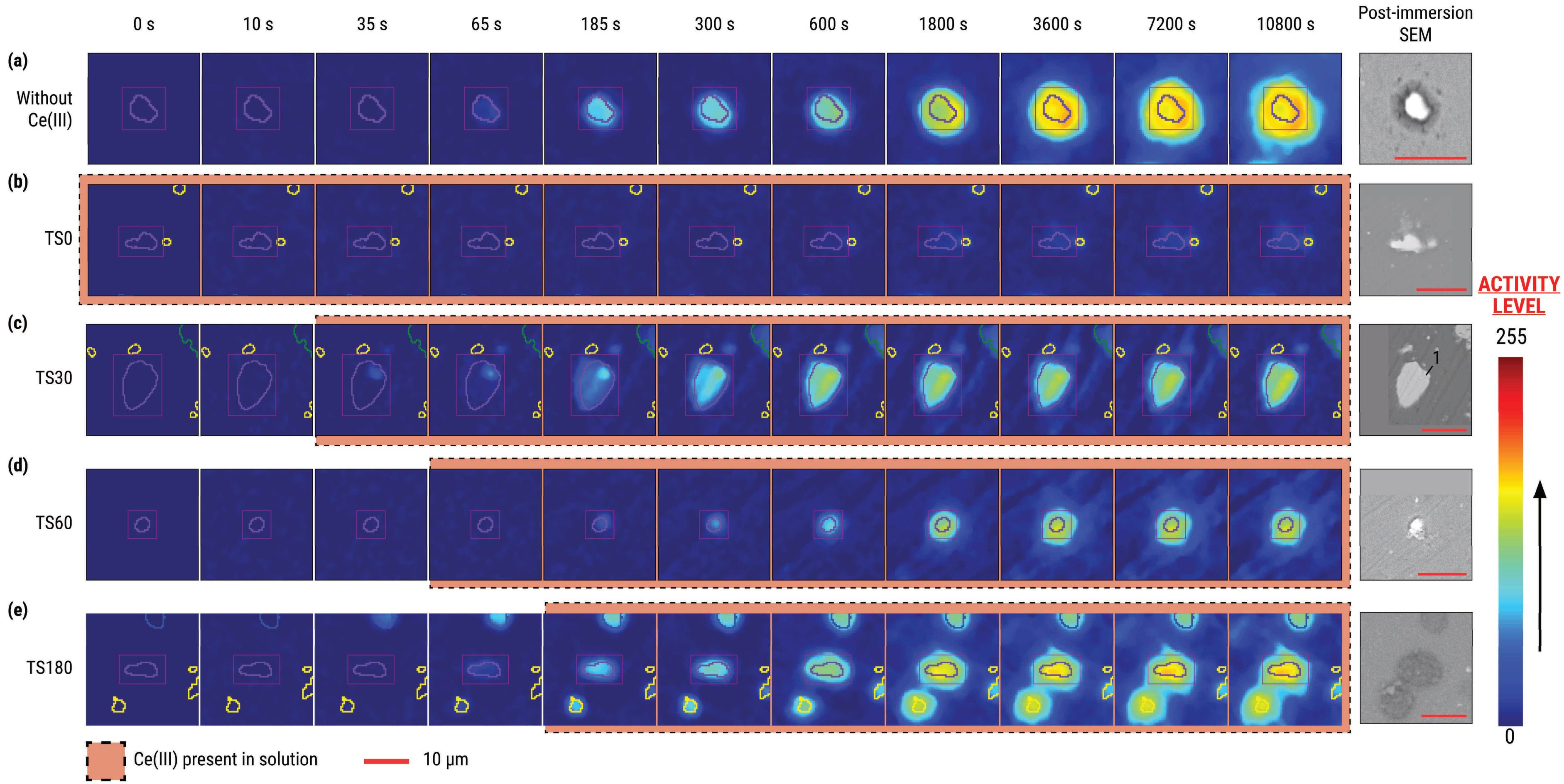

Figure 2.5. Local activity maps (LAMs) of representative θ-phase (Al_2Cu) IMPs show evolution of the surface with time during exposure to **(a)** 0.05 M NaCl and with Ce(III) supplied at **(b)** 0, **(c)** 30, **(d)** 60, and **(e)** 180 s from the start of immersion. The map colours represent the pixel activity level (i.e., change of the pixel gray-level with respect to its initial condition) at time t. The purple outline and the magenta rectangle overlaid on the map marks the IMP and RROI boundary, respectively. The LAMs highlight where the changes are happening in the context of the IMP and how extensive are the changes. The corresponding post-immersion back-scattered SEM images allude to the nature of the surface changes observed in the LAMs.

associated with deposition was observed. Surface changes consistent with growth of the deposited layer continued until around 7200 s. The post-immersion back-scattered SEM image indeed shows a dark thick deposit covering the IMP similar to the first TS60 S-phase IMP. Meanwhile, EDX analysis shows that the deposit contains Ce precipitates mixed with corrosion products (Atomic %: Ce ~ 0.80, Al ~ 14.4, O ~ 83.98; Supporting Information 2.7.5 - Figure S2.12d).

2.3.3. Local behaviour of secondary IMPs at different Ce(III) supply times

Figure 2.6a shows that active secondary IMP (i.e., AlCuFeMn or $(Al,Cu)_x(Fe,Mn)_ySi)$) behaviour in uninhibited conditions is similar to the uninhibited S-phase and θ-phase IMPs. The dealloying onset on the IMP surface was observed between 65 and 185 s, consistent with the reported lower corrosion susceptibility of secondary IMPs [14]. The subsequent increase of IMP pixel activity as well as the activation of AMX pixels followed the same course as the other IMP types. The post-immersion SEM features of the particle are consistent with dealloying and trenching on the surrounding matrix. Matrix dissolution due to Cu redistribution is also observed as dark spots beyond the main trench. It is emphasized that not all secondary IMPs exhibited activity during exposure and the LAMs shown are representative only of the active secondary particles.

Figure 2.6b shows that IMP pixel changes of the representative secondary IMP at TS0 were even more reduced than the corresponding S-phase and θ-phase IMPs. Comparison of the LAMs at 10 s and at 10800 s shows that there is slight activation of the IMP pixels. However, the activity is not as distinct from that of the surrounding matrix as with the other IMP compositions. The post-immersion SEM image shows no visible signs of dealloying or trenching, and Ce was not detected with EDX analysis (Supporting Information 2.7.5 - Figure S2.13a).

Partial activation of the IMP surface is observed for the representative secondary IMP at TS30 (Figure 2.6c). Further immersion led to slight activity increase in this location but without further involvement of the other IMP pixels or the AMX pixels. No signs of significant dealloying or trenching are observed in the post-immersion SEM image, even on the active section of the IMP surface. However, trace amounts of Ce were also detected with EDX (Atomic %: Ce ~ 0.2; Supporting Information 2.7.5 - Figure S2.13b).

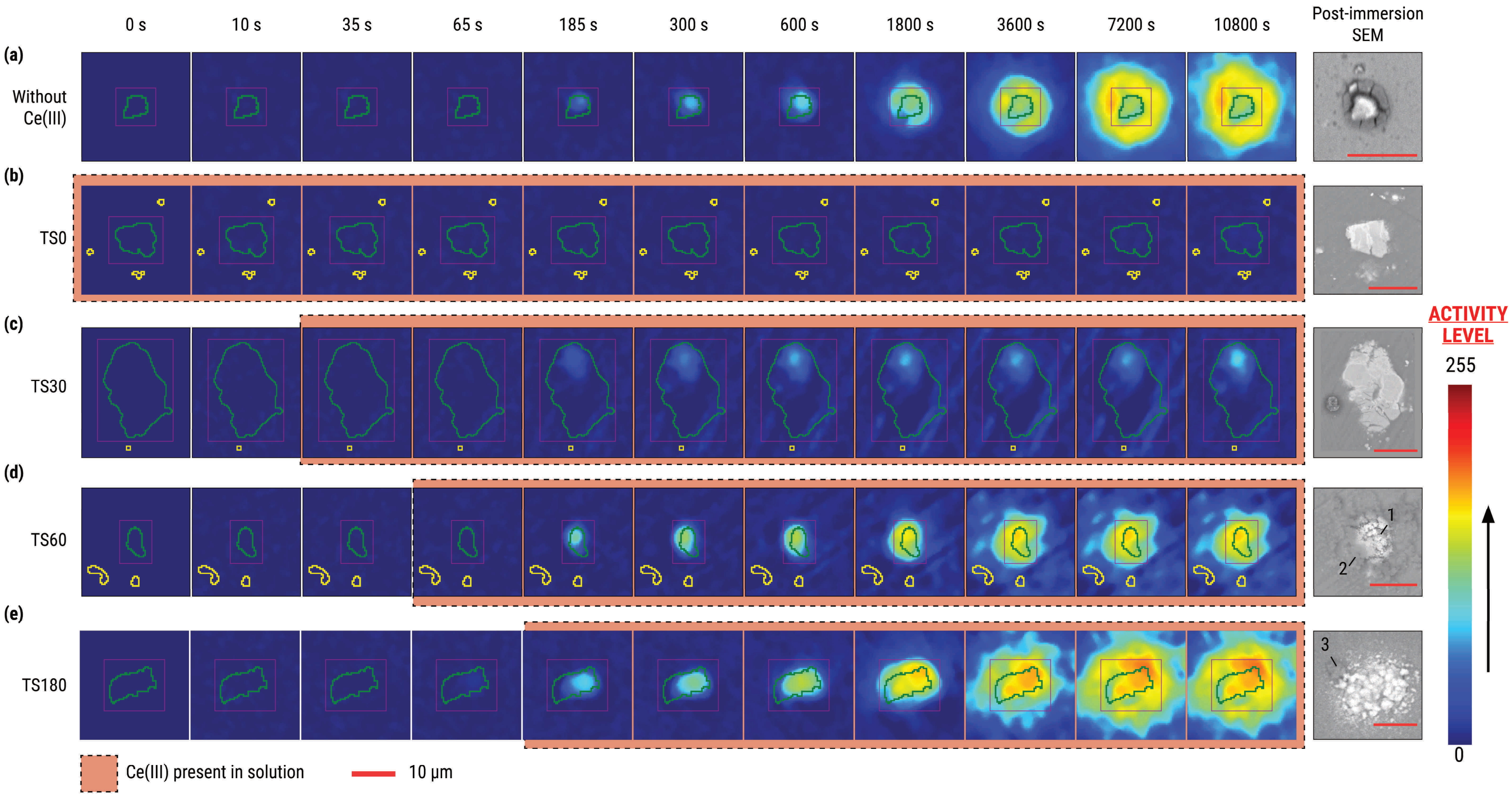

Figure 2.6. Local activity maps (LAMs) of representative secondary (AlCuFeMn and (Al,Cu)$_x$(Fe,Mn)$_y$Si) IMPs show evolution of the surface with time during exposure to **(a)** 0.05 M NaCl and with Ce(III) supplied at **(b)** 0, **(c)** 30, **(d)** 60, and **(e)** 180 s from the start of immersion. The map colours represent the pixel activity level (i.e., change of the pixel gray-level with respect to its initial condition) at time t. The green outline and the magenta rectangle overlaid on the map marks the IMP and RROI boundary, respectively. The LAMs highlight where the changes are happening in the context of the IMP and how extensive are the changes. The corresponding post-immersion back-scattered SEM images allude to the nature of the surface changes observed in the LAMs.

Activation of IMP pixels of the TS60 secondary IMP (Figure 2.6d) was more pronounced than for TS0 and TS30. Similar to the other secondary IMPs, the spread of the activity to the entire IMP surface is slower relative to that for the S-phase and θ-phase particles. Continued immersion led to activity level increase of the pixels as well as further spread to the adjacent areas. The post-immersion SEM shows that the activity on the IMP surface (point 1 in Figure 2.6d) likely corresponds to the deposition of Ce-containing precipitates (Atomic %: Ce ~ 11.8, Al ~ 15.2, O ~ 69.8; Supporting Information 2.7.5 - Figure S2.13c) while that on the AMX (point 2 in Figure 2.6d) is consistent with the deposition of corrosion products (Atomic %: Ce ~ 0.5 , Al ~ 71.0, O ~ 24.9; Supporting Information 2.7.5 - Figure S2.13d). The corrosion product deposits also appear to have originated from the edge of the area covered by cerium precipitates. This can indicate that the products might have been released from rupture sites of an initial precipitate layer formed on the IMP.

The progression of surface changes for the secondary IMP at TS180 (Figure 2.6e) is generally similar to the TS60 particle. At 1800 s, almost all of the pixels in the RROI are active. After this time, extensive deposition led to widespread activation of the matrix pixels beyond the RROI. A large area covered by Ce-containing precipitates (Atomic %: Ce ~ 6.3 , Al ~ 4.8, O ~ 87.6; Supporting Information 2.7.5 - Figure S2.13e) is apparent in the post-immersion SEM image. There are also visible corrosion product deposits (i.e., darker deposits) on the fringes of the Ce-rich area (point 3 in Figure 2.6e).

2.3.4. Activity levels and extent of inhibitor deposition

The LAMs presented in the preceding sections illustrate the progression of surface changes at different Ce(III) supply times. Additionally, they demonstrate the correlation between pixel activity level measured during immersion and the extent of these surface changes. In systems supplied with Ce(III), the extent of surface changes directly relates to the amount of Ce precipitates formed and, consequently, the thickness of the deposits. This relationship becomes more evident when comparing the surface profiles of IMPs with varying levels of activity (Figure 2.7a-c).

The low-level activity typically observed among TS0 particles is consistent with submicron changes, whereas medium- and high-level activity, observed with more delayed supply of Ce(III), are clearly related to micron-scale deposits. This correspondence is attributed to the scattering of incident light by the deposits [37]. As the deposits grow larger, they also scatter more light, resulting in a greater reduction in the intensity of light reflected back to the microscope. This then translates to darker pixels and higher LAM pixel activity level. Moreover, although the activity of the particles with significant deposition might seem similar to a typical corroded particle, the central positioning of the more active pixels can be used to distinguish deposition from advanced trenching (Figure 2.7d). In particles with deposition, the activity is highest in the IMP and then drops as we move to the surrounding matrix. On the other hand, the uninhibited particles have medium to high activity on the IMP. The activity then increases further around the IMP boundary before eventually dropping further into the surrounding matrix. The high activity regions around the IMP boundary are due to extensive trenching observed in uninhibited particles.

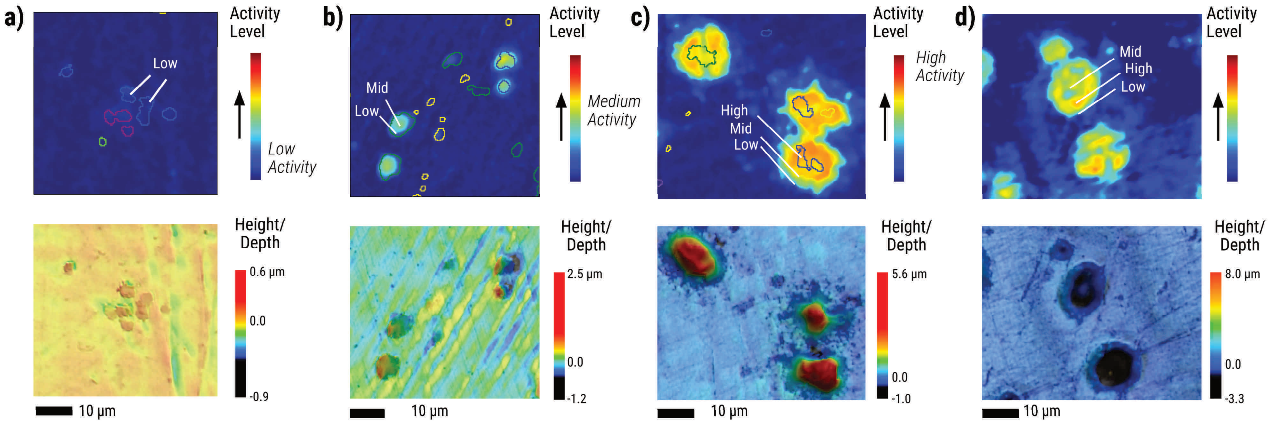

Figure 2.7. Comparison of activity maps and SLCM images for representative IMPs show relative correspondence between thickness of the deposit and the observed pixel activity level for the IMPs supplied with Ce(III). **(a)** Low-level activity observed with TS0 IMPs appear to be nanometric while **(b)** medium (TS30 IMPs), and **(c)** high activity levels (TS180 IMPs) were consistent with increasing deposit thickness. The spatial distribution of the activity levels of the particles with deposits also appears to be different from **(d)** uninhibited particles.

2.4. Discussion

2.4.1. Quantifying optical changes with simplified pixel activity distribution plots

A set of $sPAD_{IMP}(t)$ and $sPAD_{AMX}(t)$ plots were generated and compiled in Figure 2.8 for the IMPs in Figure 2.3(a-d,f), Figure 2.5, and Figure 2.6 to enable efficient comparison of the extent of surface changes among different IMP compositions and Ce(III) t_{supply}. The easiest means of comparison is by looking at activity levels at the end of the immersion (i.e., 10800 s), particularly the $midAL_{IMP}$ and $midAL_{AMX}$ as these values reflect the extent of deposition particularly for the IMPs exposed to Ce(III).

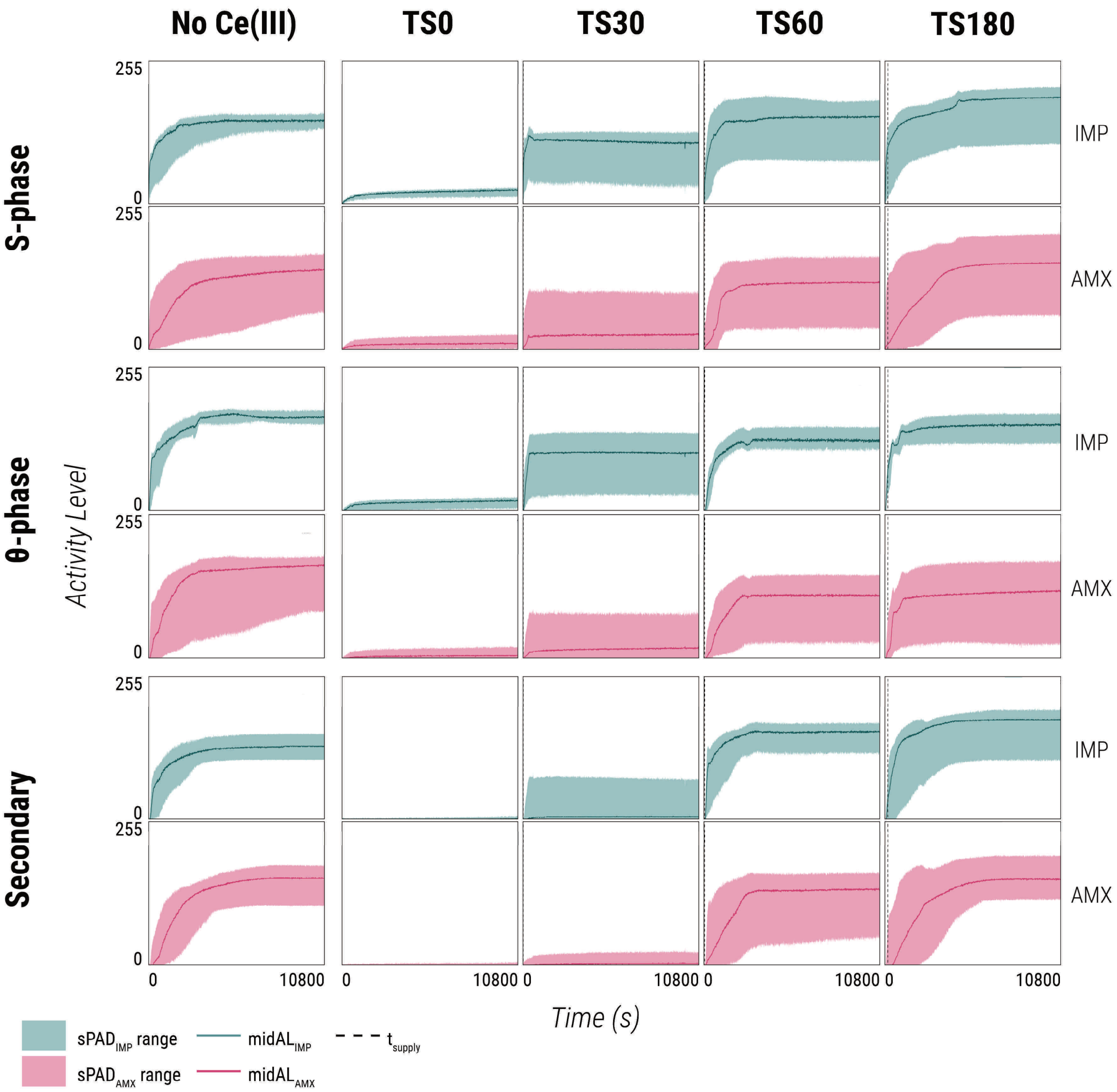

Figure 2.8. Simplified pixel activity distribution (sPAD) plots of representative S-phase (Figure 2.5a-d,f), θ-phase (Figure 2.7), and secondary (Figure 2.8) IMPs in the absence of Ce(III) and at different Ce(III) t_{supply}. The plots provide a clear picture of the period of rapid surface changes (fast period) and the period during which the surface changes slow down significantly (slow period). Activity level of the IMP and AMX pixels were separated to determine which location is more active during the immersion.

Regardless of the IMP composition, both $\mathrm{midAL_{IMP,3h}}$ and $\mathrm{midAL_{AMX,3h}}$ exhibit a drastic drop between the uninhibited and TS0 scenarios. However, the $\mathrm{midAL_{IMP,3h}}$ and $\mathrm{midAL_{AMX,3h}}$ increase again when Ce(III) is added later in time. It is noted though that the $\mathrm{midAL_{AMX,3h}}$ values remained close to zero for both TS0 and TS30 for majority of the IMPs. This corresponds to the limited activation of adjacent matrix pixels observed in the corresponding LAMs. At TS60 and TS180, both $\mathrm{midAL_{IMP,3h}}$ and $\mathrm{midAL_{AMX,3h}}$ were already comparable to their uninhibited counterparts. This poses a challenge on optically differentiating trenching around IMPs from deposition on IMPs for these t_{supply} values. Nonetheless, the values of $\mathrm{midAL_{IMP,3h}}$ and $\mathrm{midAL_{AMX,3h}}$ relative to each other appear to be useful in identifying which is the condition at hand. For trenching typically observed with uninhibited IMPs, $\mathrm{midAL_{AMX,3h}}$ is comparable if not greater than the corresponding $\mathrm{midAL_{IMP,3h}}$. On the other hand, widespread deposition on IMPs supplied with Ce(III) typically involve $\mathrm{midAL_{IMP,3h}}$ values generally greater than the corresponding $\mathrm{midAL_{AMX,3h}}$ values.

Figure 2.9 shows $\mathrm{midAL_{IMP,3h}}$ and $\mathrm{midAL_{AMX,3h}}$ statistics for the active IMPs sampled at different inhibitor supply times. The relationship of the medians of the two parameters with t_{supply} reflects the observations from the representative IMPs. It can also be observed that the increase from TS0 to TS30 is much higher for the $\mathrm{midAL_{IMP,3h}}$ than the $\mathrm{midAL_{AMX,3h}}$. This is because the initial period of uninhibited dealloying and subsequent inhibitor deposition for the TS30 particles mainly affect the IMP surface. Composition-dependent behaviour is also more easily observed from the median $\mathrm{midAL_{IMP,3h}}$ and $\mathrm{midAL_{AMX,3h}}$. For TS30 and TS60, a hierarchy of the median midAL values (i.e., S-phase > θ-phase > secondary) is observed and is associated with differences in the extent of IMP dealloying at the time when the inhibitor was added which leads to differences in degree of Ce precipitation. The same hierarchy is not distinct for TS180 likely due to the more extensive deposition. Indeed, at this t_{supply}, median $\mathrm{midAL_{IMP,3h}}$ for all IMP compositions are already higher than the median values of the uninhibited particles.

Besides quantifying the extent of surface changes, the sPAD plots also enable analysis of the time-dependence of the surface changes. Figure 2.8 shows that for most of the IMPs, both $\mathrm{sPAD_{IMP}}(t)$ and $\mathrm{sPAD_{AMX}}(t)$ are characterized by an overall period of fast activity level increase (fast period) which eventually transitions to an overall period of slow increase (slow period). The fast and slow periods themselves are composed of transitions of varying rates. The exact phenomena causing these transitions are not yet known but we attribute them either to local variations in activity due to compositional heterogeneity of the IMP, or changes in the

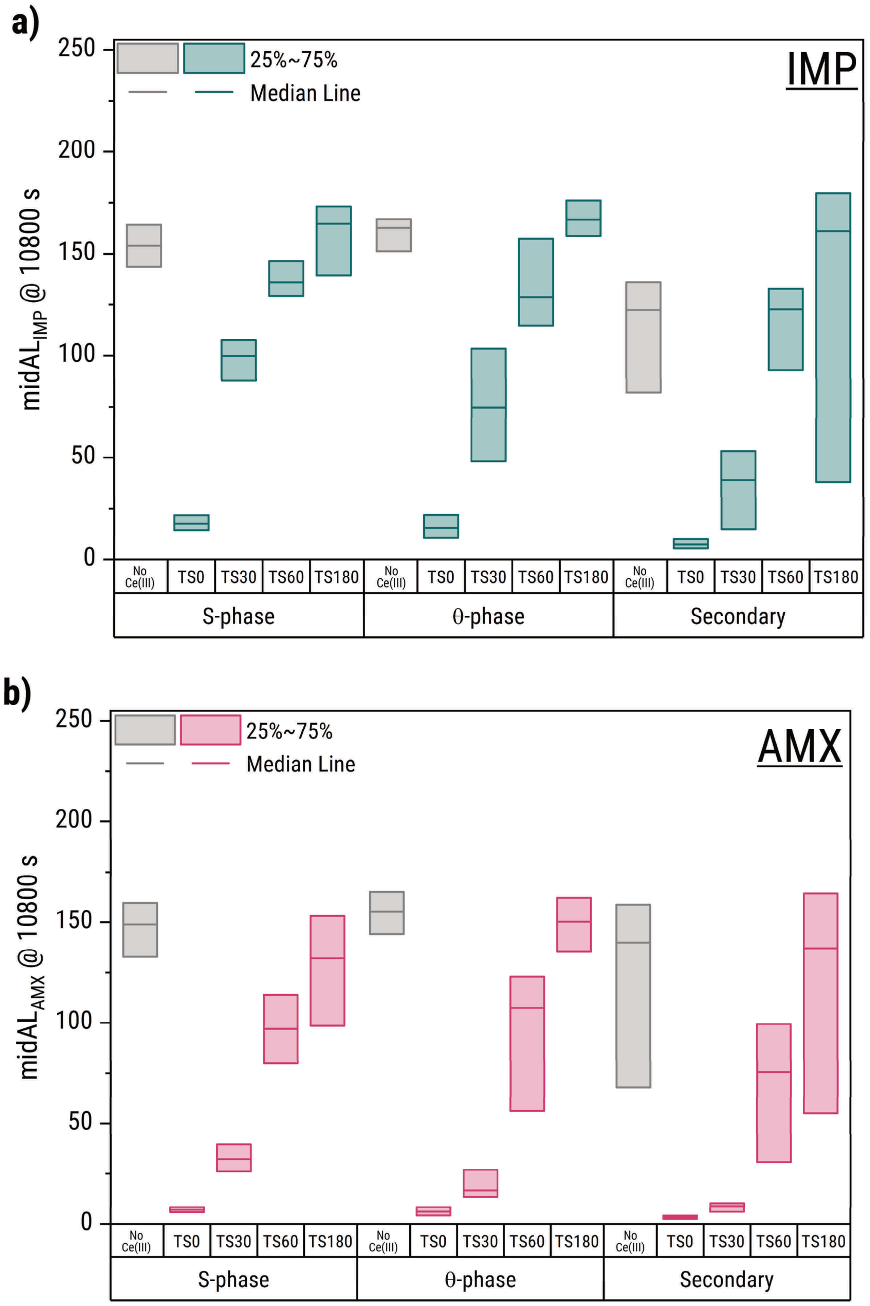

Figure 2.9. Median **(a)** midAL$_{IMP,3h}$ and **(b)** midAL$_{AMX,3h}$ for the IMPs sampled show how the extent of surface changes varies with t$_{supply}$ and with IMP composition. In an ideal scenario, the midAL$_{IMP,3h}$ and midAL$_{AMX,3h}$ are minimal. Quantities corresponding to the plots are provided in Supporting Information 2.7.8.

composition or morphology of the deposits due to combined effect of local corrosion and inhibitor deposition. The first is associated with transitions in the fast period while the latter is associated with transitions in the slow period. For analysis of inhibition though, the relationship between the overall periods is considered to be more relevant. The transition time from the active to the slow period (t$_{sp}$) can be used as a temporal indicator of the inhibitory effect of the Ce(III) at different t$_{supply}$ values. It gives information about when the slow period becomes more dominant. Visually, the t_{sp} is located around the shoulder between the active (i.e., increasing) and the slow (i.e., flat) periods of the sPAD plots. It is emphasized that estimation of the t_{sp} is only possible with IMPs that exhibit activity. The procedure for quantitative determination of t_{sp} is presented in detail in Supporting Information 2.7.7.

From the representative sPAD plots (Figure 2.8), it is clear that regardless of IMP composition, the t_{sp} of the uninhibited particles is observed much later than those of the inhibited ones. Furthermore, among the IMPs supplied with Ce(III), TS30 particles also appear to have the earliest t_{sp}. These observations are more apparent when t_{sp} statistics (Figure 2.10) are compared. Unlike with the $midAL_{IMP,3h}$ and $midAL_{AMX,3h}$ values, the effect of composition on the median t_{sp} values appears to be less pronounced although a hierarchy (i.e., S-phase < θ-phase < secondary) can be observed for most of the t_{supply} values. Given the t_{sp} is associated with the duration of active deposition, the observed hierarchy suggests that the S-phase particles are capable of forming *stable* deposits much faster. The minima of the t_{sp} at TS30 also suggests that initial uninhibited dealloying can speed up the inhibitor layer formation but only up to a certain degree.

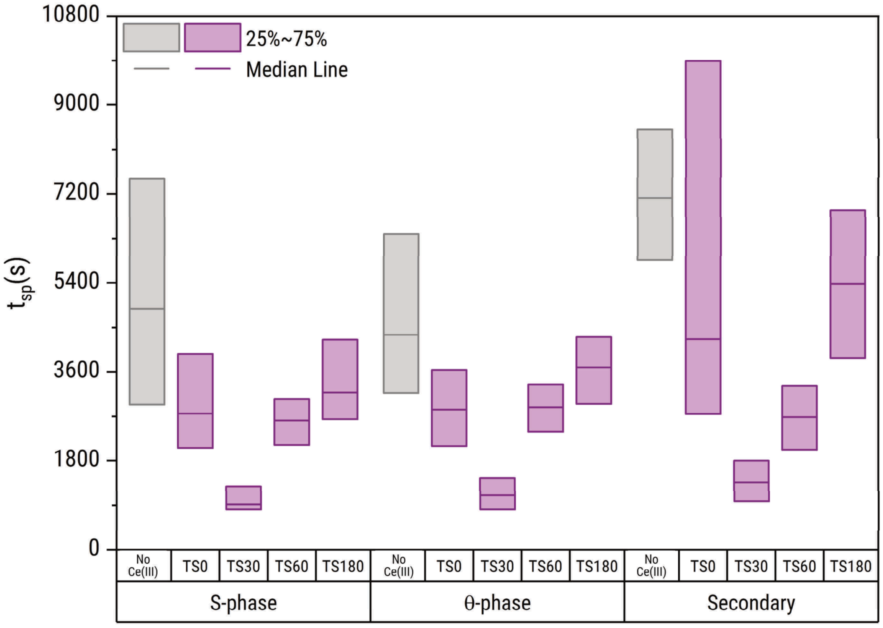

Figure 2.10. Median transition time to slow period (t_{sp}) measured for the IMPs analysed at different Ce(III) supply times show when the slow period starts to dominate. In an ideal scenario, the t_{sp} is as low as possible (i.e., surface changes stabilise early) and the degree of change after the fast period is minimal. Quantities corresponding to the plot are provided in Supporting Information 2.7.8.

2.4.2. Using reflected light microscopy to estimate the tolerable delay limit for Ce(III) supply

Given that the $\text{midAL}_{\text{IMP,3h}}$, $\text{midAL}_{\text{AMX,3h}}$, and t_{sp} provide a general overview of the surface changes, it makes sense to use them for estimating the tolerable delay for the supply of Ce(III). The tolerable delay essentially represents the maximum time after the start of the corrosion at which the inhibitor can be supplied and still obtain effective corrosion protection. From an optics-based consideration, the uninhibited parameters can be used as basis for evaluating if the behaviour at a specific t_{supply} is tolerable or not. In the case of the $\text{midAL}_{\text{IMP,3h}}$ and $\text{midAL}_{\text{IAMX,3h}}$, it is preferred that their values are less than those of a purely corroding surface. Indeed, the midAL values for the uninhibited and inhibited systems generally correspond to different surface features. They represent extent of dealloying and trenching for uninhibited IMPs and deposition for inhibited IMPs. Nonetheless, visual inspection is still one of the most accessible and intuitive means of evaluating corrosion [38–40]. As such, observing a tolerable delay limit that would not lead to confusion during maintenance inspections can be beneficial. As for the t_{sp}, it is ideal that the surface changes for the IMPs supplied with the inhibitor occur for a shorter period of time compared to the uninhibited IMPs (i.e., lower t_{sp}). This criterion provides us with a degree of certainty that the suppression of surface changes is due to the inhibitor presence and not just the inherent slowdown of local corrosion. Equations (2-1, (2-2, and (2-3 summarize the criteria for estimating the tolerable delay limit for a specific inhibition condition. The highest t_{supply} which satisfies these criteria can be defined as the tolerable delay limit for the inhibitor at the specific experimental conditions.

$$\mathit{median}(\mathit{midAL}_{IMP,3h}) < \mathit{median}(\mathit{midAL}_{IMP,3h,uninhibited}) \tag{2-1}$$

$$\mathit{median}(\mathit{midAL}_{AMX,3h}) < \mathit{median}(\mathit{midAL}_{AMX,3h,uninhibited}) \tag{2-2}$$

$$\mathit{median}(t_{sp}) < \mathit{median}(t_{sp,uninhibited}) \tag{2-3}$$

Figure 2.10 shows that the t_{sp} criterion is satisfied for all of the t_{supply} values tested. This implies that Ce(III) can still inhibit corrosion even when the supply is delayed. On the other hand, Figure 2.9a shows that the $\text{midAL}_{\text{IMP,3h}}$ of the uninhibited IMPs are exceeded at TS180, for all IMP compositions. The same is evident for the median $\text{midAL}_{\text{AMX,3h}}$ (Figure 2.9b) albeit the S-phase IMPs exhibited a slightly lower median than the uninhibited ones. Meanwhile, at TS60, the midAL values are high but they are considerably lower than the uninhibited IMPs for all compositions. In light of these observations, 60 s appears to be a sensible tolerable delay for the supply of Ce(III) to inhibit IMP local corrosion in AA2024-T3.

2.4.3. Ce(III) precipitation at different supply times

The midAL criterion used to estimate the tolerable delay limit is based on the high activity levels observed for delayed t_{supply}. These activity levels are attributed to the increase in the Ce(III) precipitation capacity of the IMPs. This is confirmed with post-immersion SEM and SLCM which showed more visible deposition compared to the TS0 IMPs. Furthermore, post-immersion EDX also highlighted increased presence of Ce at surface of the particles exposed to Ce(III) with delayed t_{supply}. The increase in the degree of precipitation is consistent with the dealloying-driven mechanism for inhibition with Ce(III). More delayed t_{supply} corresponds to longer periods of uninhibited dealloying that leads to Cu enrichment. Enriched Cu sites increase the ORR rate on the IMP which provides the alkalinity required for Ce(III) to precipitate.

The interplay between local corrosion and Ce(III) precipitation at different t_{supply}, as well as the resulting local activity maps, are summarized in Figure 2.11. Ce(III) presence right at the start of exposure (i.e., TS0) leads to highly localized precipitation which prevents dealloying from progressing significantly and, in turn, limits the extent of precipitation. It is hypothesized though that a sufficiently *thick* layer is still needed to effectively cut-off the ORR and the formation of this layer takes time. The t_{sp} values for the TS0 particles reflects the time needed to form this layer. Moreover, the apparent hierarchy of t_{sp} values among the different IMP types at TS0 also likely stems from varying capacity to support ORR and Ce(III) precipitation. The particles which dealloy easily (e.g., S-phase) can build thicker layers faster resulting to much earlier t_{sp} than the others. The slowed-down dealloying coupled with the limited Ce(III) precipitation leads to the observed low-level pixel activity concentrated at the IMP surface in the corresponding LAM.

The behaviour at TS30 can be considered as an accelerated version of TS0. The dealloying, particularly among S-phase and θ-phase IMPs, enabled faster precipitation of Ce(III) once it is added. However, since the dealloying is not yet extensive, the deposits that formed would potentially have less defects and can slowdown surface changes much earlier (i.e., lower t_{sp}). The higher extent of Ce(III) precipitation translates to higher IMP pixel activity in the LAM. The inhibitor precipitation is also rapid and protective enough to control local corrosion progression which leads to limited activity in the adjacent matrix.

Higher degree of Ce precipitation observed in TS60 and TS180 does not necessarily correspond to more effective inhibition. Visibly increased fraction of corrosion products at the end of immersion for the TS60 and TS180 IMPs, in particular, indicates reduced protectiveness of the Ce deposits despite their increased thickness. When Ce(III) supply is more delayed, local corrosion processes can still proceed underneath the deposited layer. Transport of products from these processes such as metal ions or hydrogen [41,42] could potentially introduce defects (e.g., cracks, pores) in the Ce deposits. These defects provide paths for oxygen to reach the surface which then sustains ORR. As with TS0 and TS30, sufficient accumulation of cerium precipitates (and corrosion products) is also needed to control oxygen supply. This explains the higher t_{sp} values observed with TS60 and TS180 IMPs as well as the more extensive deposition on the IMPs and their surrounding matrix by the time the surface changes slow down. In the LAMs, this is observed as high-level activity on both the IMP surface and the adjacent matrix. The presence of the inhibitor is still able to reduce the extent of local corrosion though leading to less extensive trenching relative to the uninhibited particles. This leads to pixels with highest activity levels still being situated within the boundaries of the IMPs.

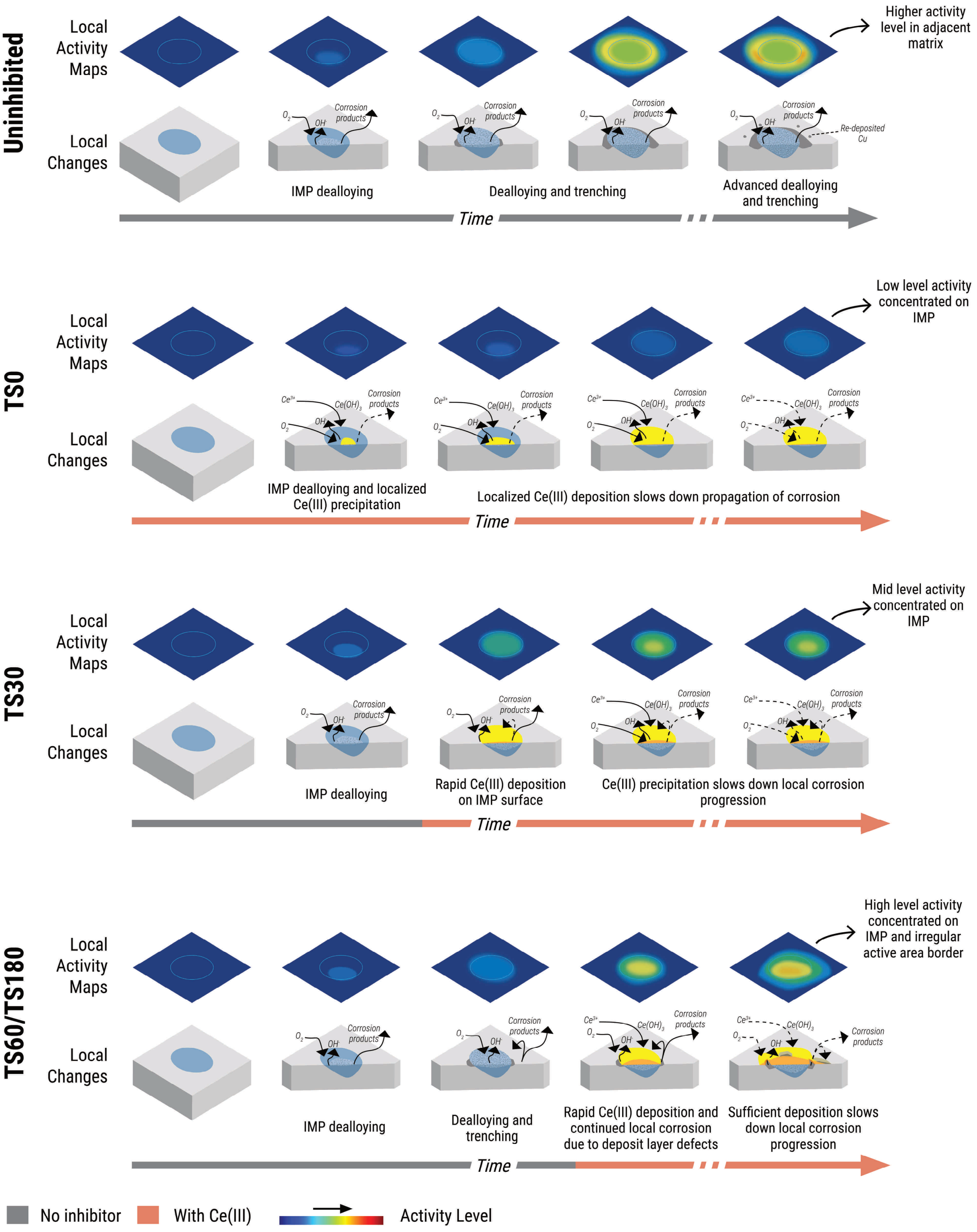

Figure 2.11. Local changes in the absence of Ce(III) (uninhibited) and when it is supplied at 0 s (TS0), 30 s (TS30), 60 s (TS60), and 180 s (TS180) from the start of exposure and their corresponding local activity maps.

2.5. Conclusion

An in situ reflected microscopy technique was used to analyse local surface changes when the availability of the inhibitor, $Ce(NO_3)_3$, was intentionally delayed to AA2024-T3. The technique combined with our image analysis protocol can be used to create GAMs (global activity maps), LAMs (local activity maps), and sPADs (simplified pixel activity level distribution). These are highly effective means of visualizing surface activation, local inhibitor deposition, and inhibitor layer growth at the intermetallic particle scale. GAMs and LAMs allow efficient analysis of the spatial dependence of the surface changes while the sPADs enable a simple method of visualizing the kinetics of said changes. Parameters extracted from the sPADs allowed comparison of the degree of changes (i.e., $midAL_{IMP,3h}$, $midAL_{AMX,3h}$) and time at which the slow period dominates (i.e., t_{sp}) of IMPs at different inhibitor supply times. Based on these parameters and the experimental conditions used, when Ce(III) is supplied to the IMPs in our model system within 60 s of exposure, the surface changes associated with deposition slow down early, and the degree of these surface changes was less extensive than purely corroding particles. The tolerable delay of 60 s can potentially be applied as a basis for fine-tuning the design of anti-corrosion coatings in order to prolong inhibitor availability. It is emphasized though that its value is established from experiments where there is a burst release of Ce(III) at the specified t_{supply} and no prior inhibitor presence. Furthermore, the results are also specific to the electrolyte and inhibitor concentrations used (i.e., 0.05 M NaCl, 0.001 M $Ce(NO_3)_3$). Assessing how this tolerable delay translates to more conventional release profiles can further enable better design and more effective screening of inhibitor delivery systems for active corrosion protection.

2.6. References

[1] L. Paussa, F. Andreatta, D. DeFelicis, E. Bemporad, L. Fedrizzi, Investigation of AA2024-T3 surfaces modified by cerium compounds: A localized approach, *Corros. Sci.* 78 (2014) 215–222. doi:10.1016/j.corsci.2013.10.001.

[2] F.F. Chen, I. Cole, A.E. Hughes, A.M. Glenn, E. Sapper, J. Osborne, Microstructure characterisation and reconstruction of intermetallic particles, *Mater. Corros.* 65 (2014) 664–669. doi:10.1002/maco.201307345.

[3] A.E. Hughes, R. Parvizi, M. Forsyth, Microstructure and corrosion of AA2024, *Corros. Rev.* 33 (2015) 1–30. doi:10.1515/corrrev-2014-0039.

[4] F. Peltier, D. Thierry, Review of Cr-Free Coatings for the Corrosion Protection of Aluminum Aerospace Alloys, *Coatings* 12 (2022) 518. doi:10.3390/coatings12040518.

[5] M.L. Zheludkevich, J. Tedim, M.G.S. Ferreira, “Smart” coatings for active corrosion protection based on multi-functional micro and nanocontainers, *Electrochim. Acta* 82 (2012) 314–323. doi:10.1016/j.electacta.2012.04.095.

[6] I.S. Cole, Smart coatings for corrosion protection: an overview, *Handb. Smart Coat. Mater. Prot.* (2014) 29–55. doi:10.1533/9780857096883.1.29.

[7] T.G. Harvey, S.G. Hardin, A.E. Hughes, T.H. Muster, P.A. White, T.A. Markley, P.A. Corrigan, J. Mardel, S.J. Garcia, J.M.C. Mol, A.M. Glenn, The effect of inhibitor structure on the corrosion of AA2024 and AA7075, *Corros. Sci.* 53 (2011) 2184–2190. doi:10.1016/j.corsci.2011.02.040.

[8] K. Xhanari, M. Finšgar, Organic corrosion inhibitors for aluminum and its alloys in chloride and alkaline solutions: A review, *Arab. J. Chem.* 12 (2019) 4646–4663. doi:10.1016/j.arabjc.2016.08.009.

[9] M. Bethencourt, F.J. Botana, J.J. Calvino, M. Marcos, M.A. Rodríguez-Chacón, Lanthanide compounds as environmentally-friendly corrosion inhibitors of aluminium alloys: a review, *Corros. Sci.* 40 (1998) 1803–1819. doi:10.1016/s0010-938x(98)00077-8.

[10] T.H. Muster, H. Sullivan, D. Lau, D.L.J. Alexander, N. Sherman, S.J. Garcia, T.G. Harvey, T.A. Markley, A.E. Hughes, P.A. Corrigan, A.M. Glenn, P.A. White, S.G. Hardin, J. Mardel, J.M.C. Mol, A combinatorial matrix of rare earth chloride mixtures as corrosion inhibitors of AA2024-T3: Optimisation using potentiodynamic polarisation and EIS, *Electrochim. Acta* 67 (2012) 95–103. doi:10.1016/j.electacta.2012.02.004.

[11] A. Kosari, H. Zandbergen, F. Tichelaar, P. Visser, P. Taheri, H. Terryn, J.M.C. Mol, In-situ nanoscopic observations of dealloying-driven local corrosion from surface initiation to in-depth propagation, *Corros. Sci.* 177 (2020). doi:10.1016/j.corsci.2020.108912.

[12] A. Kosari, F. Tichelaar, P. Visser, H. Zandbergen, H. Terryn, J.M.C. Mol, Dealloying-driven local corrosion by intermetallic constituent particles and dispersoids in aerospace aluminium alloys, *Corros. Sci.* 177 (2020) 108947. doi:10.1016/j.corsci.2020.108947.

[13] A. Boag, A.E. Hughes, A.M. Glenn, T.H. Muster, D. McCulloch, Corrosion of AA2024-T3 Part I: Localised corrosion of isolated IM particles, *Corros. Sci.* 53 (2011) 17–26. doi:10.1016/j.corsci.2010.09.009.

[14] M. Olgiati, P.J. Denissen, S.J. Garcia, When all intermetallics dealloy in AA2024-T3: quantifying early stage intermetallic corrosion kinetics under immersion, *Corros. Sci.* (2021) 109836. doi:10.1016/j.corsci.2021.109836.

[15] P.J. Denissen, S.J. Garcia, Cerium-loaded algae exoskeletons for active corrosion protection of coated AA2024-T3, *Corros. Sci.* 128 (2017) 164–175. doi:10.1016/j.corsci.2017.09.019.

[16] Z. Li, Y. Shen, Y. Li, F. Zheng, L. Liu, Doping effects of cerium ion on structure and electrochemical properties of polyaniline, *Polym. Int.* 67 (2018) 121–126. doi:10.1002/pi.5487.

[17] L.R.L. Santos, C.E.B. Marino, I.C. Riegel-Vidotti, Silica/chitosan hybrid particles for smart release of the corrosion inhibitor benzotriazole, *Eur. Polym. J.* 115 (2019) 86–98. doi:10.1016/j.eurpolymj.2019.03.008.

[18] P.J. Denissen, A.M. Homborg, S.J. Garcia, Requirements for corrosion inhibitor release from damaged primers for stable protection: A simulation and experimental approach using cerium loaded carriers, *Surf. Coat. Technol.* 430 (2022) 127966. doi:10.1016/j.surfcoat.2021.127966.

[19] E.L. Ferrer, A.P. Rollon, H.D. Mendoza, U. Lafont, S.J. Garcia, Double-doped zeolites for corrosion protection of aluminium alloys, *Microporous Mesoporous Mater.* 188 (2014) 8–15. doi:10.1016/j.micromeso.2014.01.004.

[20] P.J. Denissen, V. Shkirskiy, P. Volovitch, S.J. Garcia, Corrosion Inhibition at Scribed Locations in Coated AA2024-T3 by Cerium- And DMTD-Loaded Natural Silica Microparticles under Continuous Immersion and Wet/Dry Cyclic Exposure, *ACS Appl. Mater. Interfaces* 12 (2020) 23417–23431. doi:10.1021/acsami.0c03368.

[21] C. Li, X. Guo, G.S. Frankel, Corrosion inhibition of AA2024-T3 by a coating containing dual-pH sensitive, corrosion inhibitor loaded microspheres, *Corros. Sci.* 192 (2021) 109835. doi:10.1016/j.corsci.2021.109835.

[22] D. Snihirova, S.V. Lamaka, M.M. Cardoso, J.A.D. Condeço, H.E.C.S. Ferreira, M.F. Montemor, pH-sensitive polymeric particles with increased inhibitor-loading capacity as smart additives for corrosion protective coatings for AA2024, *Electrochim. Acta* 145 (2014) 123–131. doi:10.1016/j.electacta.2014.09.009.

[23] D. Snihirova, S.V. Lamaka, M. Taryba, A.N. Salak, S. Kallip, M.L. Zheludkevich, M.G.S. Ferreira, M.F. Montemor, Hydroxyapatite microparticles as feedback-active reservoirs of corrosion inhibitors, *ACS Appl. Mater. Interfaces* 2 (2010) 3011–3022. doi:10.1021/am1005942.

[24] K.A. Yasakau, M.L. Zheludkevich, S.V. Lamaka, M.G.S. Ferreira, Mechanism of corrosion inhibition of AA2024 by rare-earth compounds, *J. Phys. Chem. B* 110 (2006) 5515–5528. doi:10.1021/jp0560664.

[25] A. Kosari, M. Ahmadi, F. Tichelaar, P. Visser, Y. Gonzalez-Garcia, H. Zandbergen, H. Terryn, J.M.C. Mol, Editors' Choice—Dealloying-Driven Cerium Precipitation on Intermetallic Particles in Aerospace Aluminium Alloys, *J. Electrochem. Soc.* 168 (2021) 041505. doi:10.1149/1945-7111/abf50d.

[26] N.C. Rosero-Navarro, M. Curioni, R. Bingham, A. Durán, M. Aparicio, R.A. Cottis, G.E. Thompson, Electrochemical techniques for practical evaluation of corrosion inhibitor effectiveness. Performance of cerium nitrate as corrosion inhibitor for AA2024T3 alloy, *Corros. Sci.* 52 (2010) 3356–3366. doi:10.1016/j.corsci.2010.06.012.

[27] J. Li, B. Hurley, R. Buchheit, The Effect of CeCl3 as an Inhibitor on the Localized Corrosion of AA2024-T3 as a Function of Temperature, *J. Electrochem. Soc.* 163 (2016) C845–C852. doi:10.1149/2.0561614jes.

[28] L. Paussa, F. Andreatta, N.C. Rosero Navarro, A. Durán, L. Fedrizzi, Study of the effect of cerium nitrate on AA2024-T3 by means of electrochemical micro-cell technique, *Electrochim. Acta* 70 (2012) 25–33. doi:10.1016/j.electacta.2012.02.099.

[29] L. Lacroix, L. Ressier, C. Blanc, G. Mankowski, Statistical Study of the Corrosion Behavior of Al_2CuMg Intermetallics in AA2024-T351 by SKPFM, *J. Electrochem. Soc.* 155 (2008) C8. doi:10.1149/1.2799089.

[30] T. Hu, H. Shi, D. Hou, T. Wei, S. Fan, F. Liu, E.H. Han, A localized approach to study corrosion inhibition of intermetallic phases of AA 2024-T3 by cerium malate, *Appl. Surf. Sci.* 467–468 (2019) 1011–1032. doi:10.1016/j.apsusc.2018.10.243.

[31] N. Li, C. Dong, C. Man, J. Yao, In Situ Electrochemical Atomic Force Microscopy and Auger Electro Spectroscopy Study on the Passive Film Structure of 2024-T3 Aluminum Alloy Combined with a Density Functional Theory Calculation, *Adv. Eng. Mater.* 21 (2019) 1900386. doi:10.1002/adem.201900386.

[32] A. Kreta, M. Rodošek, L. Slemenik Perše, B. Orel, M. Gaberšček, A. Šurca Vuk, In situ electrochemical AFM, ex situ IR reflection–absorption and confocal Raman studies of corrosion processes of AA 2024-T3, *Corros. Sci.* 104 (2016) 290–309. doi:10.1016/j.corsci.2015.12.023.

[33] A.M. Homborg, M. Olgiati, P.J. Denissen, S.J. Garcia, An integral non-intrusive electrochemical and in-situ optical technique for the study of the effectiveness of corrosion inhibition, *Electrochim. Acta* 403 (2022) 139619. doi:10.1016/j.electacta.2021.139619.

[34] R.G. Buchheit, R.P. Grant, P.F. Hlava, B. Mckenzie, G.L. Zender, Local Dissolution Phenomena Associated with S Phase (Al_2CuMg) Particles in Aluminum Alloy 2024-T3, *J. Electrochem. Soc.* 144 (1997) 2621–2628. doi:10.1149/1.1837874.

[35] A.E. Hughes, A.M. Glenn, N. Wilson, A. Moffatt, A.J. Morton, R.G. Buchheit, A consistent description of intermetallic particle composition: An analysis of ten batches of AA2024-T3, *Surf. Interface Anal.* 45 (2013) 1558–1563. doi:10.1002/sia.5207.

[36] X. Zhang, T. Hashimoto, J. Lindsay, X. Zhou, Investigation of the de-alloying behaviour of θ-phase (Al_2Cu) in AA2024-T351 aluminium alloy, *Corros. Sci.* 108 (2016) 85–93. doi:10.1016/j.corsci.2016.03.003.

[37] P.M.F. Forte, P.E.R. Felgueiras, F.P. Ferreira, M.A. Sousa, E.J. Nunes-Pereira, B.P.J. Bret, M.S. Belsley, Exploring combined dark and bright field illumination to improve the detection of defects on specular surfaces, *Opt. Laser Eng.* 88 (2017) 120–128. doi:10.1016/j.optlaseng.2016.08.002.

[38] P.A. White, A.E. Hughes, S.A. Furman, N. Sherman, P.A. Corrigan, M.A. Glenn, D. Lau, S.G. Hardin, T.G. Harvey, J. Mardel, T.H. Muster, S.J. Garcia, C. Kwakernaak, J.M.C. Mol, High-throughput channel arrays for inhibitor testing: Proof of concept for AA2024-T3, *Corros. Sci.* 51 (2009) 2279–2290. doi:10.1016/j.corsci.2009.06.038.

[39] B. Brandoli, A.R. de Geus, J.R. Souza, G. Spadon, A. Soares, J.F. Rodrigues, J. Komorowski, S. Matwin, Aircraft Fuselage Corrosion Detection Using Artificial Intelligence, *Sensors* 21 (2021) 4026. doi:10.3390/s21124026.

[40] S. Agnisarman, S. Lopes, K. Chalil Madathil, K. Piratla, A. Gramopadhye, A survey of automation-enabled human-in-the-loop systems for infrastructure visual inspection, *Autom. Constr.* 97 (2019) 52–76. doi:10.1016/j.autcon.2018.10.019.

[41] H. Ju, S. Liu, W. Zhang, Y. Yang, J. Duan, Investigation of pitting corrosion and hydrogen evolution of aluminum and AA2024 alloy by simultaneous electrochemical measurements and imaging, *Electrochem. Commun.* 132 (2021) 107135. doi:10.1016/j.elecom.2021.107135.

[42] C. Laurent, F. Scenini, T. Monetta, F. Bellucci, M. Curioni, The contribution of hydrogen evolution processes during corrosion of aluminium and aluminium alloys investigated by potentiodynamic polarisation coupled with real-time hydrogen measurement, *NPJ Mater. Degrad.* 1 (2017) 1–7. doi:10.1038/s41529-017-0011-4.

2.7. Supporting Information

2.7.1. Preparation of epoxy-embedded metal samples

The 2 mm thick AA2024-T3 sheets were milled to a pillar using an engraver (Roland EGX-350). The specifications of the pillar are shown in Figure S2.1. The milling was performed at a feed rate of 0.1 mm/s and a pass depth of 0.1 mm to avoid any significant heating of the sample. WD-40 was also used for lubrication during the milling process.

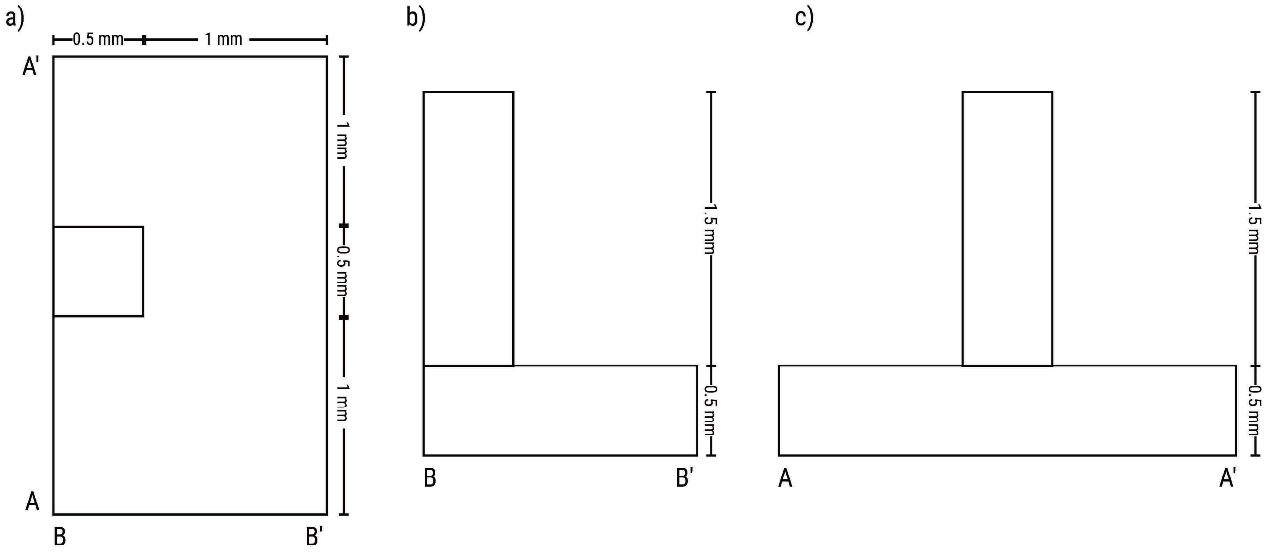

Figure S2.1. Dimensions of the AA2024-T3 pillars used for the epoxy-embedded metal samples.

The pillars were washed with ethanol and then degreased in an ultrasonic bath containing acetone until there are no more visible residues on the surface. The pillars were then air dried prior to embedding in cold curing epoxy resin. The subsequent epoxy-embedding process of metal samples was adopted from Olgiati et al. The pillars were positioned in an upright position in molds (diameter = 30 mm). A resin-binder mixture with a ratio of 25:3 g was then poured into the molds until the pillars are sufficiently submerged. The assembly was degassed in a vacuum chamber at 0.5 bar for 45 minutes and then allowed to cure for at least 12 hours in ambient conditions.

After curing, the top and bottoms faces of the epoxy disks containing the AA2024-T3 pillars were ground with SiC paper (grit 320) until the base and the top surfaces of the metal pillars were exposed. The top and bottom surfaces were further ground with SiC (up to grit 4000) and then polished with 3 μm and 1 μm diamond paste. The samples were then washed with ethanol and air dried. The base of the pillar was sputtered with a 15 nm Au layer and then covered with a Cu tape to provide sufficient electrical contact.

2.7.2. Electrolyte and inhibitor injection protocol

Our optical setup allows us to accurately determine when the surface of the metal sample is exposed to the electrolyte (Figure S2.2). This was achieved by adjusting the sample distance from the camera such that the images would be in focus when the solution is injected into the system. To a certain degree, our setup also enables visualization of the solution mixing during the delayed supply of the inhibitor. The injection of the inhibitor solution results in bulk mixing of the electrolyte which causes a brief period of fluctuations in the brightness of the images acquired (Figure S2.3).

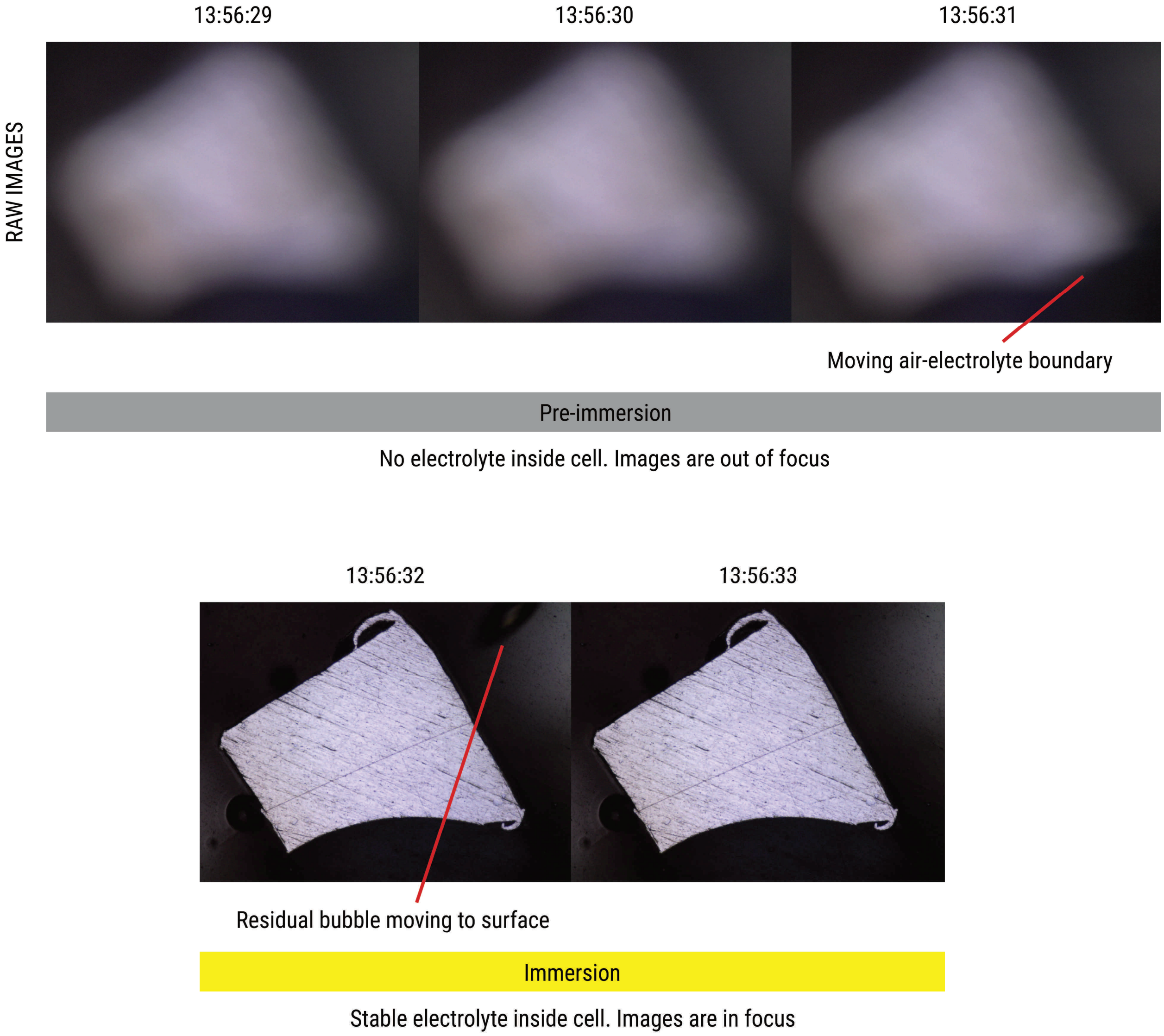

Figure S2.2. Images acquired during the first injection of the electrolyte.

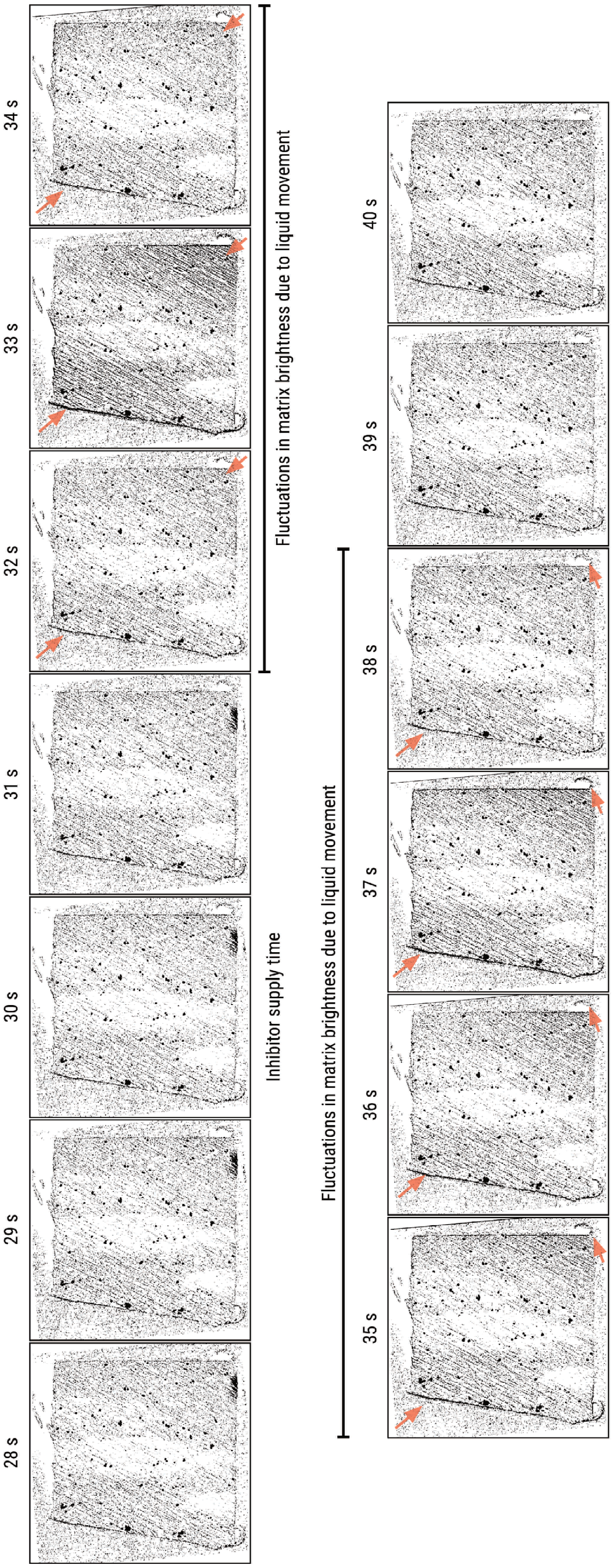

Figure S2.3. Images acquired during injection of inhibitor for systems with delayed inhibitor supply.

2.7.3. Global activity maps (GAM) of samples

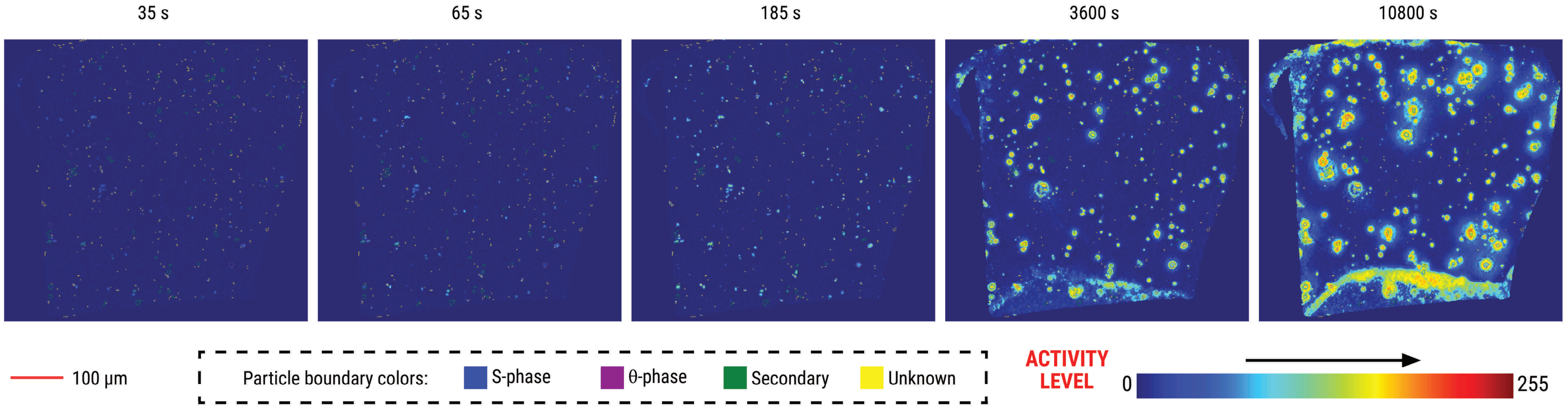

Figure S2.4. Global activity maps at selected times for embedded metal samples exposed to only NaCl (i.e., no Ce(III)). The overlaid particle boundary colours are used to indicate the relative composition of the IMP. The map colours represent the pixel activity level (i.e., change of the pixel gray-level with respect to its initial condition) at time t.

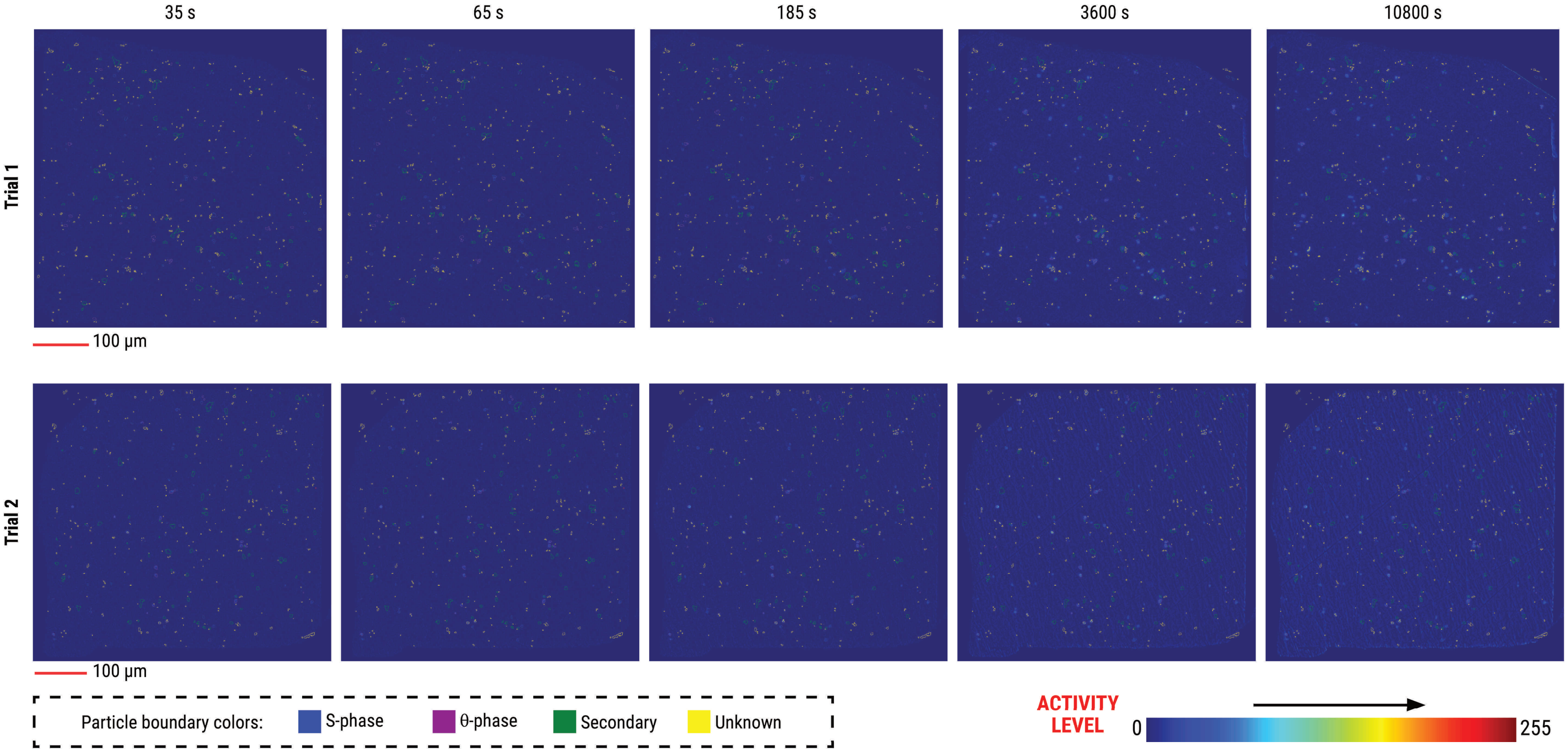

Figure S2.5. Global activity maps at selected times for embedded metal samples supplied with the inhibitor at 0 s. The overlaid particle boundary colours are used to indicate the relative composition of the IMP. The map colours represent the pixel activity level (i.e., change of the pixel gray-level with respect to its initial condition) at time t.

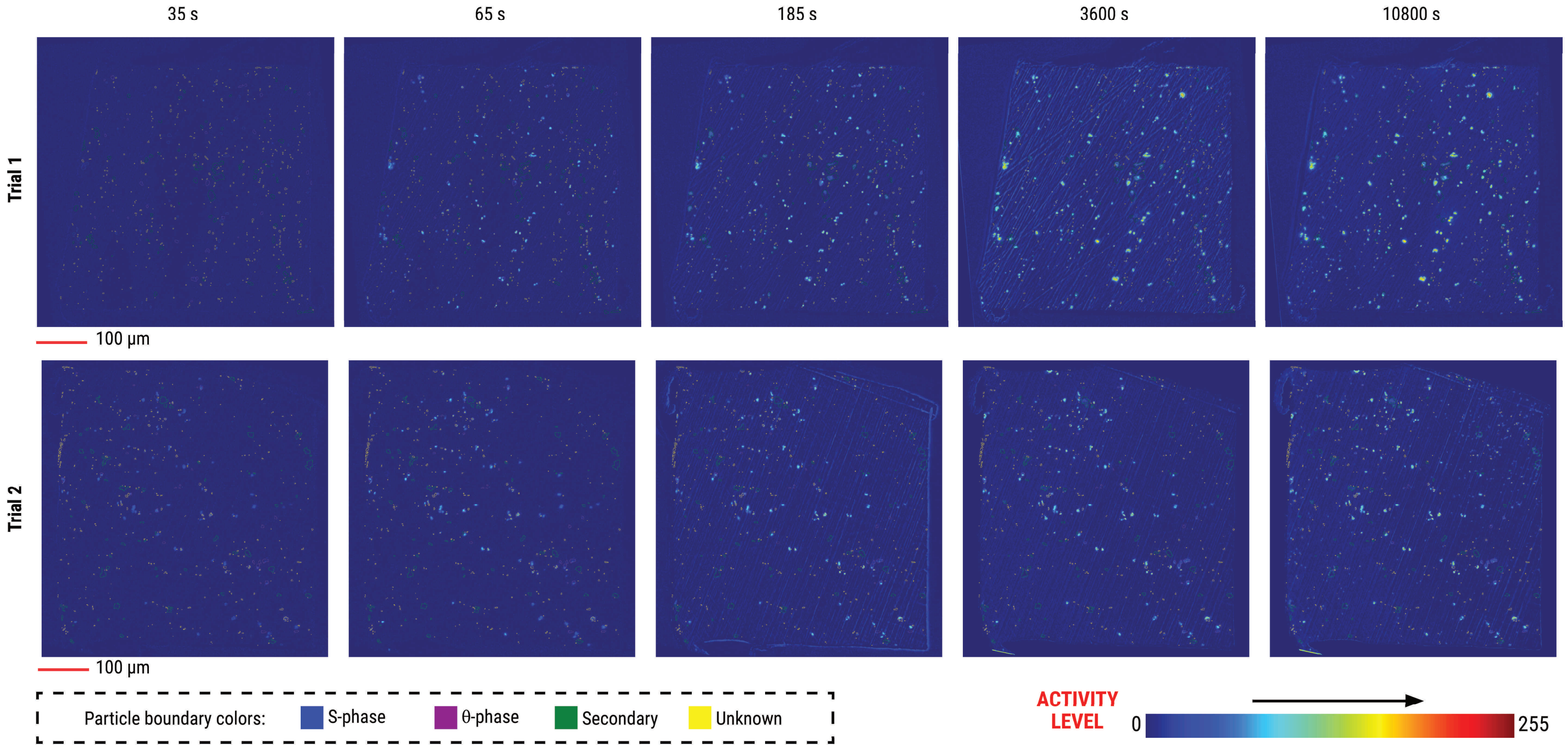

Figure S2.6. Global activity maps at selected times for embedded metal samples supplied with the inhibitor at 30 s. The overlaid particle boundary colours are used to indicate the relative composition of the IMP. The map colours represent the pixel activity level (i.e., change of the pixel gray-level with respect to its initial condition) at time t.

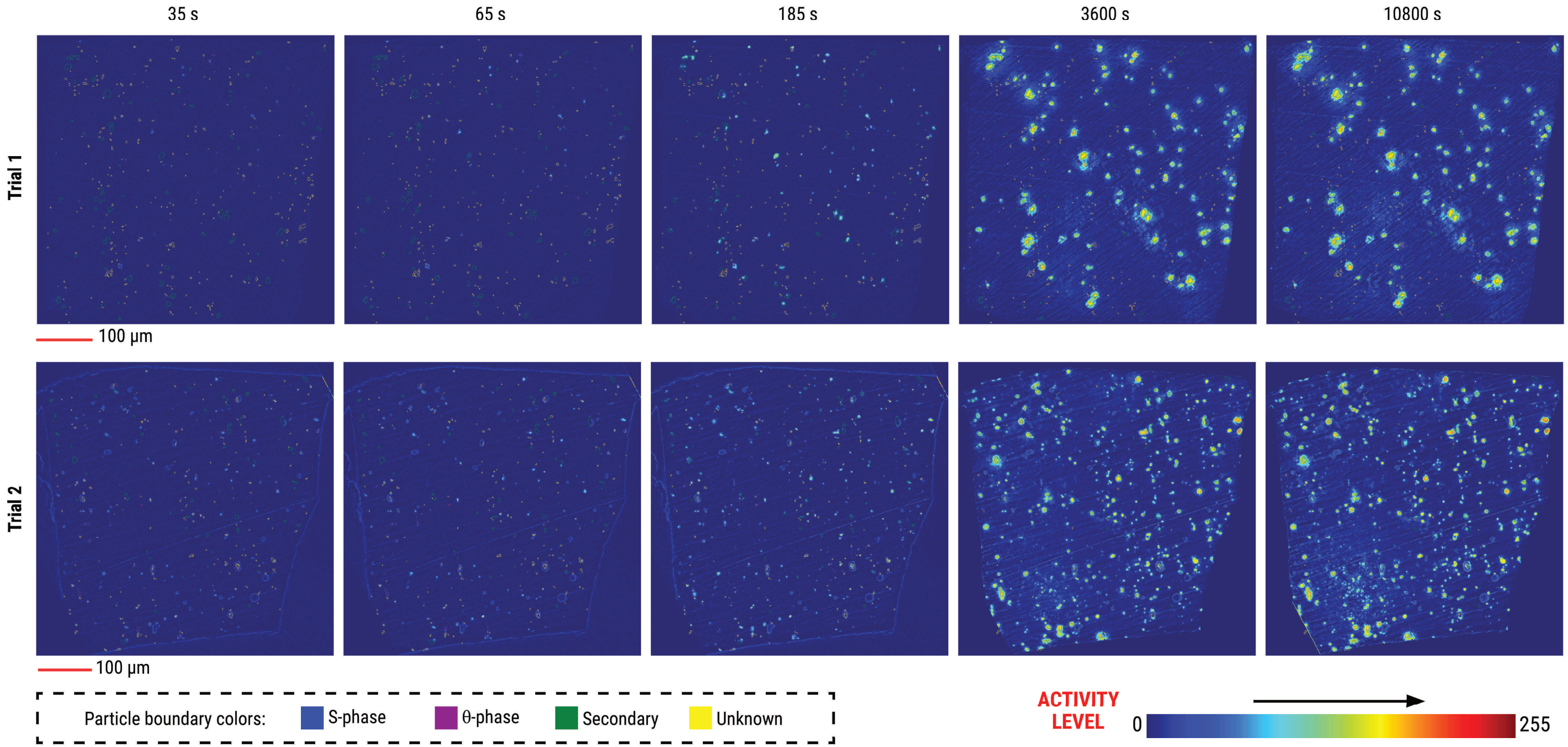

Figure S2.7. Global activity maps at selected times for embedded metal samples supplied with the inhibitor at 60 s. The particle boundary colours are used to indicate the relative composition of the IMP. The map colours represent the pixel activity level (i.e., change of the pixel gray-level with respect to its initial condition) at time t. Ring-like features in the trial 2 maps are from remnants of pits. These features appeared to be minimally active during the immersion and were not included in the analysis of local IMP activity.

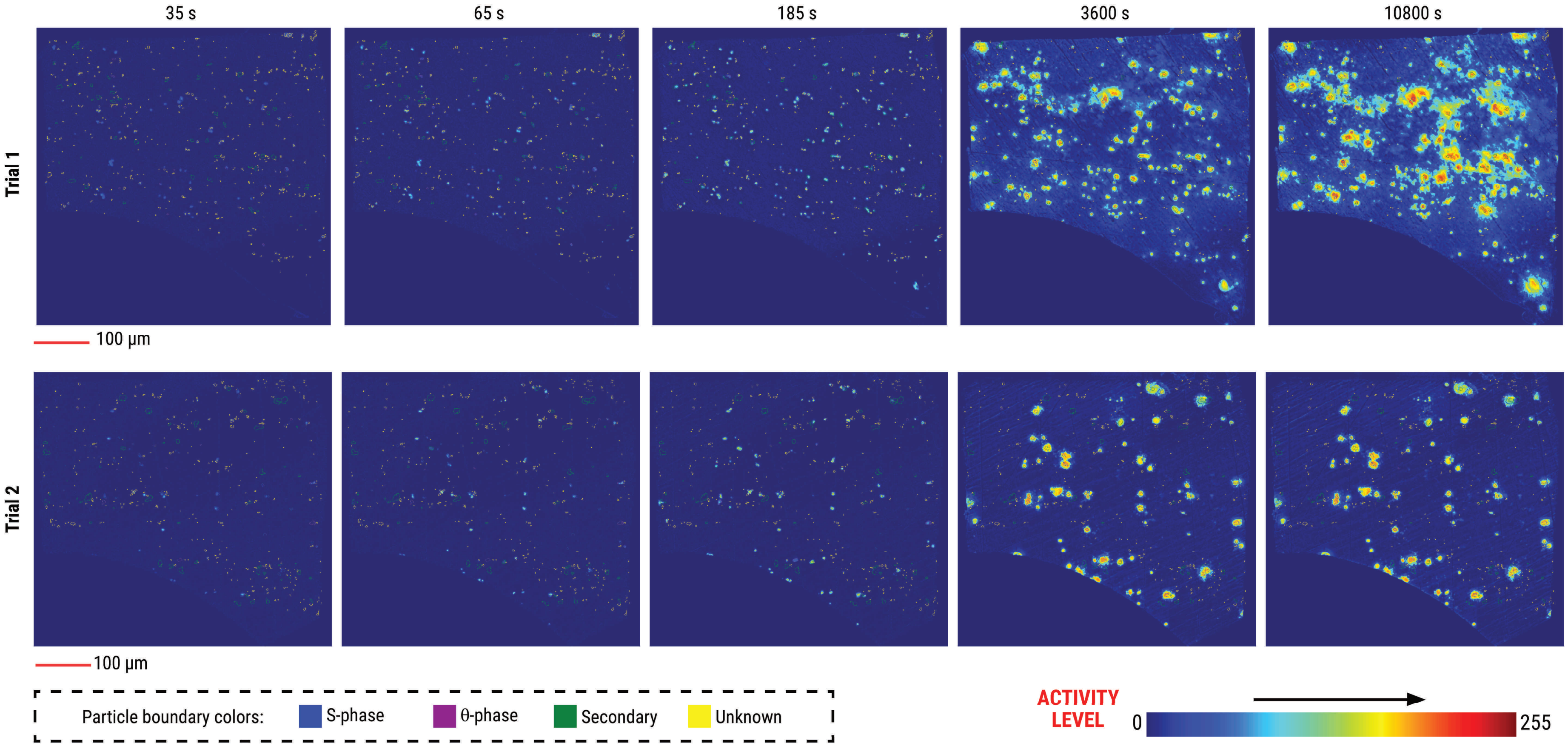

Figure S2.8. Global activity maps at selected times for embedded metal samples supplied with the inhibitor at 180 s. The overlaid particle boundary colours are used to indicate the relative composition of the IMP. The map colours represent the pixel activity level (i.e., change of the pixel gray-level with respect to its initial condition) at time t. The higher extent of global changes in trial 1 is attributed to the higher number of active particles even prior to the addition of the inhibitor.

2.7.4. Image analysis protocol

Our image analysis protocol generally has three main outputs, the global activity maps (GAM), the local activity maps (LAM) and their corresponding simplified pixel activity distribution plots (sPAD). The generation of these outputs rely on two main inputs, the intermetallic particle (IMP) map generated from pre-immersion back-scattered electron SEM images of the EMS surface, and the pre-processed (i.e, aligned, rotated, cropped, metal surface isolated) in situ optical images of the surface during exposure to the electrolyte and the inhibitor. The generation of the IMP map and the pre-processing of the optical images had already been covered in great detail by Olgiati et al. In this work, the main modification that we implemented lies in the subsequent extraction of information from the pre-processed optical images and then analysing them in a more localized scale. This analysis protocol is summarized in Figure S2.9.

The core of the protocol is the subtraction of the images at time *t* from the image at t = 0. It is emphasized that this procedure leads to the detection of pixels which became *darker* relative to their initial condition. The subtracted image is referred to as the global activity map (GAM) and is used further to generate the local activity maps. This is achieved by overlaying the coordinates of the IMP particle boundaries obtained from the IMP particle map. A bounding rectangle drawn around the original IMP boundary allows creation of the rectangular regions of interest (RROI) which constitutes the LAMs. These LAMs are then used to generate the simplified pixel activity-level distribution (sPAD) plots for a given IMP.

As the analysis of the LAMs and the sPADs were focused on active IMPs (i.e., IMPs which exhibited detectable change), we also developed a simple protocol to distinguish active IMPs from inactive IMPs. Active IMPs were prioritised because we cannot be completely certain if inactivity in the presence of the inhibitor is due to the interaction with the inhibitor or due to the inherent stability of the IMP. An initial screening of LAMs is applied to determine if an IMP is active or inactive. To achieve this, 20 regions of interest on areas of the sample without IMPs were defined. The $\mathrm{maxGL}_{\mathrm{IMP}}$ of these regions were then used to semi-quantitatively assess if the sPAD of a specific IMP is active or inactive (Figure S2.10).

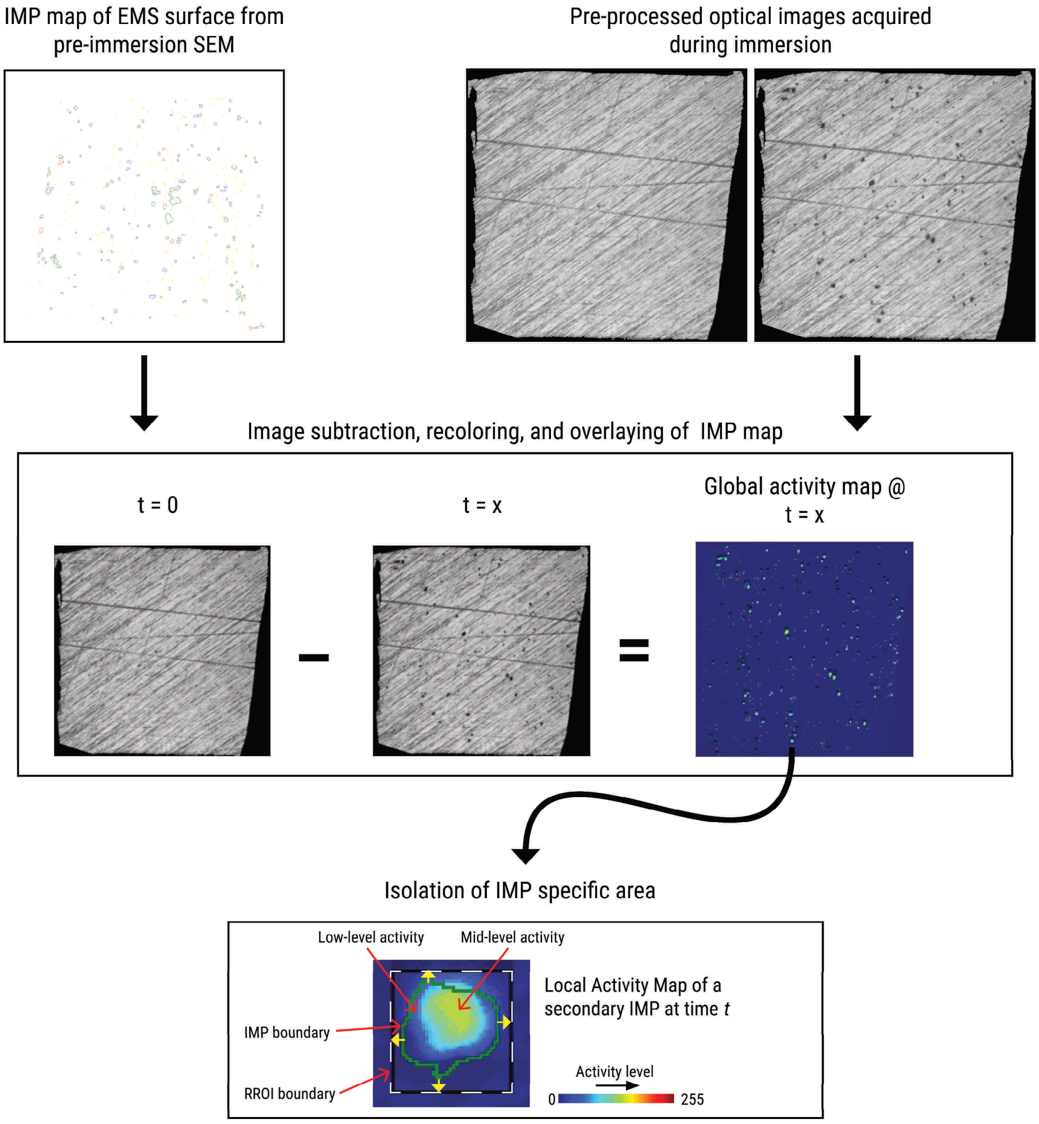

Figure S2.9. Protocol for analysis of local changes at intermetallic particles on the surface of the epoxy-embedded metal samples exposed to Ce(III) at different supply times.

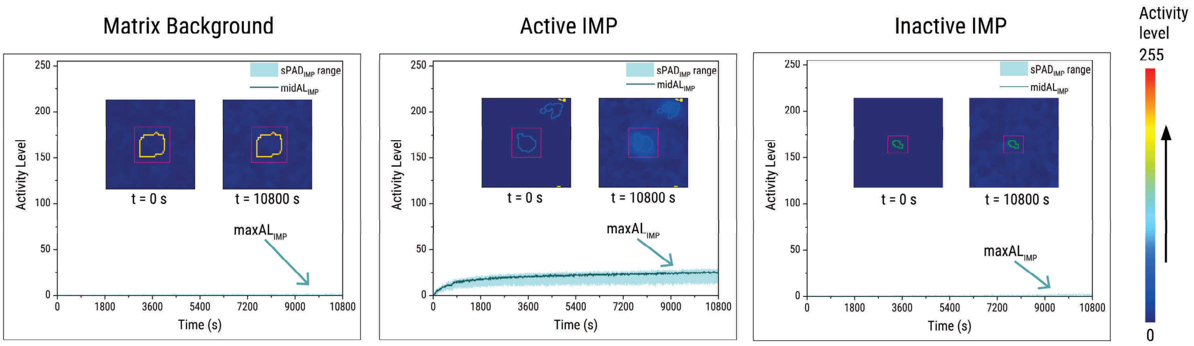

Figure S2.10. Active particles were identified by comparing their simplified pixel activity distribution to those acquired from selected regions of the matrix.

2.7.5. Post-immersion SEM-EDX of selected IMPs

The following figures show the post-immersion EDS spectra of selected intermetallics exposed to Ce(III) at different supply times.

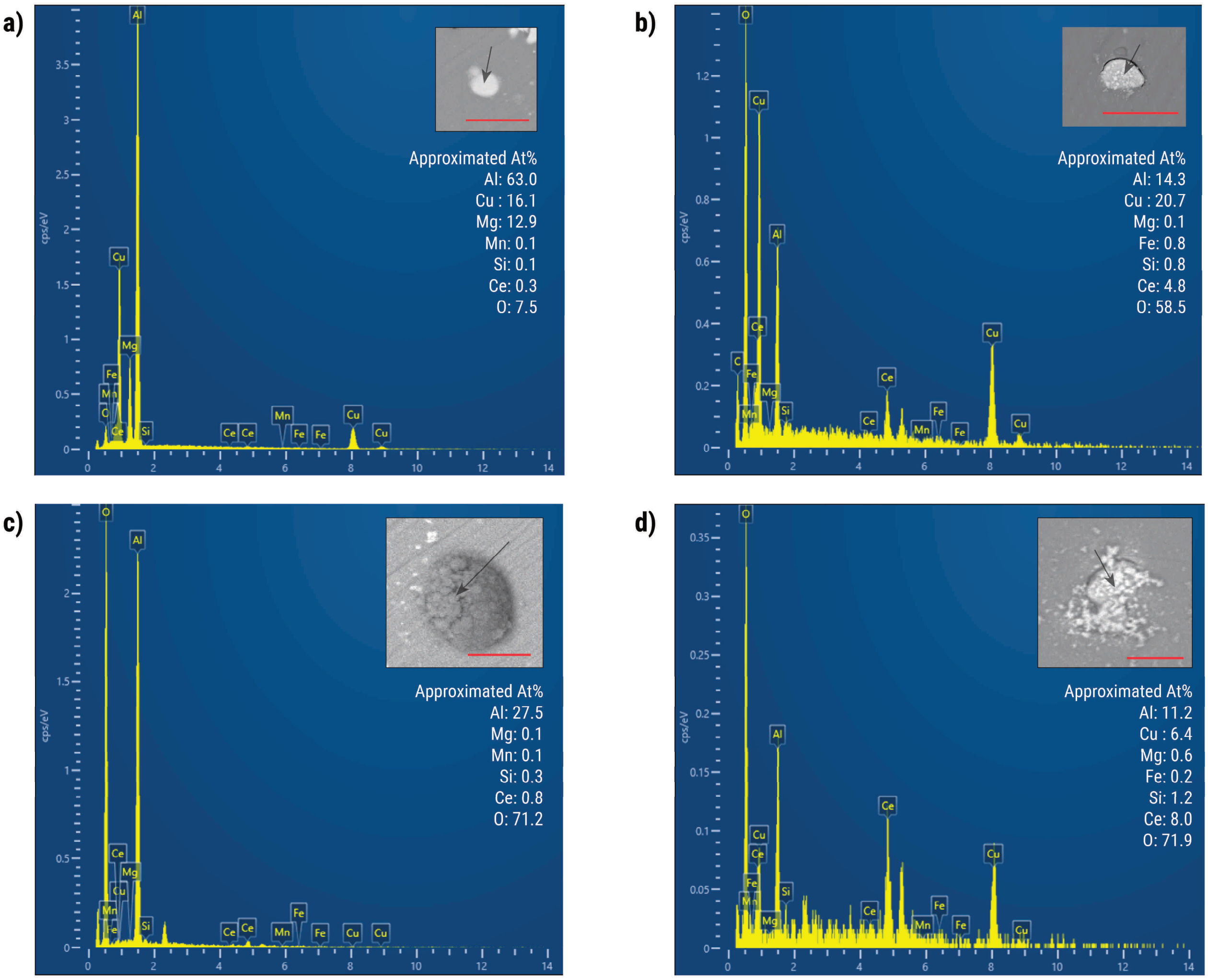

Figure S2.11. Post-immersion EDS spectra of selected s-phase intermetallics after three hours of exposure to 0.05 M NaCl and 0.001 M $Ce(NO_3)_3$ supplied at (a) 0 s, (b) 30 s, (c) 60 s, and (d) 180 s. The spectra highlight the changes in the composition of the deposits at different inhibitor t_{supply} while their corresponding back-scattered SEM images (insets) show variations in the morphology of the deposits. The colour of the deposits in the back-scattered SEM images also indicates the predominant component of the deposits. Brighter deposits likely contain more Ce while darker deposits contain more Al. The scale bars indicate 10 μm.

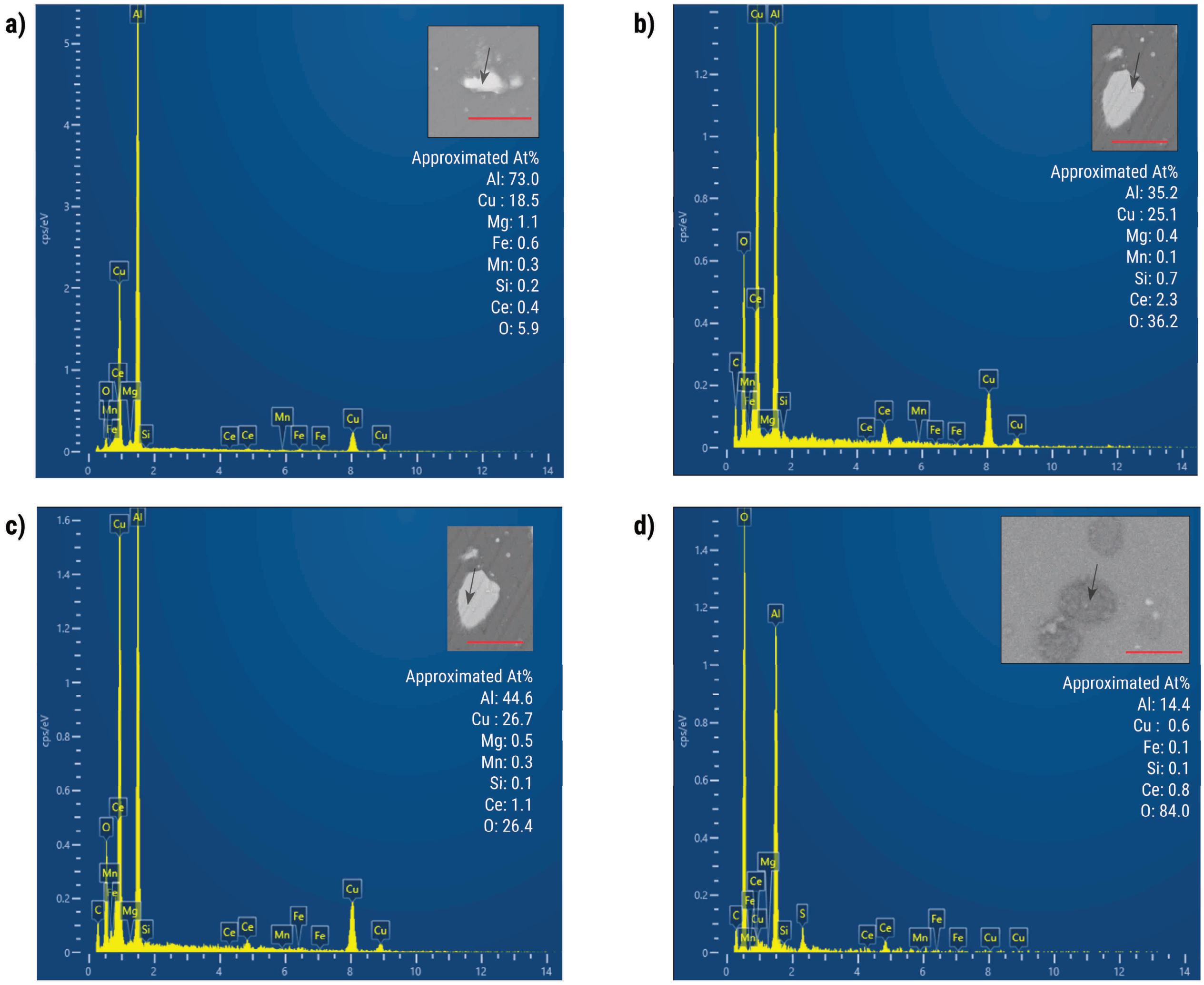

Figure S2.12. Post-immersion EDS spectra of selected θ-phase intermetallics after three hours of exposure to 0.05 M NaCl and 0.001 M $Ce(NO_3)_3$ supplied at (a) 0 s, (b, c) 30 s, and (d) 180 s. The spectra highlight the changes in the composition of the deposits at different inhibitor t_{supply} while their corresponding back-scattered SEM images (insets) show variations in the morphology of the deposits. They also show that spatial variations in the amount of precipitated Ce can occur within the IM particle itself (b, c) due to local differences in the composition of the particle. The scale bars indicate 10 µm.

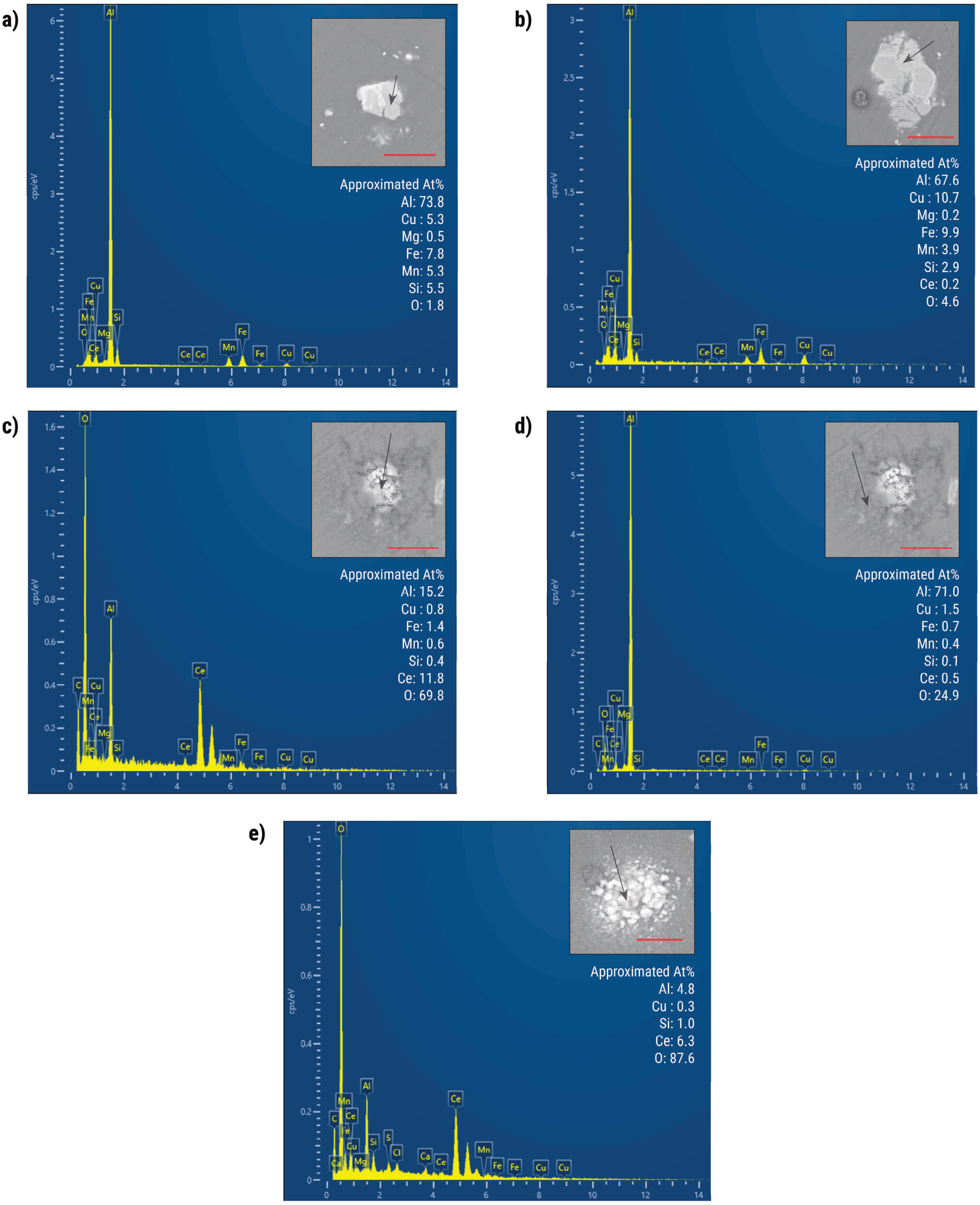

Figure S2.13. Post-immersion EDS spectra of selected secondary intermetallics after three hours of exposure to 0.05 M NaCl and 0.001 M $Ce(NO_3)_3$ supplied at (a) 0 s, (b) 30 s, (c, d) 60 s, and (e) 180 s. The spectra highlight the changes in the composition of the deposits at different inhibitor t_{supply} while their corresponding back-scattered SEM images (insets) show variations in the morphology of the deposits. They also show that variations in the composition of the deposits can occur (c, d) due to deposition of both Ce (brighter deposits) and corrosion products like aluminum (hydr)oxides (darker deposits). The scale bars indicate 10 μm.

2.7.6. Quantification of Activity Onset for Uninhibited IMPs

The estimation of the onset of activity for the θ-phase intermetallics was achieved through analysis of the simplified pixel activity-level distribution plots. Specifically, the development of the maxAL component of the plot was monitored. The time at which it started to deviate from its initial semi-flat profile marks the onset of activity of the IMP.

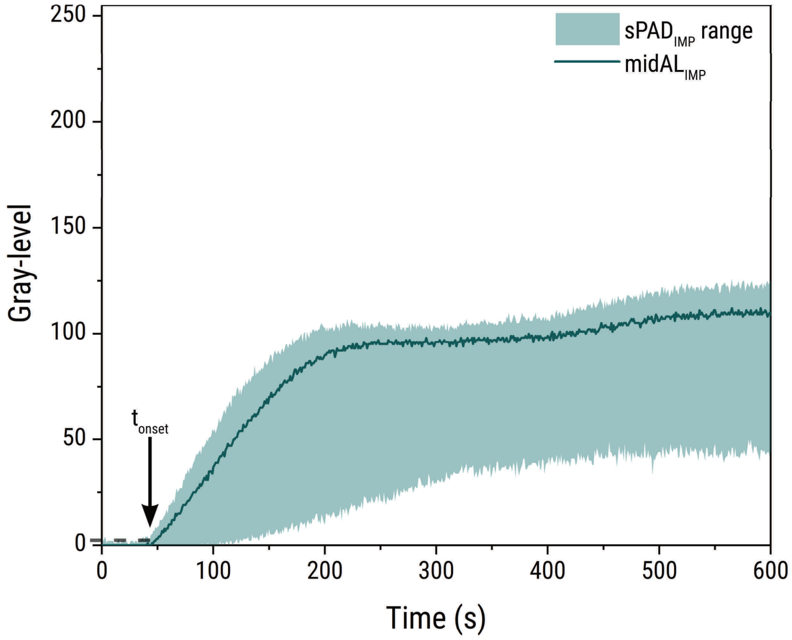

Figure S2.14. Estimation of the onset of activity from the simplified pixel-activity level distribution plots.

2.7.7. Protocol for analysis of simplified pixel activity distribution plots

For the IMPs that were identified as active, the midAL values were obtained by simply getting the values of the midAL curve at the time specified. Meanwhile, a t_{sp} is estimated for each component curve (i.e., maxAL, midAL, minAL) of both $sPAD_{IMP}(t)$ and $sPAD_{AMX}(t)$ using the scheme shown in Figure S2.15. Estimation of tsp from a component curve of the simplified pixel activity distribution plot. The tsp essentially tells us about the duration of the active period.. The scheme involves connecting the endpoints of the plot and then identifying the point with the highest perpendicular distance from the connecting line. Six component t_{sp} values are generated by applying this scheme. The highest of these values is then taken as the t_{sp} of the IMP in question.

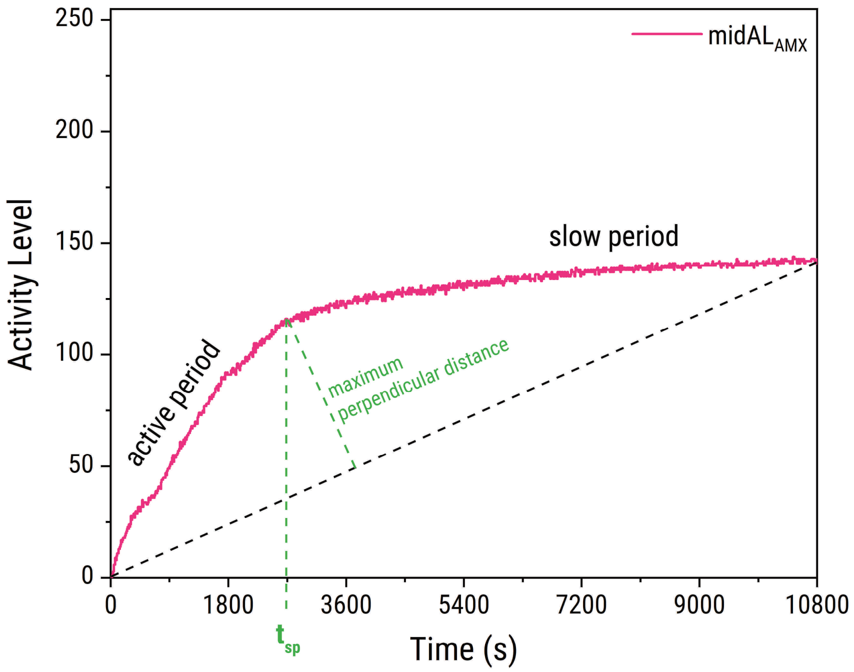

Figure S2.15. Estimation of t_{sp} from a component curve of the simplified pixel activity distribution plot. The t_{sp} essentially tells us about the duration of the active period.

2.7.8. Parameters extracted from sPADs

The quantified extracted parameters presented in Figure 2.9 and Figure 2.10 are shown in Table S2.1, Table S2.2, and Table S2.3.

Table S2.1. Quantification of extracted parameters from sPAD plots for active S-phase (Al_2CuMg) IMPs. The tabulated values include the number of active IMPs sampled (# IMP), the 1st quartile (Q1), the median, and the 3rd quartile (Q3) of the observations.

S-phase		$\text{midAL}_{\text{IMP,3h}}$			$\text{midAL}_{\text{AMX,3h}}$			t_{sp} (s)		
	# IMP	Q1	**Median**	Q3	Q1	**Median**	Q3	Q1	**Median**	Q3
No Ce(III)	35	143.5	**154.0**	164.1	132.8	**148.8**	159.6	2940	**4870**	7500
TS0	75	14.6	**17.7**	21.7	5.8	**7.0**	8.4	2059	**2760**	3960
TS30	48	87.7	**99.8**	107.5	26.1	**32.2**	39.6	820	**920**	1280
TS60	56	129.3	**135.9**	146.3	80.0	**97.0**	113.7	2125	**2615**	3050
TS180	47	139.3	**164.6**	173.2	98.5	**132.0**	153.0	2640	**3180**	4250

Table S2.2. Quantification of extracted parameters from sPAD plots for active θ-phase (Al_2Cu) IMPs. The tabulated values include the number of active IMPs sampled (# IMP), the 1st quartile (Q1), the median, and the 3rd quartile (Q3) of the observations.

θ-phase		$\text{midAL}_{\text{IMP,3h}}$			$\text{midAL}_{\text{AMX,3h}}$			t_{sp} (s)		
	# IMP	Q1	**Median**	Q3	Q1	**Median**	Q3	Q1	**Median**	Q3
No Ce(III)	12	151.2	**162.6**	167.1	144.1	**155.3**	165.1	3170	**4350**	6395
TS0	27	10.5	**15.7**	21.9	4.1	**6.1**	8.4	2100	**2840**	3640
TS30	25	48.1	**74.6**	103.3	13.5	**16.6**	26.8	820	**1100**	1450
TS60	17	114.7	**128.8**	157.3	56.1	**107.4**	122.9	2390	**2890**	3340
TS180	16	158.7	**166.7**	176.1	135.4	**150.1**	162.2	2960	**3690**	4305

Table S2.3. Quantification of extracted parameters from sPAD plots for active secondary (AlCuFeMn and $(Al,Cu)_x(Fe,Mn)_ySi$) IMPs. The tabulated values include the number of active IMPs sampled (# IMP), the 1st quartile (Q1), the median, and the 3rd quartile (Q3) of the observations.

Secondary		$\text{midAL}_{\text{IMP,3h}}$			$\text{midAL}_{\text{AMX,3h}}$			t_{sp} (s)		
	# IMP	Q1	**Median**	Q3	Q1	**Median**	Q3	Q1	**Median**	Q3
No Ce(III)	33	81.9	**122.3**	136.0	67.9	**139.9**	158.7	5860	**7120**	8510
TS0	38	5.4	**7.4**	9.9	2.5	**3.2**	4.1	2750	**4260**	9890
TS30	49	15.0	**38.9**	53.3	6.0	**9.0**	10.4	980	**1360**	1800
TS60	80	92.9	**122.8**	132.9	30.7	**75.5**	99.4	2025	**2685**	3315
TS180	47	37.9	**161.0**	179.7	55.0	**137.1**	164.3	3880	**5380**	6873

3

Local re-immersion behaviour of Ce-based inhibiting layers on AA2024-T3 intermetallics: Enhanced stability through partial dealloying and prolonged exposure

The stability of inhibiting layers on AA2024-T3 intermetallic particles (IMPs) during re-immersion in saline following an initial immersion in a Ce(III)-containing electrolyte was investigated using in situ reflected light microscopy. Re-immersion behaviour varied due to differences in IMP composition, spatial distribution, and Ce(III) precipitation. IMPs were grouped into four categories based on whether their activity was high or low during both the immersion and re-immersion stages. Majority of the high activity particles during re-immersion had low activity during immersion. Longer immersion times (up to 72 h) and a brief delay in inhibitor supply (30 s) reduced re-immersion activity by increasing Ce(III) coverage. These findings suggest that corrosion protection systems promoting greater Ce(III) precipitation may enhance re-immersion stability.

This chapter has been published as:

M. Mopon, A. Mol, S. J. Garcia, Local re-immersion behaviour of Ce-based inhibiting layers on AA2024-T3 intermetallics: Enhanced stability through partial dealloying and prolonged exposure, *Corros. Sci.* 255 (2025) 113146. doi: 10.1016/j.corsci.2025.113146.

3.1. Introduction

AA2024-T3 is broadly used in the aerospace industry due to its excellent strength-to-weight ratio. However, intermetallic particles (IMPs) formed during thermomechanical processing make the alloy prone to localized corrosion when exposed to harsh environments [1–3]. To address this, coatings are applied to shield the metal from corrosive agents. Additionally, incorporating corrosion inhibitors into the coatings [4–8] provides active protection, complementing their passive barrier function. This active protection becomes particularly valuable when the coating sustains mechanical damage, exposing the underlying metal. The damaged coating releases inhibitors which interact with the exposed metal surface to slow or prevent further corrosion. The recommended release rate is dependent on the environment and corrosion inhibitor. Oltra et al. [9] showed that there is a competition between inhibitor mass transport and the triggering time of local corrosion. This competition leads to preference for systems with initial fast release to minimize local corrosion on the exposed metal surface [10,11].

Corrosion inhibitors released from active protection systems mainly target the surface of IMPs in AA2024-T3, although they can also affect the bulk matrix [3,12]. However, it's the interaction with the IMP surface that plays the most important role in preventing local corrosion. The specific nature of this interaction is determined by the chemistry of the inhibitor, the surface state, and the environmental conditions. For example, rare earth metal inhibitors such as $Ce(NO_3)_3$ mainly form local inhibiting layers through precipitation, as the cation reacts with hydroxide ions generated during the dealloying of IMPs [13–15]. Organic inhibitors like 2,5-dimercapto-1,3,4-thiadiazole (DMTD), on the other hand, form inhibiting layers by adsorbing on the particle surface [12,16]. Regardless of the inhibitor chemistry, long-term effectiveness of protection depends on a consistent inhibitor supply as this can limit potential stability loss of the inhibiting layer [10,11,17]. This has translated to active corrosion protection design strategies that give preference to prolonged or sustained inhibitor release [8,18]. However, when inhibitors are embedded within coatings, their finite storage capacity limits long-term inhibitor availability. Inevitable depletion of the inhibitors in the coating can thus cut off inhibitor supply and leave damage sites vulnerable to failure of inhibition and corrosion attack.

Ensuring stable inhibition even when the inhibitor supply is cut off is essential for reliable active protection of AA2024-T3. However, the mechanisms of inhibition failure in a post-cut off scenario remain underexplored, as corrosion inhibitor performance is mostly evaluated in environments with continuous inhibitor availability [19–22]. Homborg et al. simulated inhibitor-depleted conditions by re-immersing AA2024-T3 in an inhibitor-free corrosive environment (e.g., 0.05 M NaCl) after initial exposure to inhibitors like $Ce(NO_3)_3$ and phytic acid [23]. Their in situ optical-electrochemical analysis revealed that $Ce(NO_3)_3$ provides relatively stable corrosion protection but is still prone to localized failure at IMPs. Similarly, Zhao et al. found that small NaCl concentrations (0.025 – 0.25 M) can lead to higher degree of DMTD chemisorption during immersion, making it more stable during re-immersion in saline environments without inhibitors [12]. They also showed that loss of inhibition, when present, is also initially observed on the surface of IMPs.

Visser et al. also explored inhibition stability during re-immersion and demonstrated that Li_2CO_3 has greater stability than 2-MBT and BTA [24]. They attributed the lower re-immersion stability of 2-MBT and BTA to the desorption tendency of the inhibiting layer previously formed. Li et al. deepened in the topic and showed the irreversibility of Li_2CO_3 conversion layers using electrochemical noise analysis and highlighted their vulnerability to localized damage under certain exposure conditions [25]. While these studies offer useful information about how different inhibitors perform during re-immersion, we still lack a clear understanding of how inhibition failure starts and spreads at the local level. Closing this gap is important for improving the reliability of active corrosion protection strategies for AA2024-T3.

This work investigates the stability, and/or loss of stability, of inhibiting layers formed on IMPs in AA2024-T3 during re-immersion in a corrosive environment. This study primarily examines how IMPs respond in inhibitor-free conditions, with their initial behaviour in the presence of inhibitors considered for context. By analysing the re-immersion behaviour, this study helps identify the factors that could lead to inhibition failure and contributes to the development of more durable corrosion protection strategies. This builds on our previous work [26] which examined how variations in inhibitor introduction at the start of exposure influenced inhibition performance under continuous inhibitor presence. In contrast, the present study shifts the focus to the other end of the inhibition timeline, when the inhibitor is no longer present in the system. Using in situ reflected light microscopy (RM), we monitored the behaviour of a large number of IMPs with high spatial and temporal resolution to assess how inhibition changes over time in the absence of continued inhibitor availability. High spatial resolution enables detailed analysis at the level of individual IMPs, while high temporal resolution is essential for capturing the rapid and dynamic processes involved in corrosion initiation. Notably, other local techniques are capable of providing more quantitative information about local corrosion development and inhibition failure on IMP sites. For example, scanning vibrating electrode technique can be used to analyse local ionic current densities to determine where local cathodic and anodic sites develop [27–30]. Scanning ion-selective electrode technique can be used to analyse local pH changes which can give insight about the progression of local corrosion [28–31]. Kelvin probe techniques (e.g., scanning Kelvin probe, scanning kelvin probe force microscopy) can be used to measure local work functions which can be used as indicators of local corrosion resistance [28–30,32]. Despite the local quantitative information that can be obtained from these techniques, they usually need to trade wide sampling area for good temporal and/or spatial resolution [28–30]. In situ RM is less sensitive to this limitation which makes it useful for tracking time-dependent surface changes over multiple sites simultaneously. The technique was thus used to monitor local surface changes arising from the formation of the inhibiting layer during immersion and monitor how these layers evolved during re-immersion. Analysing inhibition and its breakdown across many sites is essential for developing a more complete understanding of inhibitor performance. This broader approach allows us to identify the full range of re-immersion behaviour and which types of local failure are most critical to the stability of corrosion protection. Such insights are especially important for AA2024-T3, where even a single point of failure can compromise macroscale performance. $Ce(NO_3)_3$, referred to as Ce(III), served as the model inhibitor for this study.

We also looked at how the duration of exposure to inhibitor solutions and the delay in supplying the inhibitor affect the stability of the inhibiting layers during re-immersion. These two factors mimic common design strategies used in active corrosion protection coatings: exposure time is related to sustained release, while supply delay relates to initial release rates. In the fast initial release scenario, the inhibitor is present from the start of immersion (undelayed supply). Meanwhile in the slow initial release scenario (delayed supply), the metal is first exposed to a corrosive environment for a set duration before the inhibitor is added. Importantly, this analysis focuses on how these strategies affect the stability of inhibition once the inhibitor is no longer present.

3.2. Experimental

3.2.1. Materials

Commercial grade bare AA2024-T3 (Kaiser Aluminium, rolled thickness = 2 mm) was used as substrate. The substrates were embedded in epoxy to create electrodes with an exposed surface area of approximately 500 x 500 μm^2 [23,26,33]. A 0.05 M NaCl aqueous solution (>98% purity NaCl in "Millipore Elix 3 UV" treated water) was used as the stock corrosive solution. This stock NaCl solution was further used to prepare a 1 mM Ce(III) + 0.05 M NaCl solution and a 45 mM Ce(III) + 0.05 M NaCl. The more concentrated Ce(III) solution was used for the delayed addition of the corrosion inhibitor (i.e., corrosion inhibitor is added to the system after a set time from the start of exposure).

3.2.2. Experimental Protocols

Prior to immersion, the electrode surface was ground with SiC sandpaper from 320 to 4000 grit. They were then polished with 3 and 1 μm diamond paste. Pre-immersion SEM-EDX (JEOL JSM-7500F field emission scanning electron microscope coupled with energy dispersive X-ray spectroscopy) analysis was conducted on some electrodes to obtain location and initial composition of IMPs. The SEM-EDX was operated in back-scattered electron mode. The electrodes were repolished with 1 μm diamond paste and washed in an ultrasonic bath containing ethanol after pre-immersion SEM-EDX to remove any potential contaminants.

For the immersion tests, the electrodes were placed in reflected light microscopy setup, composed of an electrochemical cell (redox.me Raman electrochemical flow cell) and a reflected microscope (Dinolite AM7515MT4A, ~10 pixel μm^{-2}) in brightfield illumination for in-situ acquisition of images of the surface during immersion [26,33]. Several immersion test variants were implemented to assess the impact of exposure duration to inhibitor solution and inhibitor supply delay on re-immersion stability. These variants are summarized in Table 3.1. The immersion test protocols can be divided into the tests with no supply delay and the tests with supply delay. The tests with no supply delay (i.e., UDxx) were supplied with Ce(III) from the start of the exposure using the 1 mM Ce(III) + 0.05 M NaCl solution. The samples were then kept immersed depending on the target total immersion time. For the tests with supply delay (i.e., DSxx), 4.4 mL of the stock NaCl solution was first injected into the cell. A second solution consisting of 0.1 mL of the 45 mM Ce(III) + 0.05 M NaCl was then injected at 30 seconds from the start of exposure. Accurate determination of the start of exposure is possible with live images from the microscope during solution injection. After injection of the second solution, the net concentration of Ce(III) will be 1 mM. The samples were then kept in immersion for the target duration. Notably, the only immersion duration used for the tests with supply delay is 3 hours.

Table 3.1. Summary of immersion conditions used. Samples with no supply delay are identified as UDxx while samples with supply delay are identified as DSxx. The xx refers to the number of hours of immersion to the solution containing Ce(III).

Sample Code	Inhibitor supply time (s) with respect to start of exposure to 0.05 M NaCl	Total Immersion Time (h)
UD03	0	3
UD24	0	24
UD72	0	72
DS03	30	3

After immersion, the samples were washed with deionized water and dried with a nitrogen stream. The samples were then reloaded into the reflected light microscopy setup for the subsequent re-immersion in 4.5 mL of 0.05 M NaCl. The same re-immersion protocol is applied for both the UDxx and the DSxx samples. Re-immersion was monitored for at least three hours and up to 24 h. Once re-immersion was completed, the samples were again washed with deionized water and dried with a nitrogen stream. Duplicate tests were performed for each immersion condition.

3.2.3. Image Analysis

Brightfield reflected light microscopy observation of a polished AA2024 surface enables detection of pixel-level reduction in the intensity of light reflected back to the microscope (i.e., pixel darkening) due to surface processes such as dealloying, pitting, and oxide deposition, as discussed elsewhere [26,33]. The surface darkens because these surface processes scatter incident axial light, thereby reducing the amount reflected back to the detector. The image analysis protocol enables quantification of the pixel darkening by implementing image subtraction against a reference image. When applied to a time series image, the protocol can provide qualitative and quantitative information regarding the time dependence of the pixel changes and of their corresponding surface processes. It should be noted that image pre-processing (i.e., recursive re-alignment, image repositioning) was implemented prior to subtraction.

For the RM images from immersion, subtraction was performed with respect to an image obtained shortly before or at the start of immersion. For the RM images from re-immersion, subtraction was performed with respect to an image acquired at the start of re-immersion (i.e., image @ 0 s of re-immersion – image @ *x* s of re-immersion). The image subtraction generates the global activity map (GAM) for the sample at time x. A built-in ImageJ look-up table (i.e., Fire) was used to recolour the GAMs to enable easier visualisation of the magnitude of the changes (i.e., activity level). Each pixel in the GAM has a corresponding activity level measured in a 0 to 255 scale, with 0 indicating no change with respect to the initial condition and 255 indicating the theoretical maximum pixel darkening. It is noted that the re-immersion GAMs only show degree of pixel darkening during re-immersion and do not depict the changes observed during the prior immersion period. Furthermore, the GAMs also constitute a time series, similar to the RM images from which they were derived.

Analysis of local activity evolution around certain sites (e.g., IMPs, active sites) in GAMs was performed by superimposing object borders. Object borders were extracted either from the pre-immersion SEM images or manually defined from the RM images. A bounding rectangle with a 4 pixel margin is then defined from the object borders to create rectangular regions of interest (RROI). The RROIs allow monitoring of activity on identified sites and their adjacent areas. Evolution of the pixel activity in the RROI with time is summarized in terms of the median activity level (midAL) as previously introduced elsewhere [26]. At any given time, the individual pixels within RROI have their own activity levels. The midAL is the median of these individual pixel activity levels. It provides a semi-quantitative basis for assessing the extent of surface changes that occurred on the IMP surface and its adjacent matrix and also shows how the extent of surface changes evolve with time (Figure 3.1). The median is preferred over other measures of central tendency because it is less sensitive to extreme values.

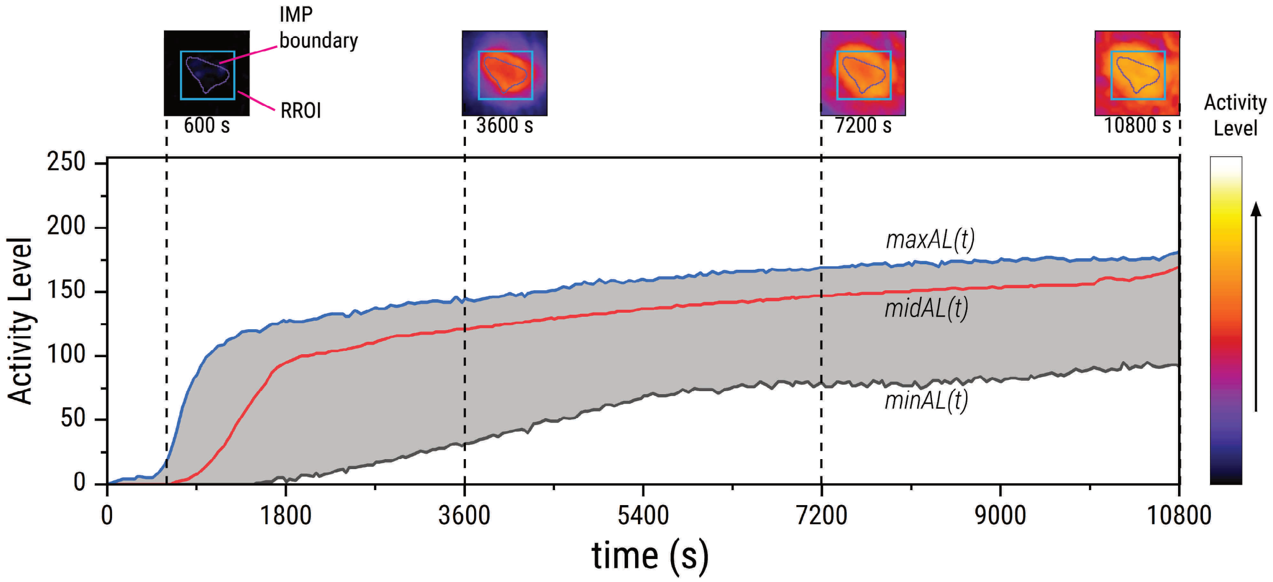

Figure 3.1. The activity level of individual pixels on the intermetallic particle (IMP) surface and its adjacent matrix (i.e., pixels within the RROI) can be summarized in terms of the maximum (maxAL), median (midAL), and minimum (minAL) activity level. The evolution of these parameters with time provides a semi-quantitative basis for analysing the kinetics of local surface changes.

3.3. Results and Discussion

3.3.1. Evolution of IMP surface during re-immersion

Local surface behaviour in the UD03 exposure condition was used as the base case for assessing the local loss of inhibition during re-immersion. The initial 3-hour immersion period for UD03 is characterized by reduced local corrosion activity in AA2024 exposed to a corrosive environment. This is highlighted by the minimal changes observed when comparing the electrode surface at 0 s (Figure 3.2a) and after 10800 s (Figure 3.2b) of immersion. Movie 3.1 shows a time-lapse of the surface changes between 0 and 10800 s. Notably, the IMPs shown in Figure 3.2 and Movie 3.1 are grouped into S-phases (Al_2CuMg), θ-phases (Al_2Cu), and secondary particles ($(Al,Cu)_x(Fe,Mn)_ySi$ or AlCuFeMn) based on their EDX-derived compositions. Their boundaries are also color-coded based on these compositions (blue: S-phase, purple: θ-phase, green: secondary particle, yellow: unknown). In uninhibited systems, local corrosion processes such as dealloying, trenching, and corrosion product deposition lead to darkening of the surface [33]. However, with Ce(III), most of the surface remained bright during immersion, except for some S- and θ-phase particles. In our previous work [26], we have shown that the pixel darkening and its corresponding activity level correlates to Ce(III) precipitation on the IMP surface. Figure 3.3 shows examples of IMPs from our previous work with varying degrees of activity after 3 hours of immersion in 0.05 M NaCl containing 0.001 M Ce(III). In Figure 3.3a, particles were exposed to Ce(III) immediately when immersion began, while in Figure 3.3b and Figure 3.3c, Ce(III) was introduced 60 seconds after the start of immersion. The activity maps and their corresponding post-immersion back-scattered electron images highlight that higher activity levels is related to more extensive Ce(III) precipitation (i.e., thicker inhibiting layers). This relationship is fundamental in the succeeding analysis of the activity maps obtained from the immersion and re-immersion tests.

Local activity maps in Figure 3.2c provide a closer look at the activity evolution of particles that maintained low activity (Region 1 and Region 4) and of particles that developed high activity (Region 2 and Region 3). Activity maps of Regions 1 and 4 show few changes during the three-hour immersion in the Ce(III)-containing electrolyte. No warm-coloured pixels were observed, and the activity of the pixels within the IMP boundaries remained comparable to the matrix. Given that most of the IMPs in these two regions are S- and θ- phases, the absence of high activity likely indicates inhibition from Ce(III). Undetectable changes further suggests the Ce-inhibiting layer has very low thickness. In Regions 2 and 3, IMP activity was observed between

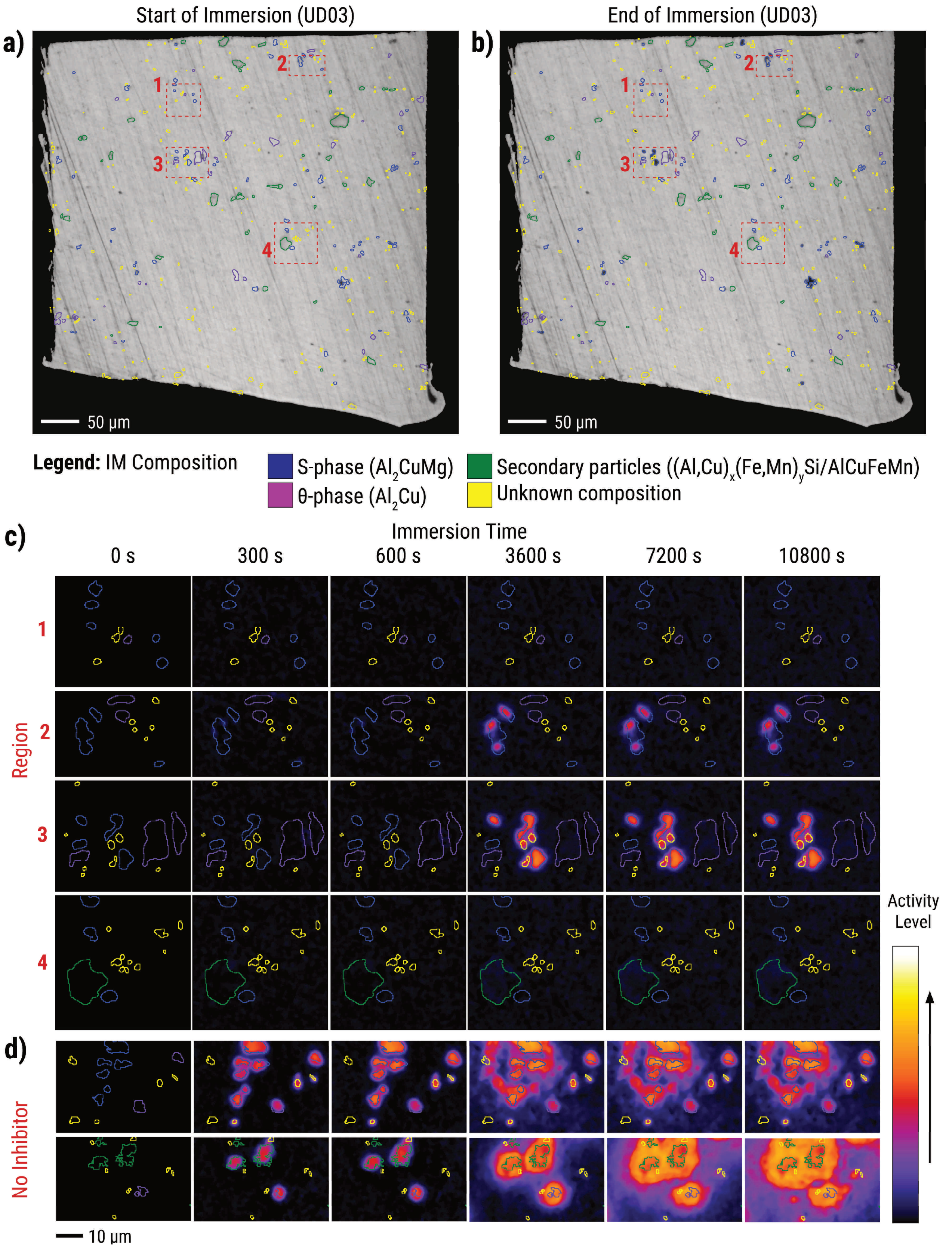

Figure 3.2. Reflected light microscopy images show the condition of a UD03 sample surface **(a)** at the start, and **(b)** at 10800 s of immersion in 0.05 M NaCl with 0.001 M Ce(III); **(c)** UD03 immersion activity maps at different times highlight the progression of surface changes during exposure to the inhibitor and show that they are minimal compared to **(d)** activity maps from the sample immersed in just 0.05 M NaCl.

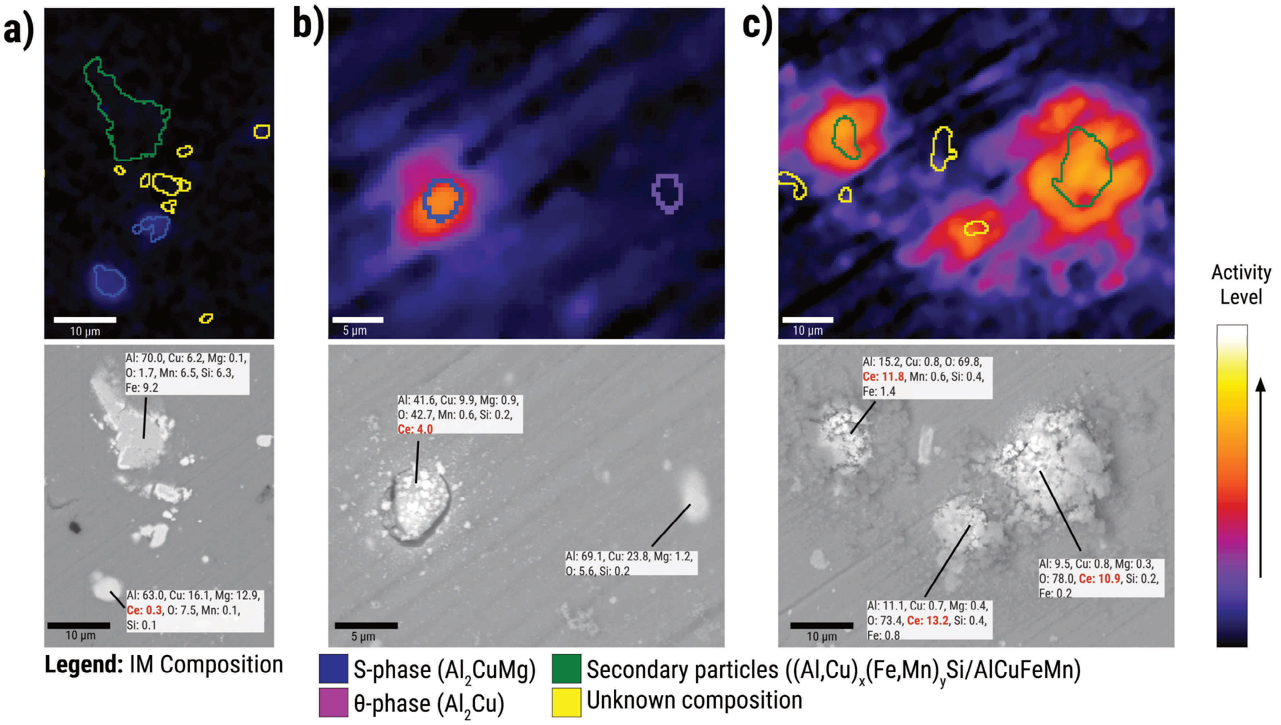

Figure 3.3. Examples of IMPs with **(a)** low activity level, and **(b, c)** high activity level at the end of 3 hours of immersion in Ce(III)-containing solution. The post-immersion backscattered electron images show the degree of Ce(III) precipitation corresponding to the activity. The particles shown are part of the results from [26].

600 and 3600 seconds. This is significantly much later than the appearance of activity in uninhibited particles (Figure 3.2d). The activity started on the IMP surfaces and did not spread to the surrounding matrix. By the end of immersion, the surfaces have activity levels in orange to yellow-orange range of the activity colour scale. The observed changes were slower, more limited, and less extensive than those in NaCl-only solutions (Figure 3.2d), where dealloying and trenching occurred. These results are in line with our previous reports on delayed inhibitor supply where we showed how Ce-based inhibiting layers become more substantial when there is dealloying prior to inhibitor addition [26]. The fact that some IMPs showed more Ce deposition than others indicates that some IMPs were dealloyed before immersion, likely due to some degree of atmospheric corrosion due to condensation on IMP surfaces prior to exposure to the electrolyte (Supporting Information 3.7.1).

Figure 3.4 shows the changes of the electrode first shown in Figure 3.2a,b during its re-immersion in 0.05 M NaCl. Movie 3.2 shows a time-lapse of the surface changes between during this re-immersion period. Figure 3.4a and Figure 3.4b show the appearance of the surface at 0 s and after 10800 s of re-immersion, respectively. The two images show a high degree of changes once the inhibitor is not present in the system anymore. Figure 3.4c shows a closer look at the regions shown in Figure 3.2c during re-immersion. As during immersion, the IMPs exhibit either low (Region 1 and 2) or high (Region 3 and 4) activity.

Region 1 (Figure 3.4c) shows particles which exhibited low activity during immersion (Figure 3.2c, Region 1). During re-immersion, the onset of activity (i.e., appearance of purple pixels) was observed on the IMP surface some time between 300 and 600 seconds of re-immersion. The activity gradually extended to the adjacent matrix, marked by the slow-spreading purple area from 600 to 10800 s (see white arrows in 3600 to 10800 s frames in Figure 3.4c, Region 1). The activity level of the pixels on and around the IMPs remained low, nonetheless, at the end of the observed period.

Region 2 (Figure 3.4c) contains two S-phase particles (s1 and s2; EDX spectra provided in Supporting Information 3.7.2) that showed visible activity localized on the IMP surfaces during immersion (Figure 3.2c, Region 2). The rest of the particles in this region exhibited low activity during immersion. The particles s1 and s2 showed minimal (light purple) activity during re-immersion. The activity started somewhere between 0 and 300 second on the matrix adjacent to the IMPs. It apparently stopped between 600 and 3600 s, as no significant activity changes were seen after 3600 s. Notably, segments of the surfaces of s1 and s2 which showed visible activity during immersion exhibited minimal activity during the re-immersion. This does not necessarily mean no further changes occurred on or under these areas since the current microscopy setup can only detect changes that further increase light scattering on the sample surface (e.g., additional deposition, significant inhibiting layer dissolution). Nonetheless, since activity on the adjacent matrix remained very low at 3 hours of re-immersion, activity of the inhibiting layer or the underlying particle are most likely very limited.

Region 3 (Figure 3.4c) contains three S-phase particles (s3, s4, and s5; EDX spectra provided in Supporting Information 3.7.2) that exhibited visible activity during immersion (Figure 3.2c, Region 3). During re-immersion, activity developed between 0 and 300 s on the matrix adjacent to these particles, spreading further with time. After 3 hours of re-immersion, the adjacent matrix of s4 and s5 showed high activity levels (i.e., orange-colored pixels) while s3 activity levels remained on the lower end. The IMP surface of s4 and s5 also exhibited some activity after three hours of re-immersion, indicating potential changes on the inhibiting layer that formed on the surface during immersion.

Meanwhile, the θ-phase IMPs (t1 and t2; EDX spectra provided in Supporting Information 3.7.2) which exhibited low activity during immersion (Figure 3.2c, Region 3) became active between

0 and 300 s of re-immersion. The re-immersion activity initiated from the defect between the two particles which was present even prior to the immersion period (Supporting Information 3.7.3). After 3 hours of re-immersion, the matrix surrounding the particles developed higher activity (i.e., yellow pixels) than the IMP surfaces (i.e., red-orange pixels). This spatial distribution of activity is consistent with a dealloyed particle surrounded by a massive trench [26].

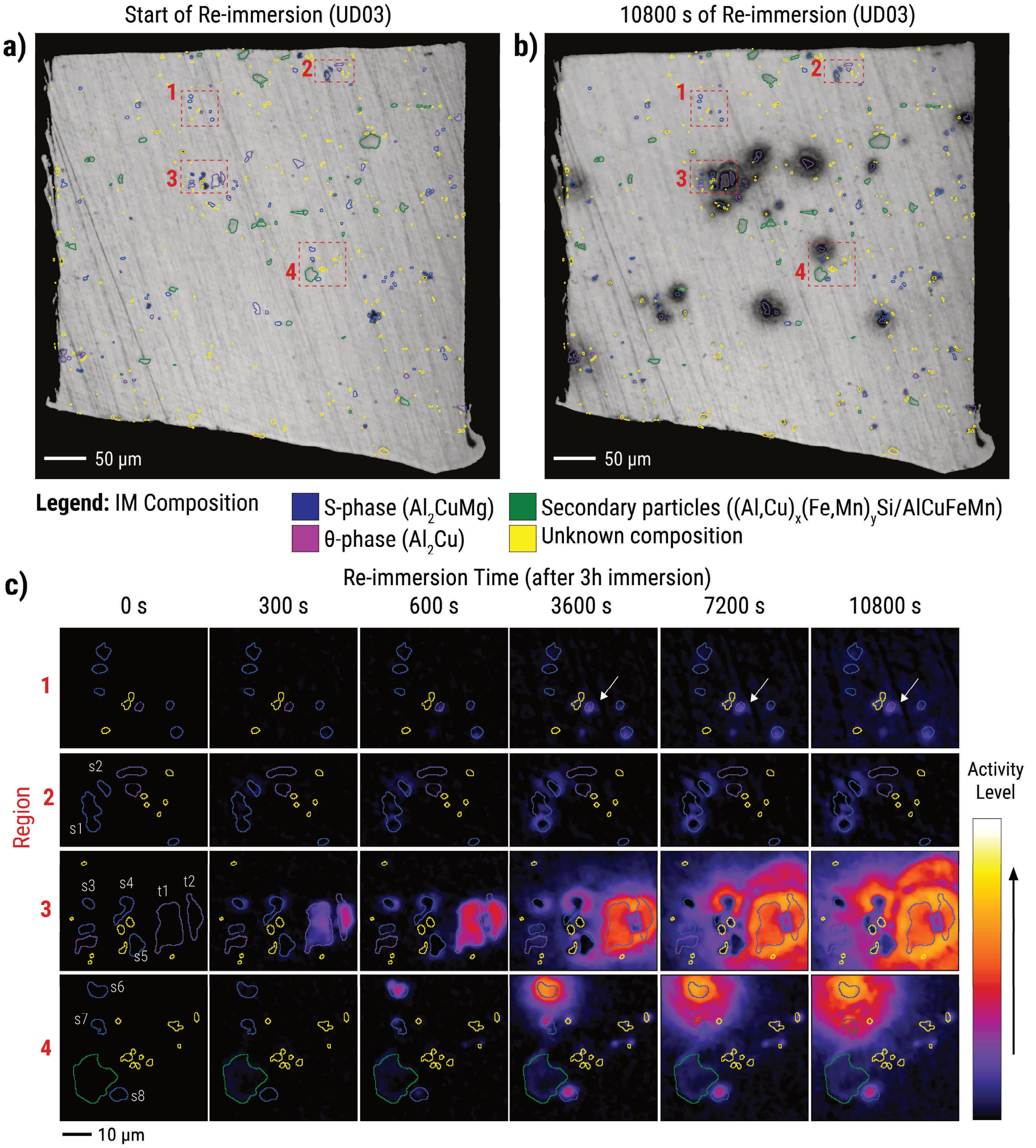

Figure 3.4. Reflected light microscopy images of a UD03 sample **(a)** at the beginning, and **(b)** at 10800 s of re-immersion in 0.05 M NaCl; **(c)** UD03 re-immersion activity maps from selected regions of the sample surface show the local onset and progression of inhibition loss.

Region 4 (Figure 3.4c) shows S-phase IMPs (s6, s7, s8; EDX spectra provided in Supporting Information 3.7.2) which had low local activity during immersion. During re-immersion, their activity initiated on the IMP surfaces between 300 and 600 seconds. This eventually spread to the adjacent matrix from 600 s and continued with further re-immersion. The particle s6 exhibited the most extensive changes on its adjacent matrix.

Figure 3.4c shows that during re-immersion in 0.05 M NaCl, the loss of inhibition for AA2024 after 3 hours of immersion in Ce(III)-containing electrolyte still starts at the IMPs, similar to uninhibited systems. Notably, there is variability in the IMP inhibition even among particles of the same composition. This variability is more apparent when the immersion/re-immersion behaviours of the IMPs sampled from two replicates (total number of sampled IMPs = 901) are taken into consideration. Figure 3.5a shows the midAL values at the end of the 3h re-immersion in inhibitor-free corrosive solution (y-axis) versus the midAL values after the initial 3h immersion to the Ce(III)-containing solution (x-axis). Along the x-axis, most particles have midALs close to 0 while a smaller group have midALs above 25. These two groups constitute the low and high activity groups during immersion. To classify the particles quantitatively, a midAL threshold of 20 is used to separate IMPs with low and high midALs. The value is based on the visual clustering of the midALs and on the threshold used by Olgiati et al. [33] for identifying active pixels. The same threshold is applied for the classification of re-immersion behaviour. Sites that exhibited midAL ≤ 20 are categorized as having L-type re-immersion behaviour and those with midAL > 20 as having H-type re-immersion behaviour. Figure 3.5a includes vertical and horizontal dashed lines at the threshold value, dividing the plot into four zones corresponding to the combinations of immersion and re-immersion behaviours: *L/L* (low activity in immersion and low activity in re-immersion), *H/L* (high activity in immersion and low activity in re-immersion), *L/H* (low activity in immersion and high activity in re-immersion), and *H/H* (high activity in immersion and high activity in re-immersion). These zones align with the optical observations in Figure 3.2c and Figure 3.4c.

The immersion/re-immersion behaviour distribution (Figure 3.5a) shows that majority of the particles (72.6%) are in the L/L zone. This includes almost all of the EDX-confirmed secondary particles (i.e., IMPs whose compositions were confirmed to be that of secondary particles through EDX) and some S- and θ-phase IMPs. Around 1.4% of the particles, mostly S-phase IMPs, were in the H/L zone. The spread in the immersion midALs of the IMPs in this zone indicates that stable inhibition can be achieved with varying degrees of Ce(III) precipitation. Around 3.2% of the IMPs, also predominantly S-phases, are in the H/H zone. There is also a

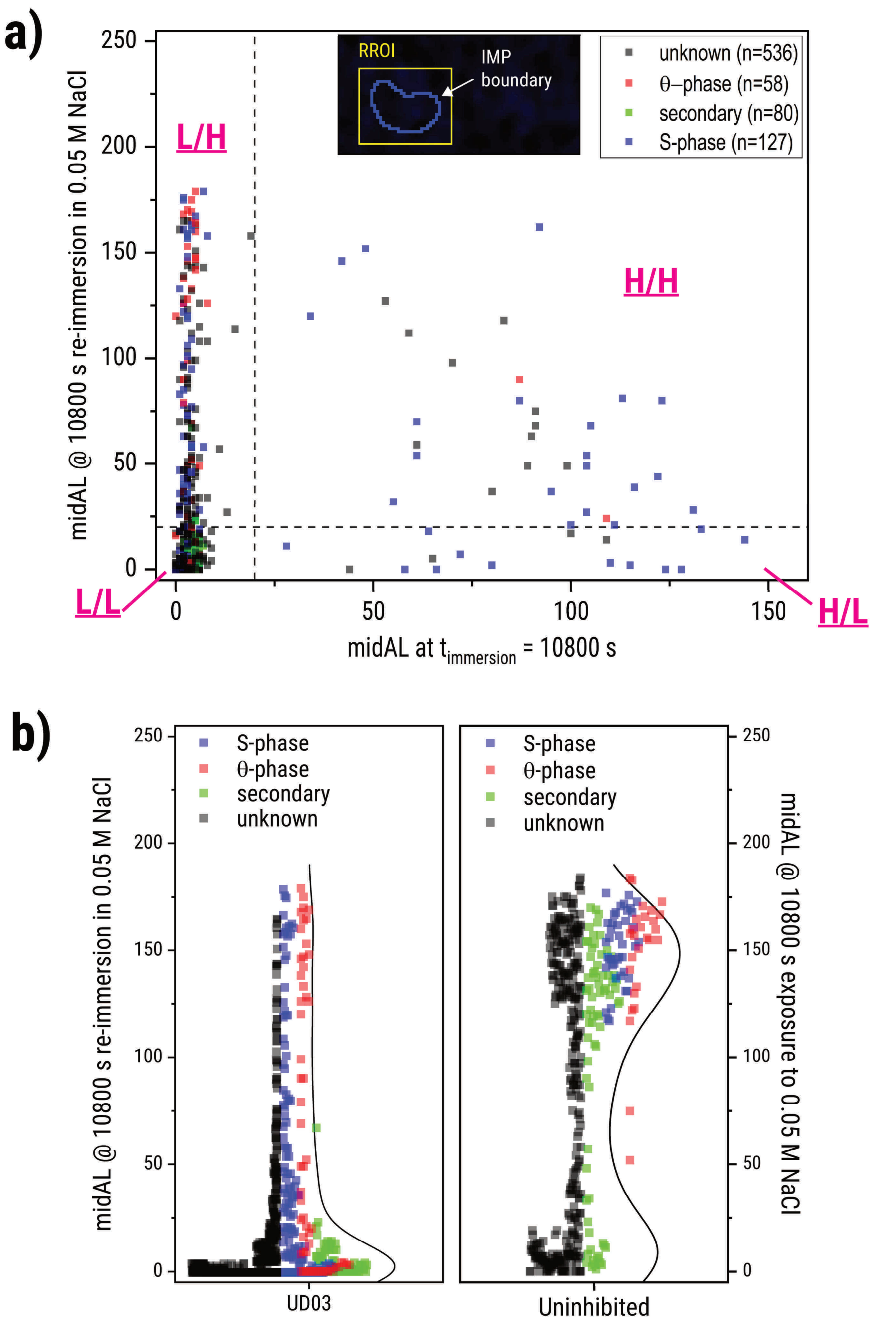

Figure 3.5. Analysis of the local changes during re-immersion of the UD03 sample in 0.05 M NaCl expressed in terms of **(a)** midAL during re-immersion correlated with the midAL during immersion in 0.05 M NaCl + 0.001 M Ce(III) (inset shows example of an RROI used to measure midAL), and **(b)** comparison of midALs of UD03 IMPs after 3h re-immersion in 0.05 M NaCl and midALs of uninhibited IMPs during a 3h exposure to the same electrolyte.

visible spread in the immersion midAL of the IMPs in this zone. A lower re-immersion midAL is observed though for particles with higher immersion midAL. The rest of the particles (~22.7%) are in the L/H zone. IMPs with EDX-confirmed compositions in this group were also S- and θ-phases. The particles in this zone exhibit visible spread in the re-immersion midAL values. Furthermore, the most active particles during re-immersion are in this zone.

Although the presence of IMPs in the H/H and L/H zones indicates inhibition failure, the initial exposure to Ce(III) still contributed to a lower frequency of active IMPs during re-immersion in 0.05 M NaCl relative to a system that is only exposed to NaCl. This is evident from comparing the midALs (Figure 3.5b) of UD03 IMPs after 3-hours of re-immersion in 0.05 M NaCl against those of the uninhibited IMPs after 3-hours of exposure to 0.05 M NaCl (i.e., without prior immersion in Ce(III)-containing electrolyte). The midAL distribution for the uninhibited IMPs shows two maxima, a low midAL maxima between 0 and 25, and a high midAL maxima between 125 and 175. The high midAL maxima is not observed among the UD03 IMPs during their re-immersion. Furthermore, the distribution also highlight a change in the IMP compositions comprising the low midAL maxima. In the uninhibited system, this low midAL maxima is dominated by EDX-confirmed secondary particles. However, in the re-immersed UD03 samples, S- and θ-phase IMPs are observed to contribute to this maxima. This is a clear indication that more S- and θ-phase exhibit reduced activity when initially exposed to the inhibitor. Altogether, the IMP midAL values for the re-immersion of UD03 and for the uninhibited immersion suggests that some of the inhibition is retained even when the inhibitor is not available in the solution anymore. Otherwise, the UD03 IMPs would have just behaved similar to the uninhibited IMPs. It is also interesting to note that secondary particles, which usually interact less with Ce(III) compared to S- and θ-phases [13], actually show the biggest difference in the number of highly active IMPs when comparing UD03 re-immersion and uninhibited conditions (Figure 3.5b). For the uninhibited IMPs, secondary particles also contribute to the high midAL maxima. However, during the re-immersion of UD03, almost all of the EDX-confirmed secondary particles are found on the low midAL maxima.

3.3.2. Immersion/re-immersion behaviour subtypes and proposed mechanisms

From the activity maps in Figure 3.4c and the immersion/re-immersion zones identified in Figure 3.5a, subtypes of the four general immersion/re-immersion behaviours (i.e., L/L, H/L, L/H, H/H) have been further identified particularly when the long-term re-immersion behaviour is considered. Examples of each subtype are presented in Figure 3.6 and potential mechanisms that explain each specific behaviour are as follows:

- **L/L (low activity in immersion and low activity in re-immersion):** Two subtypes of the L/L behaviour have been identified. The first involves minimal changes on the IMP surface and its surroundings even at prolonged re-immersion (L/L-A). The second involves IMPs with surfaces that remain clear despite extensive corrosion product deposition or matrix dissolution on its surroundings at prolonged re-immersion (L/L-B).

The L/L-A behaviour indicates that the surface is largely inactive. Figure 3.6a shows an example of an AlCuFeMn IMP that exhibits this behaviour. No signs of activity during immersion, and minimal changes during the 3h re-immersion were observed in the particle's RROI. The pixels on the IMP surface exhibited a slightly higher activity level than the adjacent matrix with further re-immersion (see Figure 3.6a - 6 h). Further increase of the pixel activity on the IMP surface was not observed with further re-immersion. The hazy purple patch observed at 20 h is due to corrosion product deposition from nearby sites. The activity propagation started from the bottom left corner of the map and moved towards the top right corner (Supporting Information 3.7.3). The propagating patch indiscriminately covered the IMP and its adjacent matrix which suggests a uniform lack of activity on the area. Such IMP inactivity is attributed to the IMP's low susceptibility to dealloying. During immersion, minimal dealloying leads to limited Ce(III) precipitation on the IMP surface and thus low activity [13,26]. During re-immersion, minimal dealloying also results to limited local corrosion observed as low activity on the IMP surface. This mechanism potentially accounts for the behaviour of certain subtypes of secondary particles (e.g., $Al_{20}Cu_2Mn_3$, $Al_{76}Cu_6Fe_7Mn_5Si_6$) that have been consistently reported to be less prone to dealloying [13,34].

Apart from stability because of IMP composition, L/L-A behaviour can also be attributed to non-exposure of the particle due to stable material layer covering the surface. This can account for the lack of changes in some of the conventionally active S- and θ-phases. Figure 3.6b shows an example of an S-phase IMP with this behaviour. Minimal activity was observed on the IMP's RROI during immersion which makes formation of a thick inhibiting layer less likely. The IMP was also minimally active during the first 3 hours of re-immersion and further re-immersion only lead to indiscriminate deposition of corrosion products (e.g., $Al(OH)_3$) from nearby particles resulting in a hazy purple patch. Several mechanisms could have generated the stable layer. It could be an oxide layer formed during exposure to the corrosive solution. SKPFM studies of AlCuMg particles by Lacroix et al. [35,36] showed that oxides can form on top of particles during exposure to corrosive electrolyte. It could also be an inhibiting layer formed from Ce(III) precipitation. In our earlier work, small amounts of Ce were detected on the surface of IMPs following immersion in conditions similar to UD03 [26].

The L/L-B behaviour also involves IMPs which exhibited minimal activity during immersion and during the first 3 hours of re-immersion. However, when surrounding matrix dissolution and corrosion product deposition became substantial with prolonged re-immersion, particles in this subtype exhibit IMP surfaces that remain relatively bright. Figure 3.6c shows an example of an S-phase particle (EDX spectra provided in Supporting Information 3.7.2) with this specific behaviour. The particle exhibited minimal activity during immersion despite its composition which suggests that a thin inhibiting layer is present. During re-immersion, visible activity developed at the top and right-most sections of the IMP surface between 600 and 3600 s of exposure to the saline environment. The activity on the surface remained relatively low (purple to violet in the colour scale) even at 3 h of re-immersion (see arrow in Figure 3.6c – 3 h). The sustained low activity suggests that some form of inhibiting layer breakdown occurred. The breakdown appears to be contained though as the IMP surface did not show extensive activation typical of dealloying particles (Figure 3.2d). Corrosion product deposition from nearby corroding sites led to a propagating active area on the surrounding matrix of the particle. The propagating area had low activity (i.e. purple in the colour scale) at 6 h. Extensive cooperative corrosion of neighbouring sites eventually lead to spreading matrix dissolution observed as high activity at 20 h (i.e., red-orange in the colour scale). The front of the propagating area which was moving towards the top right direction apparently avoided the S-phase IMP (see dashed line in Figure 3.6c – 20 h). The surface of the IMP is also partially covered by corrosion products, but the coverage appears to be less extensive as indicated by its lower activity levels (see arrow in Figure 3.6c – 20 h) compared to adjacent matrix at the top left and bottom right of the particle (i.e., points along the front of the propagating active area). Figure 3.6d shows a similarly intact surface of an AlCuFeMnSi particle surrounded by extensive matrix dissolution during re-immersion. The dissolution was also triggered by neighbouring active IMPs.

The bright IMP surfaces suggest that the IMPs are neither significantly dealloyed nor buried under corrosion products. An intact IMP indicates minimal dealloying while the absence of a corrosion product cover suggests that their surface pH (i.e., either very low or very high) does not support aluminium hydroxide deposition [37]. High pH-driven dissolution of aluminium hydroxide (i.e., $Al(OH)_3$ is converted to $Al(OH)_4^-$) is considered more likely as the intact IMP surface can facilitate cathodic reactions (i.e., oxygen reduction reaction) which generate hydroxide ions. Cathodic activity in the absence of substantial dealloying is within expected behaviour for Fe-rich secondary particles [13,34]. However, for S-phases, cathodic activity is typically accompanied by extensive dealloying. As such, the observation of low-level IMP activity that did not progress to full dealloying with signs of cathodic behaviour

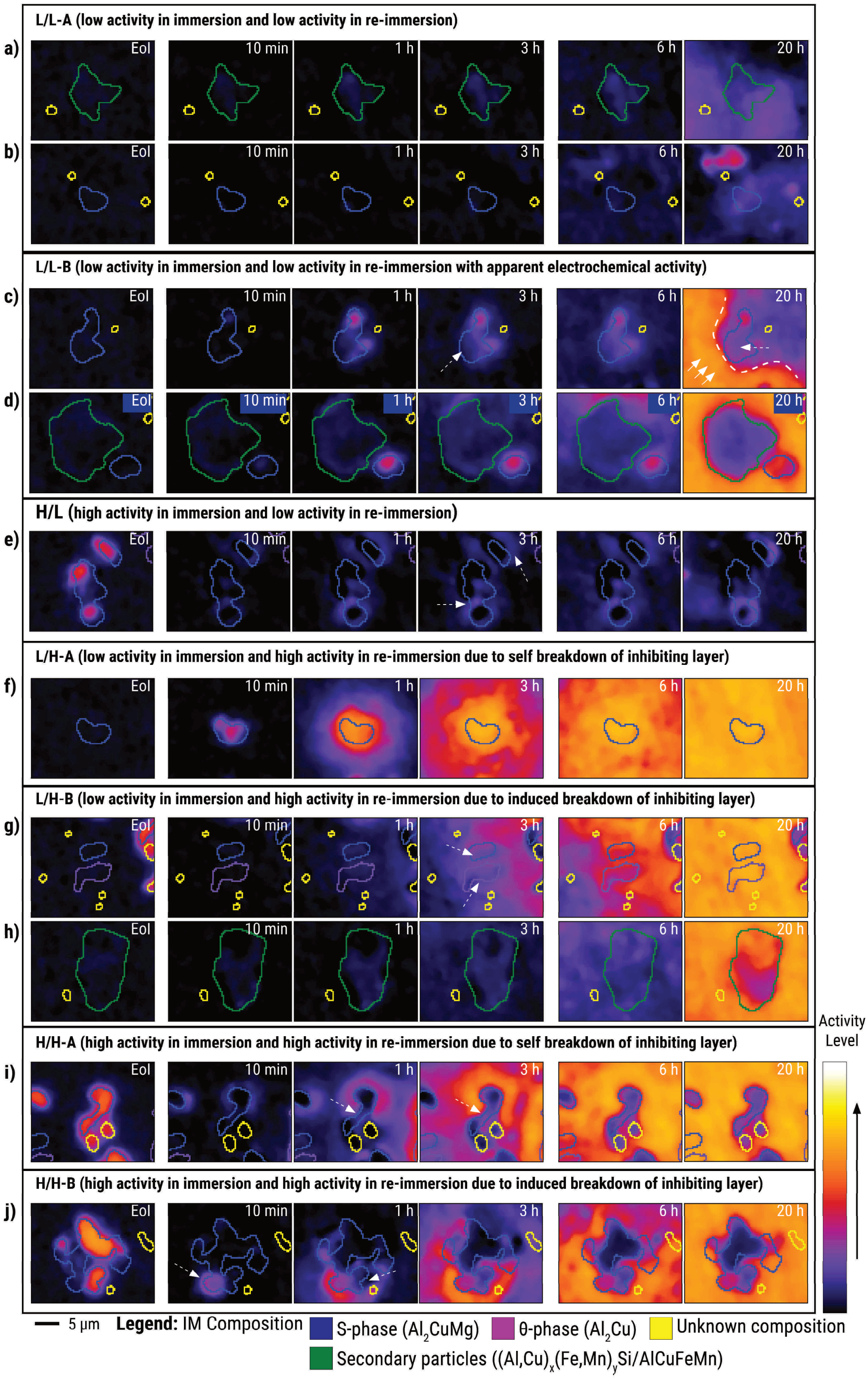

Figure 3.6. Examples of immersion/re-immersion behaviours subtypes: **(a, b)** low/low (L/L) behaviour, **(c, d)** L/L behaviour and apparent electrochemical activity, **(e)** high/low (H/L) behaviour, **(f)** low/high (L/H) behaviour, **(g, h)** L/H behaviour induced by nearby corroding sites, **(i)** high/high (H/H) behaviour, and **(j)** H/H behaviour induced by nearby corroding site. 'EoI' pertains to end of immersion in 0.05 M NaCl + 0.001 M Ce(III) for 3 hours.

may indicate the effect of the inhibiting layer. Previous works [3,13,26] have shown that slight dealloying can form a thin inhibiting layer which can isolate the underlying IMP during immersion. During re-immersion, small regions of the IMP surface not covered by the inhibiting layer could potentially enable cathodic reactions to proceed on the IMP surface. The presence of the inhibiting layer, nonetheless, prevents extensive dissolution of Al and Mg. Confirmation of the S-phase surface microstructure that leads to this behaviour is recommended for future works.

Depending on the aggressiveness of the corrosion of neighbouring sites, particles that initially showed L/L-A or L/L-B behaviour may eventually be activated and exhibit L/H behaviour (see L/H section). Additionally, since L/L-B behaviour is identified based on matrix dissolution and corrosion product build-up, some L/L-A sites situated away from major matrix damage might be undetected L/L-B sites. Nonetheless, based on the surface activity after about 20 hours of re-immersion, *at least* 23 of the 153 L/L particles with EDX-confirmed compositions (~14%) were classified as L/L-B (Supporting Information 3.7.4).

- **H/L (high activity in immersion and low activity in re-immersion):** As presented in Figure 3.4, IMPs with H/L behaviour exhibited high activity during immersion and low activity during re-immersion. Figure 3.6e shows S-phase particles with this behaviour. These are the same S-phase particles (s1 and s2) shown in Figure 3.4c. Both particles exhibited activity development on the adjacent matrix, around the precipitation sites from immersion. The activity slightly exceeded the threshold value of 20 in some places (see arrows in Figure 3.6e – 3 h). Nonetheless, the overall RROI activity remained low the during the 3 h re-immersion, and even with further re-immersion to 20 h.

  High activity during immersion is attributed to IMP dealloying which facilitated the formation of a thick Ce(III) inhibiting layer [26]. The formation of the layer is generally slow when the inhibitor is available from the start of exposure but prior partial dealloying can lead to faster precipitation [26]. This prior dealloying is only observed in a limited number of the sampled particles (~1.4%) and is likely due to partial corrosion introduced during the sample preparation step or atmospheric corrosion prior to exposure to the electrolyte. During re-immersion, the inhibiting layer slows down oxygen transport and Cu redistribution resulting to the low activity on the IMP surface and on the adjacent matrix. Changes around the adjacent matrix indicate trenching due to micro-galvanic coupling with the corroding IMP underneath the inhibiting layer. This suggests that there are defects (e.g., cracks, pores) in the inhibiting layer. The defects are not extensive though as the layer still provides considerable protection based on the slow growth of the trenches and their corresponding low-level activity.

- **L/H (low activity in immersion and high activity in re-immersion):** Two subtypes of the L/H behaviour were identified. The first subtype involved IMPs with low activity during immersion and exhibited self-breakdown of their inhibiting layers during re-immersion (L/H-A). The second subtype (L/H-B) also involved low immersion activity but had induced inhibiting layer breakdown due to activity of neighbouring particles. It is noted that processes that lead to low activity during immersion are expected to be similar to those seen for L/L behaviour – either the particle is inherently stable, or the particle had a stable thin layer that covered it and prevented further local corrosion.

  Figure 3.6f shows an S-phase (same as s6 in Figure 3.4c) that exhibited L/H-A behaviour. The particle activated within 10 mins of re-immersion but the activity remained concentrated on the IMP surface (Figure 3.6f – 10 min). This spread is slower than those of uninhibited IMPs (Figure 3.2d) and is consistent with loss of inhibition as opposed to absence of inhibition. Moreover, the activation time is also shorter than that of the L/L-B S-phase (Figure 3.6c). This behaviour is attributed to failure of the thin inhibiting layer that protected the material during immersion. The inhibiting layer's susceptibility is attributed either to limited coverage of the IMP surface or presence of defects (e.g., cracks, pores) [13]. Both scenarios lead to a portion of the IMP surface exposed to the corrosive re-immersion environment. Since the exposed area is smaller than that of an uninhibited particle, the rate of Mg or Al dissolution as well as the rate of oxygen reduction reaction are expected to be lower leading to the relatively slower IMP activation.

  It is noted that the L/H-A behaviour can also be explained by the breakdown of a passive layer (e.g., thin alloy layer or an alumina layer on top of the IMP surface) initially present on the IMP surface [35]. The passive layer can prevent IMP interaction with the corrosion inhibitor resulting to low activity during immersion. Breakdown of the passive layer during re-immersion can then lead to corrosion of the IMP and high re-immersion activity levels. Distinguishing an L/H-A scenario due to a passive layer from one due to a thin inhibiting layer requires non-destructive determination of the presence of the passive layer prior to immersion or re-immersion. Particles with such a substantial passive layer are expected to dealloy much later, if at all, in uninhibited conditions. Kinetic studies on the dealloying of S-phases in inhibitor-free NaCl solutions [26,33] showed that particles with delayed dealloying are not common. As such, attributing L/H-A behaviour to failure of thin inhibiting layers formed during immersion is considered more likely.

The L/H-B behaviour involves failure of a stable thin inhibiting layer due to induced activity from a neighbouring active sites. Figure 3.6g shows particles which are candidates for the L/H-B mechanism. These S- and θ-phase particles (EDX spectra provided in Supporting Information 3.7.2) had minimal activity during immersion and did not show signs of IMP activation within the first hour of re-immersion. At 3 hours of re-immersion, corrosion product from nearby corroding particles partially covered the IMP surfaces. However, some IMP areas remained free from corrosion products (see arrows in Figure 3.6g – 3 h) similar to the particles in the L/L-B mechanism (Figure 3.6c). With prolonged re-immersion, matrix dissolution also became more substantial leading to the activity intensification observed on the surrounding matrix (Figure 3.6g – 20 h). The surfaces of the S- and θ-phase particles still exhibited lower activity but eventually reached the same level as the adjacent matrix at around 20 h. This equalization of activity is attributed to dealloying of the IMP surfaces which suggests complete loss of inhibition of the particles. Induced activity of the particles can be due to redistributed Cu particles weakening the inhibiting layer through nano-galvanic coupling [38,39] or matrix dissolution leading to exposure of buried portions of the protected IMP [40].

This mechanism can also be extended to induced failure of inherently stable IMPs. The secondary particle in Figure 3.6h (EDX spectra provided in Supporting Information 3.7.2) is a potential candidate for this. The lower section of the particle maintained its low activity but the upper section eventually showed signs of high activity attributed to dealloying at around 20 h of re-immersion. The induced activation of inherently stable particles is very limited as it was only observed with this IMP.

Since L/H-B behaviour requires influence of neighbouring sites, the fraction of particles with confirmed L/H-B behaviour during the first 3 hours of re-immersion is only around 9 of the 87 L/H particles with EDX-confirmed compositions (~10%) (Supporting Information 3.7.4). All of these L/H-B events occurred in areas with high IMP density. Thus, majority of the L/H behaviour documented is still from the self breakdown of inhibition. It is noted though that the L/H-B fraction is expected to increase if the analysis duration for re-immersion is also increased.

- **H/H (high activity in immersion and high activity in re-immersion):** Processes that lead to high activity during immersion are similar to those in IMPs with H/L behaviour (i.e., formation of a thick inhibiting layer). As with the L/H behaviours, two subtypes of the H/H behaviour have been identified: particles which undergo self-breakdown of the inhibiting layer (H/H-A), or particles whose breakdown is induced by neighbouring activity (H/H-B).

  Figure 3.6i shows an S-phase particle (EDX spectra provided in Supporting Information 3.7.2) that shows activity evolution consistent with H/H-A. The IMP showed activity consistent with the formation of a thick inhibiting layer during immersion (Figure 3.6i - EoI). During re-immersion, the IMP exhibited activity development between 10 minutes and 1 hour of re-immersion on the matrix adjacent to the top section of the particle which suggests trenching. Between 1 and 3 hours, visible activity increase on the middle section of the IMP surface (see arrow in Figure 3.6i – 1 h, 3 h) suggests destabilization of the inhibiting layer on that area. Matrix dissolution and corrosion product deposition around the IMP also intensified based on the orange-level activity on the surrounding matrix. With prolonged re-immersion, activity increase on the IMP surface attributed to further corrosion product build-up is observed (pale purple at 20 h). The H/H-A behaviour is potentially due to inhibiting layer defects that exposed the underlying IMP to the corrosive solution. The corrosion of the IMP triggered the dissolution of the adjacent matrix and led to trenching around the IMP. This is observed as circumferential activity of the IMP.

  Figure 3.6j shows a composite particle with partial thick deposition on some sites after immersion which exhibited H/H-B behaviour. Local corrosion of the unprotected sites at the bottom left section (see arrow in Figure 3.6j – 10 min) led to potential destabilization of the inhibiting layer on the bottom right section of the particle. At 1 h re-immersion, activity attributed to inhibiting layer dissolution developed around the bottom right section (see arrow in Figure 3.6j – 1 h). Further re-immersion lead to visible trenching around the composite particle and subsequent corrosion product deposition on the surrounding matrix. As with the L/H-B behaviour, the H/H-B behaviour is likely due to the influence of nearby corroding particles. These IMPs can induce dissolution of the aluminium matrix which can then expose buried sections of the protected IMP and trigger local corrosion propagation [40]. Around 2 of the 17 H/H particles with EDX-confirmed compositions (~12%) exhibit H/H-B behaviour (Supporting Information 3.7.4).

Given the observed variability in behaviour amongst IMPs, a corrosion strategy based on the IMPs most susceptible to inhibition-loss can be a viable approach. Arguably, the IMPs which exhibit L/L and H/L behaviour (~74% of sampled IMPs) do not pose considerable risk as their protection is maintained during re-immersion. A good number of these particles are also likely to be inherently stable so leaving them to behave as they do seems to be acceptable. The particles which exhibit high activity during re-immersion need more attention as they can induce local corrosion of protected neighbours which can then lead to cooperative corrosion with prolonged re-immersion. Between H/H and L/H behaviour, the L/H IMPs have a higher incidence rate (~22.7% of sampled IMPs) and exhibited more extensive activity during re-immersion. Taking these observations together, using a strategy that reduces the number of IMPs showing low interaction with the inhibitor can potentially lead to more stable protection during re-immersion. In the case of Ce(III), this can be achieved by increasing the degree of Ce(III) precipitation on the IMP surface.

3.3.3. Effect of inhibiting layer formation conditions on inhibiting layer stability during re-immersion

Exposure to Ce-containing inhibiting solutions has been reported to increase corrosion protection with longer immersion time due to thicker inhibiting layers formed and larger surface areas covered [13,41–43]. The increase in protection supports existing preference for sustained inhibitor release in active corrosion protection systems. Time-dependent growth of the inhibiting layer is attributed to permeation of corrosive species which can lead to gradual dealloying-driven precipitation of Ce [13]. This layer growth is observed when the global activity maps of AA2024 samples exposed to 0.05 M NaCl + 0.001 M Ce(III) for 3 h (UD03), 24 h (UD24), and 72 h (UD72) are compared (Figure 3.7). Movie 3.3 and Movie 3.4 show time-lapses of the surface changes between for UD24 and UD72, respectively, during their re-immersion in 0.05 M NaCl. As can be seen in the activity maps at end of immersion (EoI), UD24 (Figure 3.7b) and UD72 (Figure 3.7c) both appear to have higher number of active sites with higher activity (orange in the colour scale) compared to UD03 (Figure 3.7a). Note that the edge activity in the UD72 EoI map is due to microscope focus changes during imaging, not precipitation events. Comparison of the end-of-immersion activity maps of the test replicates show comparable degrees of precipitation and number of active sites for UD03 (Figure 3.7a, Figure 3.8a) and UD72 (Figure 3.7c, Figure 3.8c). The UD24 replicates (Figure 3.7b, Figure 3.8b) on the other hand have a visible difference in the number of active sites. This is potentially due to the variation in IMP make-up of the two tests [44]. It also suggests that a consistent increase in inhibiting layer growth is not yet achieved with a 24-hour immersion duration. Nonetheless, re-immersion behaviour of the replicates in Figure 3.8a-c (Supporting Information 3.7.5) are consistent with those shown in Figure 3.7. It is noted that the activity that develops during re-immersion is consistent with local corrosion, as confirmed by post-re-immersion secondary electron images in Figure 3.8d and Figure 3.8e.

A closer examination of the end-of-immersion changes at the IMP level for the UD24 and UD72 samples (Figure 3.7b,c - EoI) shows that the inhibiting layers are generally similar in size and activity (orange to yellow-orange in the colour scale). The same degree of activity is observed for the sites in the replicate tests (Figure 3.8a-c). Notably, the UD72 sample in Figure 3.7 has two high-activity sites extending beyond the usual IMP boundary (white arrows in Figure 3.7c EoI map) and with much higher activity (yellow in the colour scale). These sites indicate extensive precipitation and corrosion product deposition from local corrosion of the underlying particle. However, this is uncommon, as most sites in the UD72 sample show less extensive activity. The low occurrence of such high-activity sites in UD72, despite an immersion duration three times longer than UD24, suggests that inhibiting layer growth is slow even at prolonged exposure.

Although UD24 and UD72 apparently have comparable degrees of local Ce precipitation at the end of re-immersion, their subsequent local activity during re-immersion are considerably different. During re-immersion of the UD24 sample, signs of IMP activation within the first 600 s of exposure to the inhibitor-free electrolyte similar to the UD03 sample were observed. The activity includes a low/high (see yellow arrow in Figure 3.7b - 600 s) and several high/high (see dashed white arrows in Figure 3.7b - 600 s) behaviour. Despite their early onset, the increase in activity level of these sites and the activation of their surrounding matrix were slower than their UD03 counterparts. After 3600s of re-immersion, more sites with ring-like activity (i.e., rings with low-activity centres) consistent with high/high behaviour were observed on the surface of the UD24 sample (see dashed white arrows in Figure 3.7b - 3600 s). Absence of nearby activity suggests that these sites fall under the H/H-A category. As with the other UD24 active sites during re-immersion, their activity level increase and activity spread to surrounding areas were gradual and not as extensive as the L/H IMPs in UD03. Low/high behaviour is also seen at several sites at 3600 s of re-immersion (see yellow arrows in Figure 3.7b - 3600 s). These sites had low activity during immersion but are near areas showings signs of Ce(III) deposition. The corrosion of these sites is triggered by the inhibiting layer failure on the adjacent areas between 600 and 3600 s (Movie 3.3). This makes the sites candidates for L/H-B behaviour. Substantial dealloying and trenching is observed around these sites leading to development of high activity (see yellow arrows in Figure 3.7b - 7200 s). The activation of

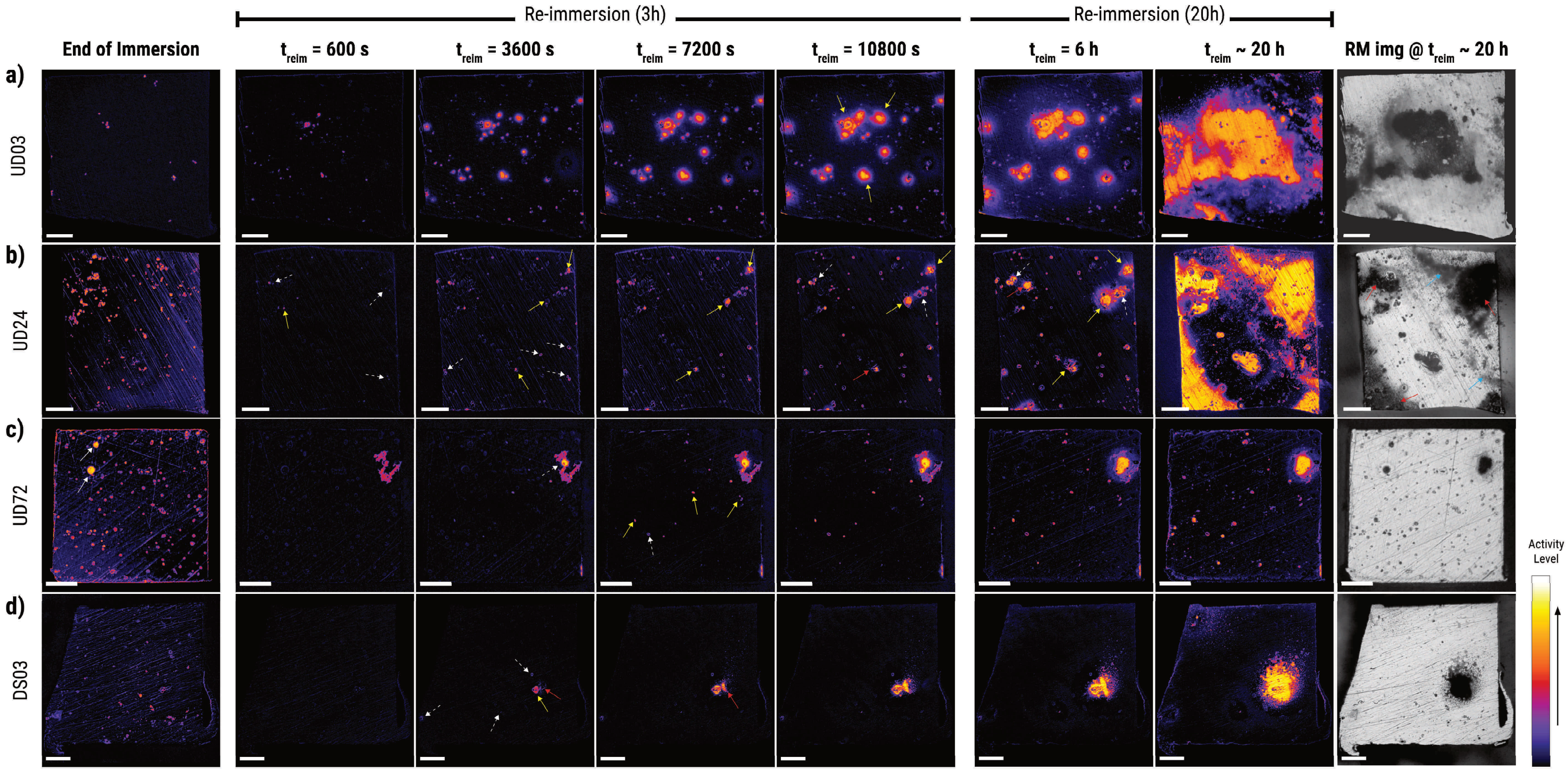

Figure 3.7. Global activity maps of AA2024 samples immersed in 0.05 M NaCl + 0.001 M Ce(III) under different conditions: **(a)** 3 hours, **(b)** 24 hours, **(c)** 72 hours, and **(d)** with a 30-second inhibitor supply delay, immersed for 3 hours. The first column shows the sample state at the end of the initial immersion. The second to fifth columns display changes during re-immersion in 0.05 M NaCl for 3 hours, while the last three columns show changes during extended re-immersion. White scale bars represent 100 µm.

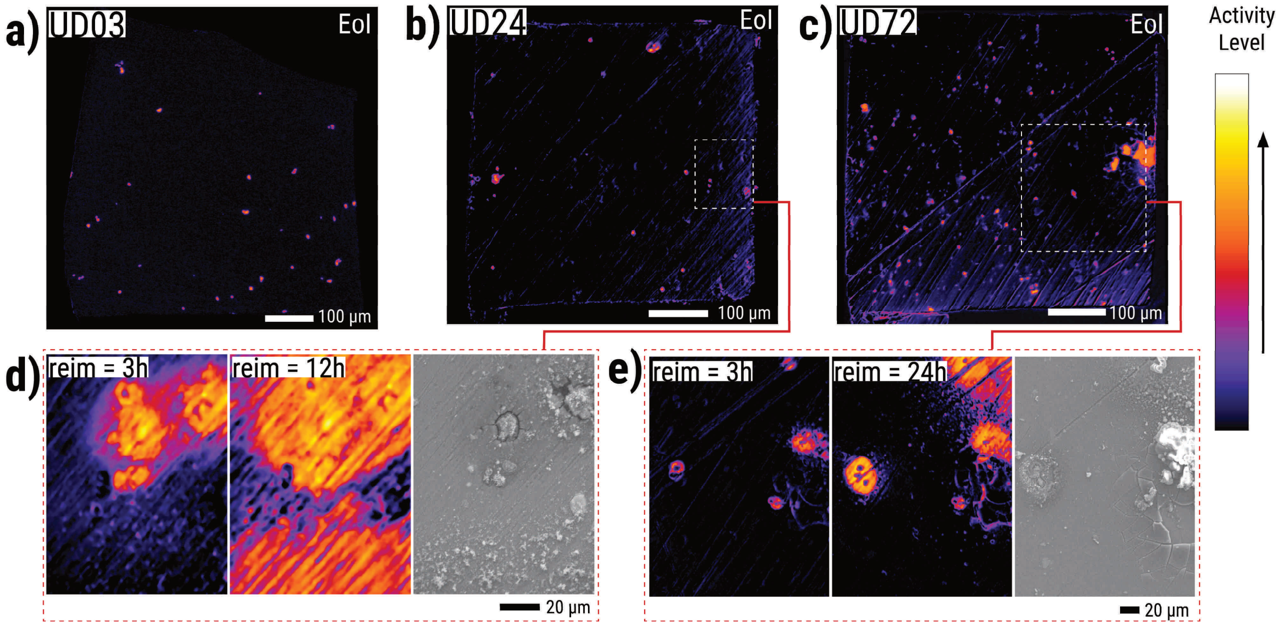

Figure 3.8. Activity maps at the end of immersion (EoI) for replicate samples exposed to 0.05 M NaCl with 0.001 M Ce(III) for **(a)** 3 hours, **(b)** 24 hours, and **(c)** 72 hours. Ce(III) was present from the start of the immersion. Panels **(d)** and **(e)** show activity maps and corresponding secondary electron (SE) images after re-immersion of the 24-hour (UD24) and 72-hour (UD72) samples, respectively. The UD24 sample was re-immersed for 12 h and the UD72 sample for 24 h before the SE images were taken.

these L/H sites shows that even with 24 hours of immersion in the inhibited solution, some particles can still present with minimal interaction with the inhibitor which makes them prone to corrosion during re-immersion. At 10800 s of re-immersion, the L/H site on the upper right corner of the sample (see yellow arrows in Figure 3.7b - 10800 s) appear to be inducing activation of nearby particles based on the visible increase in the active area from 7200 s. Meanwhile, the L/H site near the centre of the sample appear to trigger what appears to be intergranular corrosion (see red arrow in Figure 3.7b - 10800 s). Figure 3.9 provides a close up the activity progression of this site. On the other hand, the H/H sites maintain gradual activity level increase and activity spread to the surrounding areas. This is evident when the corrosion around clusters of active sites with H/H behaviour (see dashed white arrows in Figure 3.7b - 10800 s) is compared with that of active site clusters from UD03. H/H active site clusters in UD24 had limited activity spread while active site clusters in UD03 exhibited considerable development of high activity on a large portion of the matrix around the IMPs (see yellow arrows in Figure 3.7a - 10800 s). This indicates that although the thick inhibiting layers fail, they can still slow down local corrosion progression likely by limiting redistribution of Cu particles from the IMP surface. This slow progression is further observed in the status of the H/H cluster after 6 hours of re-immersion (see dashed white arrow in Figure 3.7b – 6 h). However, their relative stability is undermined by the propagating activity coming from the

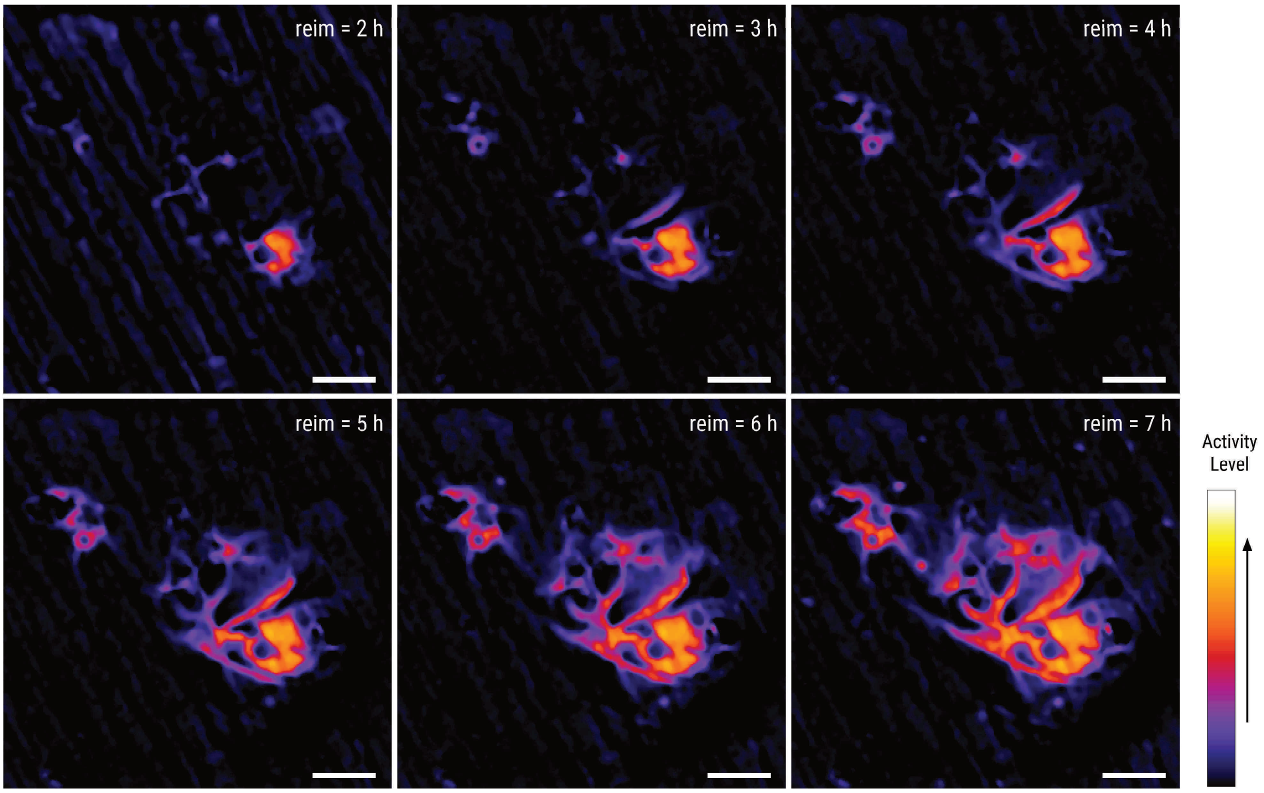

Figure 3.9. Activity progression on the suspected intergranular corrosion site in Figure 3.7b. The local corrosion is characterized by gradual growth of activity along filaments instead of the typical radial spread from an intermetallic particle. The scale bar is 20 μm.

L/H sites (see yellow arrows in Figure 3.7b – 6 h). A new L/H site near the upper left corner (see red arrow in Figure 3.7b – 6 h) also developed somewhere between 3 and 6 hours of re-immersion. Extended re-immersion to 20 h does show inhibition failure leading to significant matrix involvement (i.e., large areas of yellow-level activity) comparable to that of UD03. Corresponding raw reflected light microscopy images show that these areas have extensive matrix dissolution (see red arrows in Figure 3.7b – RM image at 20 h) and are covered by corrosion product deposits (see cyan arrows in Figure 3.7b – RM image at 20 h). Majority of the matrix dissolution and corrosion product generation can be traced to cooperative corrosion from the areas with L/H sites (Movie 3.3). L/H sites in the UD24 replicate also drove local corrosion development during re-immersion (Supporting Information 3.7.5).

Majority of the IMPs in the UD72 sample exhibited low activity (dark purple-coloured sites) during the first 600 s of re-immersion. A rapid matrix dissolution event was observed on the upper right corner of the sample surface (Movie 3.4). The visual appearance of the dissolution event is comparable to streaking corrosion reported in AA7075-T6 [45,46] which suggests that it is some form of a surface layer attack [47,48]. It is noted though that this event was only observed in this test and thus requires further validation. Nonetheless, the dissolution event appeared to have affected IMPs in that region and induced their inhibition failure. This resulted to the appearance of a highly active site (yellow-coloured site) in the area at around 1 hour of re-immersion (see dashed arrow in Figure 3.7c - 3600 s). Gradual spread of activity from this site to surrounding matrix is observed for the rest of the re-immersion. Initiation of inhibition loss in other sites also became visible at around 2 hours of re-immersion. These inhibition loss sites include several with low/high (see yellow arrows in Figure 3.7c - 7200 s) and one with high/high (see dashed white arrow in Figure 3.7c - 7200 s) behaviour. The activity increase and activity spread to the adjacent matrix of these sites were gradual based on their limited size increase at three hours of re-immersion (Figure 3.7c - 10800 s). Additionally, at three hours of re-immersion, the number of the active sites in UD72 is less than those in UD03 or UD24. Kosari et al. [13] reported that at prolonged exposure to the Ce(III)-containing environment, gradual dealloying of IMPs eventually leaves a Cu-rich remnant. This remnant can facilitate cathodic reactions with sufficient oxygen supply and subsequently lead to substantial local changes. Absence of such changes suggests that the inhibiting layer in UD72 is less permeable than those formed in UD24 or UD03. Stability of these inhibiting layers lead to low matrix involvement even at 20 hours of re-immersion (Figure 3.7c – 20 h). Local re-immersion activity in the UD72 replicate is also limited to a few H/H sites (Figure 3.8d) and areas near the edge of the sample (Supporting Information 3.7.5).

Similar to prolonged/sustained inhibitor supply, fast inhibitor release in active corrosion protection systems is expected to minimize local corrosion. This justifies the existing approach for inhibitor testing focused on immediate exposure to the inhibiting solution. Such exposure protocol is particularly relevant for AA2024 which contains IMPs that dealloy within the first minute of exposure to NaCl [33]. Sufficient mitigation of local corrosion is still possible when the inhibitor is not immediately available to the surface. This was shown in our previous work on delayed inhibitor supply for AA2024 where an inhibitor supply delay of less than or equal to one minute led to surface changes less extensive than uninhibited systems [26]. Delayed inhibitor supply approximates slower inhibitor release rates from coatings which in itself is a viable strategy to extend inhibitor availability (and prolong exposure time). Figure 3.7d shows global activity maps for AA2024 exposed to Ce(III) with delayed supply (DS03). Specifically, the introduction of Ce(III) was delayed by 30 seconds to allow limited IMP dealloying progression. Movie 3.5 shows a time-lapse of the surface changes during the re-immersion of DS03 in 0.05 M NaCl. The DS03 EoI activity map (Figure 3.7d – End of Immersion) shows that when Ce(III) is delayed, more active sites are observed at the end of the 3 h immersion time compared to UD03 (Figure 3.7a – End of Immersion). The activity levels of the sites range from purple to orange in the activity colour scale.

During re-immersion, visible loss of inhibition is not observed until around 3600 s when several high/high (dashed white arrows in Figure 3.7d – 3600 s) and low/high (yellow arrow in Figure 3.7d – 3600 s) sites are seen around the centre and left edge of the sample. The high/high sites exhibited minimal activity level increase and spread. Meanwhile, the low/high site, which appears to be a composite IMP based on the connected IMP outlines seen on the EoI in Figure 3.7d, exhibited visible changes on the IMP surfaces consistent with dealloying. The activity eventually spread to the adjacent matrix (Figure 3.7d – 7200 s) consistent with trenching. The activation also affected a right section of the composite IMP (red arrow in Figure 3.7d – 3600 s) which showed low level activity during immersion. The dealloying and trenching of this IMP led to more matrix dissolution and considerable corrosion product deposition with further re-immersion (red arrow at Figure 3.7d – 7200 s).

The midALs of active sites measured from different immersion conditions – UD03, UD24, UD72, and DS03 – were used for quantitative comparison of stability during re-immersion (Figure 3.10). Active sites are sites that exhibited activity levels above the threshold of 20 either at the end of immersion or at 3 hours of re-immersion. We focused on these sites instead of sampling all IMPs on the surface because they directly indicate local corrosion as discussed in Section 3.2. During immersion, they show Ce(III) precipitation triggered by dealloying. During re-immersion, they point to areas with dealloying, trenching, and possible corrosion product buildup, all of which signal a loss of inhibition. Additionally, we used the midAL of active sites at the 10800 s of re-immersion rather than overall surface changes because it directly shows loss of inhibition. In contrast, surface-wide metrics can exaggerate the impact of a few active sites especially when their cooperative corrosion leads to significant corrosion product deposition. Figure 3.10 shows that midAL distributions for UD24 (median midAL = 5) and UD72 (median midAL = 1) have significantly lower medians compared to UD03 (median midAL = 55.5). This is attributed to the increased frequency of active sites displaying H/L behaviour which was also seen in the activity maps during the first three hours of re-immersion. Meanwhile, the decreasing trend of mean midAL values (UD03 = 72.0, UD24 = 37.8, UD72 = 6.9) with immersion duration proves that longer exposure to the corrosion inhibitor not only improves inhibition stability when the inhibitor is present but also when the inhibitor is not available anymore. The trend is attributed to the reduction in frequency of inhibition loss events during re-immersion (i.e., L/H and H/H active sites). Meanwhile, comparison of the median midAL of UD03 and DS03 (median midAL = 2) shows higher H/L frequency with delayed supply (green points). The mean midAL of the DS03 active sites (mean = 14.9) also indicates less extensive inhibition loss events during re-immersion compared to UD03 despite their similar immersion durations. This suggests that delayed inhibitor supply is more beneficial for re-immersion stability compared to immediate availability of the inhibitor in the corrosive media. As shown in our previous work [26], delayed inhibitor supply allows limited dealloying of the IMP surface which increases its capacity to precipitate Ce. Apart from the increase in Ce precipitation capacity, the initial exposure to the corrosive environment also allows removal of passive layers which prevent IMPs from interacting sufficiently with the inhibitor during immersion. While these passive layers offer some degree of protection, their breakdown during re-immersion can lead to exposure of the underlying IMP and uncontrolled local corrosion. The findings related to delayed inhibitor supply offer insight potentially applicable in the design of active corrosion protection systems. Since delayed inhibitor supply approximates slow release, the results also suggest that fine-tuning the initial release rates may be a more efficient strategy for long-term active corrosion protection than simply increasing inhibitor storage capacity of corrosion protection systems. It is also noted that the release rate is more controllable than the exposure times to the inhibiting solution, which is highly-dependent on environmental conditions.

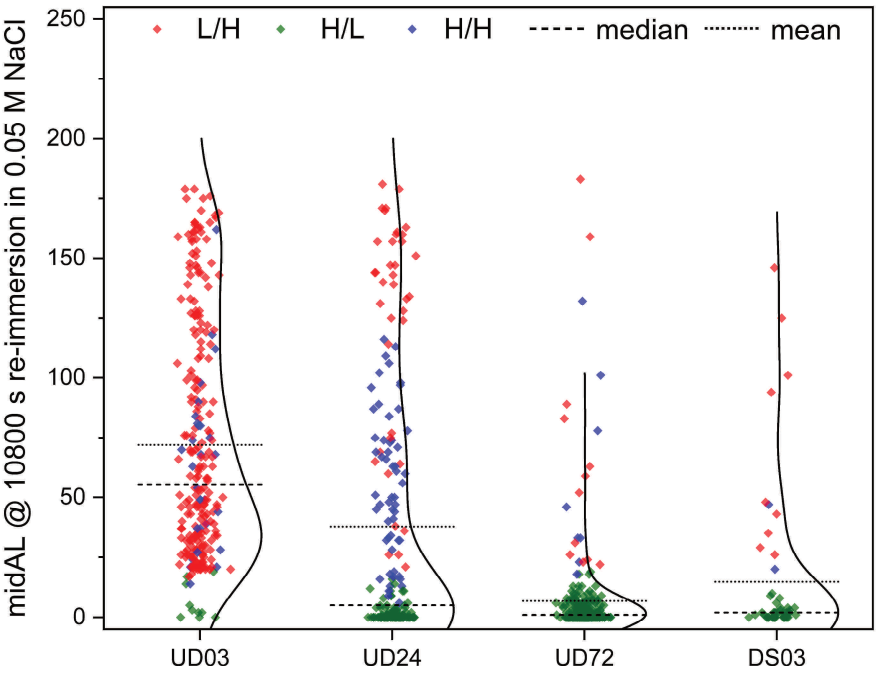

Figure 3.10. Comparison of midAL after 3 hours of re-immersion for active sites identified during initial immersion under different conditions: varying durations (UD03, UD24, UD72) and a 30-second inhibitor supply delay (DS03). Active sites are those where midAL exceeded 20 during either immersion or re-immersion.

3.4. Conclusion

The loss of inhibition at the level of individual IMPs in AA2024 during re-immersion in an inhibitor-free electrolyte shows significant variability. In general, their behaviour can be grouped based on whether they show low or high activity during the initial immersion (with inhibitor) and during re-immersion (without inhibitor). This behaviour results from a complex interplay of factors, including IMP composition, spatial distribution, and the extent of Ce(III) precipitation on their surfaces. Because these factors interact in a complex manner, the resulting immersion/re-immersion activity patterns (e.g., low/low, low/high, high/low, high/high) appear stochastic, making reliable prediction difficult. This highlights the importance of studying a large number of IMPs to capture the range of possible local corrosion behaviours. Using this analysis approach on our system (i.e., 3 h immersion in 0.05 M NaCl + 0.001 M Ce(III) followed by re-immersion in 0.05 M NaCl) revealed that the inhibiting layer formed during immersion influenced how the surface changes during re-immersion. It also introduced site-specific behaviour that would likely be missed by a global or a highly local means of analysis. The analysis also showed that most active sites during re-immersion have low activity during immersion (i.e., low degree of cerium precipitation). As such, increasing Ce(III) precipitation on the IMP surface appears to be a viable strategy for improving re-immersion stability.

Evaluation of the impact of immersion duration on re-immersion stability showed that longer exposure (e.g., up to 72 h) is indeed beneficial for minimizing loss of inhibition. Similarly, comparison of re-immersion stability for delayed (i.e., 30 s delay) and undelayed inhibitor supply for the same immersion duration (i.e. 3 h) revealed that a slight delay also enhances re-immersion performance. In both cases, the improvement is attributed to increased Ce(III) precipitation. It is noted though that these findings are specific to Ce(III)-NaCl system. Further studies are needed to assess whether similar improvements occur with other inhibitor and electrolyte combinations as well as different concentration levels. Overall, the results underscore the potential advantages of designing active corrosion protection systems that promote stronger inhibitor interaction, within limits that do not compromise system performance, to achieve better re-immersion stability.

3.5. References

[1] F.F. Chen, I. Cole, A.E. Hughes, A.M. Glenn, E. Sapper, J. Osborne, Microstructure characterisation and reconstruction of intermetallic particles, *Mater. Corros.* 65 (2014) 664–669. doi:10.1002/maco.201307345.

[2] A.E. Hughes, R. Parvizi, M. Forsyth, Microstructure and corrosion of AA2024, *Corros. Rev.* 33 (2015) 1–30. doi:10.1515/corrrev-2014-0039.

[3] L. Paussa, F. Andreatta, D. De Felicis, E. Bemporad, L. Fedrizzi, Investigation of AA2024-T3 surfaces modified by cerium compounds: A localized approach, *Corros. Sci.* 78 (2014) 215–222. doi:10.1016/j.corsci.2013.10.001.

[4] C. Li, X. Guo, G.S. Frankel, Corrosion inhibition of AA2024-T3 by a coating containing dual-pH sensitive, corrosion inhibitor loaded microspheres, *Corros. Sci.* 192 (2021) 109835. doi:10.1016/j.corsci.2021.109835.

[5] D. Snihirova, S.V. Lamaka, M.M. Cardoso, J.A.D. Condeço, H.E.C.S. Ferreira, M.F. Montemor, pH-sensitive polymeric particles with increased inhibitor-loading capacity as smart additives for corrosion protective coatings for AA2024, *Electrochim. Acta* 145 (2014) 123–131. doi:10.1016/j.electacta.2014.09.009.

[6] D. Snihirova, L. Liphardt, G. Grundmeier, M.F. Montemor, Electrochemical study of the corrosion inhibition ability of “smart” coatings applied on AA2024, *J. Solid State Electrochem.* 17 (2013) 2183–2192. doi:10.1007/s10008-013-2078-3.

[7] G. Williams, H.N. McMurray, Inhibition of filiform corrosion on organic-coated AA2024-T3 by smart-release cation and anion-exchange pigments, *Electrochim. Acta* 69 (2012) 287–294. doi:10.1016/j.electacta.2012.03.002.

[8] P.J. Denissen, S.J. Garcia, Cerium-loaded algae exoskeletons for active corrosion protection of coated AA2024-T3, *Corros. Sci.* 128 (2017) 164–175. doi:10.1016/j.corsci.2017.09.019.

[9] R. Oltra, F. Peltier, Influence of mass transport on the competition between corrosion and passivation by inhibitor release after coating breakdown, *Prog. Org. Coat.* 92 (2016) 44–53. doi:10.1016/j.porgcoat.2015.11.024.

[10] E. Javierre, S.J. Garcia, J.M.C. Mol, F.J. Vermolen, C. Vuik, S. Van Der Zwaag, Tailoring the release of encapsulated corrosion inhibitors from damaged coatings: Controlled release kinetics by overlapping diffusion fronts, *Prog. Org. Coat.* 75 (2012) 20–27. doi:10.1016/j.porgcoat.2012.03.002.

[11] S.G.R. Emad, S. Morsch, T. Hashimoto, Y. Liu, S.R. Gibbon, S.B. Lyon, X. Zhou, Leaching from coatings pigmented with strontium aluminium polyphosphate inhibitor pigment—evidence for a cluster-percolation model, *Prog. Org. Coat.* 137 (2019) 105340. doi:10.1016/j.porgcoat. 2019.105340.

[12] J. Zhao, A. Santoso, S.J. Garcia, Small concentrations of NaCl help building stable inhibiting layers from 2,5-dimercapto-1,3,4-thiadiazole (DMTD) on AA2024-T3, *Corros. Sci.* 225 (2023) 111562. doi:10.1016/j.corsci.2023.111562.

[13] A. Kosari, M. Ahmadi, F. Tichelaar, P. Visser, Y. Gonzalez-Garcia, H. Zandbergen, H. Terryn, J.M.C. Mol, Editors' Choice—Dealloying-Driven Cerium Precipitation on Intermetallic Particles in Aerospace Aluminium Alloys, *J. Electrochem. Soc.* 168 (2021) 041505. doi:10.1149/1945-7111/abf50d.

[14] K.A. Yasakau, M.L. Zheludkevich, S.V. Lamaka, M.G.S. Ferreira, Mechanism of corrosion inhibition of AA2024 by rare-earth compounds, *J. Phys. Chem. B* 110 (2006) 5515–5528. doi:10.1021/jp0560664.

[15] B.R.W. Hinton, Corrosion inhibition with rare earth metal salts, *J. Alloys Compd.* 180 (1992) 15–25. doi:10.1016/0925-8388(92)90359-h.

[16] G. Williams, A.J. Coleman, H.N. McMurray, Inhibition of aluminium alloy AA2024-T3 pitting corrosion by copper complexing compounds, *Electrochim. Acta* 55 (2010) 5947–5958. doi:10.1016/j.electacta.2010.05.049.

[17] P.J. Denissen, V. Shkirskiy, P. Volovitch, S.J. Garcia, Corrosion inhibition at scribed locations in coated AA2024-T3 by cerium- and DMTD-loaded natural silica microparticles under continuous immersion and wet/dry cyclic exposure, *ACS Appl. Mater. Interfaces* 12 (2020) 23417–23431. doi:10.1021/acsami.0c03368.

[18] F. Maia, J. Tedim, A.D. Lisenkov, A.N. Salak, M.L. Zheludkevich, M.G.S. Ferreira, Silica nanocontainers for active corrosion protection, *Nanoscale* 4 (2012) 1287–1298. doi:10.1039/c2nr11536k.

[19] S.V. Lamaka, M.L. Zheludkevich, K.A. Yasakau, M.F. Montemor, M.G.S. Ferreira, High effective organic corrosion inhibitors for 2024 aluminium alloy, *Electrochim. Acta* 52 (2007) 7231–7247. doi:10.1016/j.electacta.2007.05.058.

[20] D. Snihirova, S.V. Lamaka, P. Taheri, J.M.C. Mol, M.F. Montemor, Comparison of the synergistic effects of inhibitor mixtures tailored for enhanced corrosion protection of bare and coated AA2024-T3, *Surf. Coat. Technol.* 303 (2016) 342–351. doi:10.1016/j.surfcoat.2015.10.075.

[21] T.G. Harvey, S.G. Hardin, A.E. Hughes, T.H. Muster, P.A. White, T.A. Markley, P.A. Corrigan, J. Mardel, S.J. Garcia, J.M.C. Mol, A.M. Glenn, The effect of inhibitor structure on the corrosion of AA2024 and AA7075, *Corros. Sci.* 53 (2011) 2184–2190. doi:10.1016/j.corsci.2011.02.040.

[22] C. Özkan, L. Sahlmann, C. Feiler, M. Zheludkevich, S. Lamaka, P. Sewlikar, A. Kooijman, P. Taheri, A. Mol, Laying the experimental foundation for corrosion inhibitor discovery through machine learning, *NPJ Mater. Degrad.* 8 (2024) 21. doi:10.1038/s41529-024-00435-z.

[23] A.M. Homborg, M. Olgiati, P.J. Denissen, S.J. Garcia, An integral non-intrusive electrochemical and in-situ optical technique for the study of the effectiveness of corrosion inhibition, *Electrochim. Acta* 403 (2022) 139619. doi:10.1016/j.electacta.2021.139619.

[24] P. Visser, H. Terryn, J.M.C. Mol, On the importance of irreversibility of corrosion inhibitors for active coating protection of AA2024-T3, *Corros. Sci.* 140 (2018) 272–285. doi:10.1016/j.corsci.2018.05.037.

[25] Z. Li, A. Homborg, Y. Gonzalez-Garcia, A. Kosari, P. Visser, A. Mol, Evaluation of the formation and protectiveness of a lithium-based conversion layer using electrochemical noise, *Electrochim. Acta* 426 (2022) 140733. doi:10.1016/j.electacta.2022.140733.

[26] M. Mopon, A. Mol, S.J. Garcia, Effect of delayed inhibitor supply on AA2024-T3 intermetallic activity: A local in situ analysis with reflected microscopy, *Corros. Sci.* 230 (2024) 111910. doi:10.1016/j.corsci.2024.111910.

[27] R. Parvizi, A.E. Hughes, M. Forsyth, M.Y. Tan, Probing localised corrosion inhibition of AA2024-T3 by integrating electrode array, SVET, SECM, and SEM-EDS techniques, *Metals* 13 (2023) 1703. doi:10.3390/met13101703.

[28] Z. Lai, D. Li, S. Cai, M. Liu, F. Huang, G. Zhang, X. Wu, Y. Jin, Small-area techniques for micro- and nanoelectrochemical characterization: A review, *Anal. Chem.* 95 (2023) 357–373. doi:10.1021/acs.analchem.2c04551.

[29] W. Chang, H. Qian, Z. Li, A. Mol, D. Zhang, Application and prospect of localized electrochemical techniques for microbiologically influenced corrosion: A review, *Corros. Sci.* 236 (2024) 112246. doi:10.1016/j.corsci.2024.112246.

[30] N. Jadhav, V.J. Gelling, Review—The use of localized electrochemical techniques for corrosion studies, *J. Electrochem. Soc.* 166 (2019) C3461–C3476. doi:10.1149/2.0541911jes.

[31] L.B. Coelho, M. Taryba, M. Alves, X. Noirfalise, M.F. Montemor, M.G. Olivier, The corrosion inhibition mechanisms of Ce(III) ions and triethanolamine on graphite—AA2024-T3 galvanic couples revealed by localised electrochemical techniques, *Corros. Sci.* 150 (2019) 207–217. doi:10.1016/j.corsci.2019.02.007.

[32] T. Hu, H. Shi, D. Hou, T. Wei, S. Fan, F. Liu, E.H. Han, A localized approach to study corrosion inhibition of intermetallic phases of AA2024-T3 by cerium malate, *Appl. Surf. Sci.* 467–468 (2019) 1011–1032. doi:10.1016/j.apsusc.2018.10.243.

[33] M. Olgiati, P.J. Denissen, S.J. Garcia, When all intermetallics dealloy in AA2024-T3: quantifying early stage intermetallic corrosion kinetics under immersion, *Corros. Sci.* 192 (2021) 109836. doi:10.1016/j.corsci.2021.109836.

[34] J. Li, N. Birbilis, R.G. Buchheit, Electrochemical assessment of interfacial characteristics of intermetallic phases present in aluminium alloy 2024-T3, *Corros. Sci.* 101 (2015) 155–164. doi:10.1016/j.corsci.2015.09.012.

[35] L. Lacroix, L. Ressier, C. Blanc, G. Mankowski, Combination of AFM, SKPFM, and SIMS to study the corrosion behavior of S-phase particles in AA2024-T351, *J. Electrochem. Soc.* 155 (2008) C131. doi:10.1149/1.2833315.

[36] L. Lacroix, C. Blanc, L. Ressier, Localized corrosion mechanisms of 2024 aluminum alloy: Atomic force microscopy and Kelvin force microscopy contribution, *ECS Meet. Abstr.* MA2009-02 (2009) 1735. doi:10.1149/ma2009-02/16/1735.

[37] K.H. Gayer, L.C. Thompson, O.T. Zajicek, The solubility of aluminum hydroxide in acid and basic media at 25°C, *Can. J. Chem.* 36 (1958) 1268–1271. doi:10.1139/v58-184.

[38] A. Kosari, F. Tichelaar, P. Visser, H. Zandbergen, H. Terryn, J.M.C. Mol, Dealloying-driven local corrosion by intermetallic constituent particles and dispersoids in aerospace aluminium alloys, *Corros. Sci.* 177 (2020) 108947. doi:10.1016/j.corsci.2020.108947.

[39] A. Kosari, H. Zandbergen, F. Tichelaar, P. Visser, P. Taheri, H. Terryn, J.M.C. Mol, In-situ nanoscopic observations of dealloying-driven local corrosion from surface initiation to in-depth propagation, *Corros. Sci.* 177 (2020) 108912. doi:10.1016/j.corsci.2020.108912.

[40] X. Zhou, C. Luo, T. Hashimoto, A.E. Hughes, G.E. Thompson, Study of localized corrosion in AA2024 aluminium alloy using electron tomography, *Corros. Sci.* 58 (2012) 299–306. doi:10.1016/j.corsci.2012.02.001.

[41] A.E. Hughes, T.A. Markley, S.J. Garcia, J.M.C. Mol, Comparative study of protection of AA2024-T3 exposed to rare earth salts solutions, *Corros. Eng. Sci. Technol.* 49 (2014) 674–687. doi:10.1179/1743278214y.0000000172.

[42] T. Hu, H. Shi, T. Wei, F. Liu, S. Fan, E.H. Han, Cerium tartrate as a corrosion inhibitor for AA2024-T3, *Corros. Sci.* 95 (2015) 152–161. doi:10.1016/j.corsci.2015.03.010.

[43] S.J. Garcia, T.A. Markley, J.M.C. Mol, A.E. Hughes, Unravelling the corrosion inhibition mechanisms of bi-functional inhibitors by EIS and SEM–EDS, *Corros. Sci.* 69 (2013) 346–358. doi:10.1016/j.corsci.2012.12.018.

[44] A.E. Hughes, A.M. Glenn, N. Wilson, A. Moffatt, A.J. Morton, R.G. Buchheit, A consistent description of intermetallic particle composition: An analysis of ten batches of AA2024-T3, *Surf. Interface Anal.* 45 (2013) 1558–1563. doi:10.1002/sia.5207.

[45] R.S. Huang, C.J. Lin, H.S. Isaacs, Measuring streaking rates of an Al–Zn alloy using a difference imaging technique, *Corros. Sci.* 48 (2006) 1867–1873. doi:10.1016/j.corsci.2006.05.039.

[46] R.S. Huang, C.J. Lin, H.S. Isaacs, A difference-imaging technique used to study streaking corrosion of aluminum alloys AA7075 and AA8006 in chloride solution, *Electrochem. Solid-State Lett.* 9 (2006) B11–B14. doi:10.1149/1.2140503.

[47] Z. Zhao, G.S. Frankel, On the first breakdown in AA7075-T6, *Corros. Sci.* 49 (2007) 3064–3088. doi:10.1016/j.corsci.2007.02.001.

[48] S.S. Wang, F. Yang, G.S. Frankel, Effect of altered surface layer on localized corrosion of aluminum alloy 2024, *J. Electrochem. Soc.* 164 (2017) C317–C323. doi:10.1149/2.1541706jes.

3.6. Movies

The following movies can be accessed through the published article via the DOI link of the published article corresponding to this chapter (doi: 10.1016/j.corsci.2025.113146) or through the accompanying QR codes.

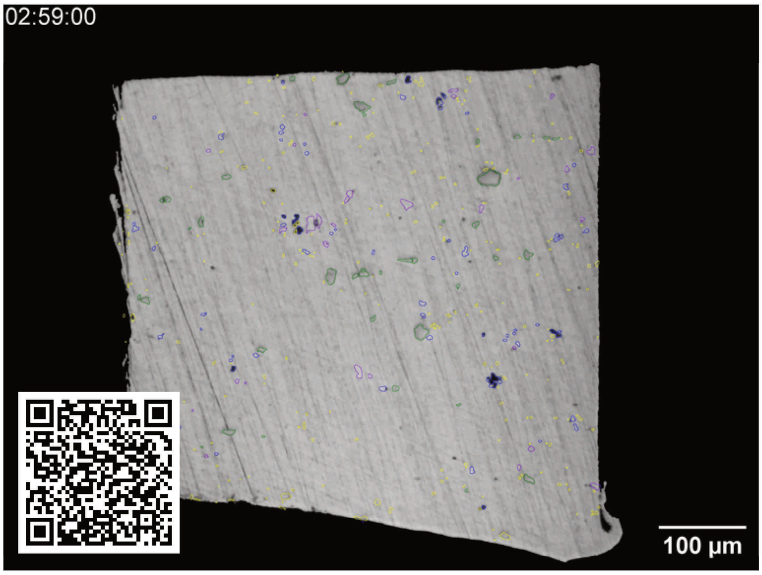

Movie 3.1. Reflected light microscopy timelapse showing the evolution of surface changes on AA2024-T3 sample during immersion in 0.05 M NaCl + 0.001 M Ce(III) for 3 hours. The coloured outlines indicate intermetallic particle composition based on pre-immersion SEM (blue: S-phase, purple: θ-phase, green: secondary particle, yellow: unknown).

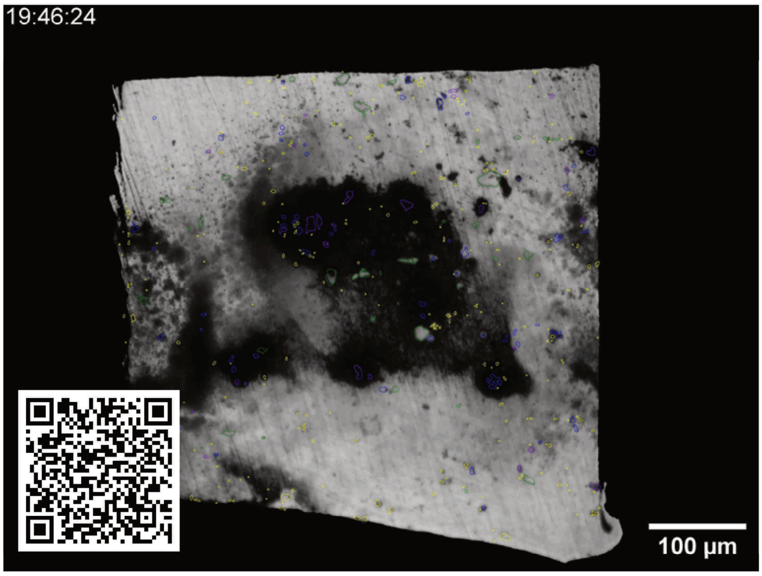

Movie 3.2. Reflected light microscopy timelapse show the evolution of surface changes on AA2024-T3 sample during re-immersion in 0.05 M NaCl. This sample was previously immersed in 0.05 M NaCl + 0.001 M Ce(III) for 3 hours. The coloured outlines indicate intermetallic particle composition based on pre-immersion SEM (blue: S-phase, purple: θ-phase, green: secondary particle, yellow: unknown).

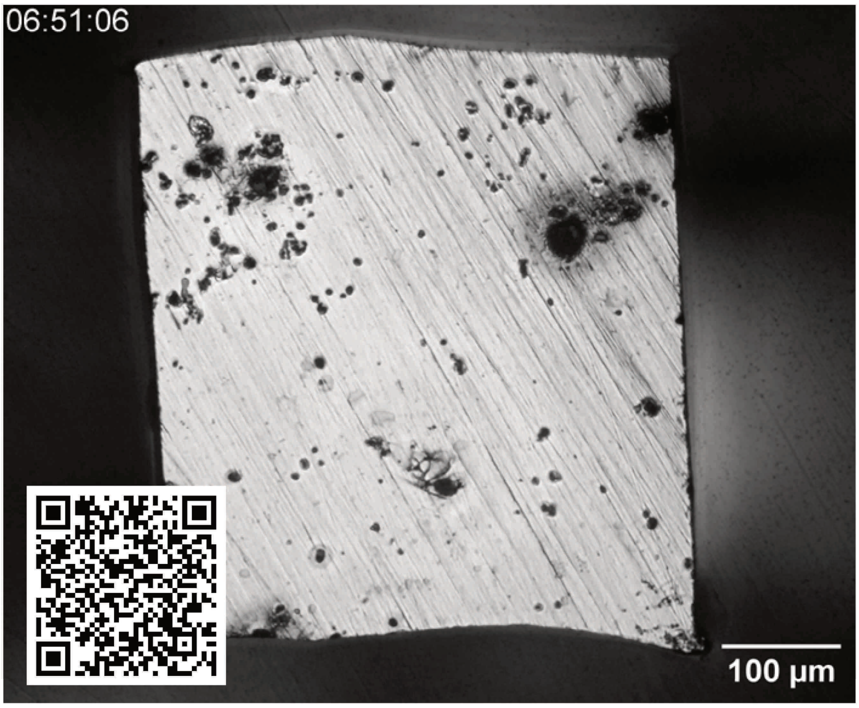

Movie 3.3. Reflected light microscopy timelapse show the evolution of surface changes on AA2024-T3 sample during re-immersion in 0.05 M NaCl. This sample was previously immersed in 0.05 M NaCl + 0.001 M Ce(III) for 24 hours.

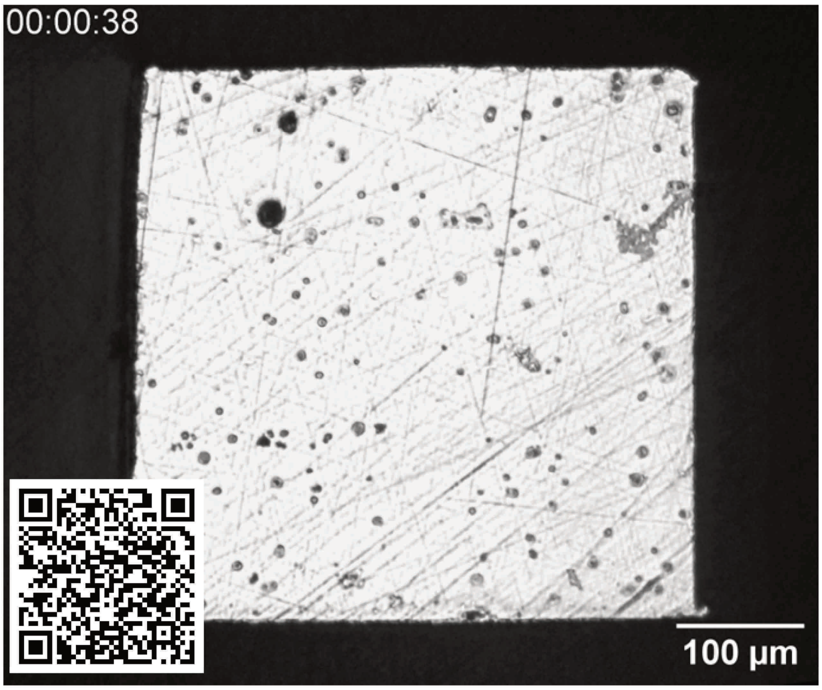

Movie 3.4. Reflected light microscopy timelapse show the evolution of surface changes on AA2024-T3 sample during re-immersion in 0.05 M NaCl. This sample was previously immersed in 0.05 M NaCl + 0.001 M Ce(III) for 72 hours.

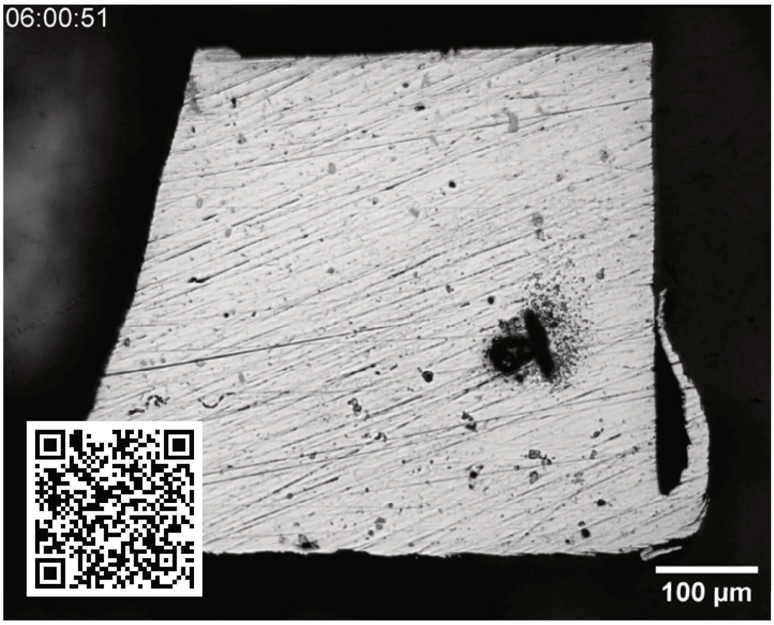

Movie 3.5. Reflected light microscopy timelapse show the evolution of surface changes on AA2024-T3 sample during re-immersion in 0.05 M NaCl. This sample was previously immersed in 0.05 M NaCl + 0.001 M Ce(III) for 3 hours with an inhibitor supply delay of 30 seconds.

3.7. Supporting Information

3.7.1. Potential atmospheric corrosion prior to immersion or re-immersion

Reflected light microscopy images of the sample surfaces during the brief period of exposure to air prior to the immersion tests show signs of condensation on the surface. The condensation forms discrete films and droplets on the surface leading to the appearance of black spots (see red arrows in Figure S3.1). The black spots disappear as soon as the electrolyte is injected into the electrochemical cell. It is noted that the dark areas that remain at the start of immersion are sample defects such as corroded intermetallics or holes.

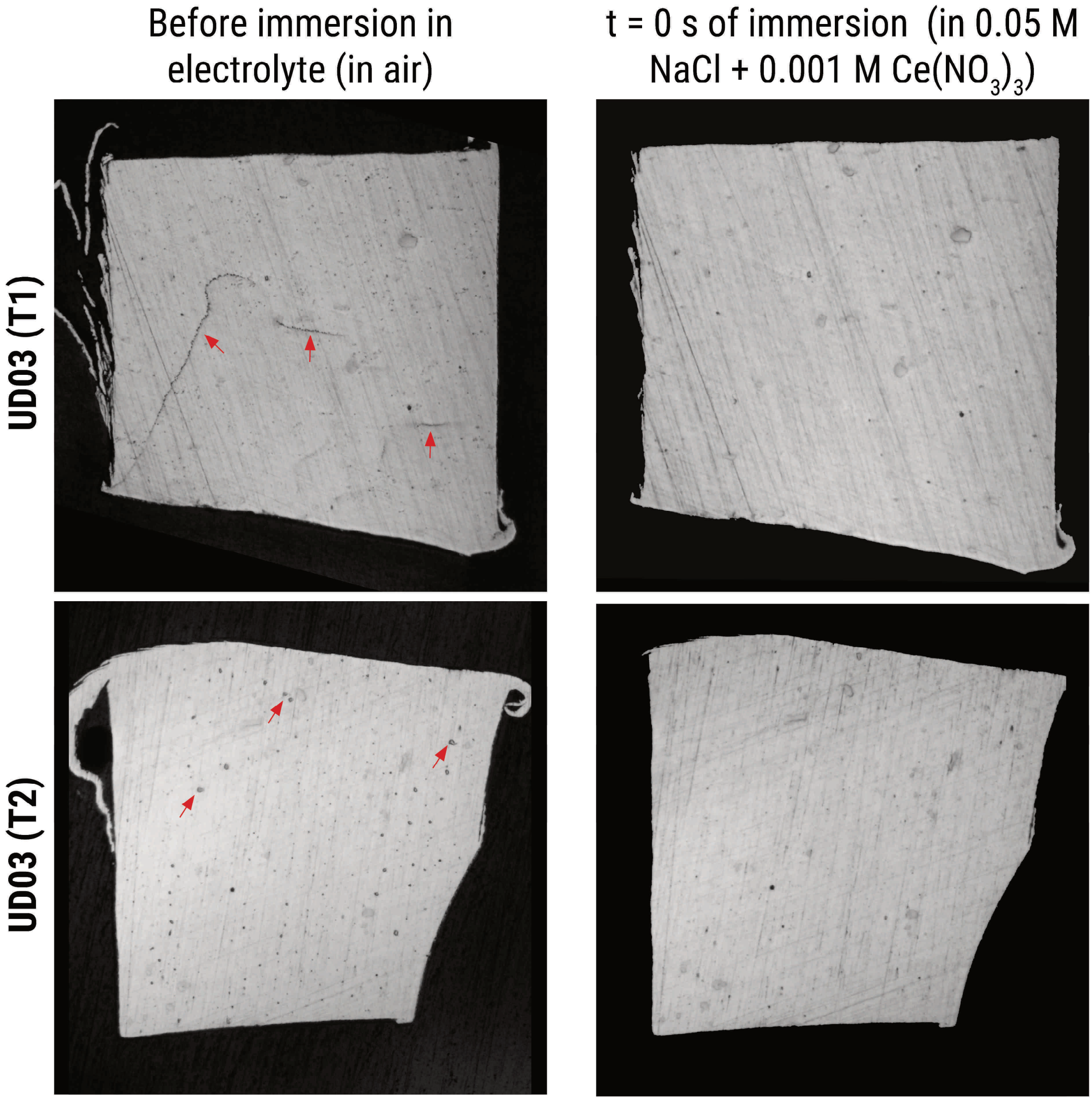

Figure S3.1. Reflected light microscopy images of the surface before immersion and on the start of immersion. Red arrows indicate microdroplets that formed on the surface when the samples were exposed to air prior to immersion.

3.7.2. EDX spectra of selected intermetallic particles

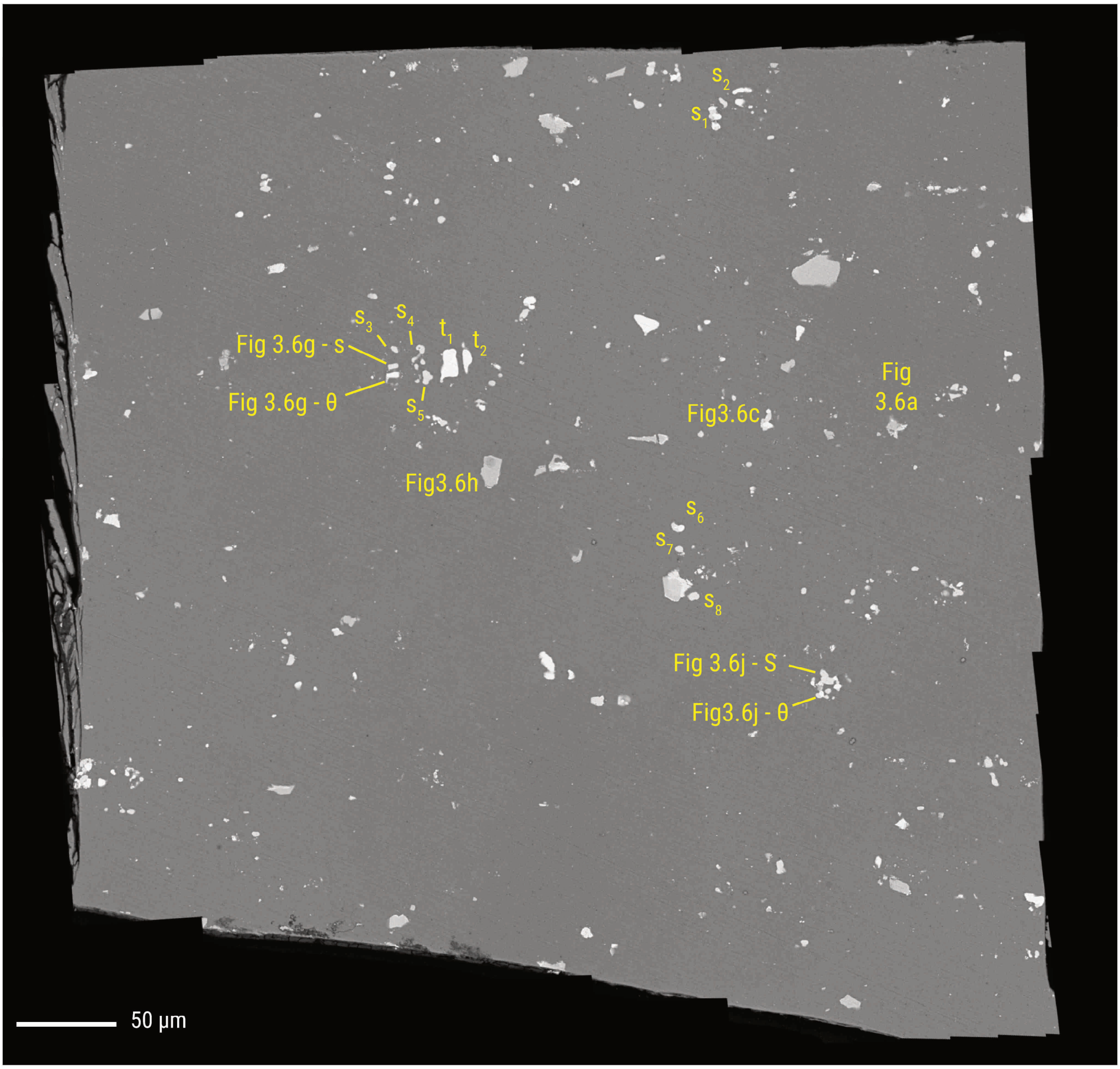

Figure S3.2. Pre-immersion secondary electron SEM image of an AA2024-T3 sample. The intermetallic particles of interest are labelled. The overall image is stitched from individual SEM images.

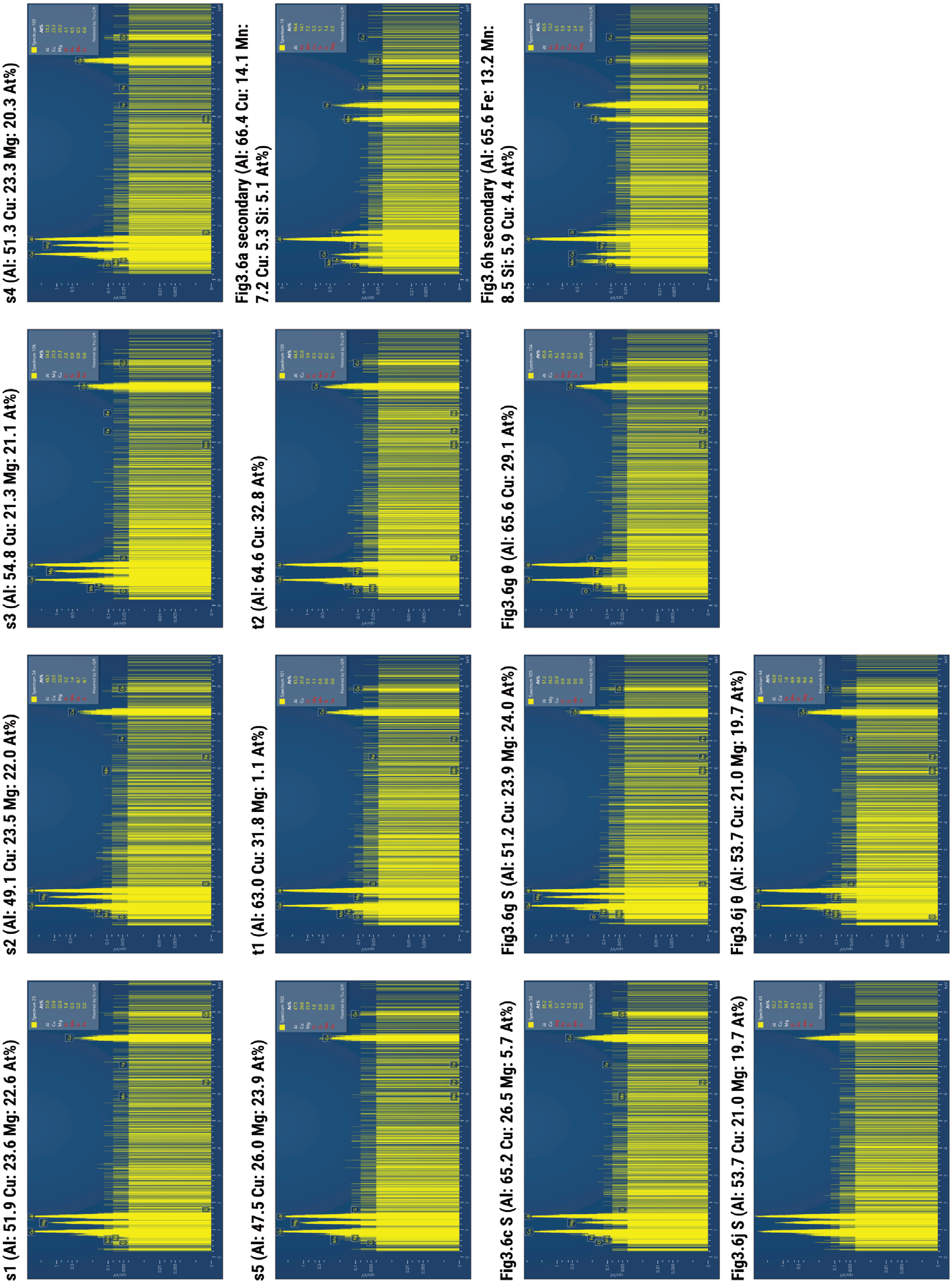

s1 (Al: 51.9 Cu: 23.6 Mg: 22.6 At%)

s2 (Al: 49.1 Cu: 23.5 Mg: 22.0 At%)

s3 (Al: 54.8 Cu: 21.3 Mg: 21.1 At%)

s4 (Al: 51.3 Cu: 23.3 Mg: 20.3 At%)

s5 (Al: 47.5 Cu: 26.0 Mg: 23.9 At%)

t1 (Al: 63.0 Cu: 31.8 Mg: 1.1 At%)

t2 (Al: 64.6 Cu: 32.8 At%)

Fig3.6a secondary (Al: 66.4 Cu: 14.1 Mn: 7.2 Cu: 5.3 Si: 5.1 At%)

Fig3.6c S (Al: 65.2 Cu: 26.5 Mg: 5.7 At%)

Fig3.6g S (Al: 51.2 Cu: 23.9 Mg: 24.0 At%)

Fig3.6g θ (Al: 65.6 Cu: 29.1 At%)

Fig3.6h secondary (Al: 65.6 Fe: 13.2 Mn: 8.5 Si: 5.9 Cu: 4.4 At%)

Fig3.6j S (Al: 53.7 Cu: 21.0 Mg: 19.7 At%)

Fig3.6j θ (Al: 53.7 Cu: 21.0 Mg: 19.7 At%)

Figure S3.3. EDX spectra of marked locations in the pre-immersion SEM image of the AA2024-T3 sample. The compositions specified correspond to the major components of the point analysed.

3.7.3. Local activity evolution of selected IMPs

3.7.3.1. t1 and t2

Figure S3.4 shows the development of activity on the θ-phase particles t1 and t2. The reflected light microscopy images during immersion shows that there is a dark spot between the two particles. No substantial change was observed on the spot or on the surface of the two θ-phase particles during immersion. This is mainly attributed to the effect of the corrosion inhibitor present in the system. During re-immersion in an inhibitor-free corrosive environment, the loss of inhibition is apparent based on the development of activity on the surface of t1 and t2. This activity is associated with intermetallic particle dealloying. Interestingly, the activity on the surface of t1 and t2 appear to increase fastest near the dark spot in between the two particles. Pre-immersion SEM (Figure S3.2) shows that the dark spot has similar appearance (i.e., colour) as the bulk matrix. This suggests that the spot is most likely a surface defect (e.g., hole) and not a component with different composition. The development of activity from the dark spot suggests that defects might influence IMP activation during re-immersion.

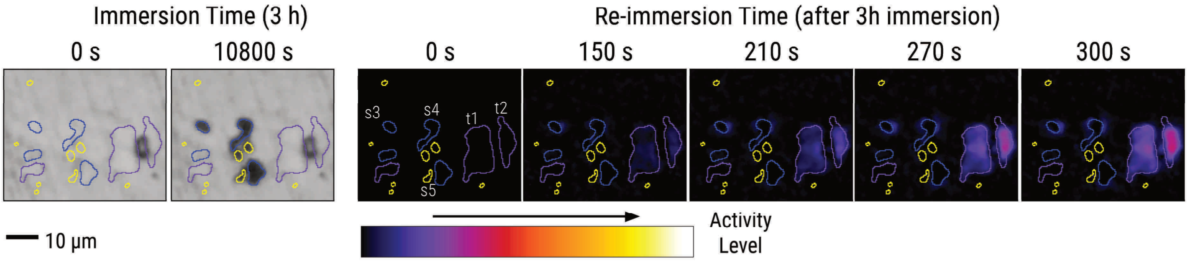

Figure S3.4. Development of activity around t1 and t2 particles shown in Figure 3.4c. The particles were initially exposed to 0.05 M NaCl + 0.001 M Ce(III) for 3 hours and then re-immersed in 0.05 M NaCl.

3.7.3.2. Secondary particle in Figure 3.6a

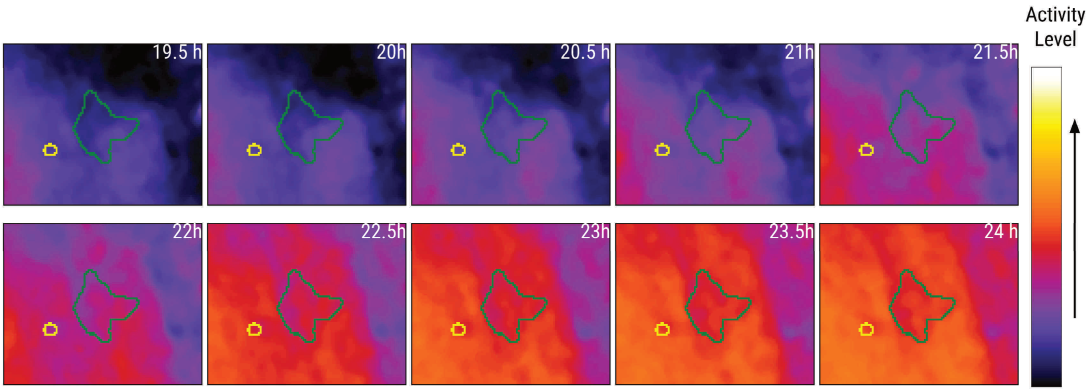

Figure S3.5. Propagation of corrosion product deposition around the particle shown in Figure 3.6a. At 19.5 hours, it can be observed that the highest activity in the region is at the lower left corner of the frame. With further re-immersion, the high activity propagated towards the top right direction.

3.7.4. Identification of immersion/re-immersion behaviour subtypes

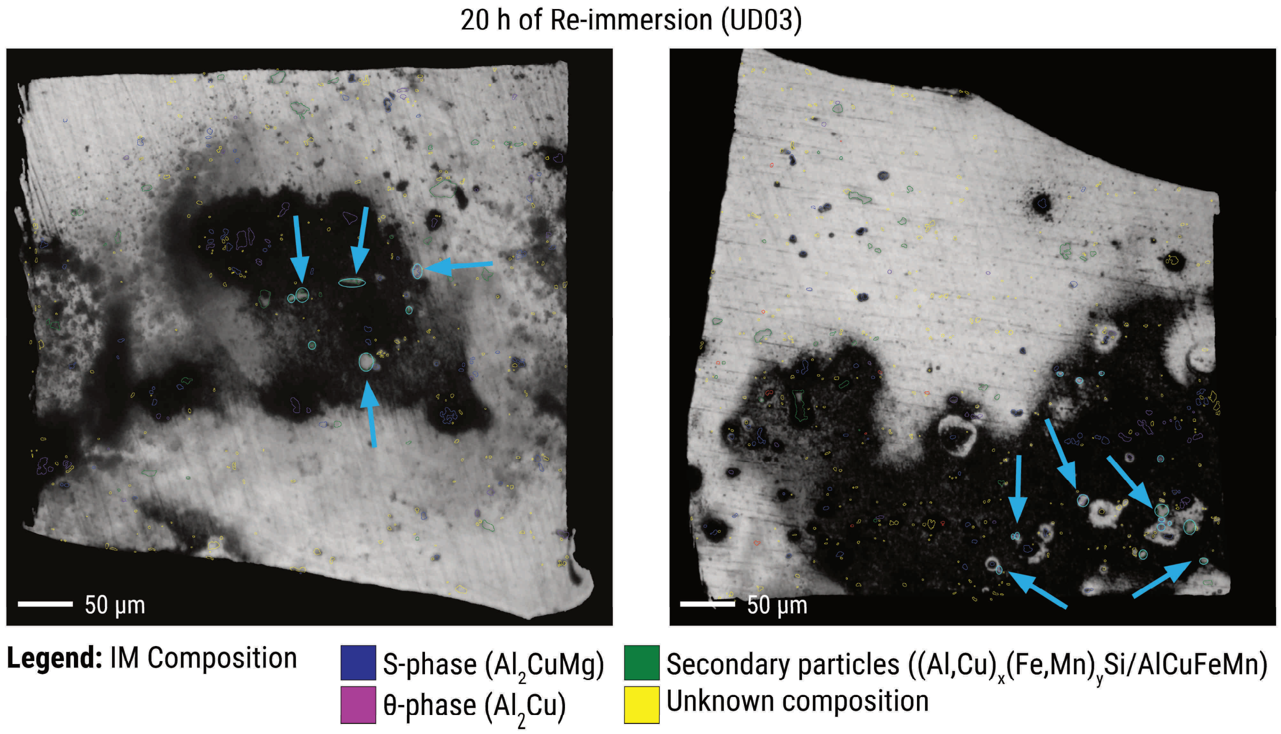
20 h of Re-immersion (UD03)

Legend: IM Composition
🟦 S-phase (Al_2CuMg)
🟩 Secondary particles ($(Al,Cu)_x(Fe,Mn)_ySi$/AlCuFeMn)
🟪 θ-phase (Al_2Cu)
🟨 Unknown composition

Figure S3.6. UD03 particles that exhibited low/low(L/L) behaviour during the first three hours of re-immersion which exhibited surfaces free of extensive corrosion product deposition or dissolution at 20 h of re-immersion (i.e., L/L-B behaviour).

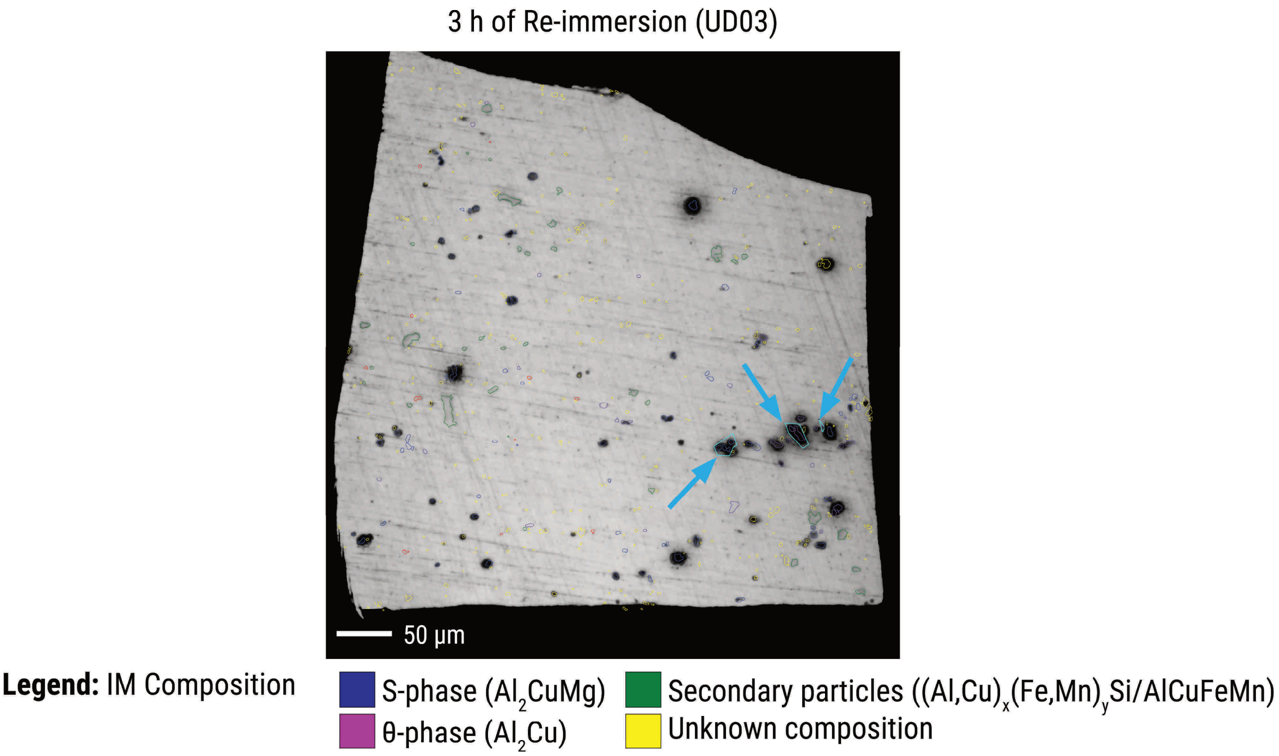
3 h of Re-immersion (UD03)

Legend: IM Composition
🟦 S-phase (Al_2CuMg)
🟩 Secondary particles ($(Al,Cu)_x(Fe,Mn)_ySi$/AlCuFeMn)
🟪 θ-phase (Al_2Cu)
🟨 Unknown composition

Figure S3.7. Cyan arrows and cyan boundaries mark UD03 particles that exhibited low/high (L/H) behaviour during the first three hours of re-immersion. These activity of these particles were triggered by activity from neighbouring active sites (i.e., L/H-B behaviour).

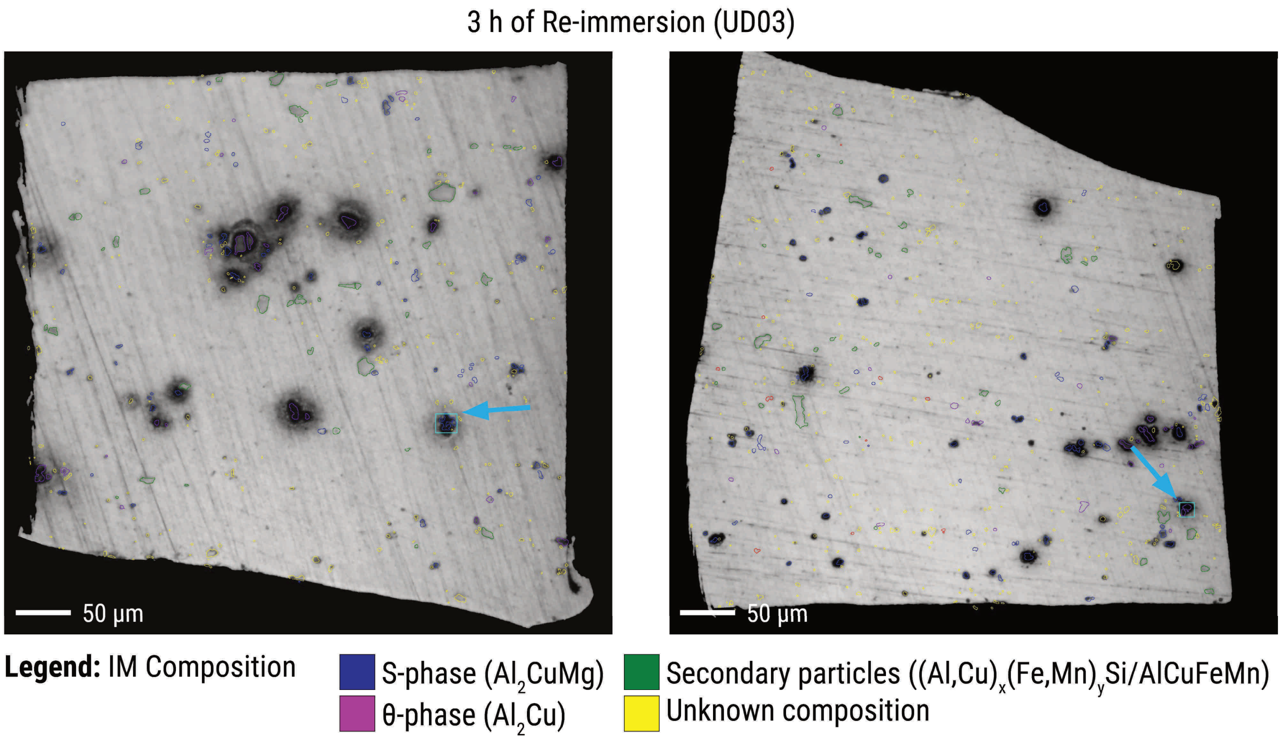

Figure S3.8. Cyan arrows and cyan boundaries mark UD03 particles that exhibited high/high (H/H) behaviour during the first three hours of re-immersion. These activity of these particles were triggered by activity from neighbouring active sites (i.e., H/H-B behaviour).

3.7.5. Replicates of tests at varying immersion conditions

This section provides global activity maps for the replicates of UD03, UD24, UD72, and DS03. Figure S3.9-UD03 (trial 2) shows precipitation at several intermetallic particles at the end of immersion for 3 hours in 0.05 M NaCl + 0.001 M Ce(III). As with UD03 trial 1 (Figure 3.2), the precipitation is limited to the intermetallic particles (IMPs) and is most probably a consequence of partial corrosion of the IMPs either during sample preparation or during the period prior to immersion wherein it was exposed to air. Nonetheless, the subsequent loss of inhibition during re-immersion for UD03 (trial 2) is consistent with behaviour seen in trial 1. Extended re-immersion (20 h) also showed extensive matrix involvement due to corrosion product deposition.

Figure S3.9-UD24 (trial 2) shows less precipitation sites at the end of immersion compared to UD24 trial 1 (Figure 3.7b). This deviation is attributed to sample-to-sample variations in IMP distribution. During re-immersion, activation of several intermetallic particles were observed at 600 s. Majority of this activation have L/H behaviour though (see arrows in Figure S3.9-UD24 (trial 2) 600 s). Nonetheless, similar to the UD24 trial 1 L/H active sites, these trial 2 sites continued to show signs of local corrosion for the rest of the re-immersion duration. At 10800 s of re-immersion, these active sites have lead to considerable changes on the bulk matrix. Meanwhile, as with trial 1, sites with high activity during immersion also showed some changes during re-immersion but remained mostly stable (see arrows in Figure S3.9-UD24 (trial 2) 10800 s. Similar to trial 1, the extent of surface changes with prolonged re-immersion is comparable to that of UD03 due to corrosion product deposition from L/H sites.

Figure S3.9-UD72 (trial 2) shows high frequency of active sites at the end of immersion, similar to UD72-trial 1 (Figure 3.7c). Its re-immersion behaviour is also dominated by a few active sites with high/high behaviour. The activity increase and spread of these sites were also gradual and did not lead to significant changes in the alloy matrix within the first 3 hours of re-immersion. Substantial changes on the matrix is observed around the top right corner of the sample at extended re-immersion (20 h). Corrosion on this region is likely aggravated by its proximity to the edge as this makes it susceptible to of crevice corrosion.

Figure S3.10 shows replicates of the DS03 immersion condition. The samples in this exposure condition also show low degree of changes during re-immersion. Interestingly, the extent of precipitation at the end of immersion for this exposure condition is not as extensive as that reported in our previous work [26] despite similar inhibitor supply delay. Figure S3.11 shows an example of a DS03 sample with more extensive precipitation. We currently don't know why there is variation in the response. It should be noted that the sample in Figure S3.11 were from tests performed over a year ago relative to the tests performed for this work. It is possible that the aging of the epoxy-embedded samples as well as the repeated grinding and polishing affected the local corrosion and inhibition behaviour of the intermetallic particles. Analysing the effect of these factors is thus recommended for future work. Nonetheless, we would like to point out that despite the difference in the extent of precipitation as well as the subsequent re-immersion behaviour, the sample shown in Figure S3.11 has less extensive surface changes compared to the UD03 samples. This is especially apparent at long term re-immersion (20 hours).

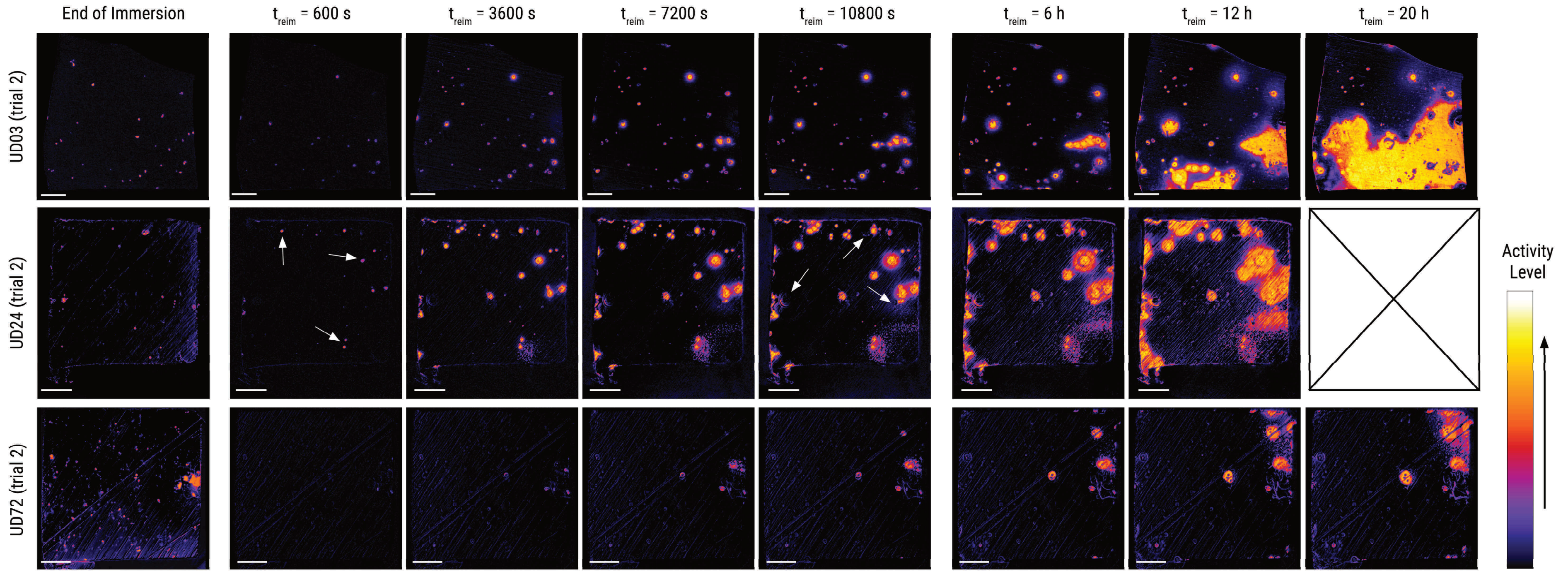

Figure S3.9. Global activity maps of AA2024-T3 samples immersed in 0.05 M NaCl + 0.001 M Ce(III) under different conditions: (UD03) 3 hours, (UD24) 24 hours, and (UD72) 72 hours. The first column shows the sample state at the end of the initial immersion. The second to fifth columns display changes during re-immersion in 0.05 M NaCl for 3 hours, while the last three columns show changes during extended re-immersion. White scale bars represent 100 µm.

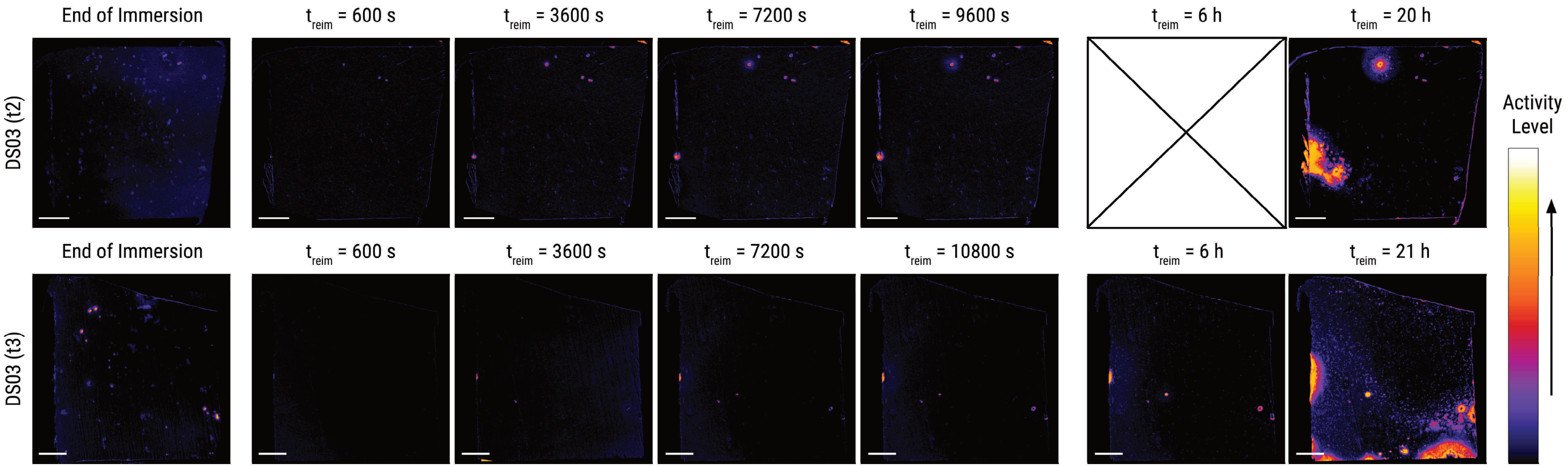

Figure S3.10. Global activity maps of AA2024-T3 samples immersed in 0.05 M NaCl + 0.001 M Ce(III) with a 30-second inhibitor supply delay, immersed for 3 hours. The first column shows the sample state at the end of the initial immersion. The second to fifth columns display changes during re-immersion in 0.05 M NaCl for 3 hours, while the last two columns show changes during extended re-immersion. White scale bars represent 100 µm.

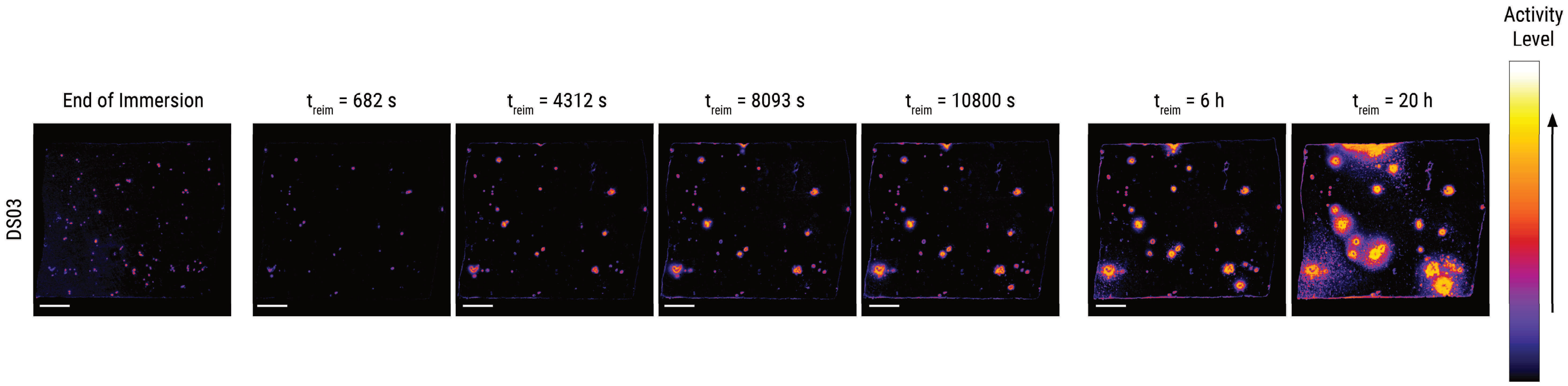

Figure S3.11. Global activity maps of AA2024-T3 sample immersed in 0.05 M NaCl + 0.001 M Ce(III) with a 30-second inhibitor supply delay, immersed for 3 hours. This sample showed more extensive activity than the other replicates. The first column shows the sample state at the end of the initial immersion. The second to fifth columns display changes during re-immersion in 0.05 M NaCl for 3 hours, while the last two columns show changes during extended re-immersion. White scale bars represent 100 μm.

4

Intermetallic particles trigger streaking corrosion in AA7075-T6

Streaking corrosion (SC) of AA7075-T6, characterized by the rapid dissolution of an altered surface layer (ASL) formed through mechanical surface treatments, is investigated. Utilizing in situ high-resolution reflected light microscopy, we reveal that SC initiates preferentially on intermetallic particles (IMP) or pre-existing pits. Optical evidence of galvanic interactions between propagating streaks and connected IMPs is observed. Concurrent in situ open circuit potential (OCP) measurements show a characteristic pattern that correlates with SC initiation, progression, and termination. This work demonstrates the effectiveness of a simple in situ optical-electrochemical setup in tracking dynamic local corrosion processes and directly linking OCP transients to specific corrosion events.

This chapter has been published as:

M. Mopon, A. Mol, S. J. Garcia, Intermetallic particles trigger streaking corrosion in AA7075-T6, *NPJ Mater. Degrad.* 9:92 (2025). doi: 10.1038/s41529-025-00631-5.

4.1. Introduction

AA7075 is an Al-Zn-Cu-Mg alloy commonly used in the aerospace industry due to its good strength to weight ratio. The microstructure that arises from its composition, however, is prone to local corrosion. Intermetallic particles (IMPs) formed due to the presence of alloying elements undergo a complex dealloying process that eventually leads to micro-galvanic coupling with the bulk matrix [1,2]. Typical AA7075 IMPs include S-phases (Al_2CuMg), θ-phases (Al_2Cu), and secondary particles, of which Al_7Cu_2Fe, $(Al,Cu)_6(Fe,Cu)$, and $MgSi_2$ are most abundant [3,4]. Local corrosion of S- and θ-phase IMPs begins with a dealloying process wherein less noble IMP components such as Mg and Al are dissolved [5,6]. This leads to enrichment of the Cu at the IMP which facilitates oxygen reduction reaction and triggers anodic dissolution of the less noble adjacent matrix (i.e., trenching). Meanwhile, some secondary particles (e.g., Al_7Fe_2Cu [7]) have been shown to be more electrochemically stable and thus may undergo slower and limited dealloying. Their local corrosion behaviour is characterized by less extensive dealloying although still accompanied by trenching [7,8]. Presence of grain boundary precipitates and precipitate-free zones in the AA7075 grain boundaries also leads to intergranular corrosion susceptibility [9,10].

Apart from the corrosion susceptibility due to its microstructure, mechanical surface treatments of the AA7075 surface (e.g., abrading, machining, polishing) can also render it vulnerable to a form of altered surface layer (ASL) attack [11–14]. This ASL attack is similar in nature to reported corrosion of near surface deformed layers (NSDL) present in aluminium alloys [15–19]. Notably, majority of these works studied NSDL in the context of filiform corrosion which occurs when the aluminium alloy is covered with an organic coating. The ASL's (or NSDL's) vulnerability has been attributed to redistribution of active alloying elements (i.e., Zn, Mg) from precipitates and IMPs into the ASL due to high shear straining during surface polishing [20]. Huang et al [12,21] referred to a form of this ASL attack as streaking corrosion due to characteristic streaks formed by its preferential propagation along abrasion grooves. Streak propagation is thought to be driven by the low pH produced by corrosion product hydrolysis. The low pH undermines passivity and pushes the streak front forward [12]. The topology of the grooves provide an ideal containment system for this low pH environment leading to the observed preferential propagation at these locations. Other aluminium alloys such as AA8006 [12] and AA7055 [11,22] have also exhibited similar streaking behaviour.

Nevertheless, there are still questions regarding initiation and propagation of streaking corrosion in the ASL. Zhao and Frankel proposed that the initiation sites for ASL attack in AA7075 during polarized conditions are active nano-grain boundaries enriched with Zn and Mg [20]. This does not account though for the highly localized occurrence of streaking corrosion especially during open circuit conditions. In this work, we used an in situ optical-electrochemical technique to deepen and clarify our understanding of the initiation and propagation of streaking corrosion in AA7075-T6 microelectrodes. The technique utilizes reflected light microscopy with high spatial and temporal resolution to monitor changes on the surface. When coupled with open circuit potential (OCP) measurements, determination of the electrochemical signal of specific corrosion events on the surface is possible. Furthermore, scanning electron microscopy (SEM) with energy-dispersive x-ray spectroscopy (EDX) was also utilized to identify features that likely contribute to initiation of streaking corrosion.

4.2. Experimental

Commercial grade bare AA7075-T6 (Kaiser Aluminium, rolled thickness = 3 mm) was used for the corrosion tests. Micropillars were produced from the metal sheets and embedded in cold-curing epoxy as reported elsewhere [23–25]. The resulting embedded sample had an exposed metal surface area of approximately 260 x 170 μm^2. The exposed area is along the rolling plane of the alloy. The sample was repolished for each new corrosion test. The solution used for the corrosion tests was a 0.05 M NaCl aqueous solution (>98% purity NaCl in "Millipore Elix 3 UV" treated water).

Prior to immersion in the corrosive solution, the sample surface was ground with SiC sandpaper from 320 to 4000 grit and then polished to 0.25 μm with diamond paste. For samples subjected to pre-exposure microstructure analysis, location and spot composition of IMPs and defects (e.g., pre-existing pits) were determined using SEM-EDX (JEOL JSM-7500F field emission scanning electron microscope coupled with energy dispersive X-ray spectroscopy) operated in back-scattered electron mode. The SEM images were used to generate the microstructure map of the sample surface. Right after SEM-EDX analysis, the sample was quickly repolished with 0.25 μm diamond paste and washed with ethanol before the immersion tests. The sample was then placed in the in situ optical-electrochemical setup composed of an electrochemical cell (redox.me Raman electrochemical flow cell) and a reflected microscope (Dinolite AM7515MT4A, ~10 pixels μm^{-2}) operating in brightfield mode for in situ acquisition of images of the surface during immersion [23,24]. The sample served as the working electrode and an Ag/AgCl(3 M KCl) reference electrode integrated into the electrochemical cell was used as the reference electrode. The OCP measurements were acquired using an Ivium CompactStat.h potentiostat. The immersion tests were conducted inside a Faraday cage to prevent interference from external sources. The cage is also equipped with blinds to remove the effect of ambient light changes on in situ imaging. Image capture and potential measurements were initiated prior to the injection of the electrolyte into the cell to enable collection of data from the very start of exposure. The sample was immersed in 4.5 mL of the electrolyte for 2 hours. Post-immersion analysis of the sample was performed with SEM-EDX. It is noted that in some cases, the post-immersion SEM images can also be used to generate the microstructure map of the sample surface.

Detailed discussion of our image analysis protocol for studying local changes in the sample surface is available in Chapter 2. Our analysis focuses on detecting and quantifying the changes which happened during immersion by implementing image subtraction on our pre-processed (i.e., conversion to grayscale, recursive realignment) optical images. It is noted that the images have been converted to grayscale, as such each pixel has an associated gray-level. With the imaging mode used (i.e., brightfield imaging), local corrosion is generally observed as pixel darkening. This happens because local corrosion changes the surface by either wearing some parts away or adding corrosion products, both of which make the surface rougher. A rougher surface scatters more light away, causing the pixels to look darker in the image. The subtraction was generally performed with respect to the first image acquired during immersion (i.e., image @ 0 s of immersion – image @ x s of immersion) unless otherwise stated. This subtraction process generated the global activity map (GAM) for the sample at time x. The GAM shows change in gray-level of individual pixels (i.e., pixel activity). A built-in ImageJ look-up table (i.e., Fire) was used to recolour the GAMs to enable easier visualisation of the magnitude of the changes. The activity levels depicted in the GAMs range from 0 to 255, with 0 indicating no change with respect to the initial condition. A threshold can also be applied to the GAM to balance signal-to-noise ratio and quantify the affected area percentage (4-1). This parameter is useful for assessing how much of the overall surface has been impacted by local corrosion processes. Cross-referencing of the evolution of surface activity with the microstructure was achieved by overlaying the microstructure map obtained through SEM onto the GAMs. The map can then be used to isolate specific areas of the GAM for analysing local surface changes (i.e., IMP level). The changes were visualized through simplified pixel activity level distribution (sPAD) plots [23]. These plots present the maximum (maxAL), median (midAL), and minimum (minAL) activity levels as a function of time for the set of pixels on the IMP surface. The midAL is useful for looking at the overall behaviour of the isolated area. Meanwhile, the maxAL and the midAL provide additional sensitivity to changes during early- and late-stage corrosion, respectively.

$$\text{Affected area } \% = \frac{\text{No. of pixels with activity level} \geq \text{threshold}}{\text{Total number of pixels in sample surface}} \text{ x } 100\ \% \qquad (4\text{-}1)$$

4.3. Results

4.3.1. Streaking corrosion initiation

Figure 4.1 shows that local corrosion processes on the surface of a roughly-polished AA7075-T6 sample (i.e., sample with visible grooves from grinding) can generally be divided into two types: (1) dealloying and trenching around IMPs and (2) streaking corrosion on the bulk matrix. Dealloying is observed optically as surface darkening within the IMP boundaries (i.e., green boundaries) while trenching is the subsequent darkening of the matrix adjacent to the IMP boundaries [23,24]. The IMPs in area 5 of the microscopy image at 10 minutes (Figure 4.1) exhibit this behaviour. Majority of the IMPs showed signs of dealloying during the first 10 minutes of exposure. Gradual trenching around the dealloyed IMPs progressed for the rest of the immersion. The image of the surface at 120 mins shows extensive IMP dealloying and trenching. However, their effect does not extend too far from the IMP boundary.

Streaking corrosion was observed as dark lines that generally grew along the direction of the abrasion grooves. The streaks initiated on four separate locations (areas 1 - 4 in Figure 4.1) within the first 10 minutes of immersion. Areas 1, 2, and 3 each exhibited one streaking initiation event, while Area 4 showed four. The area 4 streaks propagated the most and covered almost half of the sample surface within 60 minutes of immersion. Visual appearance of the streaked surfaces are consistent with optical micrographs of streaking corrosion by Huang et al [12], and of ASL attack shown by Wang et al [11] and Zhao et al [26]. The extent of streaking corrosion propagation can be further quantified with the affected area ((4-1) – a measure of the percentage of pixels in the subtracted images which exhibited gray level changes greater than or equal to a threshold. The affected area curve for this sample (Figure 4.2 – Region B) shows that the continuous streaking corrosion from 300 s until around 2400 s of exposure indeed led to rapid surface changes. The increasing part of the curve shows staircase-like features consistent with the incremental propagation of streaking corrosion. This incremental propagation suggests that the overall streaking is a sequence of smaller initiation-propagation-termination events.

Movie 4.1 shows the time-evolution of the surface activity maps, where streaking corrosion appears as fast-spreading purple lines that extend into the matrix. It provides a clearer view of streaking in Areas 1, 2, and 3 and indicates that the streak in Area 2 and Area 3 likely originated from IMPs. Movie 4.1 also shows that the activity in area 4 started with four individual streaks. Activity maps in Figure 4.3 are still frames from Movie 4.1 which show initiation and

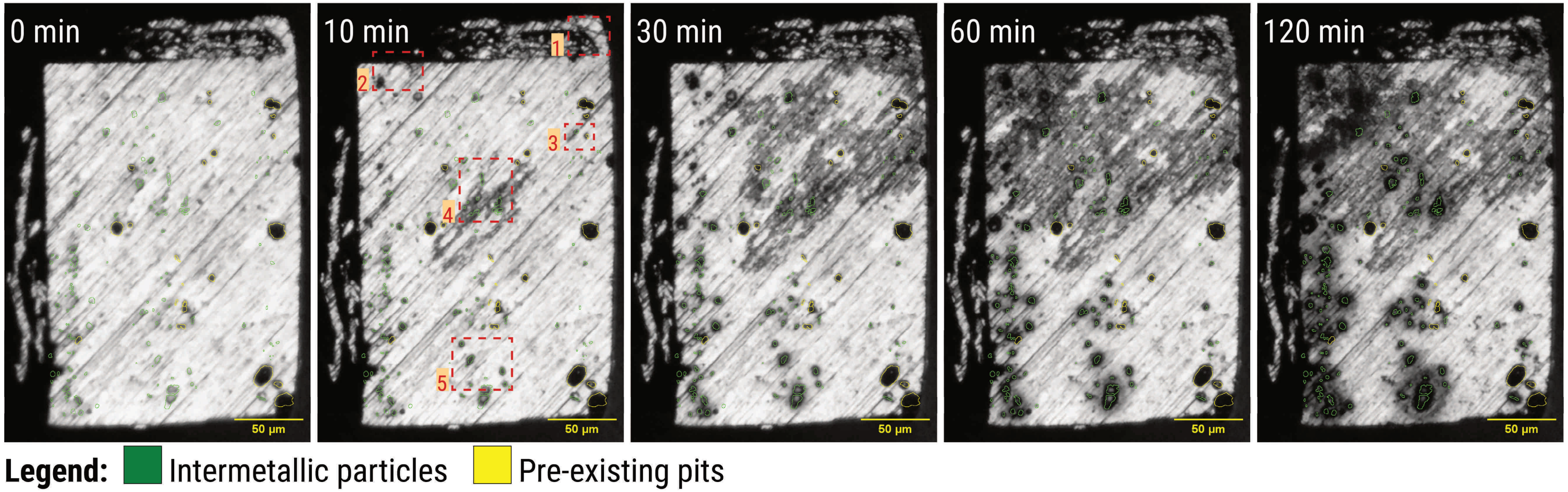

Figure 4.1. In situ reflected light microscopy images of an AA7075 surface exposed to 0.05 M NaCl at OCP show the evolution of local corrosion processes such as streaking corrosion (area 1 - 4), and IMP dealloying and trenching (area 5). The microstructure map which indicates the location of IMPs and pre-existing pits shown in this figure was created from post-immersion SEM images. The legend indicates the boundary colour for IMPs and for pre-existing pits.

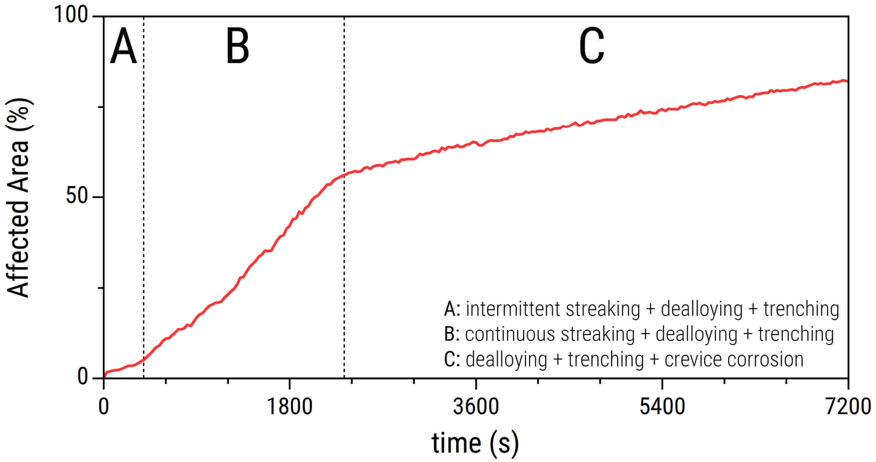

Figure 4.2. Affected area curve shows majority of the area that changed can be attributed to the propagation of streaking corrosion.

subsequent growth of the streaks. It is interesting to point out that the four streaking events did not happen at the same time. Instead, one streak initiates, propagates, and ends before another streak begins from a different location. This gives the overall impression of incremental streaking propagation shown in Figure 4.2. The first streak initiated at around 41 seconds from start of immersion (Figure 4.3a). The initiation site was on the right edge of particle P1, an S-phase IMP based on the post-mortem EDX analysis (Supplementary Figure S4.1). The streak followed a groove and propagated towards the top right direction. The streaking ended at around 54 s. The second streak initiated at the left edge of P2 (S-phase, EDX in Supplementary Figure S4.2) and propagated towards the bottom left direction (Figure 4.3b). It is noted that P2 showed signs of increasing activity on the IMP surface before the initiation of the streak. The streak front advanced through a well defined groove at 153 s and covered a distance of around 9 µm. Its estimated front speed of 4.5 µm s^{-1} is consistent with streak rate reported by Huang et al [12]. At 158 s, the streak connected to a nearby IMP (P') which then showed signs of activation and activity spread both along and lateral to the grooves in its vicinity (indicated by the dashed arrows in the activity map at 160 s). With further exposure, more active zones appeared near P'. This streaking ended at around 171 s. Figure 4.3c shows that the third streak started at the bottom edge of P3 (S-phase, EDX in Supplementary Figure S4.3) at 194 s. The streak front moved towards the top right direction and then connected to a low activity patch. This patch showed gradual increase of activity from 199 s until its apparent termination at 209 s but triggered no immediate activity spread. The fourth streak initiated at the top edge of P3, right where a smaller IMP is located (Figure 4.3d). The composition of the smaller IMP was not confirmed experimentally but based on its proximity to a cluster of S-phases, it is likely to have same composition. The streak also moved towards the top right direction where it then connected with the active patch from the third streak. This led to activity spread that headed back to P3, connected with the third streak, and then continued on as a streak front from the left edge of the IMP cluster below P3. All other streaking events during the immersion period can be traced to sites connected to the propagation of the fourth streak. Despite the large area affected by streaking corrosion, the affected depth appears to be relatively shallow. This is evident in the end-of-immersion activity map for area D (Figure 4.4a) which shows that the activity level of the streaks remained in the low level (purple in the colour scale) while that of the trenches reached a higher activity level (yellow-orange in the colour scale). This is evident in the end-of-immersion activity map for area D (Figure 4.4a) which shows that the activity level of the streaks remained in the low level (purple in the colour scale) while that of the trenches reached a higher activity level (yellow-orange in the colour scale). The post-mortem

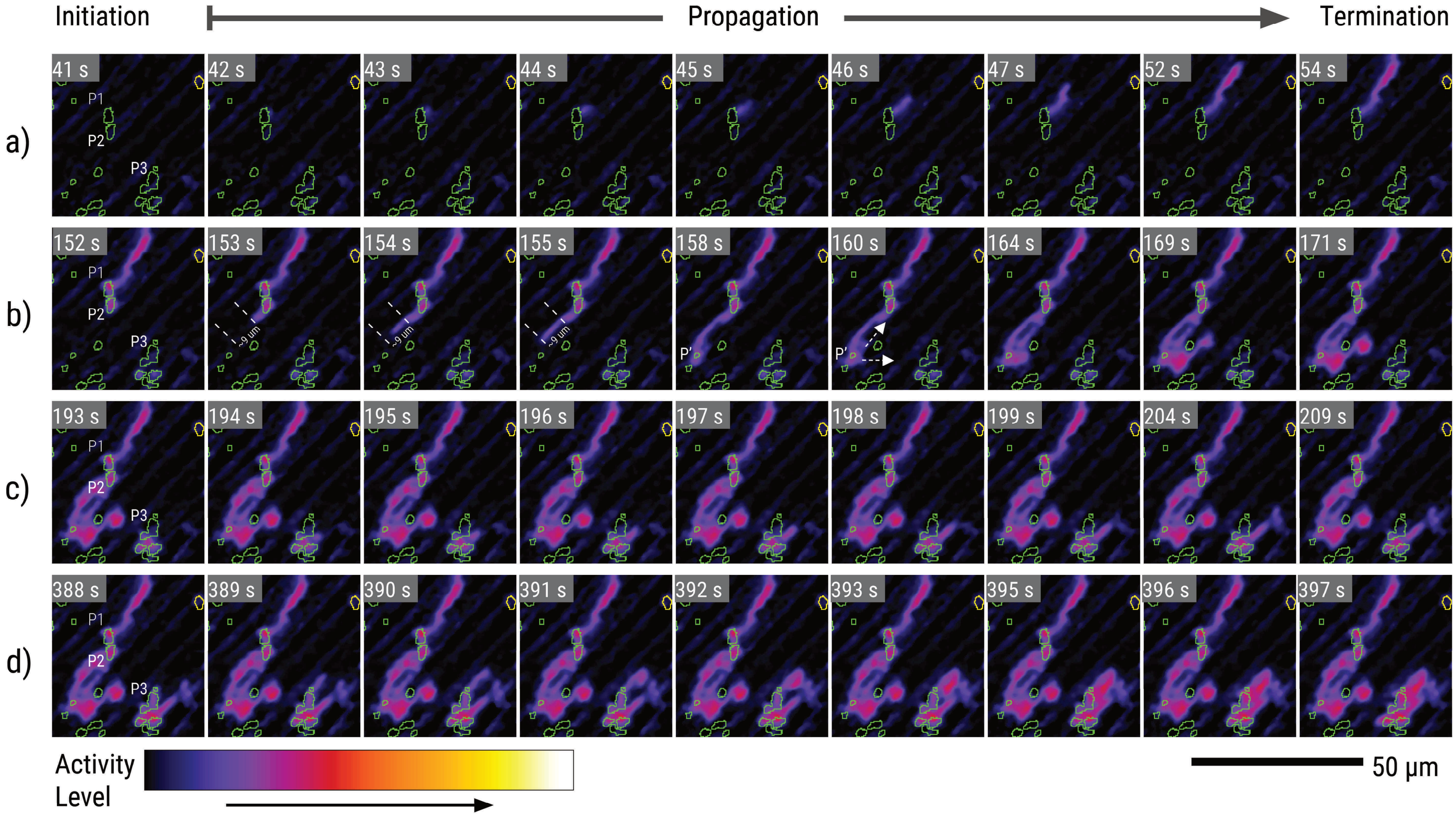

Figure 4.3. Activity maps from area 4 in Figure 4.1 show the initiation of four streaks **(a-d)** which eventually propagated to the rest of the sample surface. The activity maps were obtained by subtracting from the image at t = 0 s and without applying any threshold.

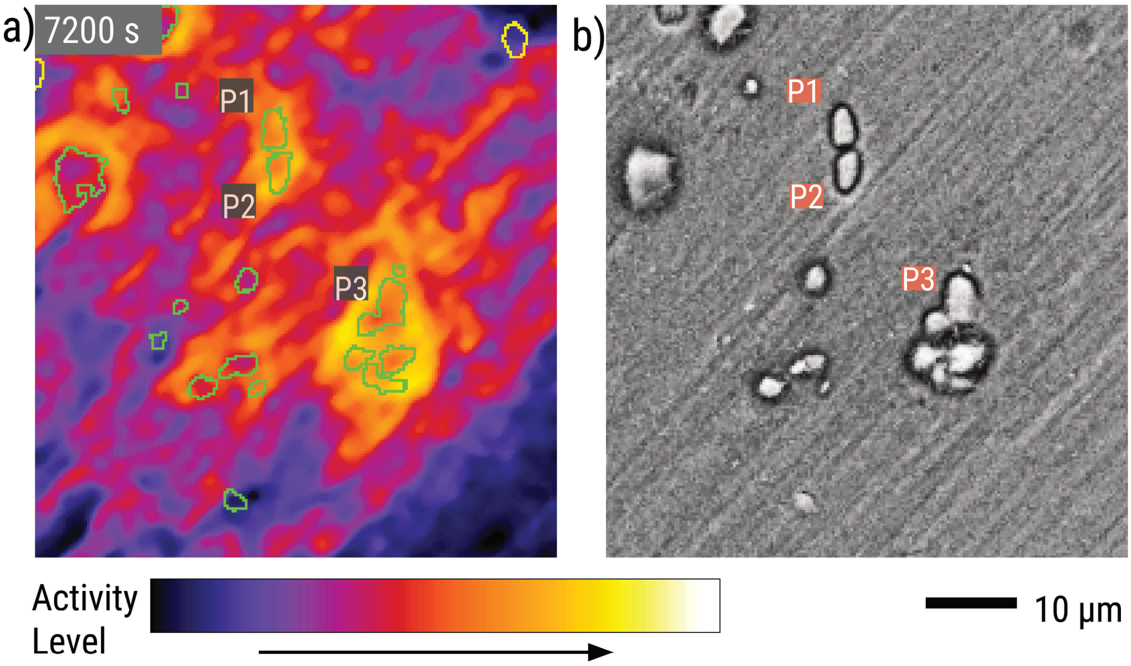

Figure 4.4. (a) Activity map of area 4 at end of immersion and its **(b)** post-mortem secondary electron image. The high activity around the particles (orange-yellow zones) indicate extensive surface change due to trenching. Streaked areas (purple zones) have shallow dissolution and do not stand out in the post-mortem electron image

secondary electron image (Figure 4.4b) also shows distinct trenches around the IMPs but not so visible streak morphology.

Analysis of the local corrosion behaviour in a smoothly-polished AA7075-T6 surface (i.e., sample with no visible grooves from grinding) was conducted to better understand streaking not confined to abrasion grooves. The RM image of the surface at the end of immersion (Figure 4.5a) shows that, in the absence of deep grooves, streaking corrosion has a patchy texture. The edges of these streaking patches are also more billowing and less sharp. A video depicting the evolution of activity of the overall surface is provided in Movie 4.2. The video highlights that the hallmark of streaking corrosion – rapid spreading across the surface – is still observed even on a smoother sample. This fast-spreading behaviour indicates that the corrosion events seen on smoothly-polished surfaces are the same as those occurring on roughly polished samples, despite the differences in surface morphology.

The overall streaking at the end of immersion of the smoothly-polished sample was traced to areas 6 and 7 in Figure 4.5a. Activity maps in Figure 4.5b and Figure 4.5c are still frames from Movie 4.2 and show the initiation and first couple of seconds of propagation of streaks in area 6. It is evident from the maps that the streaks originated from P4 and P5, both of which are S-

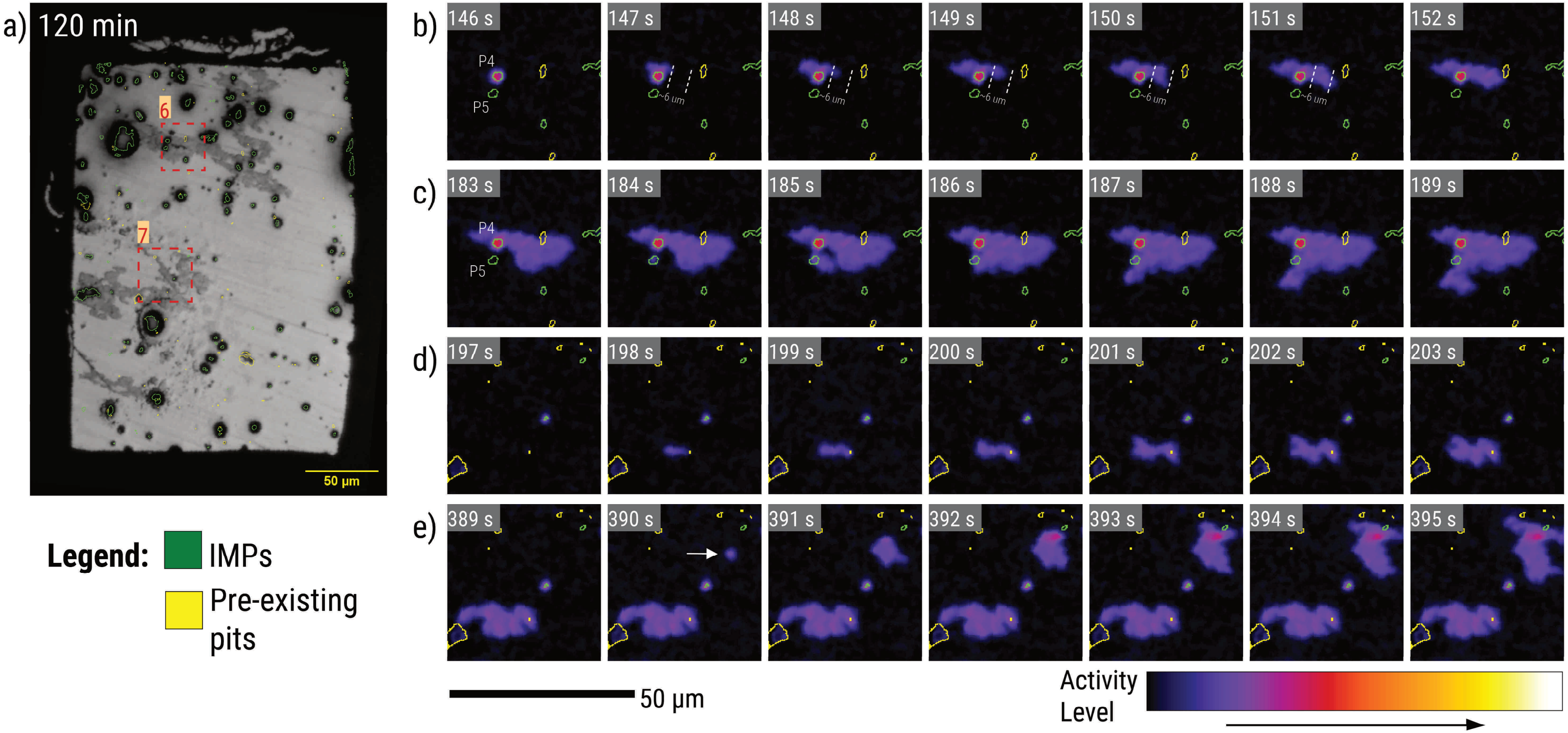

Figure 4.5. In situ reflected light microscopy image **(a)** of a polished AA7075 surface exposed to 0.05 M NaCl at OCP shows the extent of streaking corrosion in the absence of deep abrasion grooves. Activity maps show streaking initiation sites in area 6 **(b, c)**, and area 7 **(d, e)**. The activity maps were obtained by subtracting from the image at t = 0 s and without applying any threshold. The microstructure map overlay was created from pre-immersion SEM mapping. The legend indicates the boundary colour for IMPs and for pre-existing pits.

phase particles (EDX analyses in Supplementary Figure S4.4 and Figure S4.5). The streak originating from P4 (Figure 4.5b) started at its edge and propagated in a diffused manner with a linear propagation speed (~2 µm s^{-1}). This value is comparable to that observed from the rough sample. Streaking terminated at around 163 s. Similar to P2, P4 exhibited signs of increased activity on the IMP surface before the onset of streaking. The streak originating from P5 (Figure 4.5c) started on the IMP surface and then rapidly propagated to the surrounding matrix until it terminated at around 197 s. The surface was inactive prior to streak initiation. It should be noted that another streak initiates from P5 later on, at around 211 s. Figure 4.5d and Figure 4.5e present streaking initiation sites in area 7. Unlike the previous streaking events, the ones observed in this area are associated with pits and not IMPs. Pre-immersion SEM (Supplementary Figure S4.6) confirmed the presence of a pit on the same location as the initiation site of the streak in Figure 4.5d. Meanwhile, post-immersion SEM (Supplementary Figure S4.7) confirmed the presence of a pit at the Figure 4.5e streak initiation site. Streak propagation from these pits was similar in behaviour to streak propagation from IMPs. Interestingly, all the streaks initially spread to bigger areas relative to their in-groove counterparts within the same time period. Despite this, the fraction of the surface affected by streaking corrosion is visibly less than that of the roughly-polished AA7075-T6.

Post-immersion secondary electron images (Figure 4.6a) indicate that the patchy texture of streaking corrosion arise from a mix of dissolved and undissolved sections. Bright spots on the dissolved areas also point to exposure of IMPs or dispersoids during ASL dissolution. Exposure of these bright spots is most apparent on the areas traversed by streaking corrosion and not on the intact areas. Post-immersion EDX analysis of streaked and un-streaked areas (Figure 4.6b) from another smoothly-polished replicate (Supporting Information 4.8.2) was also conducted to investigate possible compositional differences. It is noted that streaking corrosion in this replicate initiated from Fe-rich IMPs (Supporting Information 4.8.2). The resulting EDX maps of the streaked areas revealed no discernible differences between the two areas. This may indicate either that a thin ASL is present on the unstreaked area but falls below the detection limit, or that all ASL material susceptible to streaking is localized to the streaked area and has been entirely removed by corrosion. The absence of detectable differences further suggests that the streaking does not result in the accumulation of substantial corrosion products on the affected surface. Instead, the dissolved metal is likely retained in the solution or redeposited beyond the analysed region. While the observed morphological differences between roughly and smoothly polished surfaces may provide additional insight into the nature of streaking corrosion, a more detailed investigation is outside the scope of this work and is recommended for future study.

Notably, among 28 streaking initiation events across three smoothly-polished samples and one roughly-polished sample, 21 originated from intermetallic particles (i.e., 6 from the sample shown in Figure 4.1, 2 from the sample in Figure 4.5, 8 from the replicate in Figure S4.17, 5 from the replicate in Figure S4.22). This indicates that 75 percent of streaking corrosion events can be traced to IMPs and suggests that these particles can act as trigger for streaking corrosion in AA7075. The rest of the streaking corrosion events can potentially be attributed to initiation from pits as shown in Figure 4.5d and Figure 4.5e.

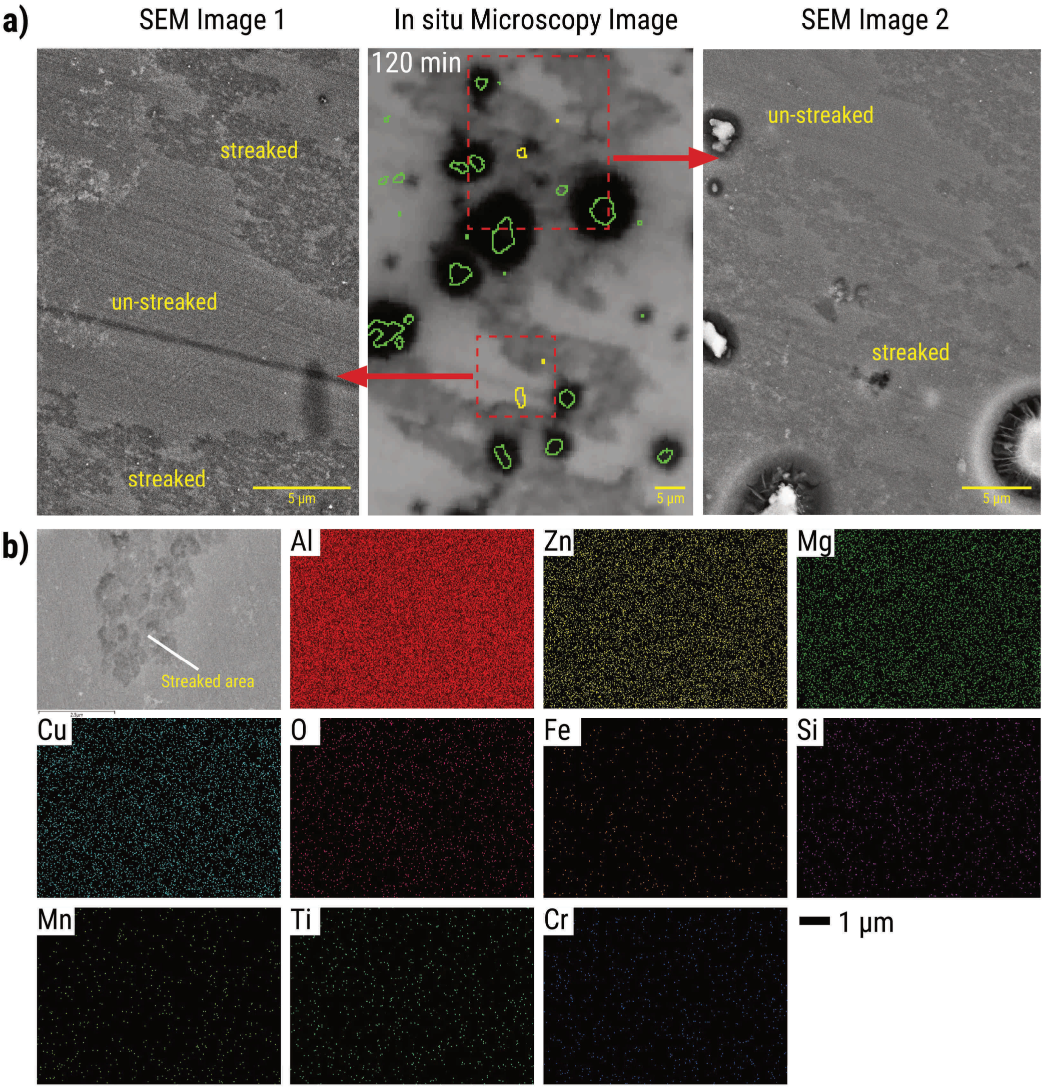

Figure 4.6. (a) In situ microscopy image of streaking corrosion and post-immersion secondary electron images of the streaking corrosion patches show the corroded areas are composed of dissolved and undissolved sections. The images also show that the depth of streaking is visibly less than trenching around intermetallic particles. **(b)** Post-immersion EDX mapping of streaked areas shows no detectable difference compared to the un-streaked areas.

4.3.2. Surface activation of IMPs that initiate and do not initiate streaks

The preceding section shows that streaking corrosion mostly initiates on IMPs and to certain extent, pre-existing defects. However, the majority of the IMPs on the samples analysed did not serve as initiation sites of streaking corrosion. Local activity of the streak-initiating IMPs was further scrutinized to see if there are any characteristic differences between them and the other IMPs. This was achieved by looking at the activation of the IMP surfaces through their corresponding simplified pixel activity level distribution (sPADs). The sPADs present the maximum (maxAL), median (midAL), and minimum (mindAL) activity level of the pixels that are within the IMP surface boundary as a function of time.

N1 (Figure 4.7a) is an IMP from the test shown in Figure 4.1 and N2 (Figure 4.7e) is an S-phase from the test shown in Figure 4.5 (Location data and EDX analyses in Supplementary Figure S4.8 and Figure S4.9). Both of these IMPs did not initiate streaking corrosion. Similar to S-phase sPADs in our previous work [23], the onset of changes for the pixels inside the IMP boundaries of N1 and N2 were within 60 seconds from the start of exposure to the electrolyte. Average activation onset time for known S-phase particles that did not initiate streaking (n = 13) from the smoothly- polished sample is 13.1 ± 4.7 s. Based on the midAL curve, the particles also exhibited an initial fast period of midAL increase followed by a slow period, both of which showed generally smooth features (i.e., no discontinuities). The midAL increase during the fast period is associated with the rapid dealloying of the IMP [23,24]. Once the particle has dealloyed substantially, transition to the slow period associated with trenching around the IMP [23,24] is observed. The activity maps in the insets show that the changes for N1 and N2 were characterized by gradual spread on the IMP surface. It is noted that the kink at around 45 seconds visible in the N2 midAL curve is due to a change in focus of the microscope during image acquisition. This is also seen in the other sPADs from the same trial (i.e., P4) and is not regarded as information on surface phenomena.

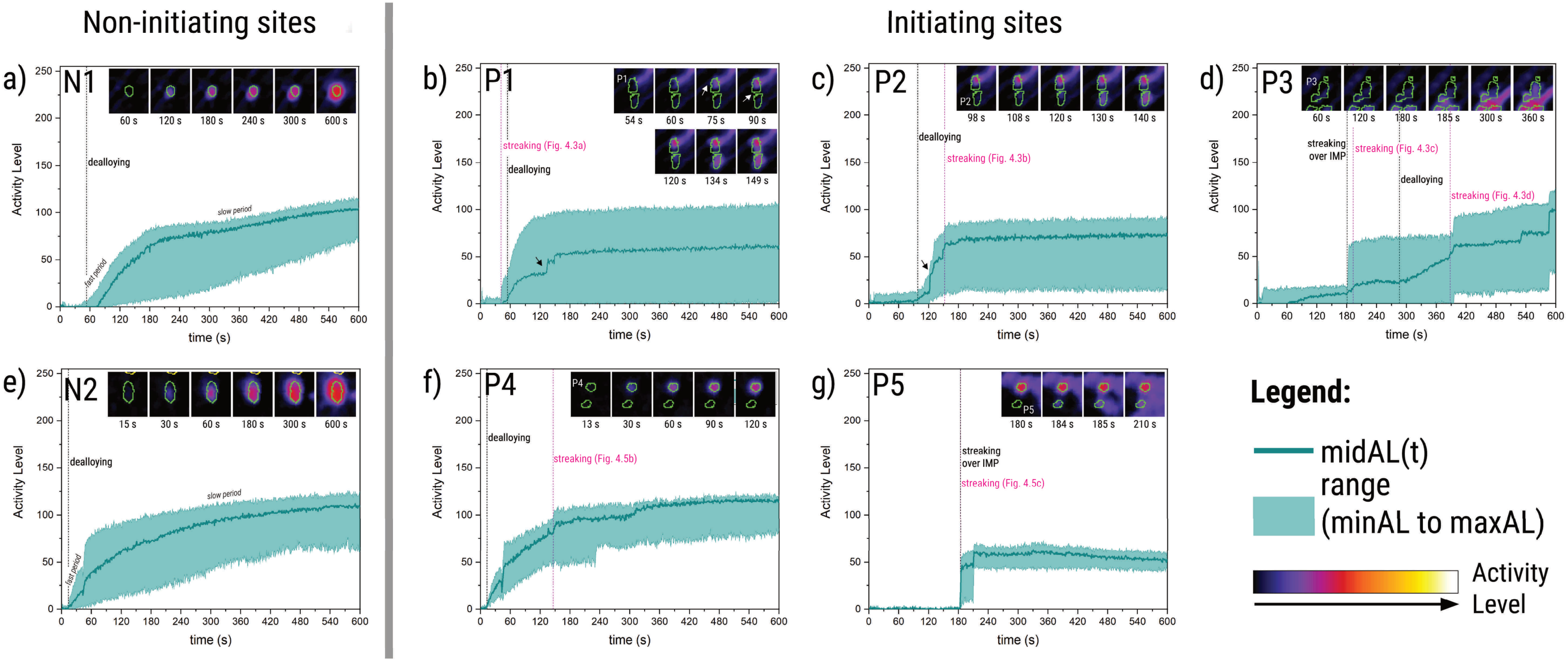

Figure 4.7. Simplified pixel activity-level distribution plot for **(a)** a non-initiating S-phase and **(b-d)** streak-initiating S-phases from the Figure 4.1 sample, and for **(e)** a non-initiating S-phase, and **(f, g)** streaking initiating S-phases from the Figure 4.5 sample. The dashed black lines indicate onset of activity on the IMP surface. The dashed magenta lines indicate streaking corrosion (outside IMP) onsets highlighted in Figure 4.3 and Figure 4.5. The insets show the activity maps of the IMPs that correspond to the plots presented.

The majority of the streak-initiating IMPs (i.e., P1, P2, P3, P5) show IMP surface activation profiles different to those from the non-initiating IMPs reported here and in previous works [23,24]. P1 sPAD (Figure 4.7b) registered a maxAL step increase at around 42 s due to streak initiation from its right edge. A gradual rise in activity from 54 s suggests surface dealloying coincident with the end of streaking corrosion shown in Figure 4.3a. The activity increase during the apparent dealloying (54 – 70 s on the midAL curve) resembles typical S-phase behaviour but eventually plateaued at an activity level of around 25. Inset activity maps reveal this plateau is due to inactivity on parts of the IMP surface near the left and bottom edges, likely caused by compositional variation. Nonetheless, midAL step increases at 134 s and 149 s (see black arrow in Figure 4.7b) indicate that these eventually registered activity consistent with streaking.

P2 activation (Figure 4.7c), marked by dealloying around 98 s, occurred before any streaking linked to the particle but significantly after typical S-phase activity onset. Its dealloying progressed more slowly than non-initiating IMPs. For reference, N1's midAL rose by 8 levels in 10 s (75–85 s), while P2 increased by only 3 over a similar period (100–110 s). A distinct midAL step increase at ~120 s (see black arrow in Figure 4.7b) signals a brief streaking event directly over the IMP surface.

Although the P3 sPAD (Figure 4.7d) shows a midAL increase at around 60 s, its almost flat maxAL suggests that the midAL increase might be due to an image subtraction artefact caused by scratches on the area and not due to actual changes on the IMP surface. Visible change in the maxAL trend at around 180 s indicates that this might be the actual IMP activation. Again, the activity step increase also suggests that the activation is due to streaking over the IMP, similar to that seen in P2. Changes in the upper section of the P3 attributed to dealloying is observed at around 286 s.

Among the IMPs in Figure 4.5 associated with streaking corrosion initiation, only P4 exhibited an initial activation profile comparable to that of a typical S-phase IMP (Figure 4.7f). Its activation onset at 13 s is consistent with a dealloying particle. Slow down of activity increase associated with trenching is observed after 60 s. At 147 s, streak initiation from the trench is observed as an instantaneous increase in the maxAL and midAL. It is noted that only one other particle in the replicate tests (Supporting Information 4.8.2) exhibited similar behaviour to P4.

Lastly, P5 activation onset (Figure 4.7g) occurred much later than typical S-phase onset. The IMP surface activation is characterized by a jump in the sPAD attributed to streaking over the

IMP surface. This also quickly transitioned to streaking corrosion outside the IMP as seen in the inset. The midAL following the sPAD jump is lower than the values seen in the non-initiating IMPs.

4.3.3. Intermetallic particle activity and streak propagation

The sPADs in Figure 4.7 highlighted generally non-typical activation of IMPs that initiated streaking corrosion. Interestingly, they also show that when an IMP is involved in streaking, step-discontinuities appear on its sPAD at the time of streaking initiation. The sPADs also exhibit near-horizontal profiles for the maxAL, midAL, and minAL during streak propagation. This behaviour points to temporary arrest of IMP activity during streak propagation. Extended sPADs of the IMPs (Figure 4.8b-d, f, g) involved with streaking corrosion show that their activity increase eventually resumed. This activity increase resumption is generally visible with the entire sPAD but is easiest seen with the minAL. The activity arrest is not limited to IMPs where streaking corrosion initiated. Figure 4.9 shows activity maps of two active particles (indicated by solid white arrow in the 600-s frame of Figure 4.9a and the 250-s frame of Figure 4.9b) activation profiles similar to the non-initiating IMPs. However, during the immersion, propagating streaks (indicated by dashed white arrow in the 1800-s frame of Figure 4.9a and the 285-s frame of Figure 4.9b) eventually linked with the surface of these IMPs (i.e., streak-linked IMPs). Their corresponding sPADs showed a transition to near-horizontal profiles at the time of connection (see 1980-s frame of Figure 4.9a and 292-s frame of Figure 4.9b). As with the streak-initiating IMPs, activity increase of streak-linked IMPs eventually resumed.

Activity increase resumption for the particles involved with the streaks was observed to be related to the overall streaking termination. For the roughly-polished sample, the termination occurred at around 40 minutes of exposure (Figure 4.2). The activity resumption for all the streak-initiating (Figure 4.8b-d) and streak-linked (Figure 4.9a) IMPs happened after this time. Streak-initiating and streak-linked IMPs from the smoothly-polished sample also showed resumed activity increase after overall streaking ended. The termination was observed at around 626 s (Supplementary Figure S4.10) and the extended sPADs of the streak-initiating (Figure 4.8f, g) and streak-linked IMPs (Figure 4.9) show activity increase resumption after this time.

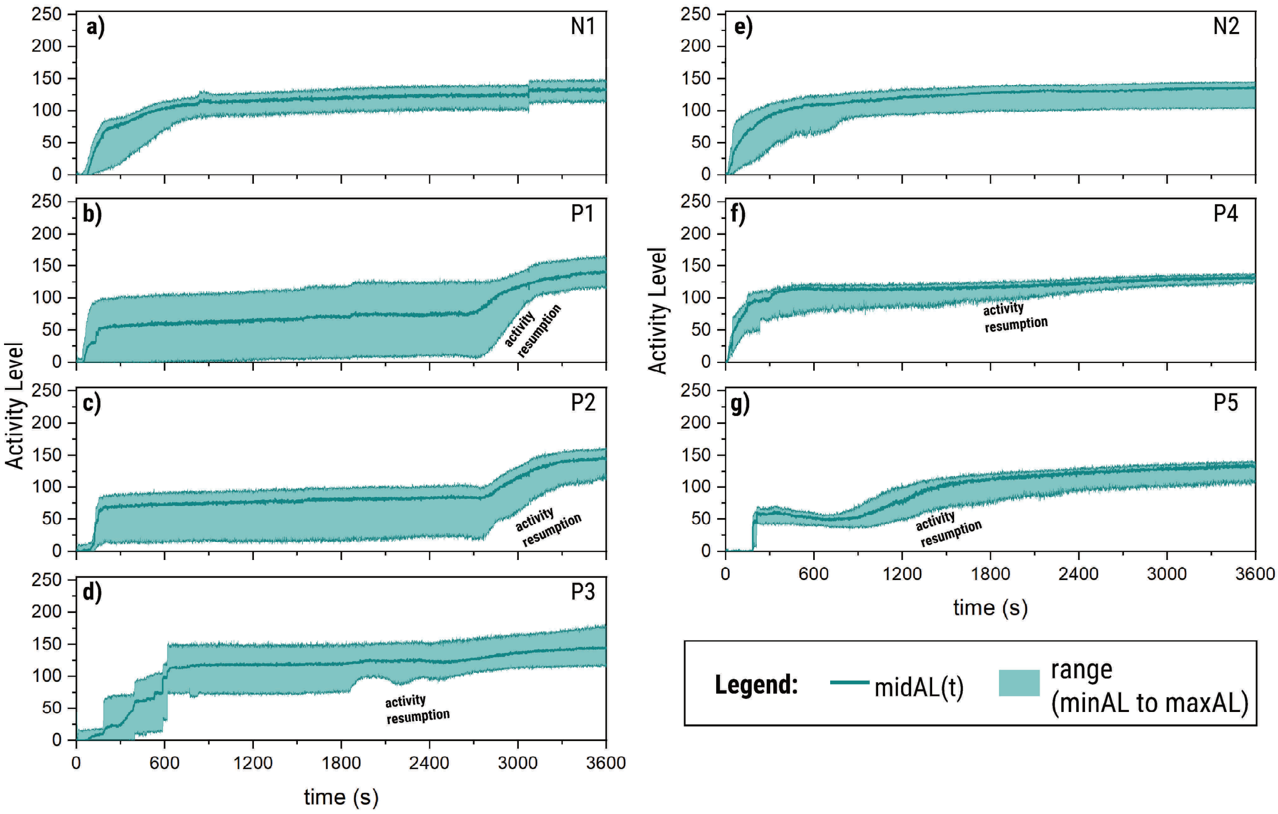

Figure 4.8. The extended simplified pixel activity-level distribution plots show that typical S-phases **(a, e)** exhibit quasi-steady behaviour during the first 1200 s of immersion while streak-initiating IMPs **(b-d, f, g)** show activity increase resumption at a later time.

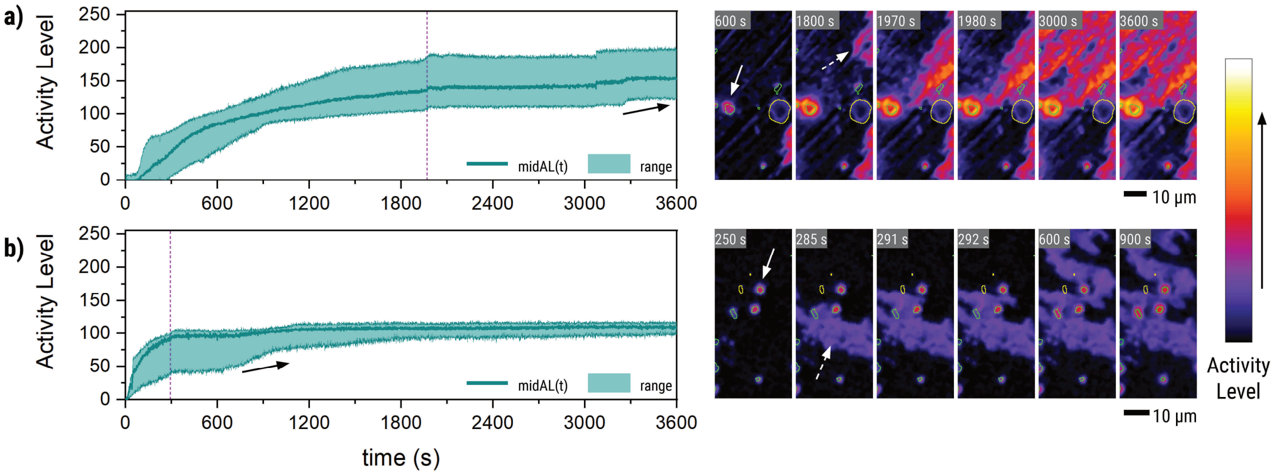

Figure 4.9. (a) sPAD of a streak-linked particle from the sample in Figure 4.1, and **(b)** sPAD of a streak-linked particle from the sample in Figure 4.5 both show arrest of activity increase and resumption at a later time when they linked to a propagating streak. The dashed magenta line in the simplified pixel activity distribution plots indicates when the propagating streak connected to the IMPs and also marks the beginning of the near-horizontal behaviours.

4.3.4. Correlation between OCP transients and streaking corrosion

Figure 4.10a shows the open circuit potential of the smoothly-polished sample during the first 10 minutes of immersion. OCP measurements for the other samples are provided in Supplementary Figure S4.11 to S4.18. Increasing OCP values associated with IMP dealloying were observed during the first two minutes of immersion [24,25]. Dashed magenta lines indicate the onset times of streaking events presented in Figure 4.5. A sudden OCP drop is observed around these onset times (i.e., when streak initiated). The drop is then followed by high frequency fluctuations around an OCP value. Once the fluctuations end, a rapid OCP increase is observed coinciding with the end of the streak propagation.

Figure 4.10b shows global activity maps corresponding to the streaking event initiating at 146 seconds. These activity maps use the reflected light microscopy image at 140 seconds as reference for image subtraction. As such, they only highlight surface changes that happened after that point in time. The maps show that the reported streaking event that initiated at P4 (Figure 4.5b) was the only major surface event happening from 140 to 170 seconds. The maps also show that the streak propagation from 147 seconds (indicated by white arrows in Figure 4.10b) matches the high frequency period observed in the OCP measurements. Absence of changes on the size of the streak between 163 and 170 seconds indicates that streaking terminated at around 163 seconds. At this time, the OCP already increased to pre-drop levels. This suggests that the rapid OCP increase corresponds with the streak approaching termination.

The streaking events at 183, 197, and 389 seconds terminated at 197, 208, and 457 seconds, respectively. As with the streaking at 146 seconds, they also exhibited the sequence of OCP drop, high frequency OCP fluctuations, and OCP increase. This suggests that this particular OCP transient pattern is characteristic of streaking corrosion. The longest interval during which the pattern was observed is from around 211 to 374 seconds. This corresponds to continuation of the streaking that initiated from area 6 and accounts for forming a major part of the streak in the top section of the sample (Figure 4.5a). The streaking corrosion that initiated from area 7 also continued from 463 until 627 s. The same transient pattern is seen during streaking events in the other samples (Supplementary Figure S4.11 to S4.13, S4.17, S4.18).

It should be noted that other features are also present in the OCP transients that go beyond the usual sequence of OCP drop, high frequency transients, and OCP increase associated with streaking corrosion. For instance, at around 250 s (Figure 4.10a), the high frequency transients exhibited a substantial peaking of the baseline. Another superposition of high frequency transients and baseline drift is also apparent at around 480 s. OCP transients for the other samples also exhibited the characteristic streaking corrosion transients. However, simultaneous occurrence with other surface events lead to variations in the observed signal. Detailed analysis of these other forms of OCP transients will be covered in another work.

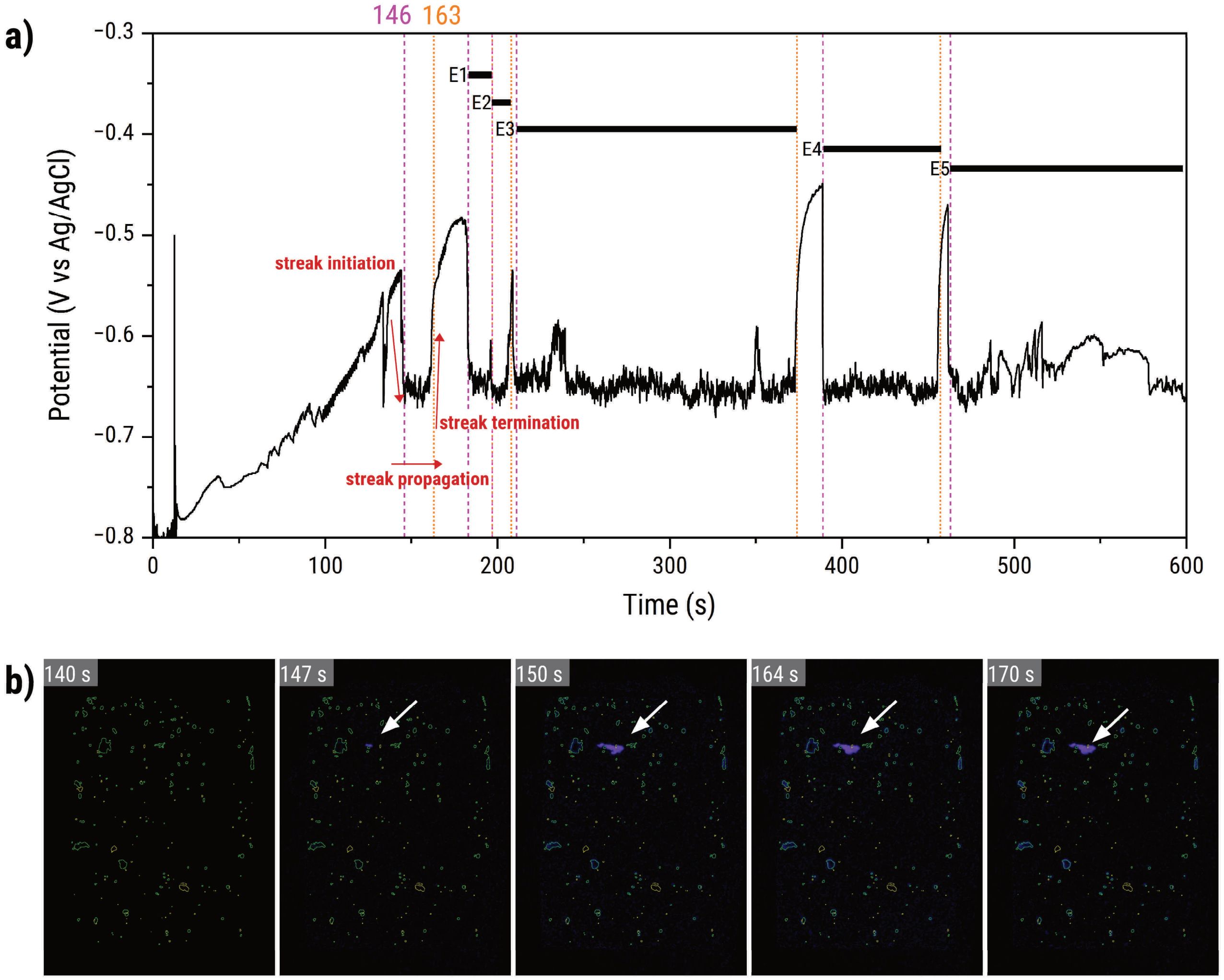

Figure 4.10. (a) Corresponding open circuit potential for the smoothly-polished sample and **(b)** global activity maps corresponding to the streaking corrosion that initiated at 146 s. The reflected light microscopy image at t = 140 s is used as reference to generate these global activity maps so as to isolate the surface processes that gave the electrochemical potential transients at the same period. The duration of the other streaking events on the surface are as follows: **(E1)** 183 – 197 s (Figure 4.5c), **(E2)** 197 – 208 s (Figure 4.5d), **(E3)** 211 – 374 s (continuation of combined streaks from Figure 4.5c and d), **(E4)** 389 – 457 s (Figure 4.5e), **(E5)** 463 – 627 s (continuation of combined streaks from Figure 4.5d and e).

4.4. Discussion

Figure 4.1 and Figure 4.5 show that localized occurrence of streaking corrosion in OCP conditions is due to preferential initiation on intermetallic particles or pre-existing pits. It is evident though that even among IMPs and pits, streaking initiation happens only with a select few. The few IMPs that served as streaking corrosion triggers can be further grouped based on their *optically-observed behaviour*: (case 1) those where the rapid, streaking-type activity occurred directly over the IMP surface, and (case 2) those where such activity emerged only from the developing trench of an IMP undergoing typical dealloying and trenching. A third case (case 3) includes instances where streaking started from pre-existing pits.

Case 1 (i.e., streaking over IMP surface) includes IMPs that exhibited streaking corrosion behaviour over the IMP surface during the course of its activation that eventually led to streaking corrosion. The streaking over the IMP surface was observed before or around the same time as when streaking propagated beyond the IMP boundary (i.e., streak initiated at IMP). Figure 4.11a provides the schematic for the proposed mechanism for this case. The streaking over the IMP surface is observed in the activity maps as rapid spread of activity or in the sPADs as a step increase in the activity level. Figure 4.7 sPADs as well as activity maps from replicate tests (Supporting Information 4.8.2) show that most streak-initiating IMPs belong to this case. P5 showed streaking over the entire IMP surface. Meanwhile, P1, P2, and P3 exhibited partial streaking. Since streaking corrosion is attributed to ASL dissolution [20], streaking over an IMP surface suggests the particle is covered by the ASL (partially or fully). In the absence of the surface layer, the IMPs would have exhibited similar dealloying behaviour as the non-initiating particles (Figure 4.7-N1,N2). Non-destructive pre-immersion analysis of the ASL around IMPs and defects is recommended to validate this. Zhao et al [20] proposed that the dissolution of the surface layer begins with passive layer breakdown, leading to the dissolution of nanograin boundaries. These nanograin boundaries have been previously observed as ~10 nm bands rich in Zn and Mg [11,13,20,26]. Their dissolution then continues through the ASL until the underlying substrate is exposed. This mechanism of ASL dissolution can hypothetically occur on any other section of the sample surface covered by the ASL. This could then trigger streaking corrosion initiation over any part of the AA7075 matrix. Experimentally observed preferential initiation on IMP surfaces here revealed suggest that the underlying particle acts as a trigger for sustained surface layer dissolution. Two possibilities can be considered - the particle caused local variations in the local ASL composition that made it more dissolution-susceptible, or the microgalvanic couple formed between the dissolving Zn- and Mg- rich nanograin boundaries and the underlying IMP promoted sustained dissolution. The second explanation is more likely, given the apparent microgalvanic coupling when IMP activity is temporary inhibited during streaking propagation (Figure 4.8) as this indicates that ASL dissolution can interact with the IMPs. Thus, the microgalvanic coupling between the IMP and ASL potentially kickstarts ASL dissolution. Once sufficiently low pH due to hydrolysis of dissolved ions is achieved, the ASL dissolution becomes autocatalytic (i.e., low pH drives dissolution and dissolution sustains low pH) and drives further propagation [12,27].

Case 2 (i.e., streaking from trench around IMP) is characterized by no detectable streaking over the IMP surface prior to streaking corrosion over the matrix (i.e., streaking initiates close to the boundary of the IMP). Instead, the streak-initiating IMP first exhibited dealloying and trenching, similar to the non-initiating IMPs. Figure 4.11b provides the schematic for the proposed mechanism for this case. This behaviour is only observed with P4 (Figure 4.7-P4) and another particle in the replicate tests (Supporting Information 4.8.2). The absence of streaking over the particle suggests that the particle has no ASL cover. Instead, the ASL is situated close to the particle boundary. The IMP dealloying and subsequent trenching potentially generates local chemistry (i.e., high pH) that triggered initial passive layer breakdown of the adjacent ASL. Microgalvanic coupling between the IMP and the ASL then drives propagation of the ASL to areas beyond the high pH vicinity of the IMP. As with case 1, once sufficiently low pH is achieved on the propagation front, the ASL dissolution becomes autocatalytic and drives further streaking corrosion propagation. Notably, the high pH zone close to the dealloying IMP surface potentially explains limited observation of this particular case among the streak-initiating IMPs since the high pH can potentially passivate ASL dissolution. This suggests that for case 2 to proceed, the high pH zone around the IMP should be relatively small, allowing the initial ASL dissolution to produce the acidic environment that will enable the ASL dissolution front to spread out to the matrix. If these conditions are not met, the IMP is more likely to follow typical pathway of localized dealloying and trenching, without initiating streaking.

Case 3 (i.e., streaking from pits) covers streaking corrosion that initiated from a pre-existing pit (Figure 4.5d). The initiation is attributed to the aggressive local chemistry, like low pH [28], which develops within the pit likely due to processes such as crevice corrosion [29]. If the pit is in close proximity to an ASL, the low pH can trigger sustained ASL dissolution (i.e., autocatalytic ASL dissolution) and lead to streaking corrosion propagation (Figure 4.11b) [12,27].

The development of sustained ASL dissolution in all of the cases potentially accounts for the observed OCP drop when streaking corrosion is initiating (Figure 4.10a). This is consistent with previous reports of streaking corrosion being a dissolution process [11,12]. Huang et al proposed that the ASL dissolution will continue propagating as long as the pH is low enough to drive breakdown ahead of the streak [12,21]. The depth of attack stemming from streaking corrosion over the matrix appears to be limited though which is why the activity levels associated with propagating streaks remain low (i.e., purple colour in the activity maps). The low activity level of the streaked areas also show minimal surface damage - shallower than trenching around most IMPs (Figure 4.4, Figure 4.6). Even though the corrosion attack is shallow, its propagation can undermine adhesion between protective coatings and the AA7075 substrate. This can then lead to issues such as filiform corrosion [15,30]. The streaking propagation also results in the high-frequency fluctuations around an OCP baseline (Figure 4.10a). It should be noted that the high-frequency fluctuations happened after an OCP drop during streaking initiation.

The propagating ASL dissolution can couple with the IMP surface, leading to slower dealloying rates. This is seen as near-horizontal profiles in the sPADs (Figure 4.7, Figure 4.8) following streaking initiation. The near-horizontal profiles confirm that the degree of change on the IMP surface is not increasing which suggests that the dealloying of the particle is not progressing. This apparent inhibition is attributed to the Zn and Mg in the ASL [11,13,20,26] acting as sacrificial anodes [31,32] which temporarily limit dissolution of less noble components of the IMPs (e.g., Al). Once the streaking stops, the sacrificial anode effect ends, and IMP dealloying resumes (Figure 4.8, Figure 4.9). The streaking corrosion termination has previously been attributed to the pH at the front not being low enough due to dilution with the bulk electrolyte [12,21]. However, there is also the possibility that streaking ceases because the compositional differences driving the phenomenon are no longer present — specifically, that the ASL has fully dissolved. As such, further experimentation is recommended to determine the mechanism behind the termination of streaking corrosion. Nonetheless, the termination of the rapid anodic dissolution of the surface layer also leads to a return of the potential to the pre-streaking state (i.e., OCP increase) wherein cathodic reactions (e.g., oxygen reduction reaction) on the IMP surfaces are balanced by dissolution of less noble components on the intermetallic particle and on the trenches (Figure 4.10a). The observed OCP increase after streaking termination can thus be interpreted as the system’s relaxation after being perturbed by the streaking corrosion.

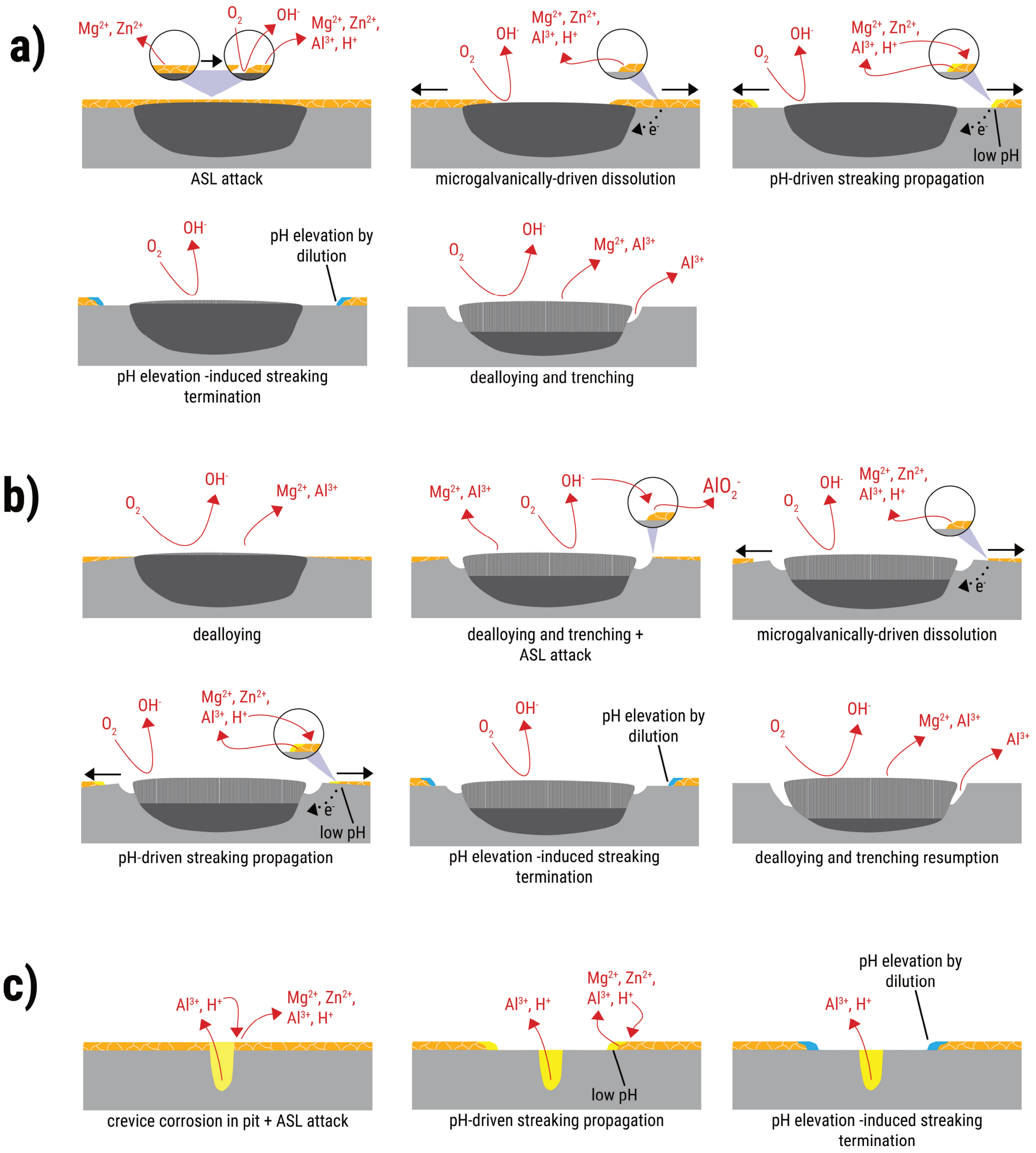

Figure 4.11. (a) initiation from an IMP with streaking over the IMP surface, **(b)** initiation from the trench of an IMP undergoing typical dealloying and trenching, and **(c)** initiation from pre-existing pits.

4.5. Conclusion

In situ quantitative reflected light microscopy analysis of AA7075-T6 exposed to a saline environment at its OCP revealed that streaking corrosion preferentially starts on intermetallic particles with characteristic surface activity and on defects. This explains why streaking does not appear uniformly across the AA7075-T6 surface, even though the altered surface layer is prone to breakdown. Optical observations show that most streak-initiating IMPs exhibit characteristic surface activity consistent with streaking, likely due to partial or full coverage by the ASL. Monitoring and quantifying changes on IMP surfaces during streaking propagation revealed previously unreported galvanic interaction between a propagating streak and connected IMPs. This interaction is observed as temporary inhibition of IMP dealloying that is maintained whilst the streak is propagating. Capturing these interactions across different sites on a corroding surface with high temporal resolution demonstrates a unique capability of in situ optical analysis, providing insights not previously documented.

Concurrent electrochemical measurements revealed a distinct OCP pattern associated with streaking corrosion. The process begins with an OCP drop to a lower baseline, marking the initiation of stable ASL dissolution. As streaking corrosion propagates, high-frequency OCP fluctuations appear around the baseline. Finally, when ASL dissolution ceases, cathodic reactions on IMP surfaces dominate and trigger a rapid OCP increase. This well-defined sequence of OCP changes could serve as a tool for detecting streaking corrosion, even in the absence of direct visual confirmation.

4.6. References

[1] A. Kosari, F. Tichelaar, P. Visser, H. Zandbergen, H. Terryn, J.M.C. Mol, Dealloying-driven local corrosion by intermetallic constituent particles and dispersoids in aerospace aluminium alloys, *Corros. Sci.* 177 (2020) 108947. doi:10.1016/j.corsci.2020.108947.

[2] A. Kumar, G.P. Chaudhari, S.K. Nath, Correlation of microstructure with corrosion performance in high zinc 7068 aluminum alloy aged using different T6 conditions, *Mater. Charact.* 191 (2022) 112133. doi:10.1016/j.matchar.2022.112133.

[3] R. Ayer, J.Y. Koo, J.W. Steeds, B.K. Park, Microanalytical study of the heterogeneous phases in commercial Al-Zn-Mg-Cu alloys, *Metall. Trans. A* 16 (1985) 1925–1936. doi:10.1007/bf02662393.

[4] Y. Zhu, K. Sun, G.S. Frankel, Intermetallic phases in aluminum alloys and their roles in localized corrosion, *J. Electrochem. Soc.* 165 (2018) C807–C820. doi:10.1149/2.0931811jes.

[5] A. Kosari, H. Zandbergen, F. Tichelaar, P. Visser, P. Taheri, H. Terryn, J.M.C. Mol, In-situ nanoscopic observations of dealloying-driven local corrosion from surface initiation to in-depth propagation, *Corros. Sci.* 177 (2020) 108912. doi:10.1016/j.corsci.2020.108912.

[6] T. Hashimoto, X. Zhang, X. Zhou, P. Skeldon, S.J. Haigh, G.E. Thompson, Investigation of dealloying of S phase (Al2CuMg) in AA2024-T3 aluminium alloy using high resolution 2D and 3D electron imaging, *Corros. Sci.* 103 (2016) 157–164. doi:10.1016/j.corsci.2015.11.013.

[7] C.F. Mallinson, P.M. Yates, M.A. Baker, J.E. Castle, A. Harvey, J.F. Watts, The localised corrosion associated with individual second phase particles in AA7075-T6: A study by SEM, EDX, AES, SKPFM and FIB-SEM, *Mater. Corros.* 68 (2017) 748–763. doi:10.1002/maco.201609312.

[8] F. Andreatta, H. Terryn, J.H.W. de Wit, Effect of solution heat treatment on galvanic coupling between intermetallics and matrix in AA7075-T6, *Corros. Sci.* 45 (2003) 1733–1746. doi:10.1016/s0010-938x(03)00004-0.

[9] L.L. Liu, Q.L. Pan, X.D. Wang, S.W. Xiong, The effects of aging treatments on mechanical property and corrosion behavior of spray formed 7055 aluminium alloy, *J. Alloys Compd.* 735 (2018) 261–276. doi:10.1016/j.jallcom.2017.11.070.

[10] W. Huo, J. Hu, H. Cao, Y. Du, W. Zhang, Y. Zhang, Simultaneously enhanced mechanical strength and inter-granular corrosion resistance in high strength 7075 Al alloy, *J. Alloys Compd.* 781 (2019) 680–688. doi:10.1016/j.jallcom.2018.12.024.

[11] S.S. Wang, J.T. Jiang, G.H. Fan, G.S. Frankel, L. Zhen, Effects of long-term natural aging on the altered surface layer on an Al-Zn-Mg-Cu alloy and on corrosion properties, *Electrochim. Acta* 266 (2018) 34–42. doi:10.1016/j.electacta.2018.02.001.

[12] R.S. Huang, C.J. Lin, H.S. Isaacs, A difference-imaging technique used to study streaking corrosion of aluminum alloys AA7075 and AA8006 in chloride solution, *Electrochem. Solid-State Lett.* 9 (2006) B11–B14. doi:10.1149/1.2140503.

[13] Y. Liu, A. Laurino, T. Hashimoto, X. Zhou, P. Skeldon, G.E. Thompson, G.M. Scamans, C. Blanc, W.M. Rainforth, M.F. Frolish, Corrosion behaviour of mechanically polished AA7075-T6 aluminium alloy, *Surf. Interface Anal.* 42 (2010) 185–188. doi:10.1002/sia.3136.

[14] J. Seong, F. Yang, F. Scheltens, G.S. Frankel, N. Sridhar, Influence of the altered surface layer on the corrosion of AA5083, *J. Electrochem. Soc.* 162 (2015) C209–C218. doi:10.1149/2.0321506jes.

[15] Y. Liu, T. Hashimoto, X. Zhou, G.E. Thompson, G.M. Scamans, W.M. Rainforth, J.A. Hunter, Influence of near-surface deformed layers on filiform corrosion of AA3104 aluminium alloy, *Surf. Interface Anal.* 45 (2013) 1553–1557. doi:10.1002/sia.5232.

[16] A. Afseth, J.H. Nordlien, G.M. Scamans, K. Nisancioglu, Influence of heat treatment and surface conditioning on filiform corrosion of aluminium alloys AA3005 and AA5754, *Corros. Sci.* 43 (2001) 2359–2377. doi:10.1016/s0010-938x(01)00019-1.

[17] A. Afseth, J.H. Nordlien, G.M. Scamans, K. Nisancioglu, Effect of thermo-mechanical processing on filiform corrosion of aluminium alloy AA3005, *Corros. Sci.* 44 (2002) 2491–2506. doi:10.1016/s0010-938x(02)00036-7.

[18] R. Ambat, A.J. Davenport, A. Afseth, G. Scamans, Electrochemical behavior of the active surface layer on rolled aluminum alloy sheet, *J. Electrochem. Soc.* 151 (2004) B53. doi:10.1149/1.1635828.

[19] B. Liu, X. Zhang, X. Zhou, T. Hashimoto, J. Wang, The corrosion behaviour of machined AA7150-T651 aluminium alloy, *Corros. Sci.* 126 (2017) 265–271. doi:10.1016/j.corsci.2017.07.008.

[20] Z. Zhao, G.S. Frankel, On the first breakdown in AA7075-T6, *Corros. Sci.* 49 (2007) 3064–3088. doi:10.1016/j.corsci.2007.02.001.

[21] R.S. Huang, C.J. Lin, H.S. Isaacs, Measuring streaking rates of an Al–Zn alloy using a difference imaging technique, *Corros. Sci.* 48 (2006) 1867–1873. doi:10.1016/j.corsci.2006.05.039.

[22] S. Wang, G.S. Frankel, J. Jiang, J. Chen, S. Dai, L. Zhen, Mechanism of localized breakdown of 7000 series aluminum alloys, *J. Electrochem. Soc.* 160 (2013) C493–C502. doi:10.1149/2.080310jes.

[23] M. Mopon, A. Mol, S.J. Garcia, Effect of delayed inhibitor supply on AA2024-T3 intermetallic activity: A local in situ analysis with reflected microscopy, *Corros. Sci.* 230 (2024) 111910. doi:10.1016/j.corsci.2024.111910.

[24] M. Olgiati, P.J. Denissen, S.J. Garcia, When all intermetallics dealloy in AA2024-T3: quantifying early stage intermetallic corrosion kinetics under immersion, *Corros. Sci.* 192 (2021) 109836. doi:10.1016/j.corsci.2021.109836.

[25] A.M. Homborg, M. Olgiati, P.J. Denissen, S.J. Garcia, An integral non-intrusive electrochemical and in-situ optical technique for the study of the effectiveness of corrosion inhibition, *Electrochim. Acta* 403 (2022) 139619. doi:10.1016/j.electacta.2021.139619.

[26] Z. Zhao, G.S. Frankel, Surface layer dissolution kinetics of aluminum alloy 7075 in various tempers, *Corrosion* 63 (2007) 613–624. doi:10.5006/1.3278411.

[27] H.S. Isaacs, C. Scheffey, R. Huang, The location of events producing potential transients during pitting of freely corroding Al and its alloys, *ECS Trans.* 11 (2008) 1–12. doi:10.1149/1.2925257.

[28] J. Xiao, S. Chaudhuri, Predictive modeling of localized corrosion: An application to aluminum alloys, *Electrochim. Acta* 56 (2011) 5630–5641. doi:10.1016/j.electacta.2011.04.019.

[29] Y. Li, Y. Tang, X. Liu, Y. Li, Insight into the crevice corrosion mechanism of AA7075-T651 high-strength aluminum alloys in neutral nitrate solution: The effect of Cl−, *Mater. Corros.* 75 (2024) 1373–1388. doi:10.1002/maco.202414334.

[30] B. Liu, X. Zhou, X. Zhang, Filiform corrosion behaviour on machined AA7150 aluminium alloy, *Trans. Nonferrous Met. Soc. China* 30 (2020) 2056–2066. doi:10.1016/s1003-6326(20)65360-2.

[31] A. Korjenic, E. Romanovskaia, J.R. Scully, Spatially resolved assessment and analysis of Al-Zn, Mg, and Mg/Al-Zn metal-rich primers applied to AA7075-T651 in full immersion, *J. Electrochem. Soc.* 171 (2024) 091505. doi:10.1149/1945-7111/ad7535.

[32] T. Vu Dinh, W.W. Sun, Y. Yue, Y. Wu, C.R. Hutchinson, S. Thomas, On the miniaturised sacrificial protection achieved by surface precipitation in aluminium alloys, *Corros. Sci.* 145 (2018) 67–79. doi:10.1016/j.corsci.2018.09.011.

4.7. Movies

The following movies can be accessed through the published article via the DOI link of the published article corresponding to this chapter or through the provided QR codes.

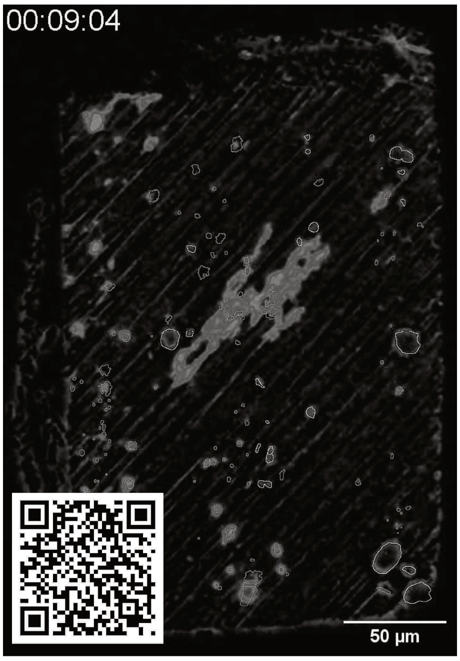

Movie 4.1. Evolution of surface changes on roughly-polished AA7075 sample during the first 10 minutes of immersion in 0.05 M NaCl

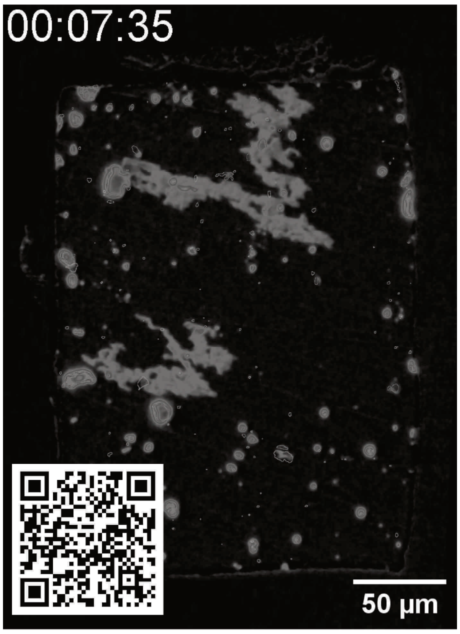

Movie 4.2. Evolution of surface changes on smoothly-polished AA7075-T6 sample during the first 15 minutes of immersion in 0.05 M NaCl

4.8. Supporting Information

4.8.1. Supplementary Figures

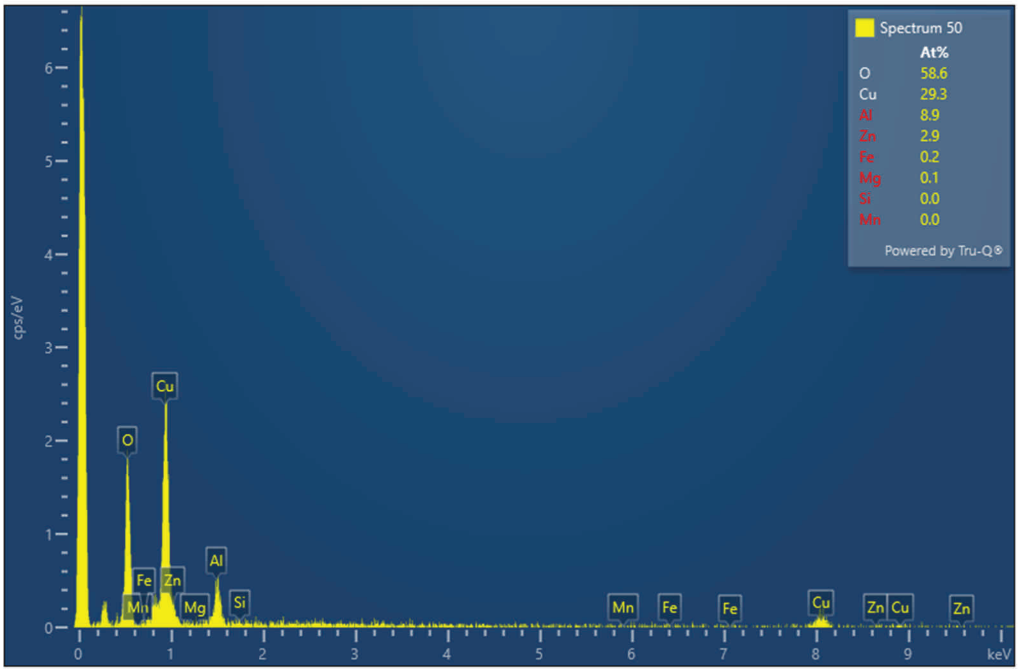

Figure S4.1. Post-mortem EDX spectrum of P1. Its high Cu atomic fraction is consistent with the composition of a dealloyed S-phase particle.

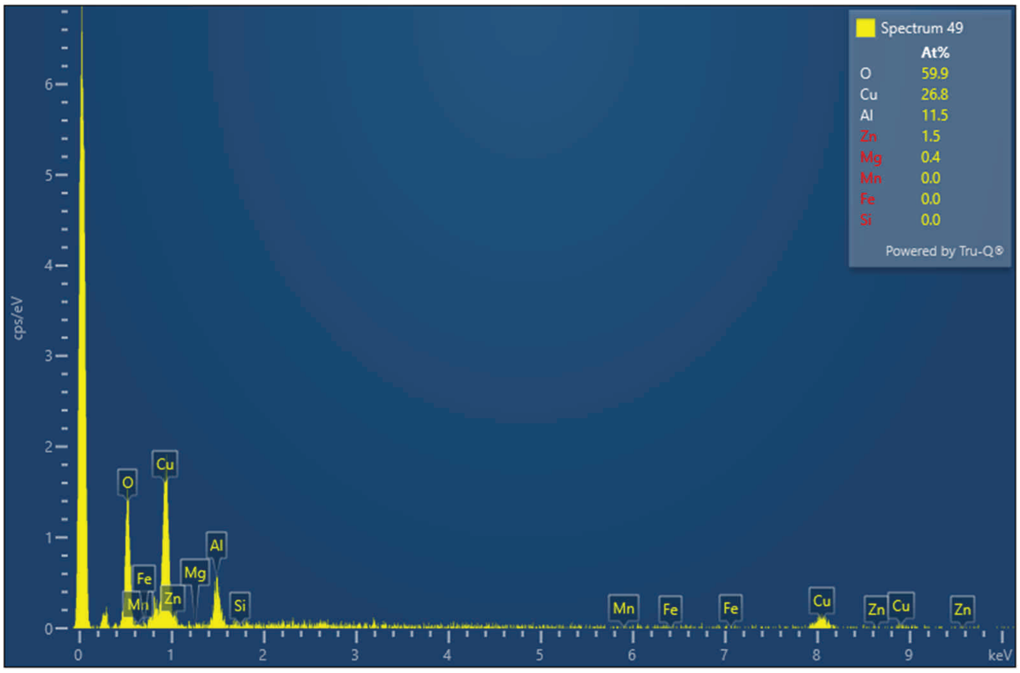

Figure S4.2. Post-mortem EDX spectrum of P2. Its high Cu atomic fraction is consistent with the composition of a dealloyed S-phase particle.

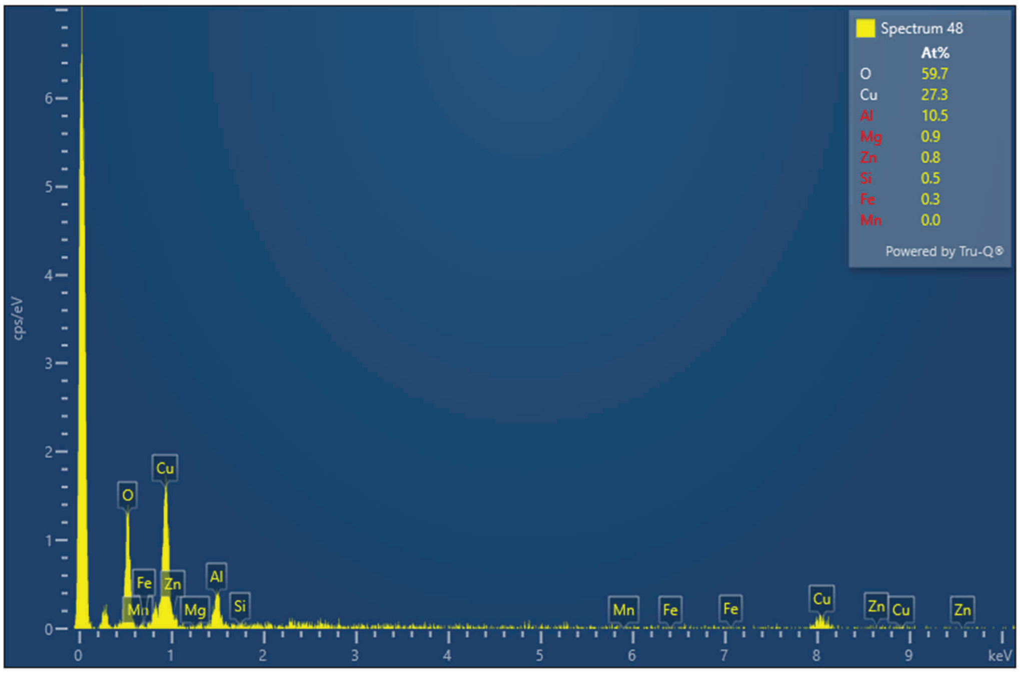

Figure S4.3. Post-mortem EDX spectrum of P3. Its high Cu atomic fraction is consistent with the composition of a dealloyed S-phase particle.

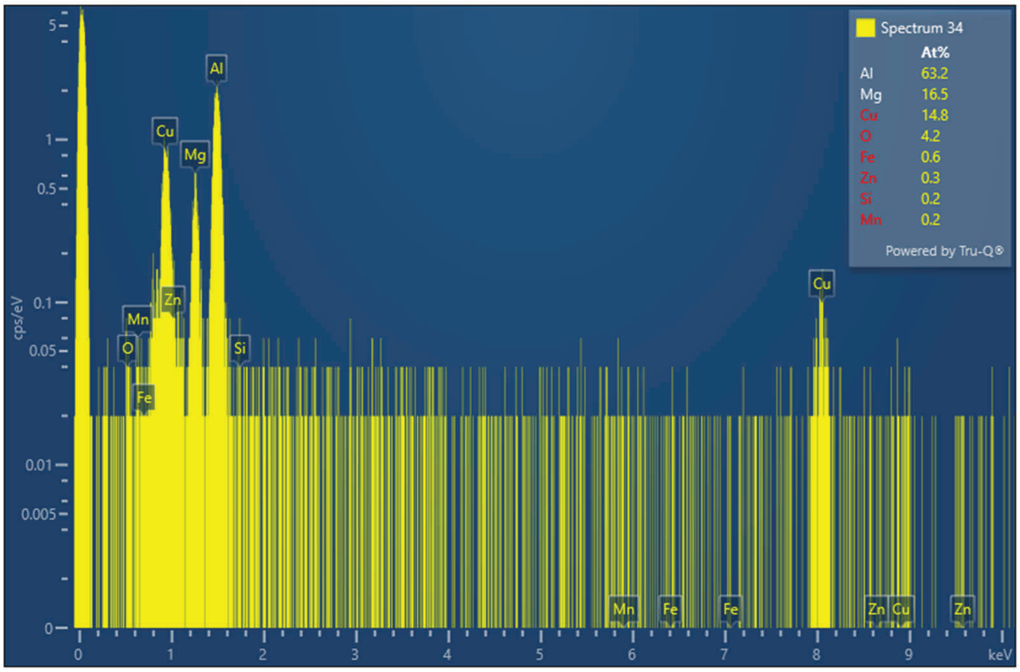

Figure S4.4. Pre-immersion EDX spectrum of P4. Its Cu and Mg fractions are consistent with an S-phase intermetallic particle.

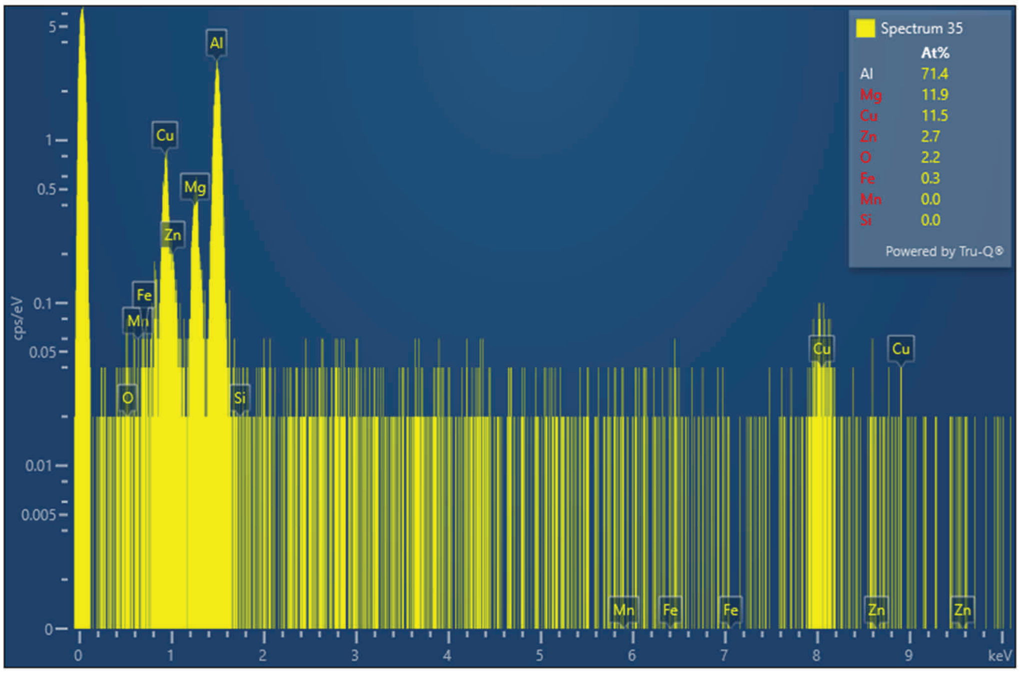

	At%
Al	71.4
Mg	11.9
Cu	11.5
Zn	2.7
O	2.2
Fe	0.3
Mn	0.0
Si	0.0

Figure S4.5. Pre-immersion EDX spectrum of P5. Its Cu and Mg fractions are consistent with an S-phase intermetallic particle.

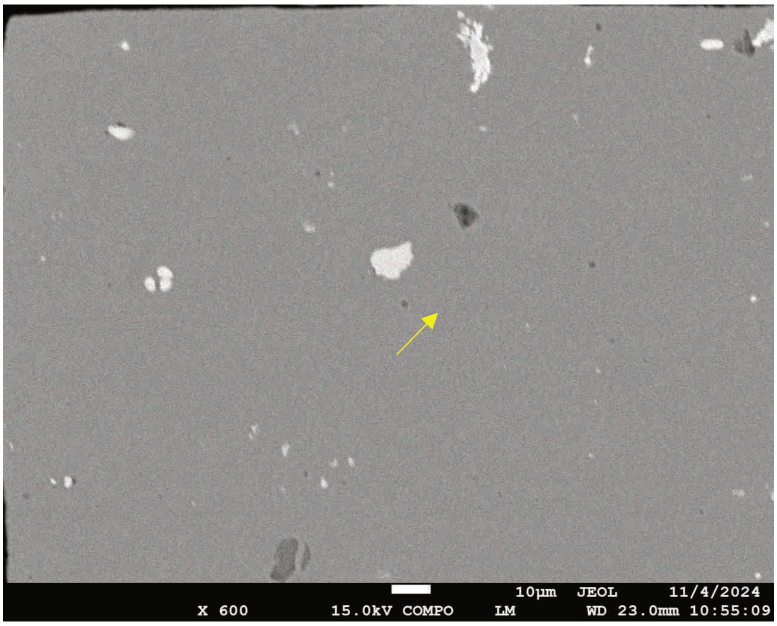

Figure S4.6. Pre-immersion secondary electron image of the Figure 4.5 sample with the pit initiating the Figure 4.5d streak indicated by the yellow arrow.

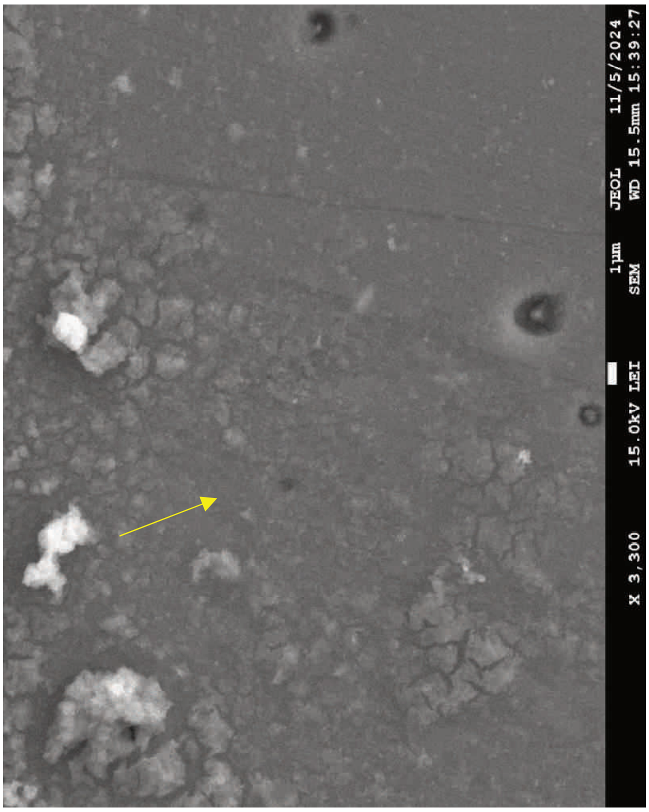

Figure S4.7. Post-immersion secondary electron image of the Figure 4.5 sample with the pit initiating the Figure 5e streak indicated by the yellow arrow. The image is rotated to match the alignment of the reflected microscopy image and activity maps presented in Figure 4.5.

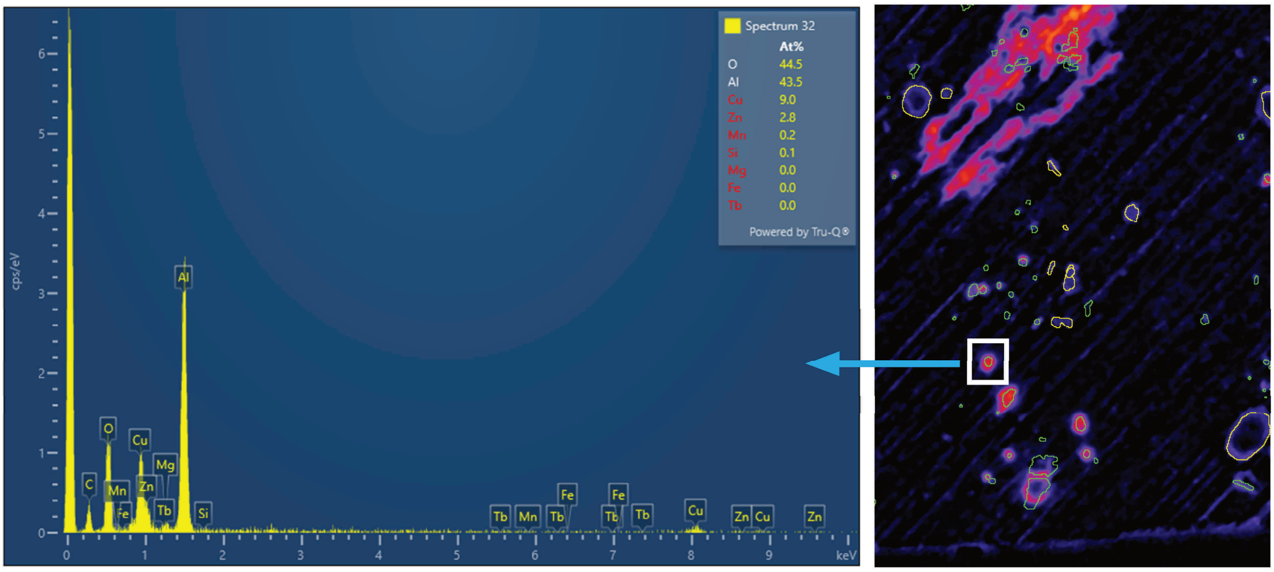

Spectrum 32

	At%
O	44.5
Al	43.5
Cu	9.0
Zn	2.8
Mn	0.2
Si	0.1
Mg	0.0
Fe	0.0
Tb	0.0

Powered by Tru-Q®

Figure S4.8. Post-mortem EDX spectrum of N1. Its high Cu atomic fraction is more or less consistent with the composition of a dealloyed S-phase particle. The white box in the right frame indicates N1's location relative to the lower portion of the sample.

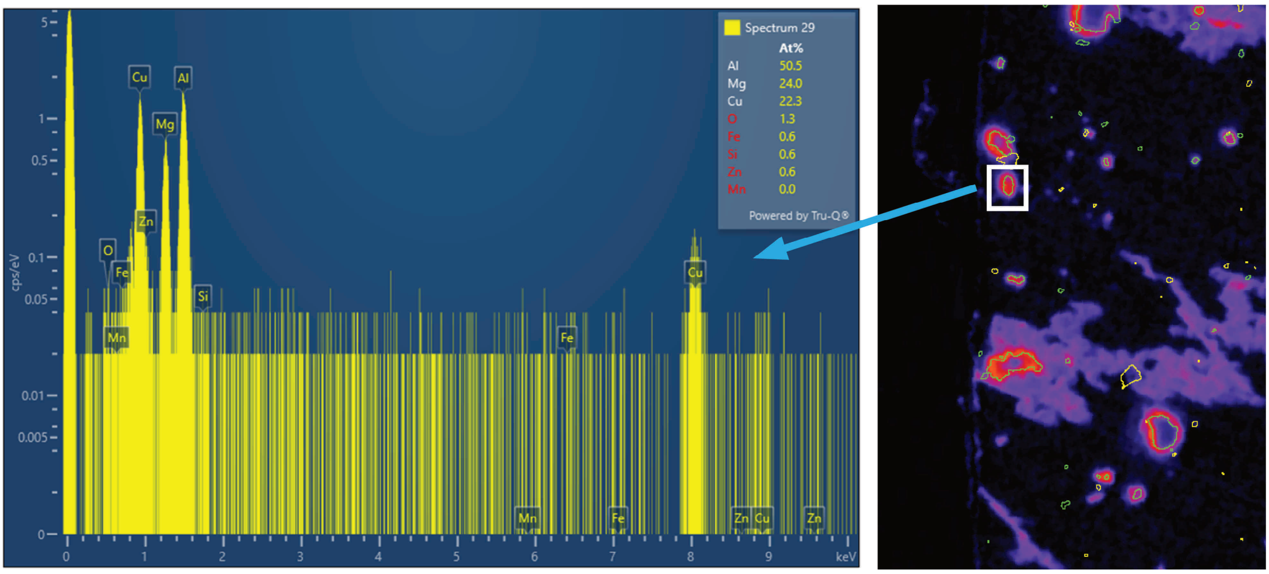

Figure S4.9. Pre-immersion EDX spectrum of N2. Its composition is consistent with an S-phase intermetallic particle. The white box in the right frame indicates N1's location relative to the lower portion of the sample.

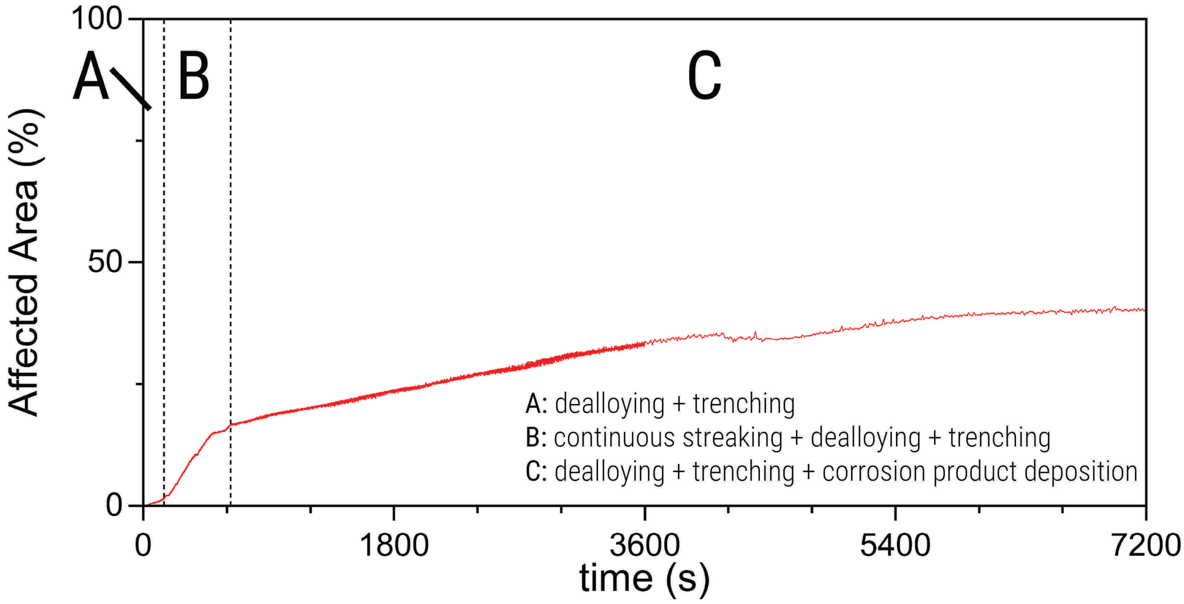

Figure S4.10. Affected area plot for smoothly-polished sample also show a distinct period with rapid affected area increase (period B). This period covers the continuous propagation of streaks originating from the areas 6 and 7 presented in Figure 4.5. Period C covers the period following streaking propagation throughout the surface. No rapid affected area increase associated with streaking corrosion is observed in this period. This is consistent with the OCP data from 600 to 7200 s shown in Figure S4.15 and Figure S4.16 which also do not show the OCP transient patterns associated with streaking corrosion.

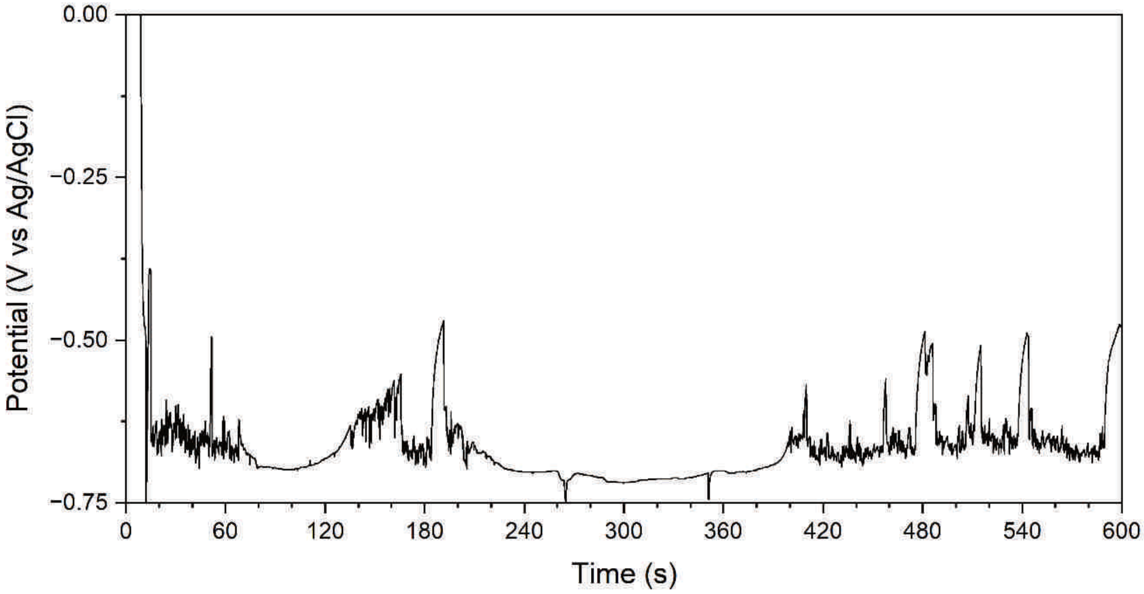

Figure S4.11. In situ OCP measurements of the roughly-polished sample from 0 to 600 s of its immersion in 0.05 M NaCl. The major streaking events referred in the main text which occurred during this period are as follows - (1) Figure 4.1 area 1: 1 – 16 s, (2) Figure 4.1 area 2: 14 – 37 s, (3) Figure 4.1 area 3: 38 – 51 s, (4) Figure 4.3a: 41 – 54 s, (5) Figure 4.3b: 153 – 171 s, with a delayed extension from 180 – 183 s, (6) Figure 4.3c: 194 – 209 s, (7) Figure 4.3d: started at around 389 s and then spread at a stepwise manner.

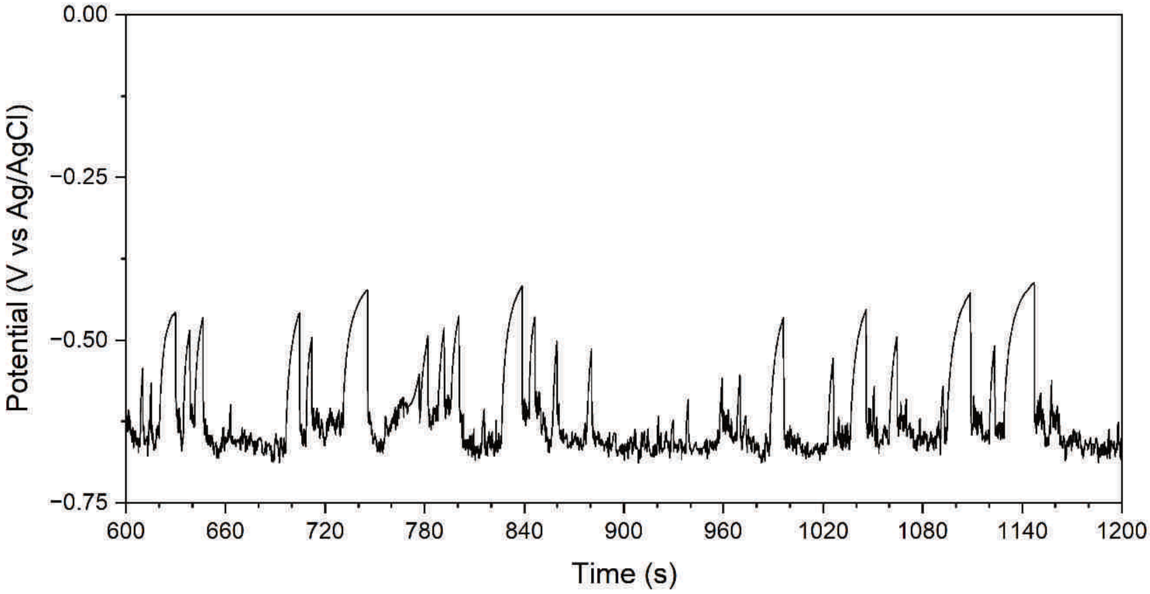

Figure S4.12. In situ OCP measurements of the roughly-polished sample from 600 to 1200 s of its immersion in 0.05 M NaCl. The transients can be traced to the stepwise growth of the streak that initiation from P3 (Figure 4.3d).

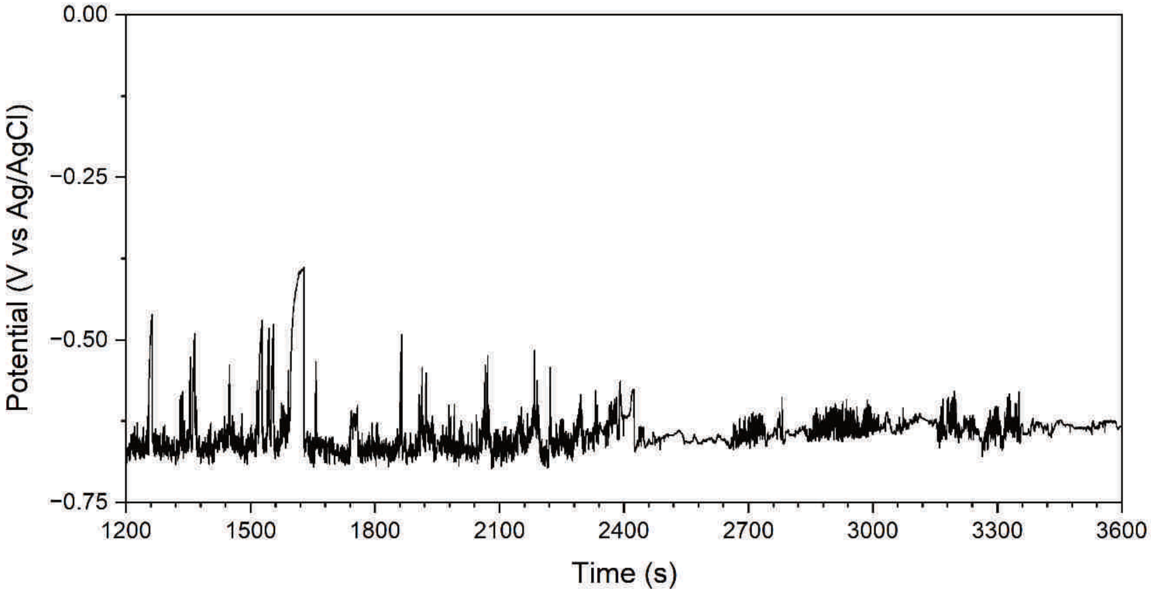

Figure S4.13. In situ OCP measurements of the roughly-polished sample from 1200 to 3600 s of its immersion in 0.05 M NaCl. It can be observed that right around the overall termination of streaking (~2400 s), a transition from high frequency to quiescent signals is observed. The transition is also consistent with the change in affected area trends (from period B to period C) shown in Figure 4.2.

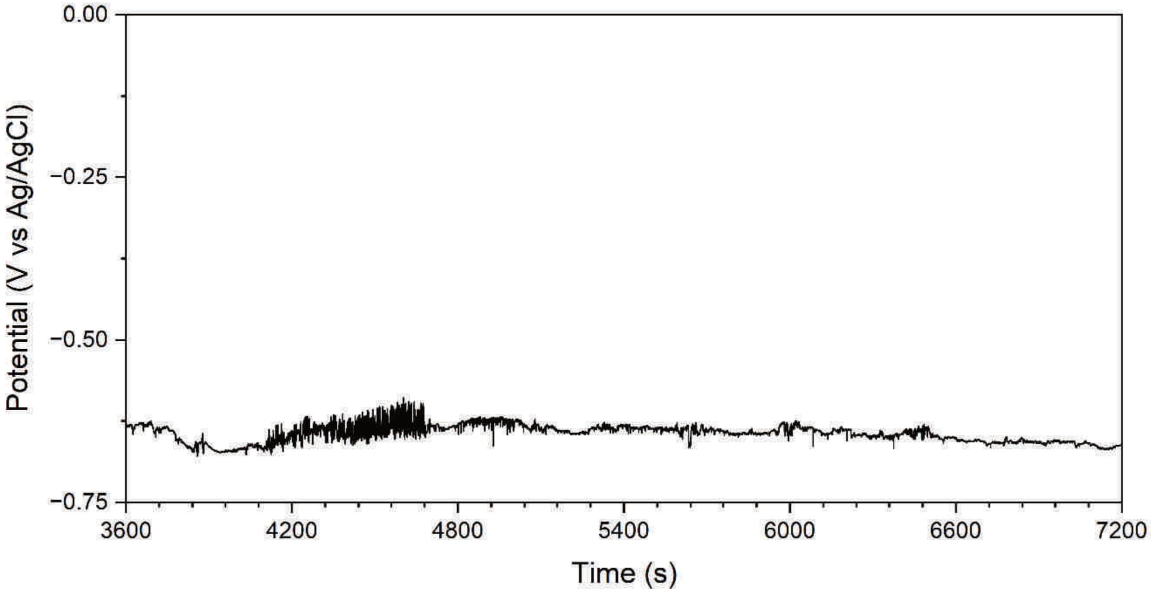

Figure S4.14. In situ OCP measurements of the roughly-polished sample from 3600 to 7200 s of its immersion in 0.05 M NaCl. It is observed that the OCP fluctuations have lower amplitude compared to the periods where streaking corrosion is present.

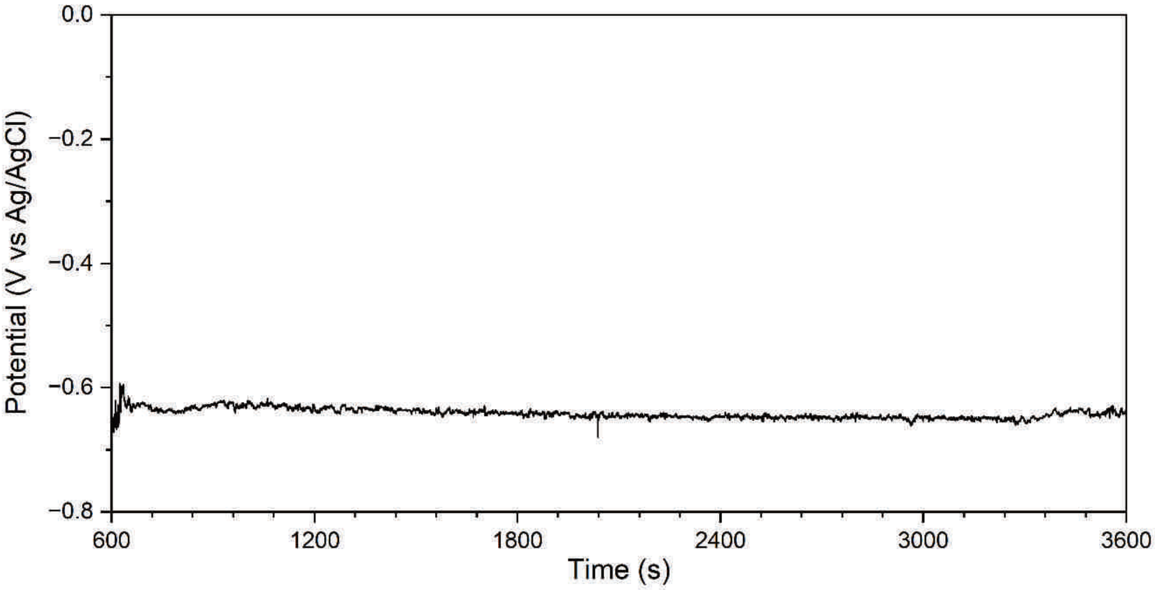

Figure S4.15. In situ OCP measurements of the smoothly-polished sample from 600 to 3600 s of its immersion in 0.05 M NaCl. Overall streaking terminated at around 626 s. After this period, the OCP measurements generally lack the high frequency transients associated with streaking propagation. The transition to this quiescent period is consistent with the shift from period A to period B shown in Figure S4.10.

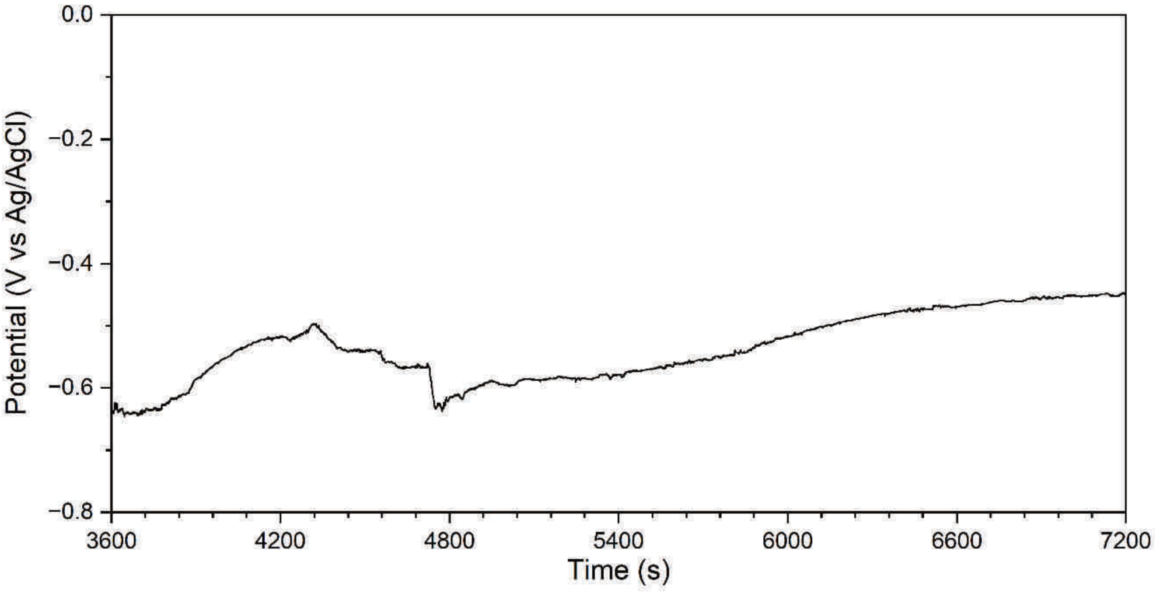

Figure S4.16. In situ OCP measurements of the smoothly-polished sample from 3600 to 7200 s of its immersion in 0.05 M NaCl. The OCP transients do not show the transient pattern that coincide with streaking corrosion propagation and is consistent with the absence of streaking highlighted in Figure S4.10.

4.8.2. Supplementary Discussion

This supplementary discussion presents analysis of the activity maps of streaking corrosion initiation sites observed in replicate runs for smoothly-polished AA7075-T3 samples exposed to 0.05 M NaCl. As presented in the main text, smoothly-polished samples refer to samples with less visible grooves from mechanical grinding and polishing of the surface.

Figure S4.17a shows similar corrosion behaviour to the smoothly polished sample in the main text (Figure 5). Its corrosion is also characterized by local corrosion around the intermetallic particles and signs of streaking corrosion marked by numbered points. It is noted that the sample was only immersed for 40 mins since we wanted to analyse the composition of the streaks with minimal interference from corrosion product deposition often encountered at later stages of immersion. Activity maps in Figure S4.17b-e and Figure S4.18b-e show streaking corrosion initiated on these sites.

Figure S4.17b shows that the streaking corrosion in point 1 started from the surface of the intermetallic particle right from the very start of immersion. There were no signs of dealloying on the surface when the streaking began. This behaviour is similar to those of P1, P3, and P5 in the main text (Figure 3, Figure 5). Post-mortem SEM confirmed that the streaking is connected to the crescent-shaped intermetallic particle and that the particle underwent dealloying and trenching after streaking. Post-mortem EDX analysis (Figure S4.19) shows that the particle has more Fe than the matrix. It also contained more oxygen likely due to its corrosion. The streaked area did not show any detectable difference from the un-streaked area. This indicates two things – (1) there are no streaking corrosion products left in the streaked area, and (2) the streaked matrix has the same composition as the un-streaked matrix. Both of these are consistent with streaking corrosion being the anodic dissolution of a thin surface layer. Surface layer dissolution has been reported to generate Zn and Mg ions [20]. These ions require alkaline pH to precipitate. Moreover, once the surface layer is removed, the remnant will simply be the bulk matrix which is expected to have the same composition as the rest of the matrix. Figure S4.17c-e show that streaking corrosion initiation in points 2 to 4 also started from particles that have similar behaviour as the crescent-shaped particle in Figure S4.17b, as well as P1, P3, and P5 in the main text (i.e., streaking over IMP surface before dealloying/trenching). Post-mortem EDX analysis of the initiating particle in point 3 (Figure S4.20) and point 4 (Figure S4.21) both show that the particles have more Fe than the matrix. As with the point 1, no difference was detected between the streaked and un-streaked areas from both points. The absence of detectable differences between streaked and un-streaked areas suggests two possibilities: (1)

EDX analysis is limited in detecting streaking because the altered surface layer (ASL) is too thin, or (2) the streaking corrosion has removed compositional differences, resulting in no detectable contrast. Distinguishing between these scenarios requires analysis with more surface-sensitive techniques, which is recommended for future work.

Figure S4.18b-e also show that the initiation in points 5 to 8 are also similar to points 1 to 4. They also initiated from intermetallic particles. The particles were also not showing signs of active dealloying and trenching prior to streaking. The reflected light microscopy image at 30 mins of immersion (Figure S4.18a) and the post-mortem SEM images (Figure S4.18b-d) also show that the particles underwent dealloying and trenching after the streaking events.

Figure S4.22a shows similar corrosion behaviour to the other smoothly polished samples. Its corrosion is characterized by local corrosion around the intermetallic particles and signs of streaking corrosion marked by numbered points. Activity maps and microscopy images in Figure S4.22b-e and Figure S4.23b-d show streaking corrosion initiated on these sites. Figure S4.22b shows reflected light microscopy images showing the evolution of streaking in point 1. The microscopy images were used instead of the activity maps because there were brightness issues encountered during the first seconds of immersion and the first clear image was only obtained after 10 seconds of immersion. Nonetheless, the microscope images show that a horizontal streak developed from an intermetallic particle located at the right side of the frame. From 10 to 14 seconds of immersion, extension of the streak on its left-most front (indicated by the red arrows) is observed. Microscopy image at 720 s of immersion shows that the initiating IMP is undergoing corrosion and trenching. As such, the streaking initiation in point 1 can of the Figure S4.22 sample is comparable to P1, P3, and P5 (i.e., streaking over IMP surface before dealloying/trenching). Figure S4.22c shows that the streaking corrosion in point 2 does not appear to be connected to an intermetallic particle based on the absence of localized pixel activity associated with dealloying and trenching. This could be another example of streak originating from a pit but this was not confirmed with post-mortem testing. Figure S4.22d shows that the streaking in point 3 originated from a region with localized pixel activity associated with intermetallic particle dealloying/trenching. However, before the streaking was observed on the matrix, a rapid activity spread over the intermetallic particle surface was first observed between 535 and 536 s. This suggests that the initiation in point 2 is comparable to P2. Figure S4.22e shows that the streaking in point 4 also originated from a region with localized pixel activity associated with intermetallic particle dealloying/trenching. The streaking on the matrix appears to be preceded by a rapid activation of the middle particle (see red arrow in Figure S4.22e – 553 s) which suggests that this might be a similar case to P2 as well. Figure S4.22f shows that the streaking in point 5 originated from a region with visible intermetallic particle dealloying and trenching. This make this initiation similar to P4 in the main text (Figure 5). Figure S4.22g and Figure S4.23b-c shows that the streaking corrosion events in points 6 to 8 do not appear to be connected to an intermetallic particle based on the absence of localized pixel activity associated with dealloying and trenching. There is also no detectable dealloying or trenching in the areas after the streaking event which makes an intermetallic particle initiation less likely. Figure S4.23d shows that there was also no activity indicative of dealloying or trenching prior to the initiation of the streaking in point 9. However, signs of dealloying and trenching (i.e., high activity localized around a site) were observed with further immersion which suggests that this particular initiation is comparable to P1, P3, and P5 in the main text.

Overall, the replicates consistently show that there is preferential streaking corrosion initiation from intermetallic particles. Moreover, the streaking initiation events presented in Figure S4.17, Figure S4.18, Figure S4.22, and Figure S4.23 also give the signature OCP transient sequence as shown in Figure S4.24 and Figure S4.25.

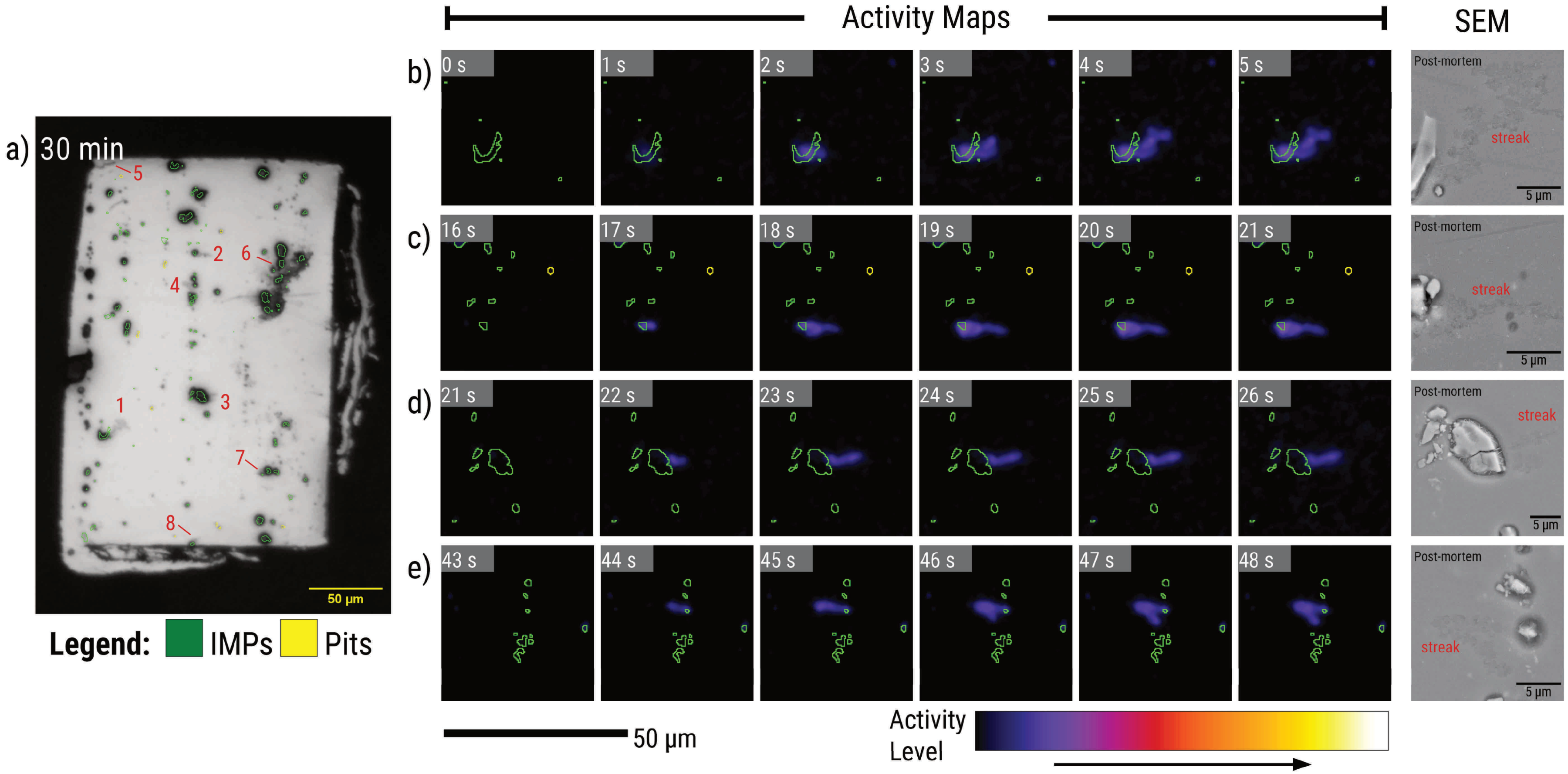

Figure S4.17. In situ reflected light microscopy images **(a)** of a polished AA7075 surface exposed to 0.05 M NaCl at OCP and the activity maps show streaking corrosion initiation sites at **(b)** point 1 (Al-Fe-Cu), **(c)** point 2(Al-Fe-Cu), **(d)** point 3(Al-Fe-Cu), and **(e)** point 4(Al-Fe-Cu). The microstructure map overlay was created from post-immersion SEM mapping. The secondary electron images in the last column show the morphology of the streaks close to the IMPs after 40 minutes of immersion. The legend indicates the colour of boundaries for intermetallic particles and for pre-existing pits.

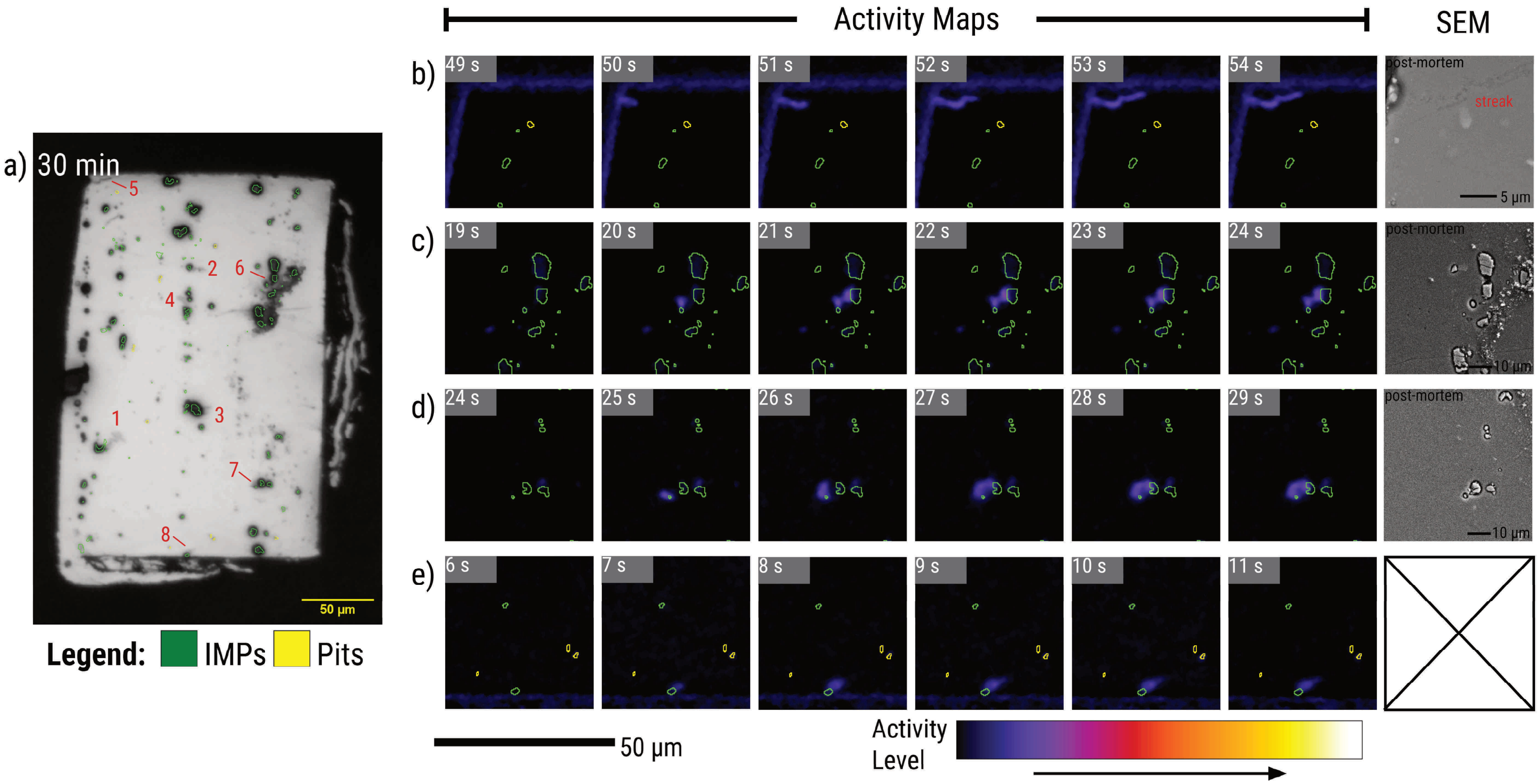

Figure S4.18. In situ reflected light microscopy images **(a)** of a polished AA7075 surface exposed to 0.05 M NaCl at OCP and the activity maps show streaking corrosion initiation sites at **(b)** point 5 (Al – 34.6, O – 48.2, Fe – 5.7, Cu – 5.2, Zn – 3.3), **(c)** point 6 (unknown composition), **(d)** point 7 (unknown composition), and **(e)** point 8 (unknown composition). The microstructure map overlay was created from post-immersion SEM mapping. The secondary electron images in the last column show the morphology of the streaks close to the IMPs after 40 minutes of immersion. The legend indicates the colour of boundaries for intermetallic particles and for pre-existing pits.

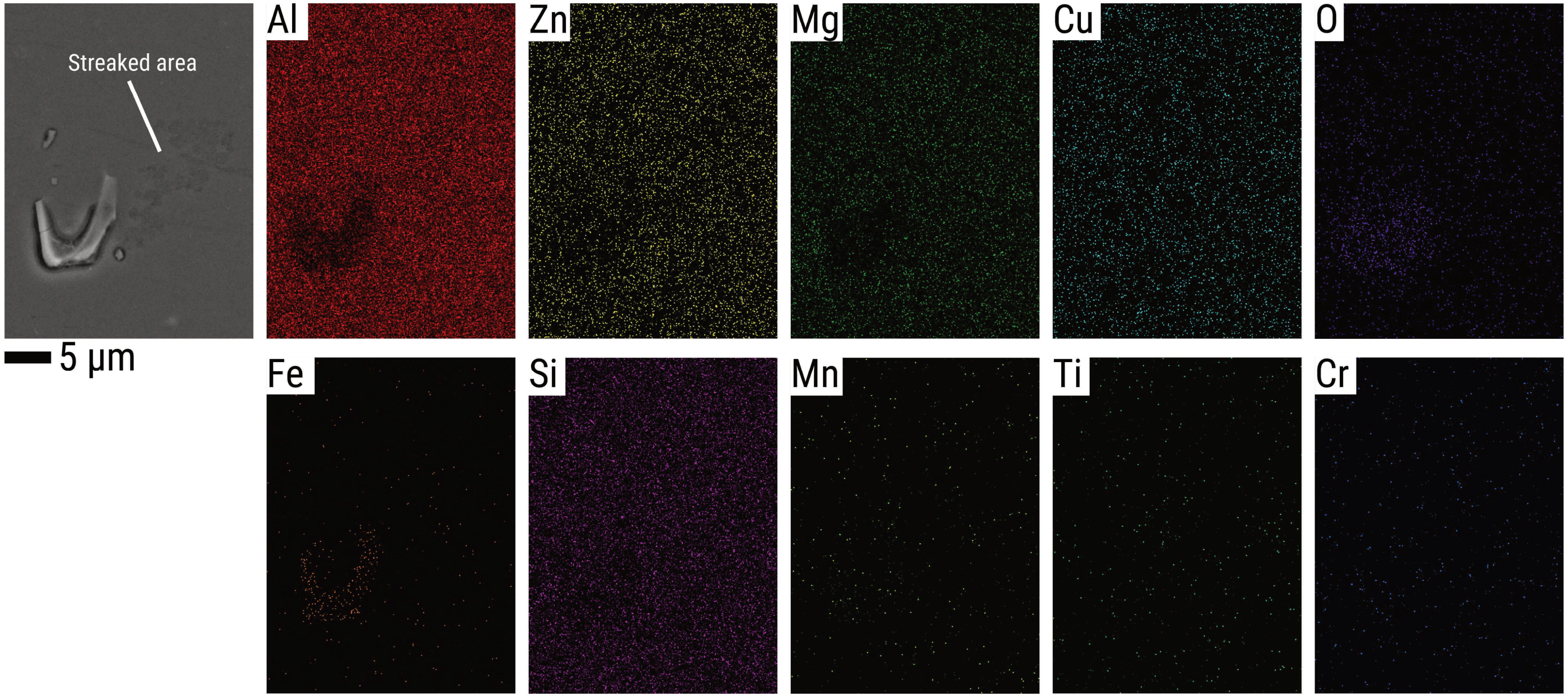

Figure S4.19. EDX maps of corrosion streak that developed around an Fe-rich intermetallic particle shown in Figure S4.17b. The maps show distinct composition differences between the particle and the surrounding matrix but no detectable differences between the streaked and un-streaked areas of the matrix.

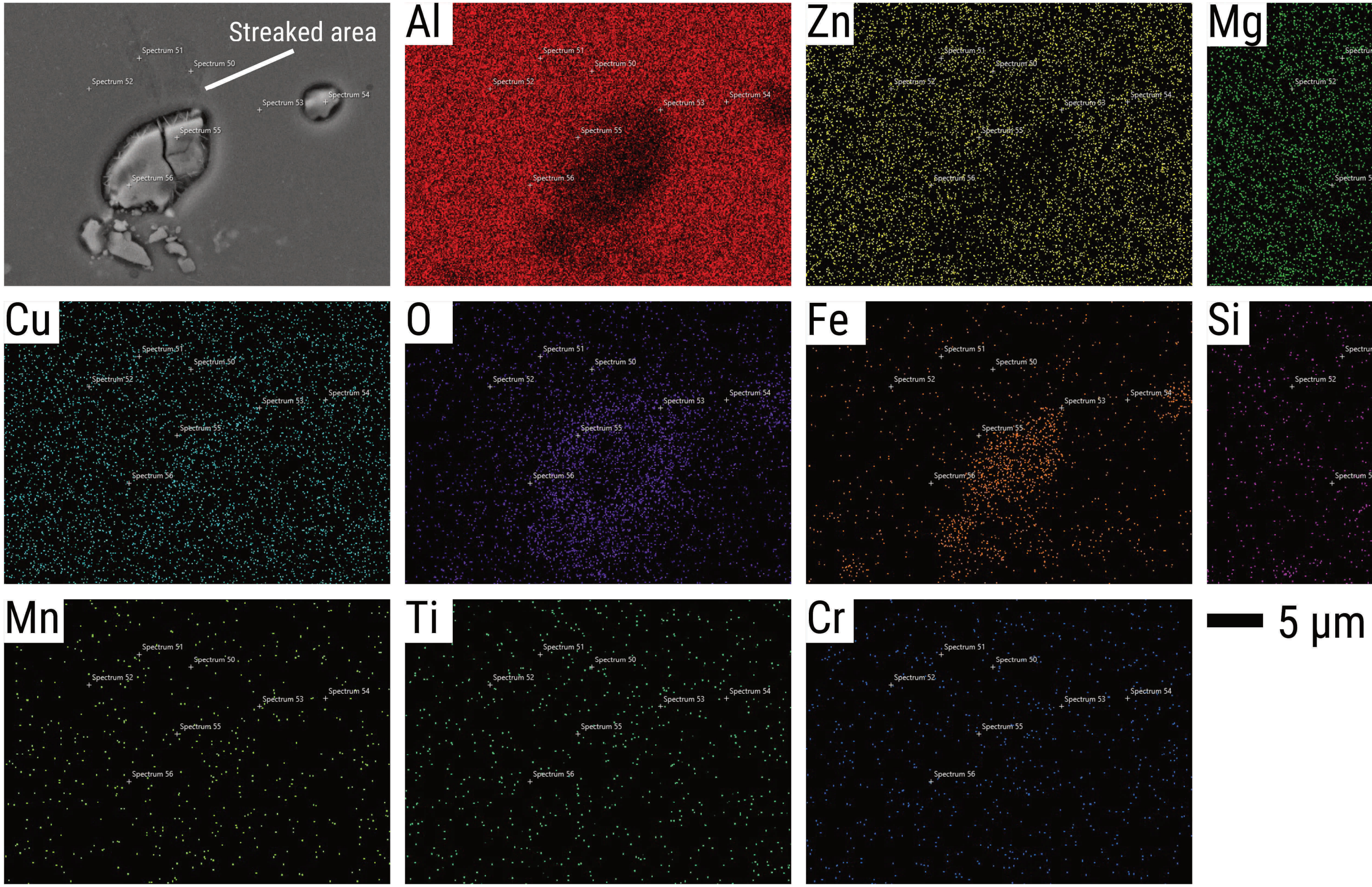

Figure S4.20. EDX maps of corrosion streak that developed around an Fe-rich intermetallic particle shown in Figure S4.17d. The maps show distinct composition differences between the particle and the surrounding matrix but no detectable differences between the streaked and un-streaked areas of the matrix. Point composition analysis of the surface of the initiating particles showed that its atomic percentages are as follows: Al – 62.6, O – 14.2, Fe – 13.9, Cu – 5.3, Zn – 2.0. The rest have atomic % below 1.

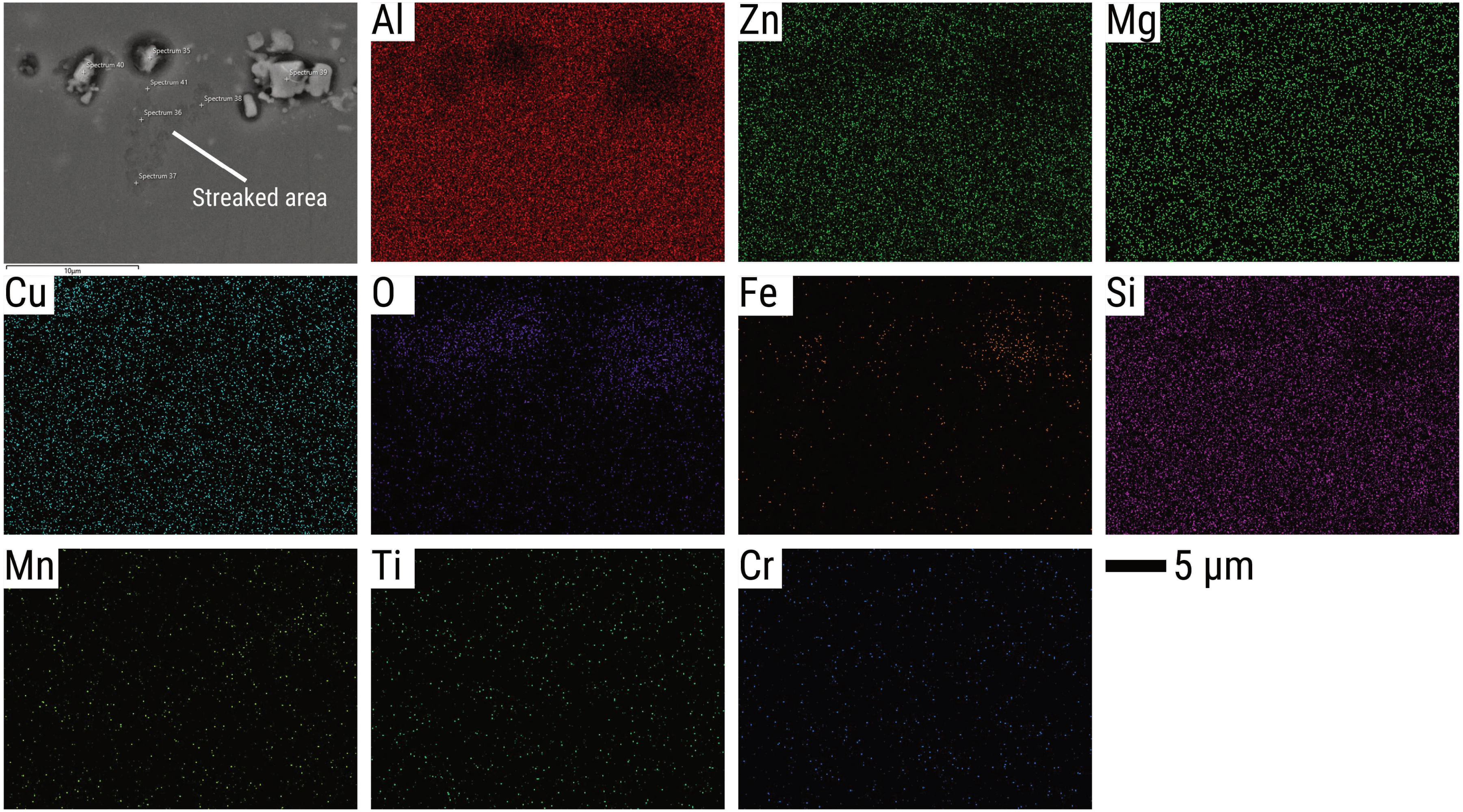

Figure S4.21. EDX maps of corrosion streak that developed around an Fe-rich intermetallic particle shown in Figure S4.17e. The maps show distinct composition differences between the particle and the surrounding matrix but no detectable differences between the streaked and un-streaked areas of the matrix. Point composition analysis of the surface of the initiating particles showed that its atomic percentages are as follows: Al – 47.9, O – 31.7, Fe – 6.9, Cu – 7.4, Zn – 3.7, Mg – 1.2. The rest have atomic % below 1.

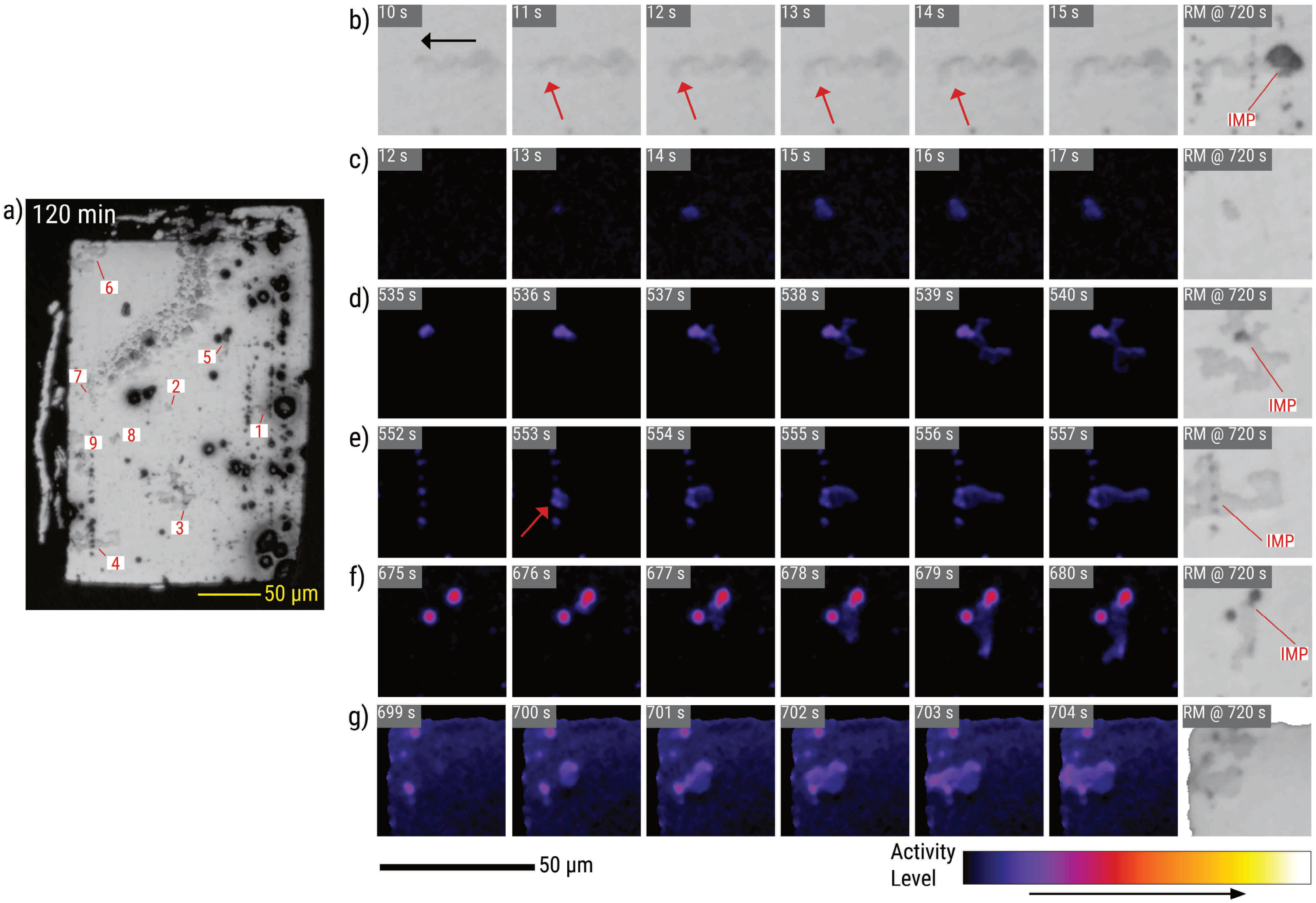

Figure S4.22. In situ reflected light microscopy image **(a)** of a polished AA7075 surface exposed to 0.05 M NaCl at OCP and the in situ microscopy images **(b)** or activity maps **(c - g)** showing streaking corrosion initiation sites at **(b)** point 1, **(c)** point 2, **(d)** point 3, **(e)** point 4, **(f)** point 5, and **(g)** point 6. The last column shows microscopy images after 6 minutes of immersion to highlight localized darkening associated with dealloying and trenching.

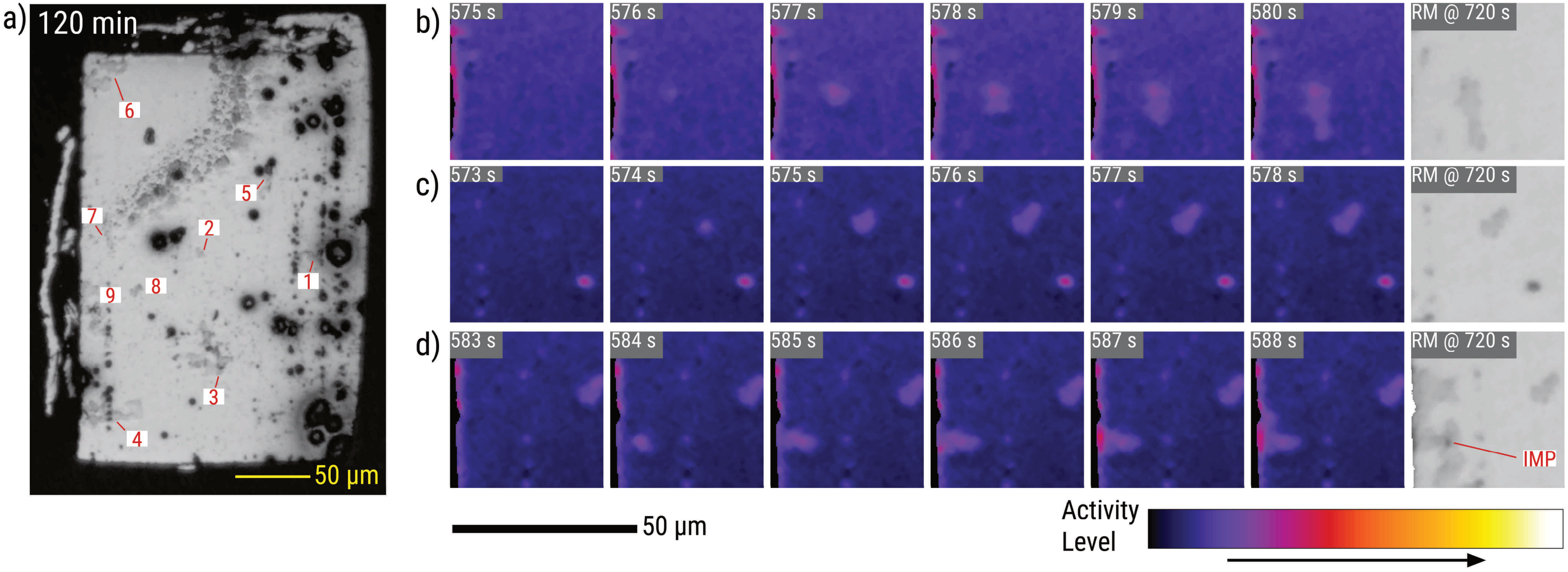

Figure S4.23. In situ reflected light microscopy image **(a)** of a polished AA7075 surface exposed to 0.05 M NaCl at OCP and the activity maps show streaking corrosion initiation sites at **(b)** point 7, **(c)** point 8, and **(d)** point 9. The purple colouration of the matrix is due to temporary brightness changes that occurred around the same time as the initiation of the streaks. Nonetheless, local streaking events can still be easily distinguished from the matrix. The last column shows microscopy images after 6 minutes of immersion to highlight localized darkening associated with dealloying and trenching (or its absence).

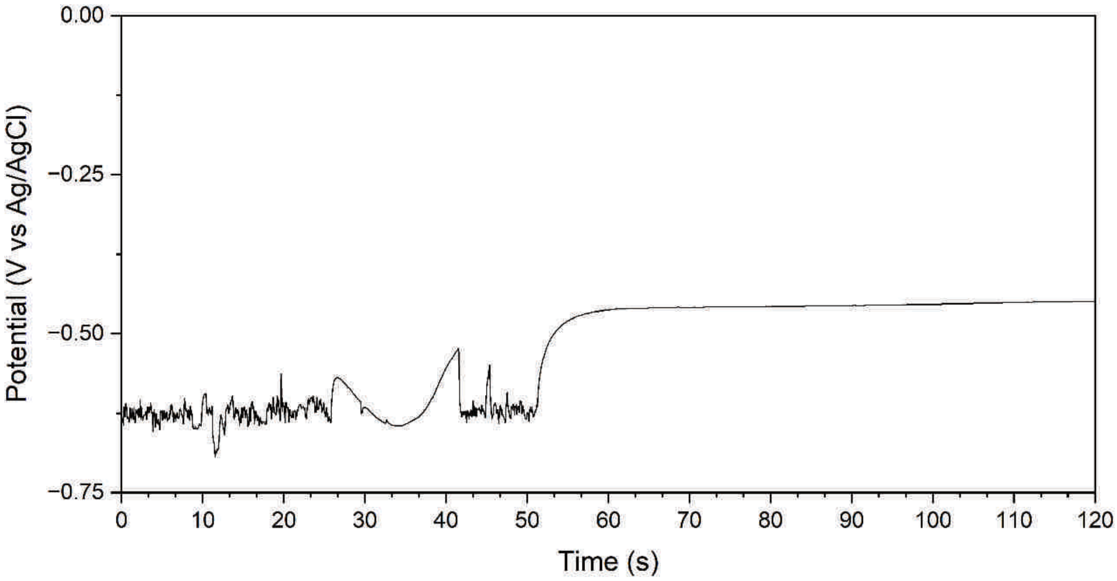

Figure S4.24. In situ OCP measurements of the sample presented in Figure S4.17 and Figure S4.18 from 0 to 120 s of its immersion in 0.05 M NaCl. This sample exhibited limited streaking corrosion, most of which happened shortly after the start of exposure. The major streaking events observed during this period are as follows: (1) Figure S4.17b: 1 – 4 s, (2) Figure S4.18e: 7 – 9 s, (3) Figure S4.17c: 17 – 19 s, (4) Figure S4.18c: 20 – 21 s, (5) Figure S4.17d: 22 – 23 s, (6) Figure S4.18d: 25 – 27 s, (7) Figure S4.17e: 44 – 47 s, (8) Figure S4.18b: 50 – 53 s.

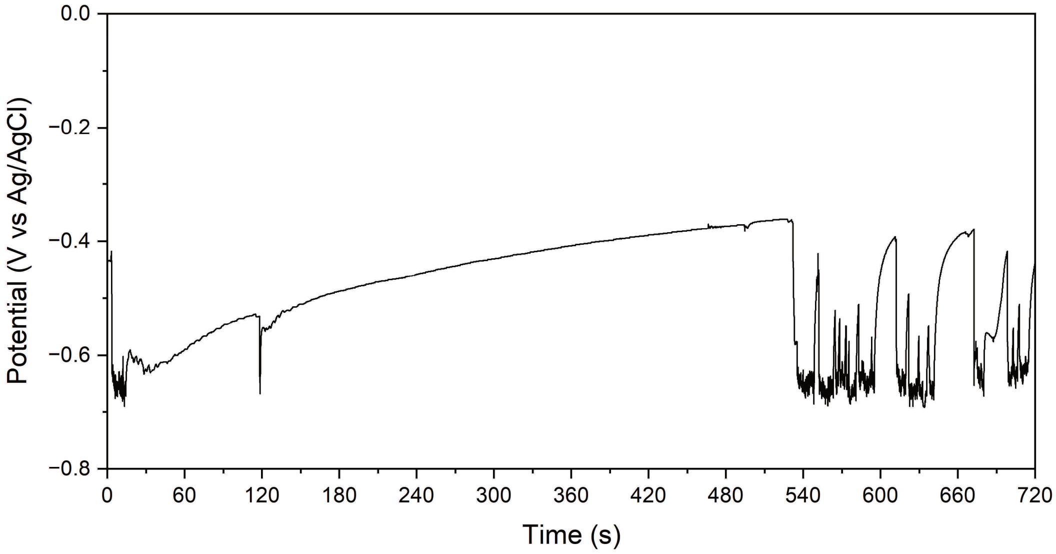

Figure S4.25. In situ OCP measurements of the sample presented in Figure S4.22 and Figure S4.23 from 0 to 720 s of its immersion in 0.05 M NaCl. This sample exhibited optically-confirmed streaking corrosion within the first 30 seconds of immersion and on from around 540 to 720 seconds of immersion. OCP transients consistent with streaking corrosion are also observed around the same periods. The major streaking events observed during this period are as follows: (1) Figure S4.22b: unknown start until ~ 13 s, (2) Figure S4.22c: 13 – 15 s, (3) Figure S4.22d: 536 ~ 549 s, with extension at 566 – 573 s, (4) Figure S4.22e: 553 – 564 s, (5) Figure S4.23c: 574 – 576 s, (6) Figure S4.23b: 576 – 582 s, (7) Figure S4.23d: 584 – 596 s, with a extension at 613 – 620 s, (8) streaking adjacent to site in Figure S4.22e: 623 – 642 s, (9) Figure S4.22f: 676 – 681 s, (10) Figure S4.22g: 700 – 716 s.

5

Galvanic coupling between AA7075-T6 and AA2024-T3 intensifies local corrosion

This study demonstrates that galvanically coupling AA2024-T3 and AA7075-T6 affects localized corrosion even with the alloys' comparable electrochemical behaviour. In situ reflected light microscopy tracked corrosion initiation and trench propagation, while zero resistance ammeter measurements quantified galvanic current density and potential. This combined approach allowed direct correlation between electrochemical signals and optically detectable surface phenomena. Galvanic coupling increased cathodic activity at AA2024-T3 intermetallic particles (IMPs) and caused the surrounding matrix to dissolve more extensively beyond the trench that formed around the particles. Local activity analysis revealed initial IMP dealloying was unaffected by galvanic coupling. However, lateral growth of trenches in both alloys was accelerated under coupling compared with electrically-isolated conditions. Correlation of optical activity with electrochemical measurements showed that trends and fluctuations in galvanic current and potential reflect different stages of local corrosion, facilitating the morphological and physicochemical interpretation of the electrochemical data.

This chapter has been published as:

M. Mopon, A. Mol, S. J. Garcia, Galvanic coupling between AA7075-T6 and AA2024-T3 intensifies local corrosion, *Electrochim. Acta* 541 (2025) 147335. doi: 10.1016/j.electacta.2025.147335.

5.1. Introduction

Aluminium alloys AA2024 (Al-Cu-Mg) and AA7075 (Al-Zn-Mg-Cu) are widely used in aerospace and automotive applications due to their high strength-to-weight ratios and favourable mechanical performance. Despite these advantages, both alloys are susceptible to corrosion, particularly in chloride-containing environments due to the presence of intermetallic particles (IMPs) formed during manufacturing and thermomechanical processing [1–5]. In AA2024, localized corrosion initiates with particle dealloying followed by dissolution of the surrounding matrix (i.e., trenching) once microgalvanic coupling is established [6–8]. This sequence of events is observed across IMP compositions, though S-phase (Al_2CuMg) particles corrode fastest [8] and reportedly account for the majority of local corrosion events [9]. Other IMPs present in AA2024 include θ-phases (Al_2Cu) and Fe-containing particles. AA7075 shows similar local corrosion behaviour albeit with slight differences in the composition of IMPs involved. It also contains the active S-phases due to its Cu and Mg content, as well as Fe-containing particles (e.g., $Al_7Fe_2Cu(Mn)$, $Al_{15}(FeMn)_3(SiCu)_2$, Al_7Cu_2Fe), which are less active but still dealloy to varying degrees and can cause trenching [10–12]. Apart from local corrosion around IMPs, AA7075 is also prone to the rapid dissolution of an altered surface layer [13,14]. The dissolution of this surface layer leads to rapidly propagating corrosion streaks, earning it the name streaking corrosion [15–17]. In a recent work [15], we have shown that streaking corrosion preferentially initiates at intermetallics and is also characterized by a distinct sequence of transients when concurrent open-circuit potential (OCP) measurements are performed.

In practical applications, AA2024 and AA7075 are often joined with other metals or alloys. The presence of electrical contact and a bridging electrolyte to complete the circuit can lead to the creation of galvanic couples between the aluminium alloys and the other materials, which can further complicate and potentially aggravate their corrosion behaviour. Common pairings, such as AA2024 or AA7075 with steel [18–25], titanium [25–29], or carbon fibre composites [30–33], have been extensively studied due to their widespread use in multi-material assemblies. In these combinations, the aluminium alloys represent the less noble component and therefore corrode preferentially. Although AA2024 and AA7075 are both aluminium-based, galvanic coupling can also occur between them due to differences in their alloying elements - primarily copper in AA2024 and zinc in AA7075. Such coupling, while less common, is relevant in structural configurations where both alloys are in electrical contact, such as in the skin-stiffener assemblies of aircraft [34,35]. Notably, corrosion studies on this specific AA2024–AA7075 configuration focused primarily on the local corrosion behaviour arising from the microstructural zones created by friction-stir welding of the two alloys [36–39]. Using a similar system composed of AA2024 and AA7475 (i.e., an AA7XXX alloy with lower amounts of Fe and Si, and lower IMP density), Bugarin et al. [40] reported low impedances at the stir zone of the welded alloys due to the galvanic coupling of their thermomechanically affected zones (TMAZ), with the AA2024 TMAZ acting as the cathode and AA7475 as the anode. They noted, though, that the impedance values of the stir zone are closer to those of the AA2024 TMAZ which they attributed to its higher concentration of precipitate particles rendering higher electrochemical activity. Local studies by de Abreu et al [41] on friction-stir welded AA2024-AA7475 also showed that galvanic coupling of the system might lead to selective dissolution of Zn. The dissolved Zn can then redeposit on the surface of Al-Cu-Mg IMPs at prolonged exposure (~24 h) to a corrosive environment. They also reported that the redeposition of Zn affected the dealloying behaviour of the Al-Cu-Mg IMPs. These findings highlight the interdependent relationship between localized corrosion at the IMP level and macroscale galvanic coupling. Interestingly, few studies analyse this interdependence even though corrosion of alloys like AA2024 and AA7075 has already been established to be highly local in nature. Furthermore, the few available studies mostly focus on welded configurations, which limits quantitative analysis of electrochemical interactions between the two alloys.

Other works that looked into the interplay between macroscale galvanic coupling and local corrosion mainly considered AA2024 coupled with more noble materials. Coelho et al. [28] showed that galvanic coupling between AA2024-T3 and Ti6Al4V of equal areas only led to faster disruption of the AA2024 passive layer, but not to any substantial dissolution. They attributed the absence of effective galvanic coupling to higher oxygen reduction reaction kinetics on AA2024, particularly on the Cu-rich sites, than that on the Ti alloy. Another work by Coelho et al. [42] on galvanically-coupled graphite and AA2024-T3 demonstrated that galvanic coupling behaviour is significantly dependent on the area ratio of the coupled materials. They reported that at an AA2024/graphite ratio of 10, only partial anodic polarization of the AA2024 surface is achieved. However, at an AA2024/graphite ratio of 1.5, complete anodic polarization of the AA2024 surface was observed through a combination of scanning vibrating electrode technique and scanning ion-selective electrode technique. They also reported minimal trenching around IMPs for this area ratio, potentially due to anodic polarization driving a relatively uniform dissolution of the alloy surface.

This work investigates how IMPs and their surrounding areas corrode when AA2024-T3 and AA7075-T6 are galvanically coupled in a chloride-rich aqueous environment. Unlike most material pairings studied in literature, these two alloys have comparable OCPs and are both prone to highly localized corrosion. Because of their electrochemical similarities, their coupling is considered a minor issue which leads to limited data on galvanic corrosion between them. Additionally, their tendency for localized attack makes it difficult to distinguish whether the observed corrosion is caused by galvanic coupling between the two alloys or simply by the usual microgalvanic interaction between IMPs and the surrounding matrix. Our recent works have shown that in situ reflected light microscopy can effectively reveal and quantify the kinetics of local degradation processes such as dealloying, trenching, oxide deposition, and streaking corrosion, with high spatial and temporal resolution [8,15,43,44]. Here, the technique is used to monitor local corrosion initiation and propagation at the surfaces of both alloys, capturing the morphological evolution of local attack. Simultaneously, in situ electrochemical measurements through a zero resistance ammeter (ZRA) provide a quantitative assessment of the galvanic interactions between the alloys during corrosion. By correlating visual and electrochemical data, this work aims to advance the mechanistic understanding of localized galvanic corrosion in dissimilar aluminium alloys.

5.2. Experimental

5.2.1. Materials

Commercial grade bare AA2024-T3 (Kaiser Aluminum, rolled thickness = 2 mm) and AA7075-T6 (Kaiser Aluminium, rolled thickness = 3 mm) were used for the corrosion tests. The metal sheets were used to prepare aluminium pillars (Figure 5.1a) with exposed areas around 0.13 mm^2 as described elsewhere [8,43]. It is noted that the three sides of the pillar are specifically labelled (i.e., facing plane - FP, top plane - TP, bottom plane - BP) in the figure since they are relevant for positioning the pillars to form the assembly. A 0.05 M NaCl aqueous solution (>98% purity NaCl in “Millipore Elix 3 UV” treated water) was used as the corrosive solution.

5.2.2. Sample preparation

The AA2024-T3 pillar was embedded in cold-curing epoxy through a previously established procedure described elsewhere [43]. Once fully cured, the epoxy was ground to expose side FP of the pillar. The unembedded AA7075-T6 pillar was then positioned next to the embedded AA2024-T3 pillar with the FP sides of both pillars facing each other. Insulating tape was placed between the two pillars to ensure the distance between them was minimized while at the same time preventing electrical contact. The separation distance for the pillars was ~170 μm. The AA2024-AA7075 assembly was re-embedded in cold-curing epoxy to fix their positions (Figure 5.1b). After complete curing, the top and bottom surfaces of the assembly were ground to expose the surfaces of the pillars. Electrical wire was connected to the BP side of each pillar to establish external electrical contact for in situ electrochemical measurements. Electrical separation between the pillars was confirmed with a multimeter. The bottom side of the assembly was embedded again in epoxy to maintain the placement of external connections and to avoid unwanted galvanic coupling between the copper contacts and the exposed surfaces of the aluminium pillars. After complete curing of the bottom side, side TP was ground to ensure that the top surfaces of the pillars are completely exposed. The final assembly had an AA2024 to AA7075 exposed area ratio close to 1.

5.2.3. In situ optical-electrochemical corrosion testing

The experimental protocol for immersion in the NaCl solution is similar to our previous work [8,43]. Prior to immersion, the sample surface was ground with SiC sandpaper from 320 to 4000 grit and then polished with 1 μm diamond paste. Pure ethanol was used for grinding and

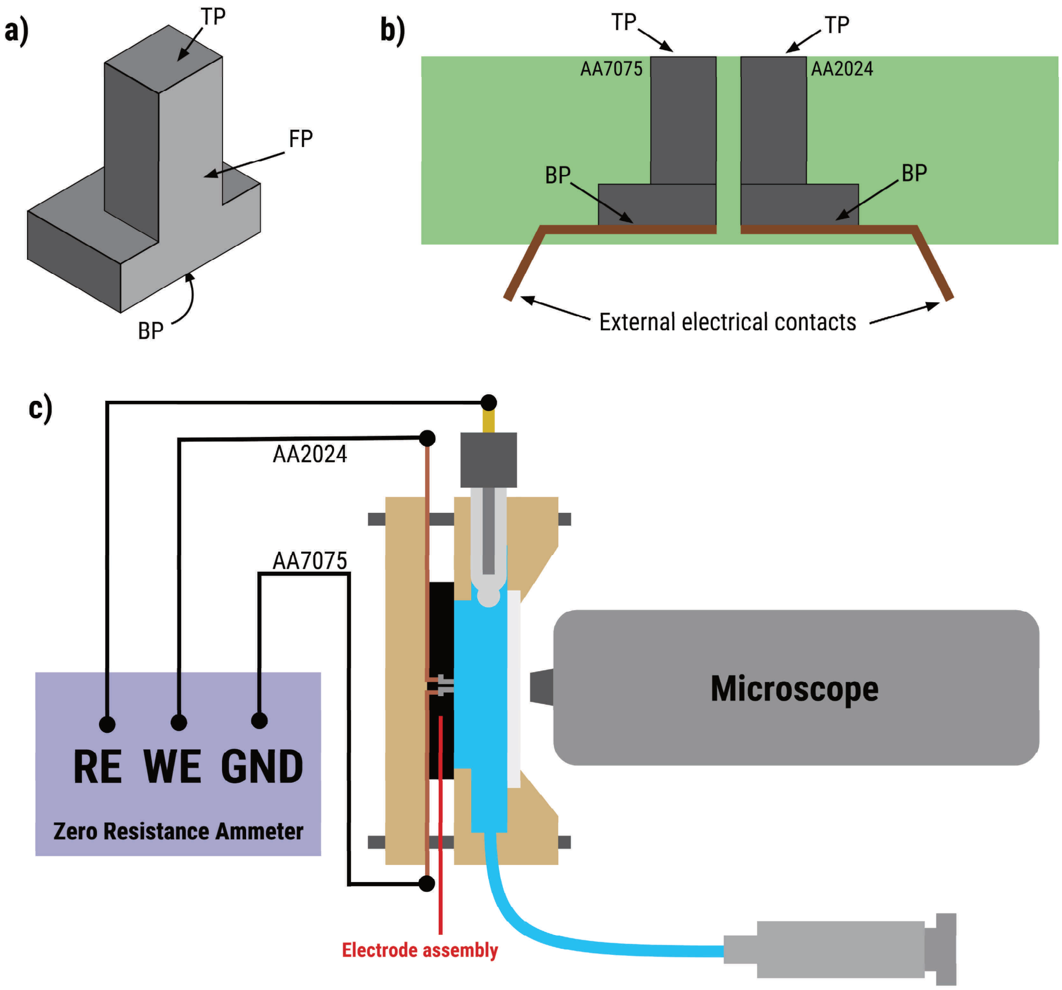

Figure 5.1. Schematic of **(a)** an individual pillar with the labelled sides (top plane TP, bottom plane BP, facing plane FP), **(b)** the multi-pillar assembly embedded in epoxy, and **(c)** optical-electrochemical setup used for in situ analysis during immersion in corrosive electrolyte under galvanically-coupled conditions. During open-circuit tests (galvanically-uncoupled), the ground (GND) cable is connected to the laboratory earth ground and the working electrode (WE) cable is connected to either the AA2024 or the AA7075 pillar. The Ag/AgCl(3 M KCl) electrode remained connected as the reference electrode (RE).

polishing. For immersion tests (Figure 5.1c), the sample was placed in an electrochemical cell (redox.me Raman electrochemical flow cell) and mounted to a holder for in situ imaging during immersion with a reflected microscope (Dino-lite AM7515MT4A, ca. 7-10 pixels μm^{-2}) operating in brightfield mode [8,43]. An Ivium CompactStat.h potentiostat was used to implement ZRA tests for the coupled alloys. The AA2024-T3 pillar was connected to the working electrode (WE) cable while the AA7075-T6 pillar was connected to the ground (GND) cable. The potential of the couple was measured against an Ag/AgCl(3 M KCl) reference electrode (RE) mounted to the electrochemical cell. In this configuration, a positive galvanic current corresponds to a net electron flow out of the working electrode (Supporting Information 5.7.1). Electrically-isolated (EI) tests wherein the alloys are separately corroding at their respective OCPs were also performed with the electrochemical cell. For these tests, the GND cable was connected to the earth ground while the WE cable was connected to the AA2024 or the AA7075 external electrical connection. The RE cable remains connected to the Ag/AgCl electrode. Once the assembly was mounted and recording started, a 5 mL volume of the electrolyte was injected into the cell using a syringe and monitoring proceeded for 2 hours. Post-immersion analysis of the surfaces of the pillars was performed with scanning electron microscopy coupled with energy dispersive x-ray spectroscopy (SEM-EDX, JEOL JSM-7500F). Secondary electron images were acquired at a 15 kV accelerating voltage and a 10 μA emission current.

5.2.4. Image Analysis

The image analysis protocol used for studying local changes in the sample surfaces is similar to our previous works [43,44]. Changes on both the AA2024 and AA7075 surfaces were quantified through image subtraction of the pre-processed (i.e., conversion to grayscale, recursive realignment) microscopy images. It is noted that the images converted to grayscale each have an associated pixel gray-level. With the imaging conditions reported in Section 5.2.3 (i.e., brightfield imaging), local corrosion is observed as darkening of pixels. Image subtraction was performed with respect to the first image acquired during immersion (i.e., image at 0 s of immersion – image at x s of immersion) unless otherwise stated. The subtraction process quantifies the gray-level increase of a pixel at time t (i.e., activity level at time *t*). Its output is the global activity map (GAM) for the sample surface at time *t*. A built-in ImageJ look-up table (i.e., Fire) was used to colormap the GAMs for easier visualisation of the magnitude of the changes. The activity levels depicted in the GAMs range from 0 to 255, with 0 indicating no change with respect to the initial condition. Specific areas of the GAM were isolated for analysis of local surface changes (i.e., IMPs, trenches). This was achieved by overlaying boundaries manually extracted from active sites observed on the sample surface. It is noted that not all active sites present in the alloys were analysed. Sites with well-defined boundaries were prioritized for analysis. Supporting Information 5.7.2 shows the boundaries used for analysing changes on IMP surfaces and for assessing growth of trenches. The changes of the pixels within the defined boundaries were quantified and visualized through simplified pixel activity level distribution (sPAD) plots [43]. These plots present the maximum (maxAL), median (midAL), and minimum (minAL) activity levels as a function of time for the set of pixels on the IMP surface and reflect the intensity of the local changes.

5.3. Results and Discussion

5.3.1. Local corrosion progression of uncoupled AA2024 and AA7075

Figure 5.2a shows the corrosion behaviour of uncoupled AA2024 and AA7075 immersed in 0.05 M NaCl for two hours. Reflected light microscopy (RLM) images at 7200 s highlight the characteristic localized corrosion of both alloys consistent with previous studies [8,15,43]. As previously reported for AA2024 [8,43], its local corrosion features include visible dealloying of IMPs and trenching around them (see blue arrows in Figure 5.2a – 7200 s). Corrosion product deposition (as indicated by cyan arrows in Figure 5.2a – 7200 s) arising from cooperative corrosion of IMP clusters was also observed. Dealloying of IMPs, seen as darkening of their surfaces, is due to the dissolution of less noble components (e.g., Al, Mg) of the particles [6–8,43,44]. It is noted that the extent of dealloying is dependent on IMP composition. Particles with components that have a significant difference in nobility (e.g., Cu vs. Al and Mg in S-phases) are more prone to extensive dealloying. Trenching, observed as dark circumferences around the particles, arises from microgalvanic coupling between the IMPs and the AA2024 matrix. Cathodic reactions on the IMP surface (e.g., oxygen reduction reaction) facilitate the anodic dissolution of the matrix [10,45]. Moreover, cathodic activity on the IMP surface generates local alkaline environments [7,43,46], which destabilize the passive oxide layer and promote lateral trench propagation [6,45].

As with AA2024, several forms of local events are also visible on the surface of AA7075. These include (1) dealloying of IMPs with associated trenching, visible as gray centres surrounded by dark rings (see black arrows in Figure 5.2a-7200 s); (2) corrosion product deposition, seen as irregular dark gray areas around clusters of corroded particles (see orange arrows in Figure 5.2a-7200 s); and (3) streaking corrosion, observed as elongated patches aligned with surface scratches (see magenta arrows in Figure 5.2a-7200 s). The streaking corrosion is associated with the dissolution of an altered surface layer rich in Zn and Mg. It is produced by the high shear strains during mechanical grinding and polishing of the AA7075 surface [16,17]. This type of corrosion spreads quickly across the metal surface, as demonstrated by the activity evolution in Movie 5.1 and as discussed in detail in our recent work [15].

Local activity maps in Figure 5.2b show how local corrosion in AA7075 (Area 1 and Area 2) and AA2024 (Area 3 and Area 4) evolved with time. It is noted that these activity maps are still frames from Movie 5.1. Area 1 activity maps show that some IMPs at the AA7075 surface activated during the first 60 s of immersion. At around 300 s, these particles show signs of

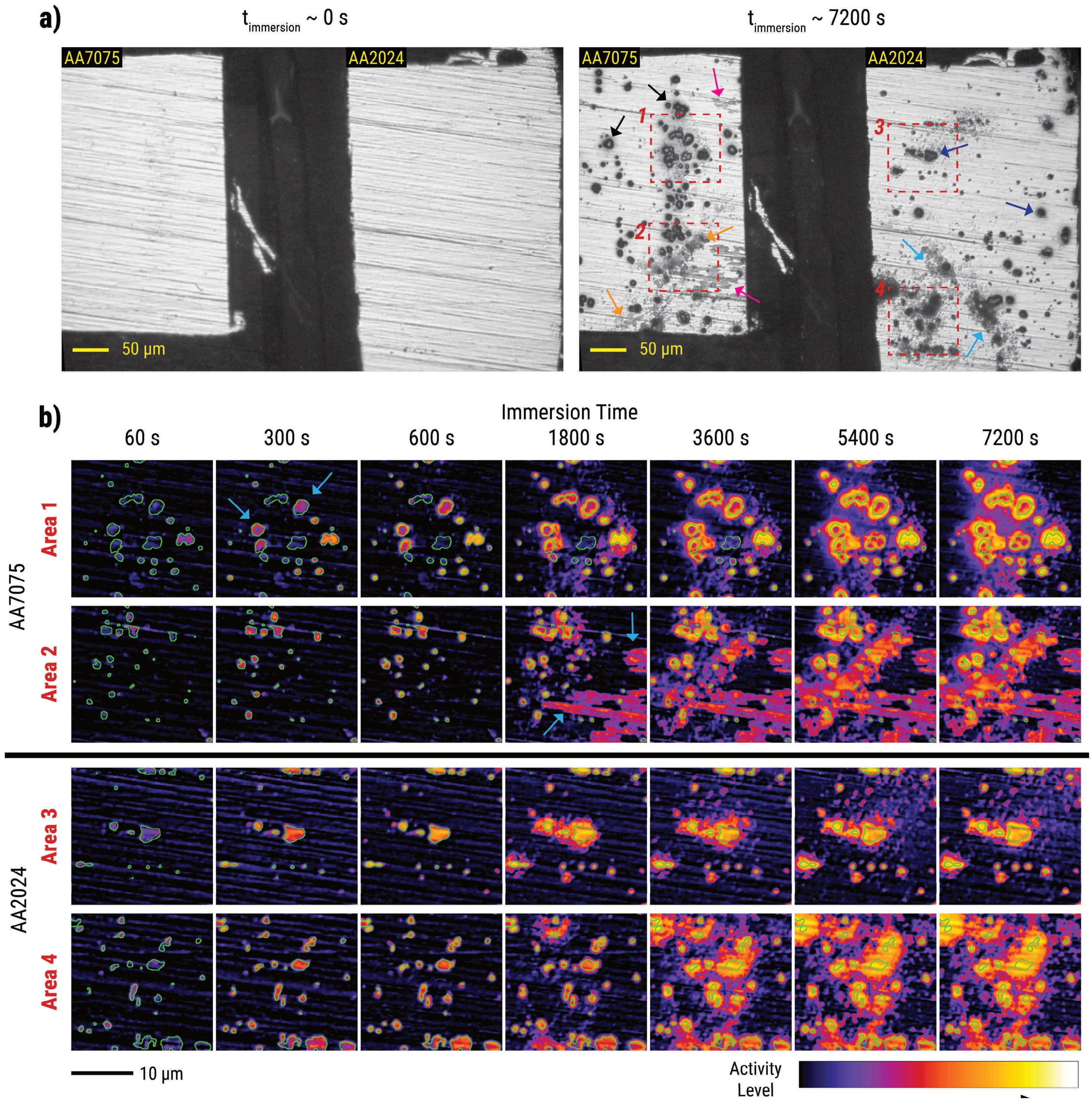

Figure 5.2. Raw reflected microscopy images of the AA2024 and AA7075 samples **(a)** right before immersion and after 7200 s of immersion in 0.05 M NaCl. The alloys are not electrically connected and are corroding in open circuit conditions. Evolution of local changes on the surfaces of the corroding alloys are shown in **(b)** activity maps of selected areas from the visible sections of the alloys. It is noted that the surface of the AA7075 is partially outside of the field of view of the microscope. The green boundaries indicate the boundaries used for analysing IMP activity.

extensive trenching based on the development of high activity on their periphery (see cyan arrows in Figure 5.2b-Area 1 @ 300 s). Local corrosion progression resulted in visible corrosion product deposition around the particles at around 1800 s. Cathodic reactions on the dealloyed IMPs and dissolution of their adjacent matrices continued with further immersion resulting in wide trenches and substantial corrosion product deposition at 7200 s. Area 2 shows similar local corrosion behaviour as Area 1 except for the appearance of streaking corrosion between

600 and 1800 s (see cyan arrows in Figure 5.2b-Area 2 @ 1800 s). Area 3 and Area 4 activity maps also show development of activity associated with IMP dealloying during the first 60 s of immersion. This is consistent with the onset of IMP dealloying reported in previous works for AA2024 [8,43]. Particles from both areas exhibited an increase in activity level and surface spreading with time indicative of dealloying progressing into trenching of the matrix adjacent to the particles. Further dissolution of the matrix led to corrosion product deposition beginning around 1800 s and continuing until the end of immersion.

OCP measurements of the AA2024 and AA7075 surfaces were taken sequentially (i.e., first monitoring AA2024 until 4800 s and then monitoring the AA7075 until the end of immersion) as shown in Figure 5.3. The AA2024 OCP is around -0.5 V vs. Ag/AgCl while that of the AA7075 is around -0.65 V vs. Ag/AgCl. The AA2024 OCP is within the range of the previously reported OCP values for AA2024 [8,47] while that of the AA7075 is slightly more positive than the previously reported AA7075 OCP values (i.e., ~ -0.75 V vs Ag/AgCl for 3.5 wt% NaCl [13], ~ -0.8 V vs Ag/AgCl for 0.1 M NaCl [48]). This more positive AA7075 OCP is probably due to the higher contribution of intermetallic particle surfaces like Al_7Cu_2Fe which have been reported to have more positive corrosion potentials (~ -0.5 V vs Ag/AgCl) [11]. The potential difference of the OCPs of the alloys nonetheless highlights that there is a risk of galvanic corrosion when they are electrically connected, with AA2024 likely acting as the global cathode and AA7075 as global anode.

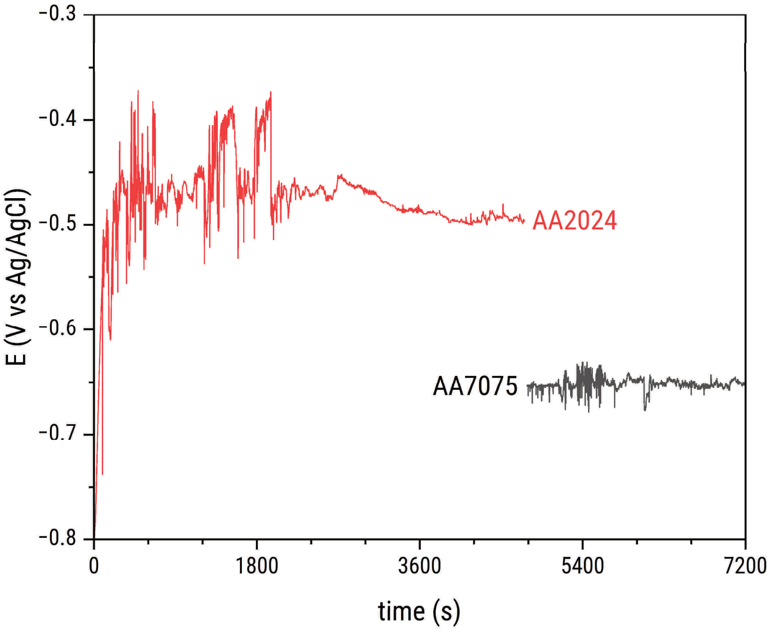

Figure 5.3. OCP measurements for AA2024 and AA7075 during the immersion shown in Figure 5.2. The OCP measurements of the two surfaces were performed one at a time. The AA2024 surface was measured during the first ~4800 s while that of the AA7075 from ~4800 s to 7200 s.

5.3.2. Impact of galvanic-coupling on local corrosion of AA2024 and AA7075

Figure 5.4a presents the galvanic current density (j_{gal}) and potential (E_{gal}) measured from two trials of 2-h immersion tests in 0.05 M NaCl with the alloys in the assembly externally connected via a ZRA. Analysis of the j_{gal} and E_{gal} will be covered in a subsequent section. The non-zero j_{gal} values indicate electron flow between the two alloys in the assembly. Furthermore, the negative j_{gal} values suggest that the electron flow is from AA7075 (i.e., anode) to AA2024 (i.e., cathode), as expected from the global OCPs of the two alloys (Figure 5.3).

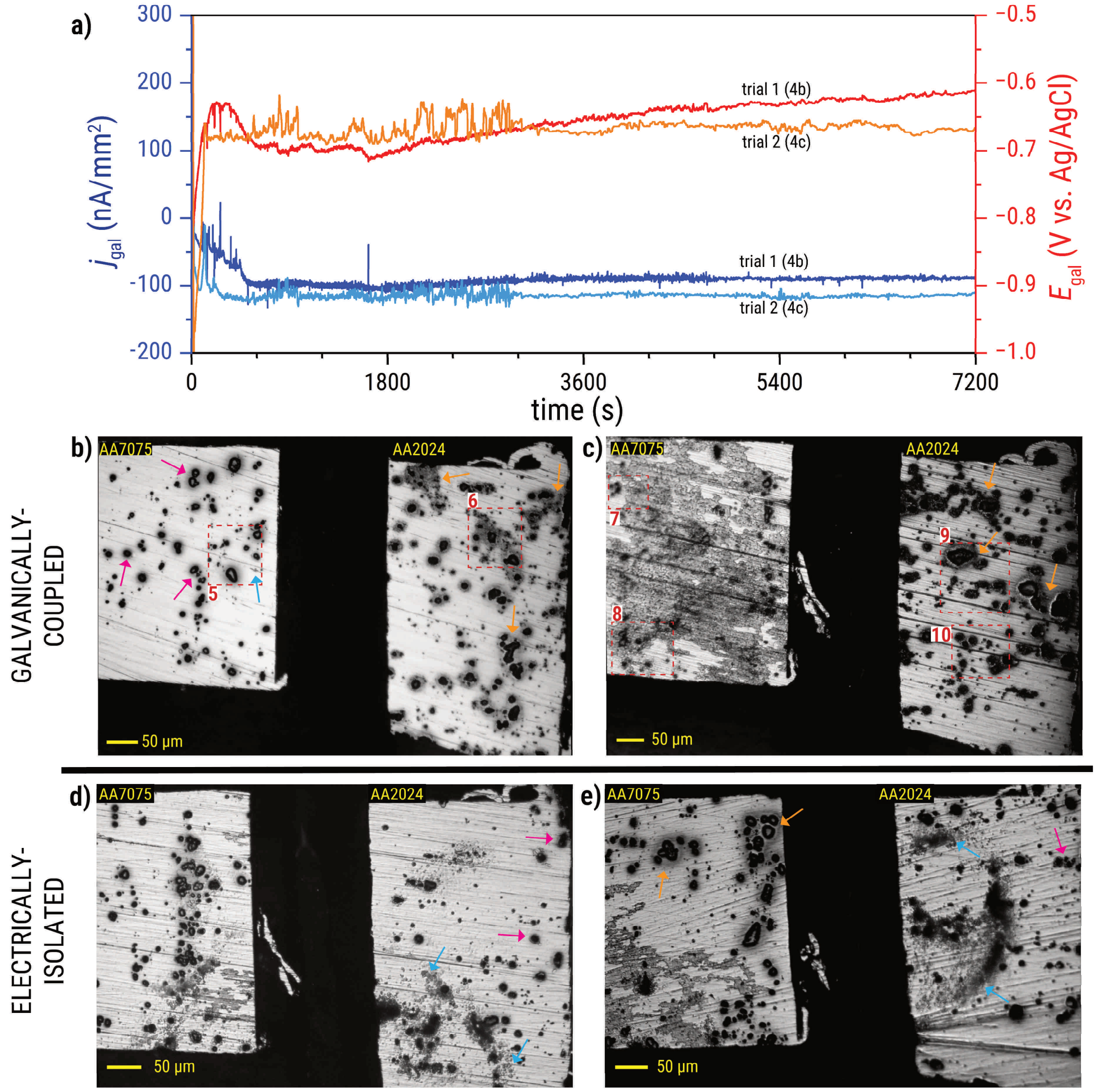

Figure 5.4. (a) Galvanic current and potential measured during 2-hour immersion tests in 0.05 M NaCl for two trials of galvanically-coupled AA2024 and AA7075 samples. The alloys were electrically connected via a zero resistance ammeter. Reflected light microscopy images at the end of immersion are shown for **(b)** trial 1 and **(c)** trial 2, highlighting the extent of surface corrosion under galvanic conditions. **(d)** and **(e)** show microscopy images from two separate trials conducted under electrically-isolated conditions in the same electrolyte.

The microscopy images corresponding to the galvanically-coupled (GC) alloys at the end of the immersion are shown in Figure 5.4b and Figure 5.4c. The evolution of the surface activities of the AA2024 and AA7075 from these trials is shown in Movie 5.2 and Movie 5.3, respectively. It is noted that these trials are repeats of the 2-h galvanically-coupled immersion test in 0.05 M NaCl. For reference, reflected microscopy images of the assembly after 2-h immersion tests in 0.05 M NaCl under EI conditions are also presented in Figure 5.4d and Figure 5.4e. It is noted that the image in Figure 5.4d is from the same test as Figure 5.2. The end-of-immersion images show that the GC alloys exhibit localized corrosion around intermetallic particles (i.e., dealloying and trenching), similar to that observed for the alloys immersed in EI conditions.

A closer look shows that changes in behaviour attributable to galvanic coupling are most apparent on the AA2024 side of the assembly. These changes include: (1) more widespread dark gray areas surrounding the trenches – referred to here as beyond-trench (BT) activity (see orange arrows in Figure 5.4b and Figure 5.4c), and (2) a general decrease in corrosion product deposition across the surface. While BT activity is also seen in some AA2024 particles under EI conditions (see magenta arrows in Figure 5.4d and Figure 5.4e), it occurs less frequently. Notably, although BT activity shares some visual characteristics with corrosion product deposition, the two can be distinguished by their spatial distribution. BT activity is localized around trenches, whereas corrosion product deposition can occur at locations distant from IMPs, including areas with no visible IMP activity (see cyan arrows in Figure 5.4d and Figure 5.4e).

Figure 5.5a and Figure 5.5b show close-up images of Area 9 and Area 10 on the galvanically-coupled AA2024 surface highlighted in Figure 5.4c. Their corresponding post-immersion SEM images are shown in Figure 5.5c and Figure 5.5d. Post-immersion EDX analysis was used to identify the most probable composition type of the IMPs in these areas. The absence of visible deposits around the trenches confirms that BT activity in AA2024 is distinct from corrosion product deposition. Moreover, occurrence of BT activity on both Fe-containing particles (i.e., AlCuFeMnSi, AlCuFeMn) and Cu-rich particles (i.e., S- and θ-phases) suggests that it is not limited by IMP composition. High-magnification images (Figure 5.5e and Figure 5.5f) of the particles in Figure 5.5c and Figure 5.5d (see dashed orange rectangles) reveal that BT activity is more consistent with matrix dissolution. The dissolution is observed as smooth areas on the outer side of the trenches (see magenta arrows in Figure 5.5e and Figure 5.5f). The grooves from grinding and polishing are less distinct on these areas, suggesting that some process evened out the morphological differences. Since no deposits are observed, the smoothing is

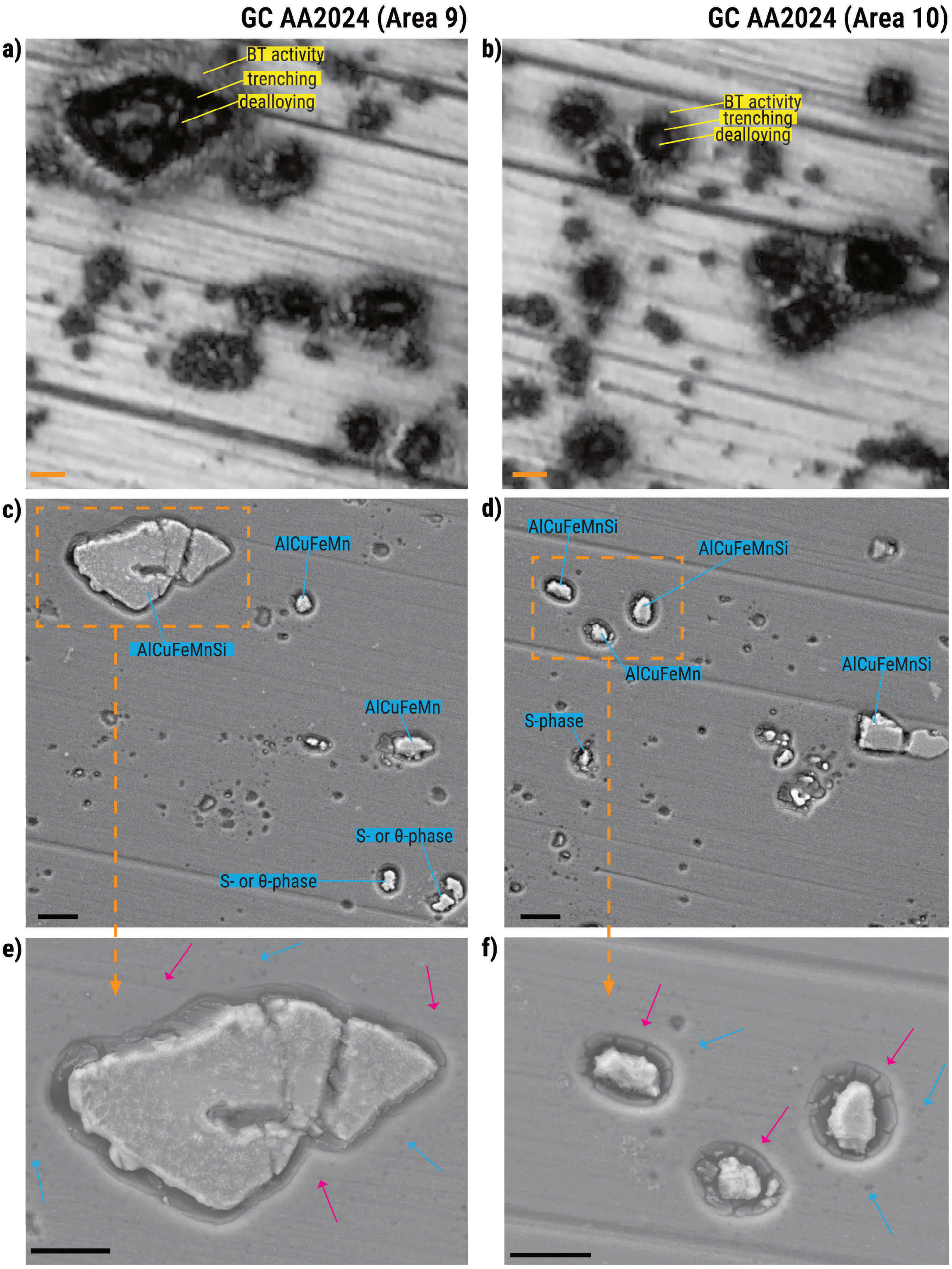

Figure 5.5. Close-up light microscopy images of **(a)** Area 9 and **(b)** Area 10 from the assembly shown in Figure 5.4c after 2 hours of immersion. Corresponding post-immersion secondary electron images with IMP composition types identified by EDX are shown in **(c)** for Area 9 and **(d)** for Area 10. High-magnification views of selected particles are presented in **(e)** and **(f)**. Scale bar: 10 μm.

more likely due to material loss (i.e., dissolution) rather than infill. Apart from the apparent smoothing, dark spots were also observed on the areas corresponding to BT activity (see cyan arrows in Figure 5.5e and Figure 5.5f). These features are likely related either to local dissolution induced by Cu redeposited from the dealloyed IMPs [6,7] or attack of dispersoids present around the larger IMP [7].

Extensive dark areas beyond trenches, resembling BT activity observed in this study, have also previously been reported in the AA2024 side of friction-stir welded AA2024-AA7475 under cathodic polarization [40], and in AA2024 corroding in alkaline solutions (pH = 10) [49]. Similar to bulk alkaline solutions, cathodic polarization of IMPs generates local alkalinity near the IMP surface through the oxygen reduction reaction. Both scenarios suggest that BT activity is driven by pH and may represent an extension of the same processes responsible for lateral trench propagation. The broader extent of dissolution beyond trenches under GC conditions suggests that galvanic coupling of the two alloys may have enhanced the local alkaline environment around the AA2024 IMPs compared to EI conditions. Such enhancement potentially explains the observed extent of local corrosion reported on the AA2024 side of friction-stir welded AA2024-AA7475 after a 24-h immersion in 0.01 M NaCl under open-circuit conditions [40], and on the AA2024 side of friction-stir welded AA2024-AA7075 after a 12-h immersion in 3.5 wt% NaCl also under open-circuit conditions [39]. Furthermore, the development of the local alkaline environment also explains the delayed acidification of the AA2024 side observed during pH variation tests for friction-stir welded AA2024-AA7475 [41].

The corrosion of the AA7075 side under GC conditions is more varied than that of AA2024, particularly in terms of the extent of streaking corrosion. The AA7075 sample from trial 1 exhibited dealloying events accompanied by extensive trenching and limited streaking corrosion (see cyan arrow in Figure 5.4b). Dark gray areas (i.e., BT activity) around the trenches are also observed (see magenta arrows in Figure 5.4b), although not as extensive as that in the AA2024 surface. Similar behaviour is observed in some of the AA7075 IMP clusters immersed under EI conditions (see orange arrows in Figure 5.4e). Although SEM images of these sites are not available, post-immersion SEM analysis of IMPs from another AA7075 sample immersed in similar conditions (Figure 5.6) shows that this kind of darkening is due to dissolution, not corrosion product build-up. On the other hand, the AA7075 sample from trial 2 (Figure 5.4c) exhibited extensive streaking corrosion which impacted almost the entire surface, in addition to the dealloying and trenching around IMPs. A closer look at the microscopy and post-immersion SEM images of Area 7 and Area 8 on the AA7075 surface (Figure 5.7) shows features of streaking corrosion, as well as dealloying and trenching around IMPs. Although the surface changes due to streaking corrosion registered substantial activity levels, the SEM images of the streaked areas show that the streaking corrosion depth is barely perceptible. In Figure 5.7a, the streaked area on the right side of the SEM image has a patchy texture with slight darker colour than the un-streaked matrix. The same patchy texture is observed in the SEM images of the

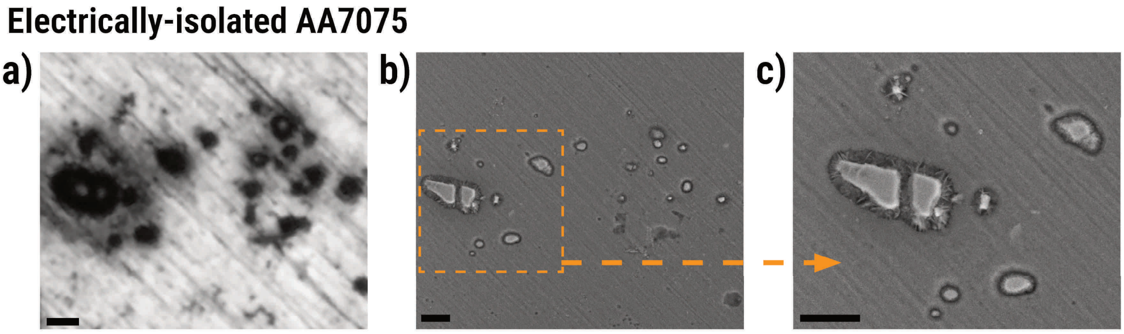

Figure 5.6. **(a)** Reflected light microscopy image of IMPs immersed in electrically-isolated conditions, and their corresponding post-immersion **(b, c)** secondary electron images showing that the dark gray areas surrounding the trenches have no visible corrosion product deposition. These images are from another AA7075 sample immersed in 0.05 M NaCl for 2 hours. Scale bar indicates 10 μm.

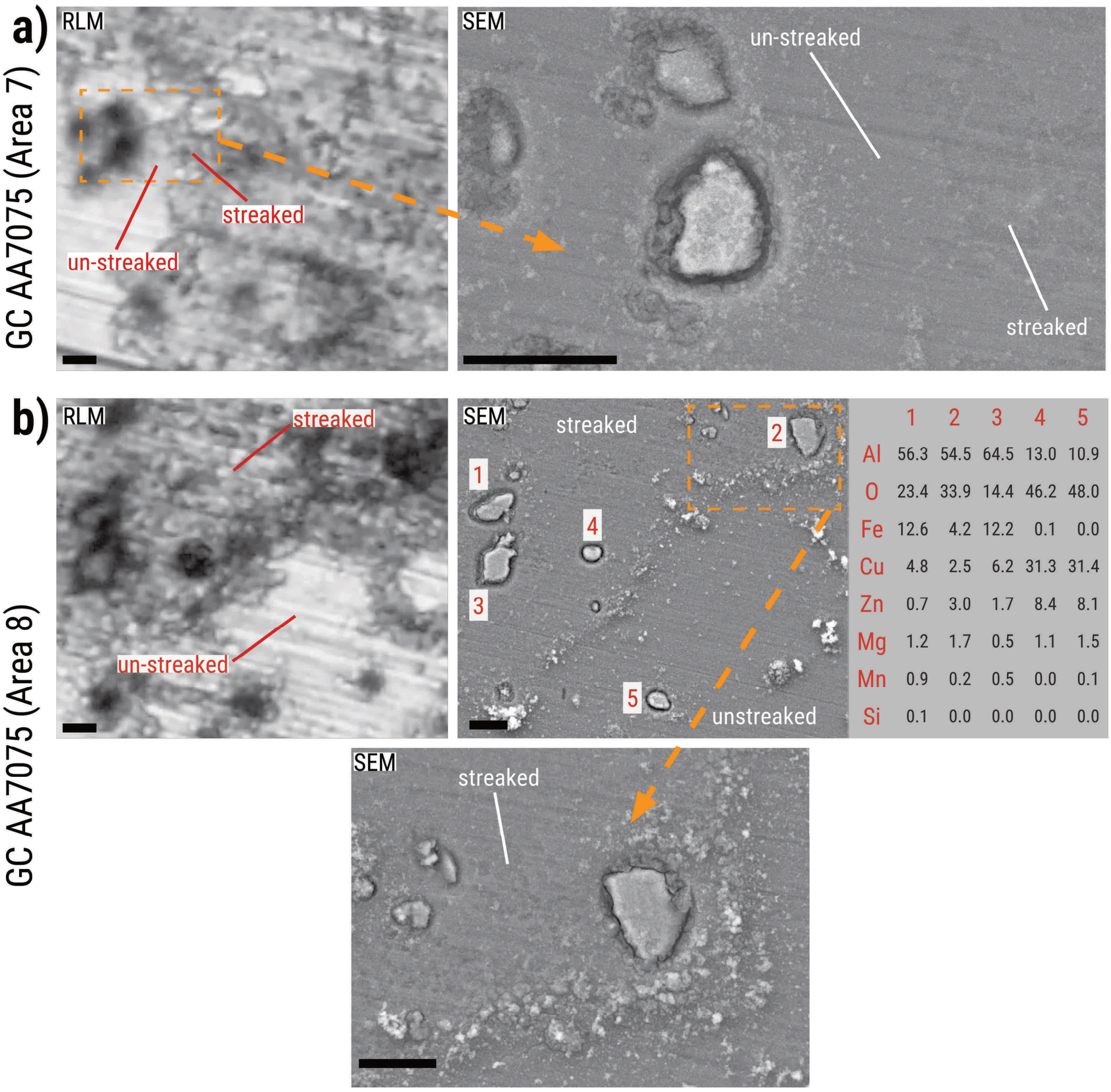

	1	2	3	4	5
Al	56.3	54.5	64.5	13.0	10.9
O	23.4	33.9	14.4	46.2	48.0
Fe	12.6	4.2	12.2	0.1	0.0
Cu	4.8	2.5	6.2	31.3	31.4
Zn	0.7	3.0	1.7	8.4	8.1
Mg	1.2	1.7	0.5	1.1	1.5
Mn	0.9	0.2	0.5	0.0	0.1
Si	0.1	0.0	0.0	0.0	0.0

Figure 5.7. Close-up reflected light microscopy images of **(a)** Area 7 and **(b)** Area 8 from the galvanically coupled assembly in Figure 5.4c after 2 hours of immersion, with corresponding post-immersion SEM images. These show streaking corrosion features and the extent of dealloying and trenching around IMPs. Post-immersion EDX compositions of the particles are also shown for **(b)**. Scale bars: 10 μm.

streaked areas in Figure 5.7b. Apart from the streaking, the trenching appears to be less extensive than that observed for the AA2024 IMPs under GC immersion (Figure 5.5) or the AA7075 IMPs under EI immersion (Figure 5.6). Post-immersion EDX analysis of the IMPs marked in Figure 5.7b indicates that particles 1, 2, and 3 are Fe-rich while particles 4 and 5 are Cu-rich. Interestingly, the Cu-rich particles registered higher Zn atomic percentages than the Fe-rich particles or the AA7075 matrix. This suggests considerable Zn precipitation on the more active particles of AA7075, which may influence the extent of cathodic reactions on the IMP surface.

Overall, the corrosion on the AA7075 surfaces in both GC trials appears comparable to that observed in the EI trials (Figure 5.4d and Figure 5.4e). The AA7075 IMPs in the EI trials also exhibited dealloying and trenching combined with varying degrees of streaking corrosion. IMPs from both GC and EI conditions also exhibited some degree of BT activity. The similarities suggest that while galvanic coupling had visible effects on AA2024, its impact is less distinct on the AA7075 side despite the negative galvanic currents measured.

5.3.3. Local corrosion progression of galvanically-coupled AA2024 and AA7075

The progression of local corrosion on AA7075 and AA2024 IMPs was examined in detail to understand how the final states shown in Figure 5.4b and Figure 5.4c developed. Due to variation in the extent of streaking between the two GC immersion trials, their local corrosion behaviour was analysed separately.

Local activity maps in Figure 5.8 show time-resolved local surface changes in Areas 5 and 6 (Figure 5.4b) of the first trial of the GC immersion. The maps are still frames of Movie 5.2. As with the uncoupled system in Figure 5.3, activity initiation associated with dealloying was observed on area 5 in the early stages of immersion (Figure 5.8a – 60 s). This gave way to dissolution of the adjacent matrix seen in some particles as higher activity on the IMP edge (see cyan arrows in Figure 5.8a – 300 s) or as an increase of the active area in others. A short-lived streaking corrosion event was also recorded between 60 and 300 s (see white arrow at 300 s in Figure 5.8a). The trenches around the IMPs continued growing with further immersion and was observed as increase in both activity level and width of the trenched areas. At around 1800 s, BT activity (i.e., purple zones around the warm-coloured trenches) developed around some IMPs (see green arrows in Figure 5.8a). As with the trenches, these BT areas exhibited an increase in both activity level and affected area with further immersion. Notably, the growth of the trenches appears to slow down as there is a less pronounced change in the width of the

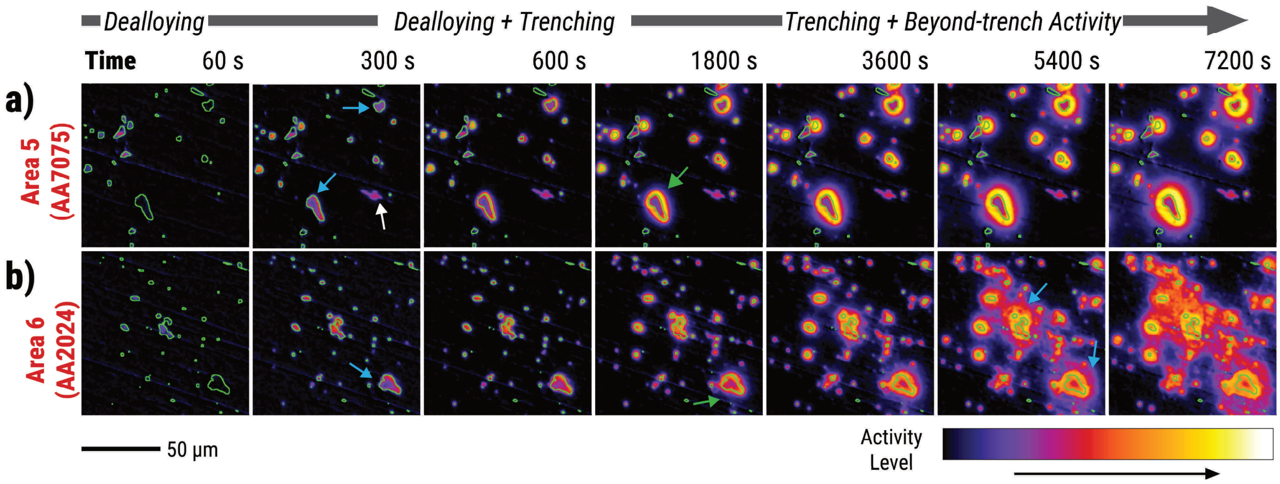

Figure 5.8. Time-resolved activity maps showing localized corrosion sites on **(a)** Area 5 and **(b)** Area 6 from the AA7075 and AA2024 surfaces in the assembly shown in Figure 5.4b, respectively. Green overlays indicate intermetallic particle boundaries used for analysing intermetallic activity. Warmer colours indicate higher activity levels.

trenches (yellow-coloured areas in the Figure 5.8a maps) between 1800 s and 7200 s. Comparable sequence of local corrosion events was observed in Area 6: IMP dealloying in the first minutes (Figure 5.8b – 60s) followed by trenching (see cyan arrows in Figure 5.8b – 300 s) and then BT activity onset (see green arrows at 1800 s in Figure 5.8b). At around 5400 s, BT activity (see cyan arrows in Figure 5.8b – 5400 s) reached considerably high levels (i.e., reddish-orange in the activity level colour scale) indicating intensification of the underlying process.

Similar corrosion features were observed in the second GC immersion trial, even though the AA7075 surface showed more extensive streaking corrosion than in the first trial. Figure 5.9a and Figure 5.9b show activity maps for Areas 7 and 8 (AA7075) from the second trial, taken as still frames from Movie 5.3. The activity maps of both areas exhibit the spread of streaking corrosion, first appearing in Area 7 at 600 s and in Area 8 at 300 s (see white arrows). It eventually dominated surface activity and affected the visibility of other local corrosion events on the surface before ending between 1800 s and 3600 s (see Movie 5.3). Apparent BT activity was observed in one particle from around 1800 s (see cyan arrow in Figure 5.9b–1800 s). However, identifying BT activity in other AA7075 IMPs was more difficult due to the extent of streaking corrosion on the surface. On the AA2024 side, Areas 9 and 10 (Figure 5.9c, d) showed a corrosion sequence comparable to the first trial: early-stage IMP dealloying and trenching followed by development of BT activity (see cyan arrows in Figure 5.9c, d–3600 s). It became substantially high with further immersion leading to a similar appearance to some of the trenches (see cyan arrow in Figure 5.9c, d–7200 s). It is noted that the activity maps for areas

9 and 10 correspond to the end-of-immersion microscopy images and post-immersion SEM images shown in Figure 5.5.

A visible drop in activity was observed on the streaked regions of Areas 7 and 8 between 3600 s and 5000 s (Figure 5.9a, b). This suggests changes on the already-streaked areas. The reduction in activity is potentially due to the release of nanograin remnants of the altered surface layer into the solution [14]. This loss of grain remnants likely reduced the roughness of the surface resulting in a decrease in the degree of light scattering and a corresponding drop in the pixel activity levels. Interestingly, this reduction in activity is most apparent in the streaked areas farther from the IMP sites. A further drop in apparent activity between 5000 and 7200 s is due to changes in lighting conditions.

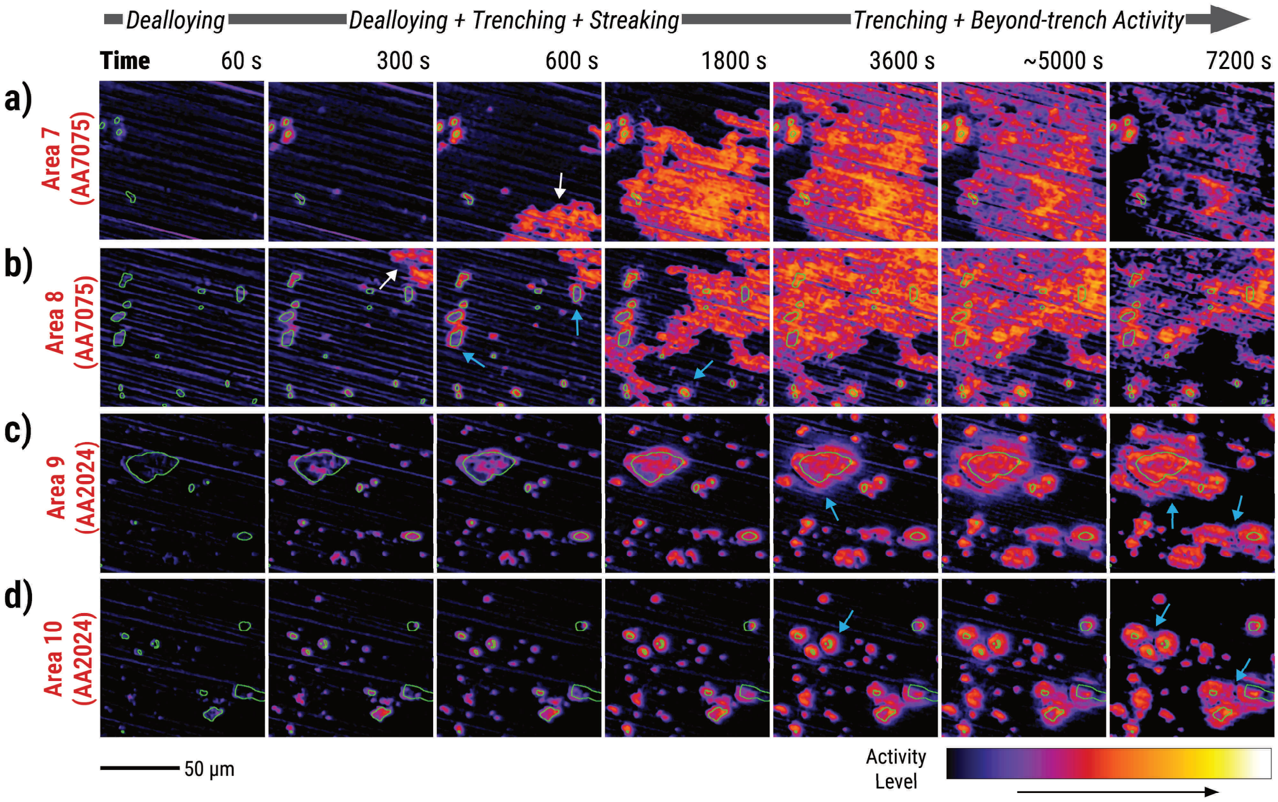

Figure 5.9. Time-resolved activity maps showing localized corrosion sites on **(a)** Area 7, **(b)** Area 8, **(c)** Area 9, and **(d)** Area 10 from the AA7075 and AA2024 surfaces in the assembly shown in Figure 5.4c. Green overlays indicate the boundaries used for analysis of IMP activity. Warmer colours indicate higher activity levels. The drop in the apparent activity of the matrix between 5000 and 7200 s is due to changes in the lighting conditions.

The overall local corrosion progression in both trials can be summarized in three stages based on the optically-dominant process: (Stage 1) dealloying-dominated stage, (Stage 2) trenching-dominated stage (with varying degrees of streaking corrosion), and (Stage 3) BT activity-dominated stage. Interestingly, both Stage 1 and Stage 2 were also observed in the uncoupled systems (Figure 5.2). Some form of Stage 3 was also seen in certain IMPs from the EI tests but they more closely resembled the BT activity observed in the AA7075 side of the GC assembly (i.e., uniform and low-level activity) than the high activity seen in AA2024 under GC conditions. These similarities between the GC and EI systems indicate that the local corrosion stages identified are not exclusive to GC systems. Despite the similarities, Stage 3 in the AA2024 side of the GC system developed more aggressively than that of the AA2024 in the EI system. This suggests that galvanic coupling of AA2024 and AA7075 does not change which stages occur, but likely increases the rate and severity of their progression, as will be analysed in the following section.

5.3.4. Kinetics of local corrosion processes in AA2024-AA7075 couple

Kinetic descriptors for the stages of local corrosion (i.e., dealloying-dominated, trenching-dominated, BT activity-dominated) were extracted from the local activity maps to assess the potential impact of galvanic coupling between AA2024 and AA7075. The descriptors are extracted from the simplified pixel activity level distribution (sPAD) plots (see the sample plot in Figure 5.10a) for the pixels within the IMP boundary. The descriptors include the onset of rapid activity increase on the IMP (t_{onset}) and the dealloying-to-trenching transition point (t_{tp}). Figure 5.10a shows a sample plot marking how these values were extracted. The t_{onset} is associated with the start of dealloying and can be used to estimate the beginning of Stage 1. The t_{tp} indicates where the rapid activity increase begins slowing down and marks the shift from Stage 1 to Stage 2 [8]. As shown in the local activity maps corresponding to the sample sPAD (Figure 5.10b), there is still some degree of dealloying during Stage 2. However, the trenching process contributes most to the activity level increase as well as the spread of active areas. The t_{onset} and t_{tp} values were numerically estimated from the sPADs and are subject to the tolerances used for estimation. In cases wherein there is noise or discontinuity in the data, the values of the parameters were manually estimated through a combined analysis of the sPADs and visual inspection of the activity maps. Additional details of the estimation procedure are provided in Supporting Information 5.7.3.

The t_{onset} distributions (Figure 5.11a) for AA2024 were nearly identical: 33 ± 23 s under GC conditions and 21 ± 19 s under EI conditions. Similarly, AA7075 showed comparable distributions, with a t_{onset} of 45 ± 44 s (GC) and 52 ± 54 s (EI). The high standard deviations are expected, since the t_{onset} values reported come from particles of varying composition. The t_{tp} distributions (Figure 5.11b) were also comparable between the EI and GC conditions. For AA2024, the mean t_{tp} values were 181 ± 61 s (GC) and 171 ± 49 s (EI), while AA7075 showed

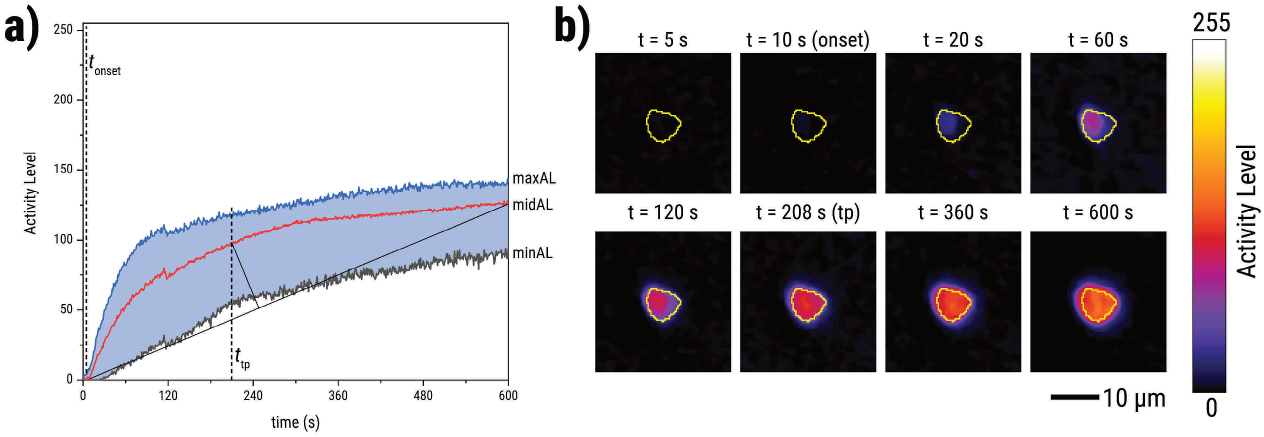

Figure 5.10. (a) Simplified pixel activity level distribution plot during the initiation of activity in an intermetallic particle, and **(b)** the corresponding local activity maps showing the corresponding surface changes at different points in time around the characteristic times (i.e., t_{onset}, t_{tp}) extracted from the plot.

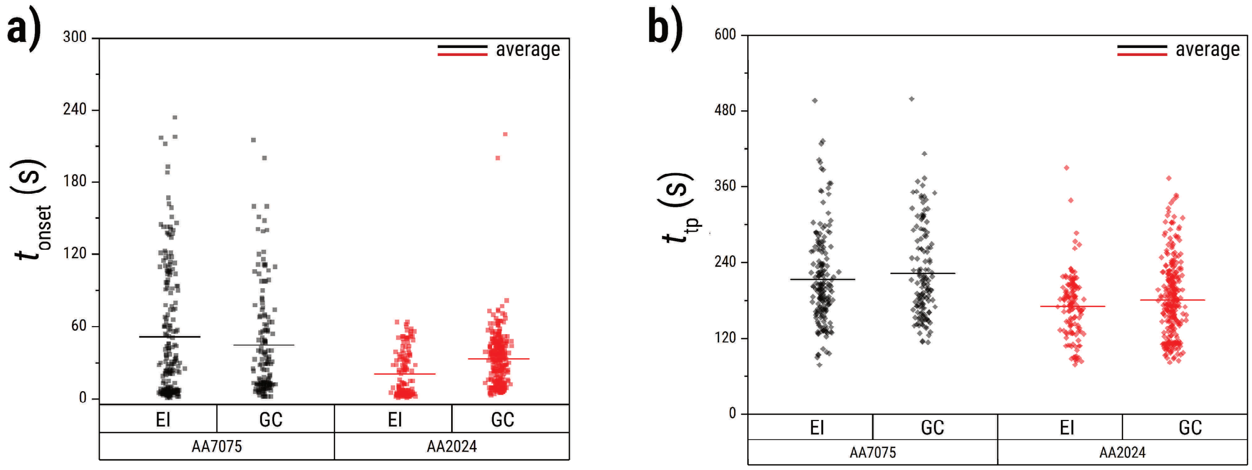

Figure 5.11. (a) Onset time of dealloying and **(b)** time of transition from dealloying-dominated to combined trenching and dealloying, for AA7075 and AA2024 particles. Results are shown for both electrically-isolated (EI) and galvanically-coupled (GC) conditions in the assembly (1:1 area ratio).

values of 223 ± 73 s (GC) and 214 ± 73 s (EI). Comparable t_{onset} and t_{tp} distributions for EI and GC conditions suggest that galvanic coupling had minimal effect on the dealloying-dominated stage (Stage 1). Activity level increase rates can also be calculated for the period between t_{onset} and t_{tp}. These values are presented in Supporting Information 5.7.3 and also indicate comparable Stage 1 behaviour for IMPs in EI and GC immersion conditions.

The effect of galvanic coupling on the subsequent trenching-dominated stage (Stage 2) was examined by selecting regions of interest that match the full width of the trenches seen at the end of immersion (Figure 5.12a). To isolate trench behaviour, a mask was applied to exclude the IMP pixels, so only the area covered by the trench was analysed. As the trench grows, more pixels reach higher activity levels. A threshold of 5 was used to identify active pixels while minimizing noise. The number of active pixels indicates the expanding trench area. Once the trench fully spans the region of interest, the number of active pixels levels off. The point when this plateau occurs is defined as the trench full-width time (t_{fwt}). This t_{fwt} not only marks the completion of the trench's lateral growth but also helps to indicate when BT activity might begin. After t_{fwt}, further increase in activity within the trench area mainly reflects deepening while activity spreading beyond the trench is attributed to the onset of BT activity (Figure 5.12b). It is noted that the current method for estimating t_{fwt} is less accurate for small trenches because the resolution of the imaging system starts to affect the distinction between IMP pixels and trench pixels.

Figure 5.13a and Figure 5.13b compare the t_{fwt} distribution as a function of trench area (i.e., the estimated area of the trench surrounding particle) for IMPs in AA2024 and AA7075, under both EI and GC conditions. For AA7075 (Figure 5.13a), galvanic coupling (orange dots) resulted in relatively lower t_{fwt} values (GC t_{fwt} mean: 1132 ± 559 s, EI t_{fwt} mean: 2232 ± 1154 s) than EI conditions (blue squares) particularly for bigger trenches (i.e., above ~40 μm^2). This suggests that, on average, AA7075 trenches under GC conditions reached their full width earlier (i.e., in around half the time) than those in EI conditions.

As for AA2024 (Figure 5.13b), the overall distribution of t_{fwt} from the GC trials is slightly earlier than that from the EI conditions (GC t_{fwt} mean: 2202 ± 1182 s, EI t_{fwt} mean: 2926 ± 1752 s). Moreover, when the GC data are separated with the extent of streaking in mind, the t_{fwt} values from trial 1, which had limited streaking, appear lower (2407 ± 1153 s) than those from trial 2 (3055 ± 1293 s), which had extensive streaking. The trial 1 t_{fwt} values suggest that galvanic coupling potentially accelerated trench propagation in AA2024 IMPs. However, the trial 2 t_{fwt} values suggest that the trench propagation of AA2024 IMPs was slower when there was extensive streaking corrosion on the AA7075 side. Identification of a slowdown of trenching on the AA7075 side is difficult to confirm due to the extensive streaking corrosion.

The t_{fwt} values indicate that the onset of BT activity (Stage 3) for most IMPs in the GC system happened within the first hour of immersion. This suggests that for most of the immersion period, the local corrosion processes happening on the surface of the alloys were a mixture of trench deepening and BT activity propagation. Both of these processes are forms of matrix dissolution. Quantitative analysis of BT propagation poses some challenges because it often involves overlapping areas from multiple IMPs, especially when they are clustered. Additionally, BT activity can sometimes be indistinguishable from corrosion product deposition and requires additional context (e.g., SEM data) to resolve the differences.

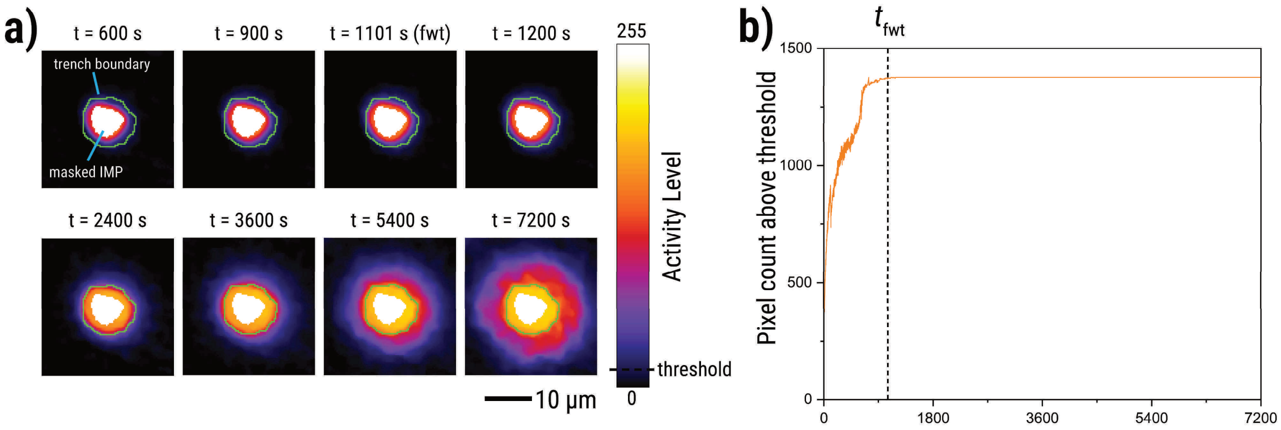

Figure 5.12. (a) Local activity maps showing surface changes at different times around the trench full-width time (t_{fwt}). A white mask is applied to the IMP pixels in order to focus the analysis on the spreading trench. The green boundary corresponds to the coverage of the trench defined from end-of-immersion optical observations. **(b)** Number of pixels inside the trench boundary with activity level above the threshold of 5 plotted against time used for estimating t_{fwt}.

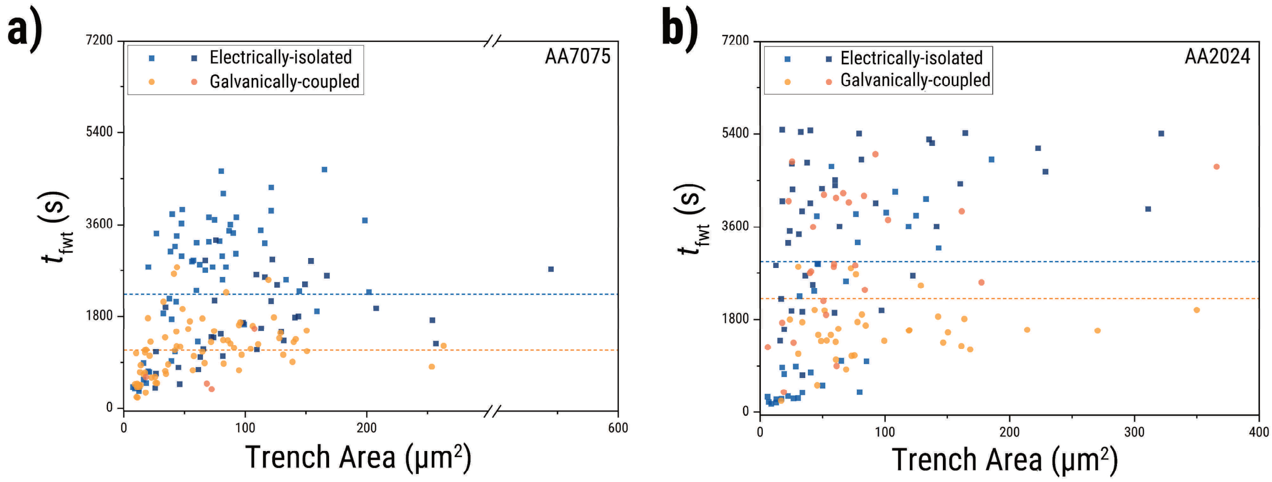

Figure 5.13. Estimated trench full-width time (t_{fwt}) for intermetallic particles in **(a)** AA7075 and **(b)** AA2024 under electrically-isolated and galvanically-coupled conditions. The area ratio between AA2024 and AA7075 is 1:1. Different shades (e.g., light blue and dark blue) represent values from different experimental trials. The dashed lines indicate the average t_{fwt} of electrically-isolated and galvanically-coupled data points.

5.3.5. Galvanic current density and potential of AA2024-AA7075 couple

The j_{gal} and E_{gal} trends measured during immersion reflect the overall electrochemical response to localized corrosion processes described in Sections 5.3.2 and 5.3.3. Changes in these signals over time are directly linked to the initiation and progression of dealloying, trench formation, and BT activity on the AA2024 and AA7075 surfaces. To better understand how these local corrosion events developed under GC conditions, the E_{gal} and j_{gal} behaviour are examined in relation to the three main stages of localized corrosion: Stage 1 (dealloying-dominated), Stage

2 (trenching-dominated), and Stage 3 (BT activity-dominated). The distribution of optics-based characteristic times (Figure 5.14a, Figure 5.15a) were aligned in time with the E_{gal} and j_{gal} curves (Figure 5.14b, Figure 5.15b) to correlate the microscopy data with the electrochemical data.

In trial 1 (Figure 5.14), E_{gal} ranged between approximately -0.7 and -0.6 V vs. Ag/AgCl. This is more negative than the OCP of AA2024 and slightly more positive than that of AA7075, consistent with a mixed potential arising from galvanic coupling between the two alloys. As previously shown in Figure 5.4a, the negative j_{gal} values indicate electron flow from AA7075 to AA2024. Electrochemical signal trends of the trial 1 assembly in each local corrosion stage are as follows:

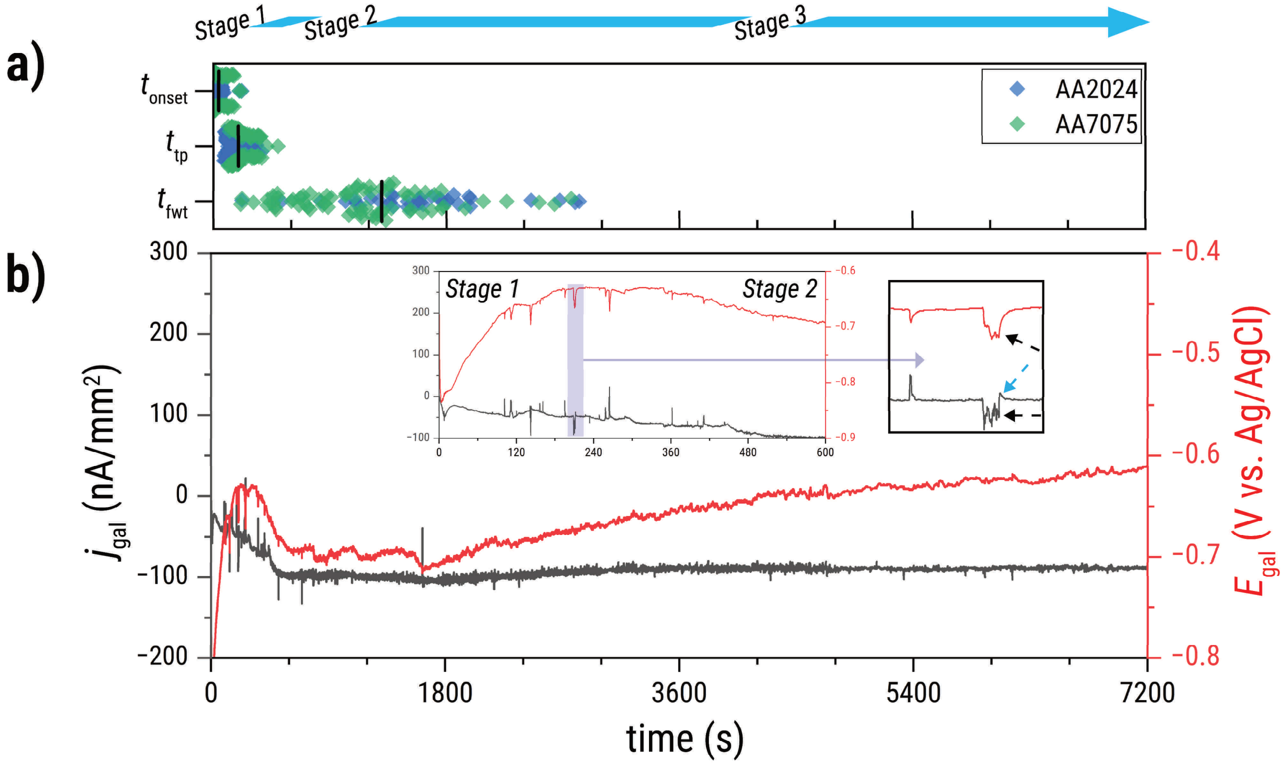

Figure 5.14. Time-aligned **(a)** optics-based kinetics parameters (t_{onset}, t_{tp}, t_{fwt}) and **(b)** galvanic potential and current density for trial 1 of the galvanically-coupled immersion shown in Figure 5.4b and Figure 5.8.The black vertical bars in **(a)** indicate the mean of the kinetic parameter. The insets in **(b)** show the first 600 s of immersion and a magnified section corresponding to the streaking corrosion.

- **Stage 1 (trial 1):** The dealloying-dominated stage occurred between 0 and approximately 193 s, based on the average t_{tp} values of the sampled IMPs from both AA2024 and AA7075 (Figure 5.14a). This stage is mainly driven by dealloying, as supported by the t_{onset} distribution, which mostly falls within this time range (with an average t_{onset} of 41 s). During this period, E_{gal} gradually shifted to more positive values with only minor fluctuations (transients), while j_{gal} steadily became more negative, indicating increasing electron flow between the two alloys.

- **Stage 2 (trial 1):** The trenching-dominated stage is estimated to begin around 193 s and transition to the next stage around 1300 s - the average t_{fwt} of sampled trenches from both AA2024 and AA7075 (Figure 5.14a). During this stage, E_{gal} exhibited a change in trend and began a drift to more negative values, which reflected increased anodic activity specifically associated with the growth of trenches around the IMPs. The drift was accompanied by several high-amplitude transients, predominantly in the negative direction, with amplitudes up to ~40 mV. Meanwhile, j_{gal} exhibited a shift to more negative values and exhibited transients with amplitudes up to ~100 nA mm^{-2}. It is noted that the E_{gal} transients matched the timing of the j_{gal} transients. The j_{gal} drift to more negative values suggests that the increase in anodic activity is more extensive for the AA7075 surface, leading to increased electron flow from AA7075 to AA2024.

  One of the transients in this stage (see dashed black arrows in the magnified inset in Figure 5.14b) corresponds to the brief streaking corrosion (see white arrow in Figure 5.8a – 300 s) observed from 208 s to 213 s. The E_{gal} transient sequence during this event is consistent with the streaking corrosion behaviour reported in our previous work [15], characterized by an almost instantaneous potential drop, followed by high-frequency transients, and then a gradual return to the pre-streaking potential. The initial potential drop and the subsequent high-frequency transients are attributed to the anodic nature of the streaking initiation and propagation (i.e., dissolution of Zn and Mg [14,15]) dominating the electrochemical response of the surface. The return to the pre-streaking potential is interpreted as the system's relaxation to a state wherein the cathodic reactions are balanced by the other dissolution processes on the IMPs and on the trenches [15]. A comparable response was observed in j_{gal}: an initial current drop, followed by high-frequency fluctuations, and then a return to pre-streaking levels. The initial drop indicates increased electron flow from AA7075 to AA2024 and is consistent with the presence of a dominating anodic process on AA7075. The high-frequency fluctuations reflect the electron flow from the streaking propagation. The return to pre-streaking levels corresponds to the termination of the anodic process associated with streaking corrosion. Interestingly, the j_{gal} trend corresponding to streaking corrosion termination is not smooth like that of E_{gal}. Instead, j_{gal} overshoots slightly and goes above the pre-streaking level before coming back down (see dashed cyan arrow in Figure 5.14b inset). This overshoot suggests that streaking corrosion termination causes a temporary decrease in the current from AA7075 to AA2024. The exact cause of this overshoot is not yet known and is recommended for further investigation.

- **Stage 3 (trial 1):** The BT activity-dominated stage is estimated to begin around 1300.3 s (Figure 5.14a). As more particles transition into Stage 3, a corresponding E_{gal} shift to more positive values (i.e., closer to AA2024 OCP) is observed. This trend suggests an overall ennoblement of the assembly. The shift was accompanied by low amplitude transients (up to ~10 mV). Meanwhile, j_{gal} exhibited a slight drift to less negative values combined with low amplitude transients (up to 20 nA mm^{-2}) around the same time.

E_{gal} and j_{gal} measurements from the second trial (Figure 5.15) showed comparable behaviour to that of the first trial. The E_{gal} also ranged between approximately -0.7 and -0.6 V vs. Ag/AgCl and its $\mathrm{j}_{\mathrm{gal}}$ was persistently negative as previously shown in Figure 5.4a. The E_{gal} and j_{gal} trends for trial 2 at each local corrosion stage are as follows:

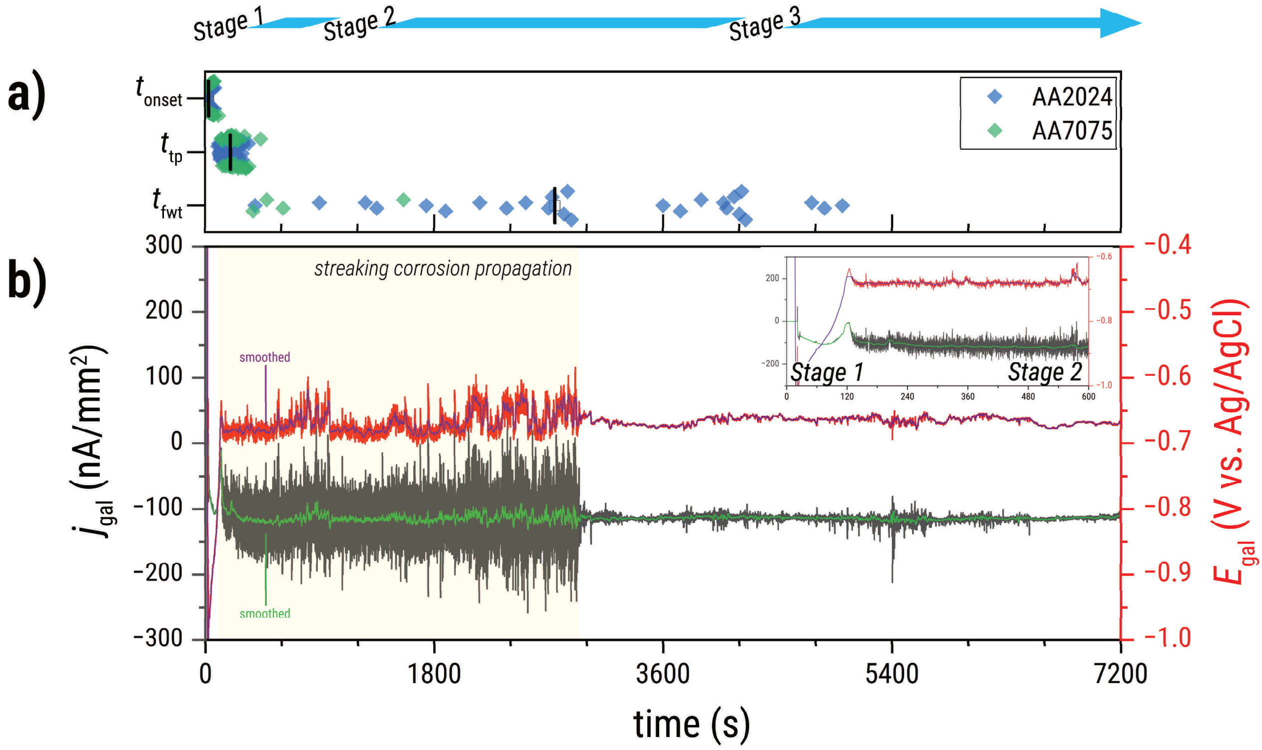

Figure 5.15. Time-aligned **(a)** optics-based kinetics parameters (t_{onset}, t_{tp}, t_{fwt}) and **(b)** galvanic potential and current density for trial 2 of the galvanically-coupled immersion shown in Figure 5.4c and Figure 5.9.The black vertical bars in **(a)** indicate the mean of the kinetic parameter. High-frequency high-amplitude transients between 0 and 3000 s are due to streaking corrosion propagation on the surface of the AA7075 alloy.

- **Stage 1 (trial 2):** The dealloying-dominated stage occurred between 0 and approximately 199 s (i.e., average t_{tp} from both AA2024 and AA7075). All of the dealloying onsets of the sampled IMPs from both alloys fall within this period (average t_{onset} = 29 s). As with trial 1, E_{gal} gradually shifted to more positive values with minimal transients. The j_{gal} was also generally noise-free and initially drifted to more negative values before slightly shifting to more positive values.

- **Stage 2 (trial 2):** The trenching-dominated stage is estimated to begin around 199 s and transitions to the next stage around 3056 s (the average t_{fwt} of sampled trenches from both AA2024 and AA7075). However, well-defined E_{gal} and j_{gal} trends are not observed during this stage for trial 2 due to massive streaking corrosion initiation and propagation. The streaking corrosion also limited analysis of trenching events in trial 2 resulting in a low number of AA7075 t_{tp} data points. Similar to the streaking corrosion event documented in trial 1, the streaking corrosion event in trial 2 leads to a drop in E_{gal} and j_{gal} to more negative values. The more negative E_{gal} is consistent with the anodic nature of streaking corrosion. Meanwhile, the more negative j_{gal} indicates that the streaking corrosion in this trial also increased the electron flow to AA2024. Due to the prolonged streaking during this test, the high-frequency fluctuations also became much more apparent. The smoothed j_{gal} curve (green curve in Figure 5.15b) shows that the average current density during this period is relatively stable at around -120 nA mm^{-2}. The fluctuations, on the other hand, caused j_{gal} to swing between ~-200 to ~0 nA mm^{-2}. This is consistent with the current density fluctuation briefly observed in trial 1 due to the limited streaking corrosion propagation. Interestingly, the j_{gal} fluctuations exhibit much higher amplitudes as more IMPs transition out of Stage 2. More transient peaks are observed going close to 0 nA mm^{-2} and beyond -200 nA mm^{-2}. Despite the j_{gal} fluctuations, overall negative values indicate that the AA2024 remained the cathode of the couple.

- **Stage 3 (trial 2):** The BT activity-dominated stage is estimated to begin around 3056 s based on the mean t_{fwt} values. Interestingly, this coincides with the termination of streaking corrosion marked by the disappearance of the high-frequency fluctuations in both E_{gal} and j_{gal}. The correlation between the transition from Stage 2 to Stage 3 and the electrochemically measured parameters gives more weight to the GC-accelerated trenching pathway proposed for Stage 2. As more particles transition into stage 3, the E_{gal} also starts gradually shifting to more positive values while exhibiting low amplitude transients (up to ~10 mV). The E_{gal} shift is not as extensive as that in trial 1. Comparison of the baseline in Stage 2 with that in Stage

3 (see smoothed blue curve in Figure 5.15b) shows an increase of around 10 mV between stages. Unlike trial 1, the j_{gal} baseline remained semi-stable during the transition from Stage 2 to Stage 3.

Overall, the electrochemical responses observed across both trials reflect a correlation between the evolving galvanic signals and the progression of localized corrosion processes on the AA2024-AA7075 assembly. Both trials yielded comparable Stage 1 electrochemical behaviour. However, the electrochemical patterns became more complex once dissolution of the matrix occurred. The higher magnitude of Stage 2 current densities measured in both tests does show that the galvanic coupling became more established once matrix dissolution is involved. These findings suggest that the evolution of macroscale galvanic interactions between AA2024 and AA7075 is intimately tied to the progression of local corrosion processes. The development of the galvanic measures suggests that IMPs must first activate and then initiate matrix dissolution before substantial macro-galvanic interactions develop.

5.3.6. Mechanism of local corrosion in AA2024-AA7075 couple

A local corrosion mechanism (Figure 5.16) is proposed, based on the previously discussed optical and electrochemical observations, to describe how the microstructures of AA2024 and AA7075 interact under galvanic coupling and contribute to the macroscale galvanic interactions observed.

In Stage 1, localized corrosion begins with the dealloying of IMPs in both alloys. During this dealloying-dominated stage, E_{gal} gradually shifts to more positive values, which is consistent with the previously reported behaviour for dealloying in AA2024 under open-circuit conditions [8,50]. This positive shift reflects the ennoblement of the dealloying particles, as they lose their less noble components (e.g., Mg, Zn). The corresponding negative j_{gal} indicates the flow of electrons from AA7075 to AA2024 during this stage. However, its magnitude is still not as large as that observed in the later stages despite the rapid changes observed on the surface. This suggests that during Stage 1, electron flow from the dealloying and early-stage trenching is still contained to the local corrosion sites and likely has minimal contribution to the macroscale galvanic coupling. Comparable Stage 1 kinetic descriptors (t_{onset}, t_{tp}) for the EI and GC immersion conditions further support this observation. If the galvanic coupling of AA2024 and AA7075 is closely tied to the initial IMP activation, it is reasonable to expect changes in how the particles activate. However, since this is not the case, this raises the question on the nature of the process or processes that contribute to the early-stage galvanic current from AA7075 to

AA2024. One potential candidate is the dissolution of anodic particles in AA7075, such as Mg_2Si and $MgZn_2$ [48]. These particles are typically too small to be detected by reflected light microscopy, which limits their visibility in the in situ optical analysis. Another potential pathway is the direct galvanic coupling between the bulk AA2024 and AA7075 matrices resulting in the loss of Mg and Zn from the AA7075 matrix. However, the activity of the matrices is also closely tied to the activation of the IMPs, making it difficult to isolate the changes due to microgalvanic coupling from those due to the galvanic coupling of AA2024 and AA7075.

In Stage 2, local corrosion becomes trenching-dominated, with both AA2024 and AA7075 developing trenches around IMPs due to their microgalvanic coupling with their surrounding matrix. The electrochemical and optical responses during this stage are also influenced by the presence or absence of streaking corrosion on the AA7075 surface. Trenching generally corresponds to the anodic dissolution of the matrix adjacent to the IMPs. As such, in the absence of streaking, the onset of trenching in both AA2024 and AA7075 results in a visible drift of E_{gal} to more negative values (Figure 5.14b). The E_{gal} drift is also accompanied by further increase in the magnitude of j_{gal}, which indicates increased electron flow from AA7075 to AA2024. For AA7075, faster widening of trenches was observed in GC systems based on their lower t_{fwt} values (Figure 5.13a). The faster widening indicates higher matrix dissolution rates, which could also have contributed to the electron flow between AA7075 and AA2024. Increasing j_{gal} suggests more cathodic activity than anodic activity on the AA2024 side. While the electron flow could potentially passivate the AA2024 matrix, this appears to lead instead to faster trench widening as seen in the lower t_{fwt} of the AA2024 IMPs. This suggests that one aspect of galvanic coupling between AA7075 and AA2024 is potentially between the AA7075 matrix and the AA2024 IMPs. The galvanic current density potentially intensifies the cathodic activity of AA2024, thereby enhancing reactions already occurring on the IMP surface (i.e., oxygen reduction reaction) and leads to a rise in the local pH. Enhanced local alkalinity likely destabilizes the adjacent oxide layer faster, causing an apparent acceleration of trench propagation relative to EI conditions (Figure 5.13a). This also potentially explains similarities in the optical microscopy images at the end of immersion in GC conditions (Figure 5.4b, c) and previous observations of AA2024 corroding in elevated pH [49].

When streaking is present, a Mg- and Zn-rich surface layer dissolves rapidly [14,15], temporarily dominating the overall electrochemical response. The dissolution of this surface layer contributes to the galvanic current flowing to the AA2024 surface, as seen in the j_{gal} and E_{gal} transients observed concurrently with streaking corrosion propagation (Figure 5.14b,

Figure 5.15b). The presence of streaking corrosion leads to bursts of electron flow from AA7075 to AA2024. In our previous work, it was shown that streaking corrosion can temporarily inhibit dealloying of IMPs [15]. Interestingly, the trenching on the AA7075 side also appears to have been impacted by the streaking corrosion as it is less extensive (Figure 5.4c, Figure 5.7) than that seen in EI conditions. This suggests that the main anodic reaction on AA7075 potentially became the dissolution of the surface layer associated with streaking corrosion. As a result, the impact of microgalvanic coupling on the bulk matrix dissolution may have been reduced. The processes on the AA2024 side also appear to have been affected by extensive streaking. Specifically, the trench growth appeared to have been slowed down by the widespread surface layer dissolution, resulting in higher t_{fwt} values than trial 1. The slowdown may be due to the surface layer serving as a sacrificial anode for the AA2024 matrix. It is noted that the sizes of trenches on AA2024 side remained comparable to the EI conditions despite the slower growth which could be due to the resumption of trench propagation after streaking corrosion on the AA7075 side ended.

In Stage 3, corrosion behaviour is dominated by BT activity. For both alloys, the process underlying BT activity is potentially the dissolution of the oxide layer on the matrix surrounding the trenches due to the local pH generated on the IMP surface. This progresses at a more aggressive rate for AA2024 resulting in a more severe transformation. The local pH increase generated by IMP activity continues to rise, destabilizing the oxide layer and potentially creating conditions that are unfavourable for aluminium hydroxide precipitation [51]. This may explain the absence of visible corrosion products at the end of immersion. As trenching deepens, IMPs can also detach, exposing surrounding matrix areas to further attack due to copper redeposition from the IMPs. Despite also containing Cu-rich particles, AA7075 does not show a similar extent of copper redeposition or aggressive matrix attack as AA2024. One possible explanation is that Zn released during corrosion precipitates onto IMP surfaces (Figure 5.7b), passivating them and limiting cathodic reactions [40,41]. This helps suppress further degradation. The passivation of AA7075 IMPs might also explain why, at later stages of immersion, electrons generated by the dissolution of the AA7075 matrix flow to the AA2024 sites instead of being kept locally. The observed E_{gal} shift towards more positive values in trial 1 is consistent with copper redeposition. Meanwhile, the modest j_{gal} decrease in magnitude can be explained by the detachment of some IMPs in AA2024 or the reduction of AA7075 IMP activity due to Zn precipitation.

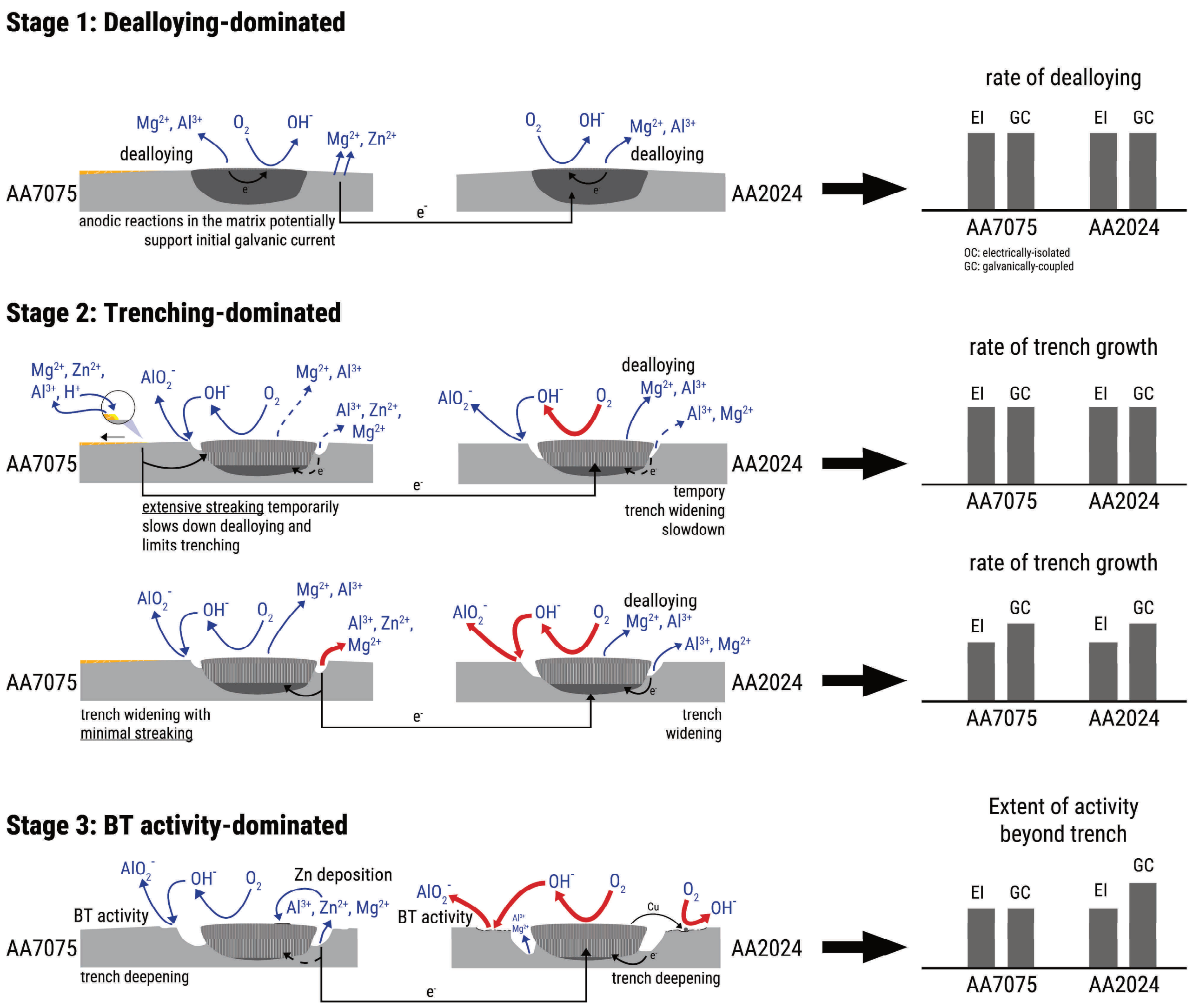

Figure 5.16. Proposed mechanism for the progression of localized corrosion under galvanically-coupled (GC) conditions for AA2024 and AA7075, along with a schematic representation of the associated effects on optically-detected surface phenomena. Thick red arrows denote processes that are potentially accelerated relative to electrically-isolated (EI) conditions, while dashed arrows indicate processes that may be suppressed or decelerated.

5.4. Conclusion

By combining in situ reflected light microscopy with galvanic current and potential measurements, this study revealed how galvanic coupling between AA2024 and AA7075 affects microscale local corrosion processes on both alloys. The results showed that such coupling drives electron flow from AA7075 to AA2024, increasing the cathodic activity of intermetallic particles in AA2024 and thereby intensifying local corrosion, despite the alloys' relatively small galvanic mismatch. The increased cathodic activity not only caused more extensive dissolution beyond the AA2024 IMP trenches, but also potentially increased the local pH near the AA2024 surface, which hindered corrosion product deposition. Galvanic coupling appeared to have minimal influence on the initial dealloying of IMPs in either alloy, though it modestly accelerated trench growth, with AA7075 trenches reaching full width in roughly half the time compared to electrically-isolated conditions. Streaking corrosion on AA7075 further modified the galvanic interaction, producing transients in the galvanic current and potential. Notably, extensive streaking corrosion coincided with reduced trenching on AA7075 and a temporary slowdown in trench widening on AA2024. Overall, this work highlights how macroscale galvanic coupling affects localised corrosion processes. It also shows the power of combining electrochemical techniques with site-resolved optical analysis to uncover mechanisms that would otherwise be overlooked or misidentified as typical local corrosion behaviour. At the same time, this integrated approach offers a pathway to link local corrosion dynamics with macroscale galvanic responses. Such insights may enable the use of galvanic measurements as practical indicators for tracking corrosion progression in real-life systems.

5.5. References

[1] L. Paussa, F. Andreatta, D. De Felicis, E. Bemporad, L. Fedrizzi, Investigation of AA2024-T3 surfaces modified by cerium compounds: A localized approach, *Corros. Sci.* 78 (2014) 215–222. doi:10.1016/j.corsci.2013.10.001.

[2] F.F. Chen, I. Cole, A.E. Hughes, A.M. Glenn, E. Sapper, J. Osborne, Microstructure characterisation and reconstruction of intermetallic particles, *Mater. Corros.* 65 (2014) 664–669. doi:10.1002/maco.201307345.

[3] A.E. Hughes, R. Parvizi, M. Forsyth, Microstructure and corrosion of AA2024, *Corros. Rev.* 33 (2015) 1–30. doi:10.1515/corrrev-2014-0039.

[4] J.V. de Sousa Araujo, I. Costa, X. Zhou, Comparison of constituent intermetallic particles in different aluminium alloys, *Metallogr. Microstruct. Anal.* 14 (2025) 106–119. doi:10.1007/s13632-025-01170-w.

[5] A.S. Hammad, H. Lu, M.M. El-Sayed Seleman, R.Q. Dzakyprasetyo, A. Anawati, Corrosion behaviour of aluminum alloy AA7075-T651, *IOP Conf. Ser. Mater. Sci. Eng.* 541 (2019) 012006. doi:10.1088/1757-899X/541/1/012006.

[6] A. Kosari, H. Zandbergen, F. Tichelaar, P. Visser, P. Taheri, H. Terryn, J.M.C. Mol, In-situ nanoscopic observations of dealloying-driven local corrosion from surface initiation to in-depth propagation, *Corros. Sci.* 177 (2020) 108912. doi:10.1016/j.corsci.2020.108912.

[7] A. Kosari, F. Tichelaar, P. Visser, H. Zandbergen, H. Terryn, J.M.C. Mol, Dealloying-driven local corrosion by intermetallic constituent particles and dispersoids in aerospace aluminium alloys, *Corros. Sci.* 177 (2020) 108947. doi:10.1016/j.corsci.2020.108947.

[8] M. Olgiati, P.J. Denissen, S.J. Garcia, When all intermetallics dealloy in AA2024-T3: Quantifying early stage intermetallic corrosion kinetics under immersion, *Corros. Sci.* 192 (2021) 109836. doi:10.1016/j.corsci.2021.109836.

[9] T. Hashimoto, X. Zhang, X. Zhou, P. Skeldon, S.J. Haigh, G.E. Thompson, Investigation of dealloying of S phase (Al_2CuMg) in AA2024-T3 aluminium alloy using high resolution 2D and 3D electron imaging, *Corros. Sci.* 103 (2016) 157–164. doi:10.1016/j.corsci.2015.11.013.

[10] Y. Zhu, K. Sun, G.S. Frankel, Intermetallic phases in aluminum alloys and their roles in localized corrosion, *J. Electrochem. Soc.* 165 (2018) C807–C820. doi:10.1149/2.0931811jes.

[11] N. Birbilis, M.K. Cavanaugh, R.G. Buchheit, Electrochemical behavior and localized corrosion associated with Al_7Cu_2Fe particles in aluminum alloy 7075-T651, *Corros. Sci.* 48 (2006) 4202–4215. doi:10.1016/j.corsci.2006.02.007.

[12] S. Niverty, C. Kale, K.N. Solanki, N. Chawla, Multiscale investigation of corrosion damage initiation and propagation in AA7075-T651 alloy using correlative microscopy, *Corros. Sci.* 185 (2021) 109429. doi:10.1016/j.corsci.2021.109429.

[13] S.S. Wang, J.T. Jiang, G.H. Fan, G.S. Frankel, L. Zhen, Effects of long-term natural aging on the altered surface layer on an Al-Zn-Mg-Cu alloy and on corrosion properties, *Electrochim. Acta* 266 (2018) 34–42. doi:10.1016/j.electacta.2018.02.001.

[14] Z. Zhao, G.S. Frankel, On the first breakdown in AA7075-T6, *Corros. Sci.* 49 (2007) 3064–3088. doi:10.1016/j.corsci.2007.02.001.

[15] M. Mopon, A. Mol, S.J. Garcia, Intermetallic particles trigger streaking corrosion in AA7075-T6, *NPJ Mater. Degrad.* 9 (2025) 92. doi:10.1038/s41529-025-00631-5.

[16] R.S. Huang, C.J. Lin, H.S. Isaacs, A difference-imaging technique used to study streaking corrosion of aluminum alloys AA7075 and AA8006 in chloride solution, *Electrochem. Solid-State Lett.* 9 (2006) B11–B14. doi:10.1149/1.2140503.

[17] R.S. Huang, C.J. Lin, H.S. Isaacs, Measuring streaking rates of an Al–Zn alloy using a difference imaging technique, *Corros. Sci.* 48 (2006) 1867–1873. doi:10.1016/j.corsci.2006.05.039.

[18] U. Donatus, G.E. Thompson, X. Zhou, Effect of near-ambient temperature changes on the galvanic corrosion of an AA2024-T3 and mild steel couple, *J. Electrochem. Soc.* 162 (2015) C42–C46. doi:10.1149/2.0551501jes.

[19] L. Shi, Y. Song, P. Zhao, H. Wang, K. Dong, D. Shan, E.H. Han, Variations of galvanic currents and corrosion forms of 2024/Q235/304 tri-metallic couple with multivariable cathode/anode area ratios: Experiments and modeling, *Electrochim. Acta* 359 (2020) 136947. doi:10.1016/j.electacta. 2020.136947.

[20] L. Shi, Y. Song, K. Dong, H. Wang, D. Shan, E.H. Han, The change of cathode/anode roles and corrosion forms in 2024/Q235/304 tri-metallic couple with the variation of oxygen concentrations and area ratios, *Corros. Sci.* 184 (2021) 109400. doi:10.1016/j.corsci.2021.109400.

[21] V. Torres, R. Mayen-Mondragon, J. Genesca, Assessment of the galvanic corrosion of bi-metallic couple 7075-T6-aluminum alloy/microalloyed dual-phase steel, *Mater. Corros.* 73 (2022) 940–949. doi:10.1002/maco.202112934.

[22] R. Montoya, A.G. Ruiz-García, A. Ortiz-Ozuna, B. Ramírez-Barat, J. Genesca, Acidification of the electrolyte during the galvanic corrosion of AA7075: A numerical and experimental study, *Mater. Corros.* 72 (2021) 1259–1269. doi:10.1002/maco.202012274.

[23] M. Montoya, J. Genesca, R. Montoya, The AA7075–CS1018 galvanic couple under evaporating droplets, *Corros. Mater. Degrad.* 5 (2024) 92–108. doi:10.3390/cmd5010005.

[24] R.S. Marshall, A. Goff, C. Sprinkle, A. Britos, R.G. Kelly, Estimating the throwing power of SS316 when coupled with AA7075 through finite element modeling, *Corrosion* 76 (2020) 476–484. doi:10.5006/3438.

[25] Z. Feng, G.S. Frankel, C.A. Matzdorf, Quantification of accelerated corrosion testing of coated AA7075-T6, *J. Electrochem. Soc.* 161 (2014) C42–C49. doi:10.1149/2.059401jes.

[26] S. Niverty, N. Chawla, 4D microstructural characterization of corrosion and corrosion-fatigue in a Ti–6Al–4V/AA7075-T651 joint in saltwater environment, *Mater. Sci. Eng. A* 825 (2021) 141886. doi:10.1016/j.msea.2021.141886.

[27] S. Policastro, R. Anderson, C. Hangarter, D.J. Horton, J.A. Keith, M.C. Groenenboom, Galvanic corrosion of AA7075-T6 caused by doped titanium oxides in a controlled atmospheric environment, *ECS Trans.* 80 (2017) 527–539. doi:10.1149/08010.0527ecst.

[28] L.B. Coelho, M. Hacha, Y. Paint, M.G. Olivier, Highlighting the effect of the aluminium alloy self-corrosion on the AA2024-T3/Ti6Al4V galvanic coupling in NaCl media, *Surf. Interfaces* 16 (2019) 15–21. doi:10.1016/j.surfin.2019.04.004.

[29] D. Snihirova, D. Höche, S. Lamaka, Z. Mir, T. Hack, M.L. Zheludkevich, Galvanic corrosion of Ti6Al4V–AA2024 joints in aircraft environment: Modelling and experimental validation, *Corros. Sci.* 157 (2019) 70–78. doi:10.1016/j.corsci.2019.04.036.

[30] S. Palani, T. Hack, J. Deconinck, H. Lohner, Validation of predictive model for galvanic corrosion under thin electrolyte layers: An application to aluminium 2024–CFRP material combination, *Corros. Sci.* 78 (2014) 89–100. doi:10.1016/j.corsci.2013.09.003.

[31] J.M. Vega, E. García-Lecina, J. Genesca, R. Montoya, The AA2024/CFRP galvanic couple under a dynamic electrolyte drop: Modeling and experimental, *Electrochim. Acta* 432 (2022) 141137. doi:10.1016/j.electacta.2022.141137.

[32] N.M. André, A. Bouali, E. Maawad, P. Staron, J.F. dos Santos, M.L. Zheludkevich, S.T. Amancio-Filho, Corrosion behavior of metal–composite hybrid joints: Influence of precipitation state and bonding zones, *Corros. Sci.* 158 (2019) 108075. doi:10.1016/j.corsci.2019.07.002.

[33] Z. Liu, M. Curioni, P. Jamshidi, A. Walker, P. Prengnell, G.E. Thompson, P. Skeldon, Electrochemical characteristics of a carbon fibre composite and the associated galvanic effects with aluminium alloys, *Appl. Surf. Sci.* 314 (2014) 233–240. doi:10.1016/j.apsusc.2014.06.072.

[34] M.M.Z. Ahmed, M.M. El-Sayed Seleman, D. Fydrych, G. Çam, Friction stir welding of aluminum in the aerospace industry: The current progress and state-of-the-art review, *Materials* 16 (2023) 2971. doi:10.3390/ma16082971.

[35] A. Murphy, W. McCune, D. Quinn, M. Price, The characterisation of friction stir welding process effects on stiffened panel buckling performance, *Thin-Walled Struct.* 45 (2007) 339–351. doi:10.1016/j.tws.2007.02.007.

[36] S. Bocchi, M. Cabrini, G. D'Urso, C. Giardini, S. Lorenzi, T. Pastore, The influence of process parameters on mechanical properties and corrosion behavior of friction stir welded aluminum joints, *J. Manuf. Process.* 35 (2018) 1–15. doi:10.1016/j.jmapro.2018.07.012.

[37] A. Abdelfatah, M. Abu-Okail, L.Z. Mohamed, Corrosion behavior of the pre-heated friction stir welded AA2024 alloy reinforced with AA7075 in 3.5% NaCl solution, *Int. J. Electrochem. Sci.* 16 (2021) 151001. doi:10.20964/2021.01.44.

[38] C. Zhang, G. Huang, Q. Liu, Research on local corrosion behavior of thermo-mechanically affected zone in dissimilar AA2024/7075 friction stir welds, *Intermetallics* 130 (2021) 107081. doi:10.1016/j.intermet.2020.107081.

[39] C. Zhang, G. Huang, Y. Cao, Q. Li, Y. Zhu, X. Huang, Q. Liu, Investigation on microstructure and localized corrosion behavior in the stir zone of dissimilar friction-stir-welded AA2024/7075 joint, *J. Mater. Sci.* 55 (2020) 15005–15032. doi:10.1007/s10853-020-05072-w.

[40] A.F.S. Bugarin, C.P. de Abreu, M. Terada, H.G. de Melo, I. Costa, Effect of friction stir welding (FSW) on the electrochemical behavior and galvanic coupling of AA2024-T3 and AA7475-T651, *Mater. Today Commun.* 25 (2020) 101591. doi:10.1016/j.mtcomm.2020.101591.

[41] C.P. de Abreu, I. Costa, H.G. de Melo, N. Pébère, B. Tribollet, V. Vivier, Multiscale electrochemical study of welded Al alloys joined by friction stir welding, *J. Electrochem. Soc.* 164 (2017) C735–C746. doi:10.1149/2.0391713jes.

[42] L.B. Coelho, M. Taryba, M. Alves, M.F. Montemor, M.G. Olivier, Unveiling the effect of the electrodes area on the corrosion mechanism of a graphite–AA2024-T3 galvanic couple by localised electrochemistry, *Electrochim. Acta* 277 (2018) 9–19. doi:10.1016/j.electacta.2018.04.187.

[43] M. Mopon, A. Mol, S.J. Garcia, Effect of delayed inhibitor supply on AA2024-T3 intermetallic activity: A local in situ analysis with reflected microscopy, *Corros. Sci.* 230 (2024) 111910. doi:10.1016/j.corsci.2024.111910.

[44] M. Mopon, A. Mol, S.J. Garcia, Local re-immersion behaviour of Ce-based inhibiting layers on AA2024-T3 intermetallics: Enhanced stability through partial dealloying and prolonged exposure, *Corros. Sci.* 255 (2025) 113146. doi:10.1016/j.corsci.2025.113146.

[45] A. Boag, A.E. Hughes, A.M. Glenn, T.H. Muster, D. McCulloch, Corrosion of AA2024-T3 part I: Localised corrosion of isolated IM particles, *Corros. Sci.* 53 (2011) 17–26. doi:10.1016/j.corsci.2010.09.009.

[46] A. Kosari, M. Ahmadi, F. Tichelaar, P. Visser, Y. Gonzalez-Garcia, H. Zandbergen, H. Terryn, J.M.C. Mol, Editors' choice—Dealloying-driven cerium precipitation on intermetallic particles in aerospace aluminium alloys, *J. Electrochem. Soc.* 168 (2021) 041505. doi:10.1149/1945-7111/abf50d.

[47] A.M. Homborg, M. Olgiati, P.J. Denissen, S.J. Garcia, An integral non-intrusive electrochemical and in-situ optical technique for the study of the effectiveness of corrosion inhibition, *Electrochim. Acta* 403 (2022) 139619. doi:10.1016/j.electacta.2021.139619.

[48] O. Gharbi, S.K. Kairy, P.R. De Lima, D. Jiang, J. Nicklaus, N. Birbilis, Microstructure and corrosion evolution of additively manufactured aluminium alloy AA7075 as a function of ageing, *NPJ Mater. Degrad.* 3 (2019) 40. doi:10.1038/s41529-019-0101-6.

[49] E. Michailidou, P. Visser, J.M.C. Mol, A. Kosari, H. Terryn, K. Baert, Y. Gonzalez-Garcia, The effect of pH on the corrosion protection of aluminum alloys in lithium-carbonate-containing NaCl solutions, *Corros. Sci.* 210 (2023) 110851. doi:10.1016/j.corsci.2022.110851.

[50] P.J. Denissen, A.M. Homborg, S.J. Garcia, Interpreting electrochemical noise and monitoring local corrosion by means of highly resolved spatiotemporal real-time optics, *J. Electrochem. Soc.* 166 (2019) C3275–C3283. doi:10.1149/2.0341911jes.

[51] K.H. Gayer, L.C. Thompson, O.T. Zajicek, The solubility of aluminum hydroxide in acidic and basic media at 25 °C, *Can. J. Chem.* 36 (1958) 1268–1271. doi:10.1139/v58-184.

5.6. Movies

The following movies can be accessed online through the provided links presented in the movie captions the accompanying QR codes, or the DOI of the corresponding journal.

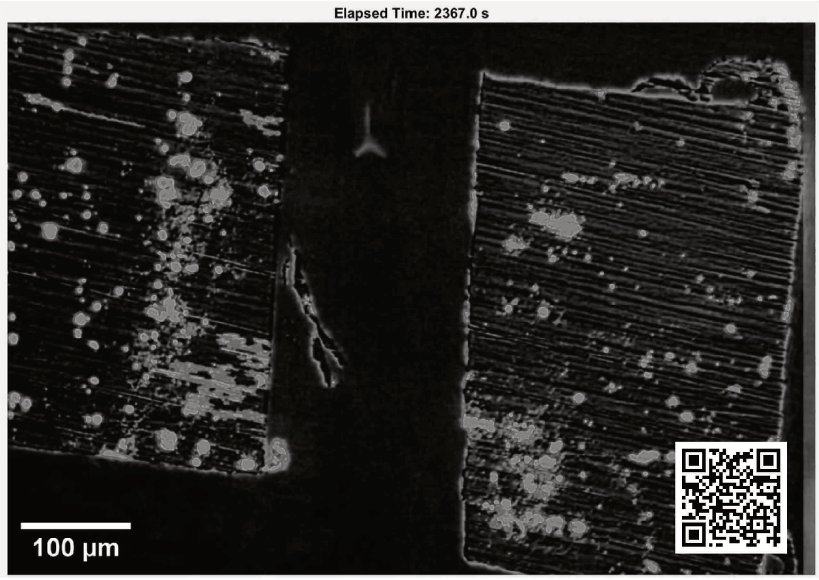

Movie 5.1. Timelapse video showing the development of local corrosion in AA7075-T6 (left) and AA2024-T3 (right) during a 2-h immersion in 0.05 M NaCl. The alloys are not electrically connected and are corroding under open-circuit conditions. (https://youtu.be/2T37g1tINFs)

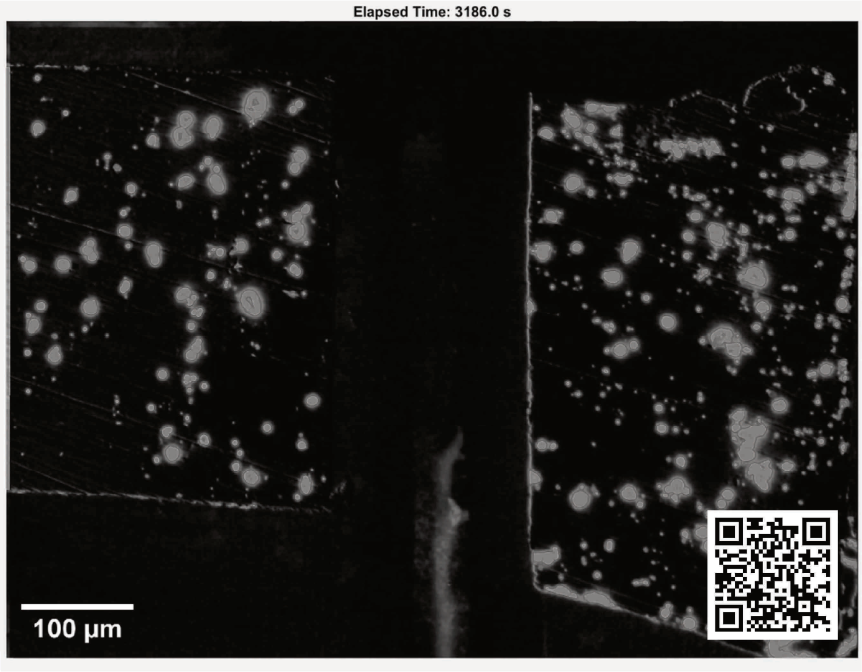

Movie 5.2. Timelapse video showing the development of local corrosion in AA7075-T6 (left) and AA2024-T3 (right) during trial 1 of a 2-h immersion in 0.05 M NaCl. The alloys are electrically connected externally via a zero-resistance ammeter and are thus corroding under galvanically-coupled conditions. The AA7075 did not exhibit extensive streaking corrosion in this trial. (https://youtu.be/nsQ4Xx7xSdU)

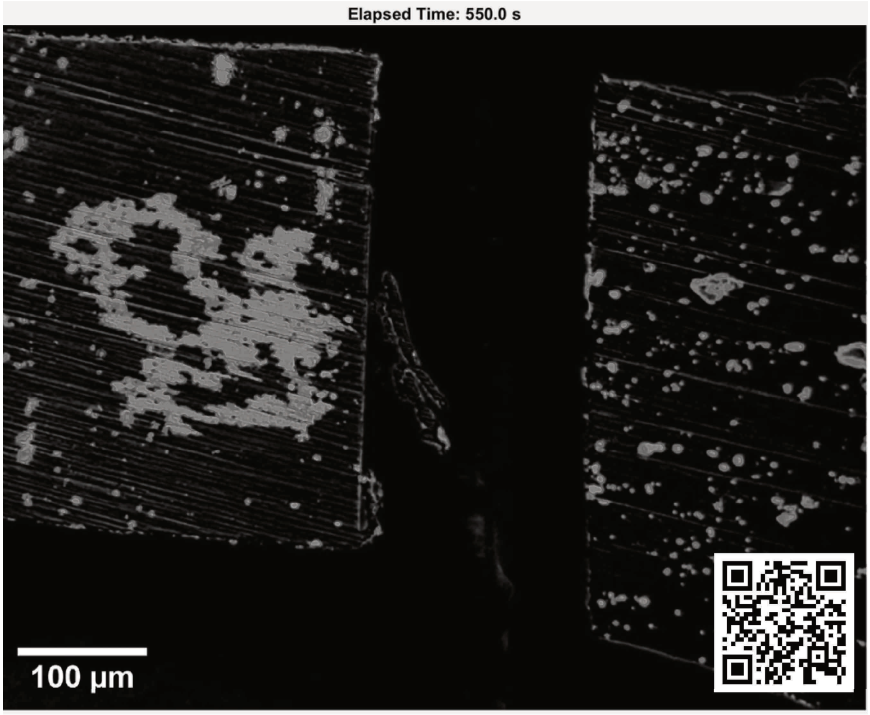

Movie 5.3. Timelapse video showing the development of local corrosion in AA7075-T6 (left) and AA2024-T3 (right) during trial 2 of a 2-h immersion in 0.05 M NaCl. The alloys are electrically connected externally via a zero-resistance ammeter and are thus corroding under galvanically-coupled conditions. The AA7075 exhibited extensive streaking corrosion in this trial. (https://youtu.be/0ff50jqROAM)

5.7. Supporting Information

5.7.1. Validation of direction of electron flow

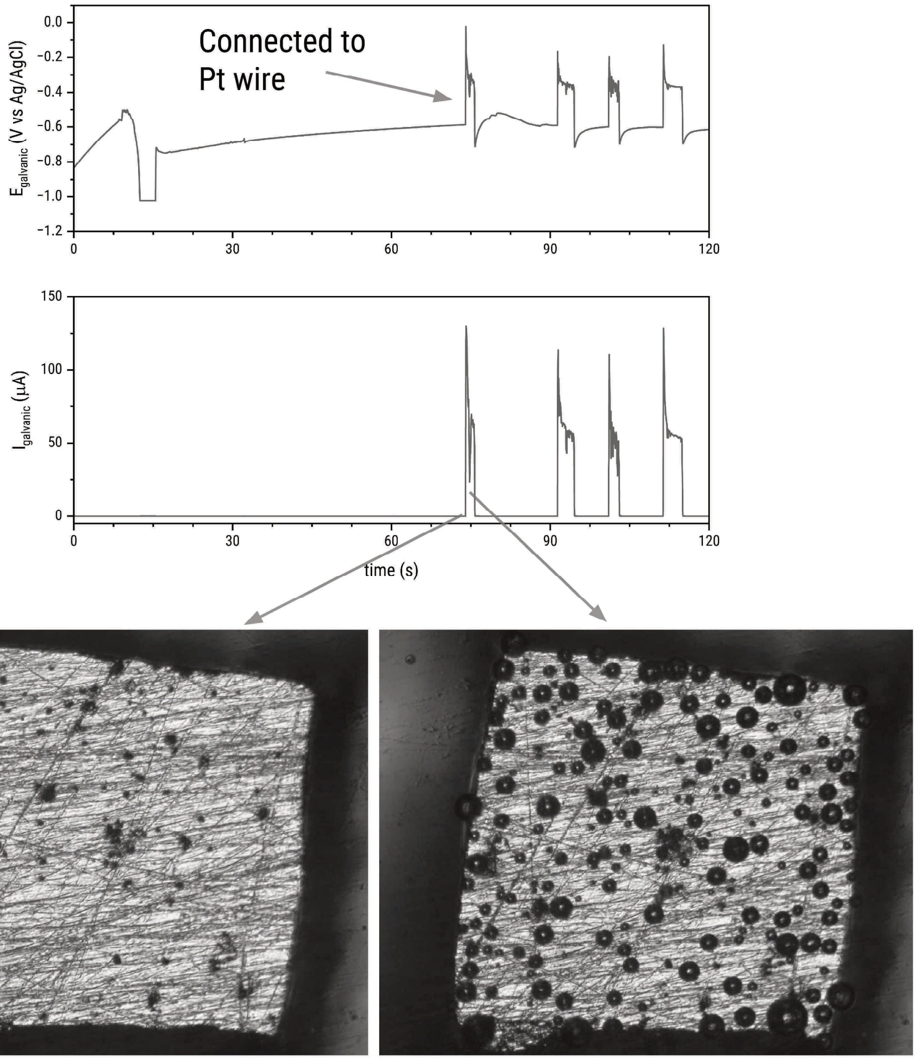

Figure S5.1. Galvanic current and galvanic potential measurements when the AA2024 sample was intermittently connected to the Pt wire. The non-zero galvanic current corresponds to the time when the AA2024 and Pt electrodes are galvanically connected. The impact of the galvanic coupling was optically confirmed with in situ reflected light microscopy.

The direction of electron flow corresponding to the measured galvanic current was determined by using an AA2024 sample embedded in epoxy and the integrated Pt wire in the Raman cell (Redox.me). An Ivium compactstat.h was used as the zero resistance ammeter. The electrochemical measurement configuration was assembled by connecting the working electrode cable to the embedded AA2024 and intermittently connecting the ground cable to the Pt wire. The reference electrode cable was connected to a Ag/AgCl (3 M KCl) reference electrode. The surface of the AA2024 sample was monitored with the Dino-lite camera.

Figure S5.1 shows that when AA2024 is electrically connected to the Pt wire, the galvanic current ($I_{galvanic}$) measured becomes non-zero. The galvanic potential ($E_{galvanic}$) measured also becomes more positive than the known open-circuit potential of AA2024. When the Pt wire is disconnected, the $E_{galvanic}$ returns to the AA2024 baseline and the $I_{galvanic}$ returns to zero. In the configuration implemented (working electrode: AA2024, ground electrode: Pt), a positive $I_{galvanic}$ is measured when AA2024 and Pt are connected. Based on their known galvanic potentials, Pt will behave as the cathode and the AA2024 will behave as the anode. As such, the electron flow will be from AA2024 to Pt (i.e., working to ground). This indicates that a positive current is measured when the electrons are flowing out of the working electrode. By extension, a negative current is measured when electrons are flowing into the working electrode.

5.7.2. Regions of interest used for local analysis

Figure S5.2 to Figure S5.7 show the regions of interest (green boundaries) used to analyse local changes in sites associated with intermetallic particles (IMP) and trenches. It is noted that not all IMP boundaries have there corresponding trench boundaries because not all trenches have well-defined boundaries. Some trenches are surrounded by excessive corrosion product deposition while others share boundaries with other trenches.

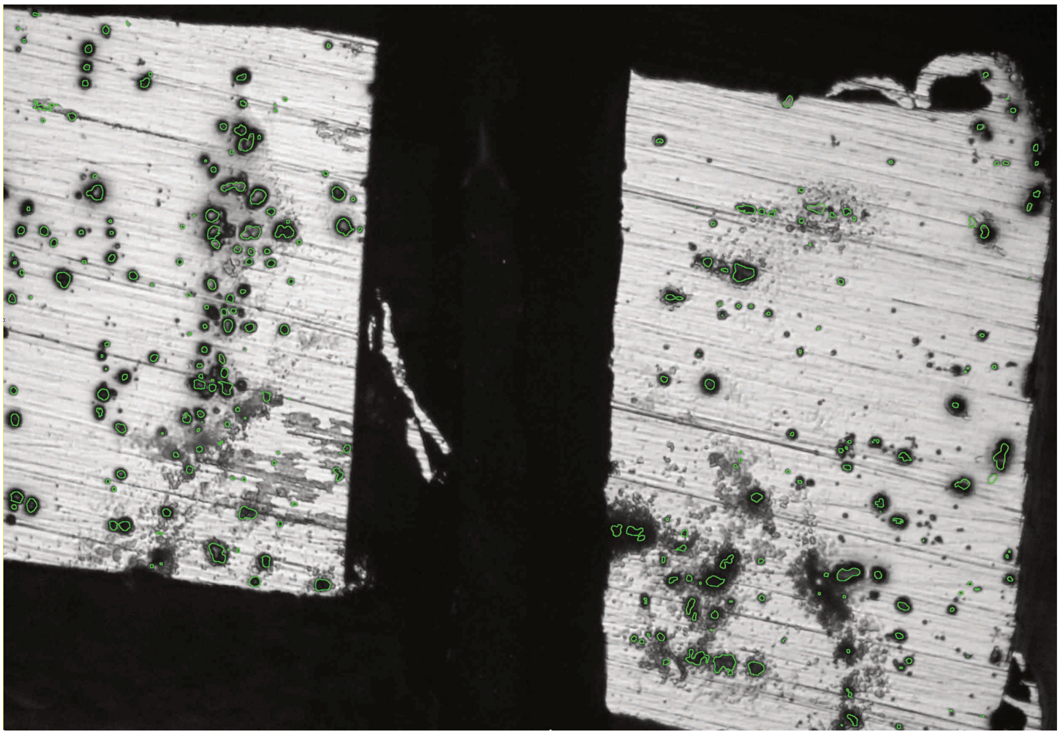

Figure S5.2. Boundaries used for the analysis of sites associated with intermetallic particle activity in the sample shown in Figure 5.2.

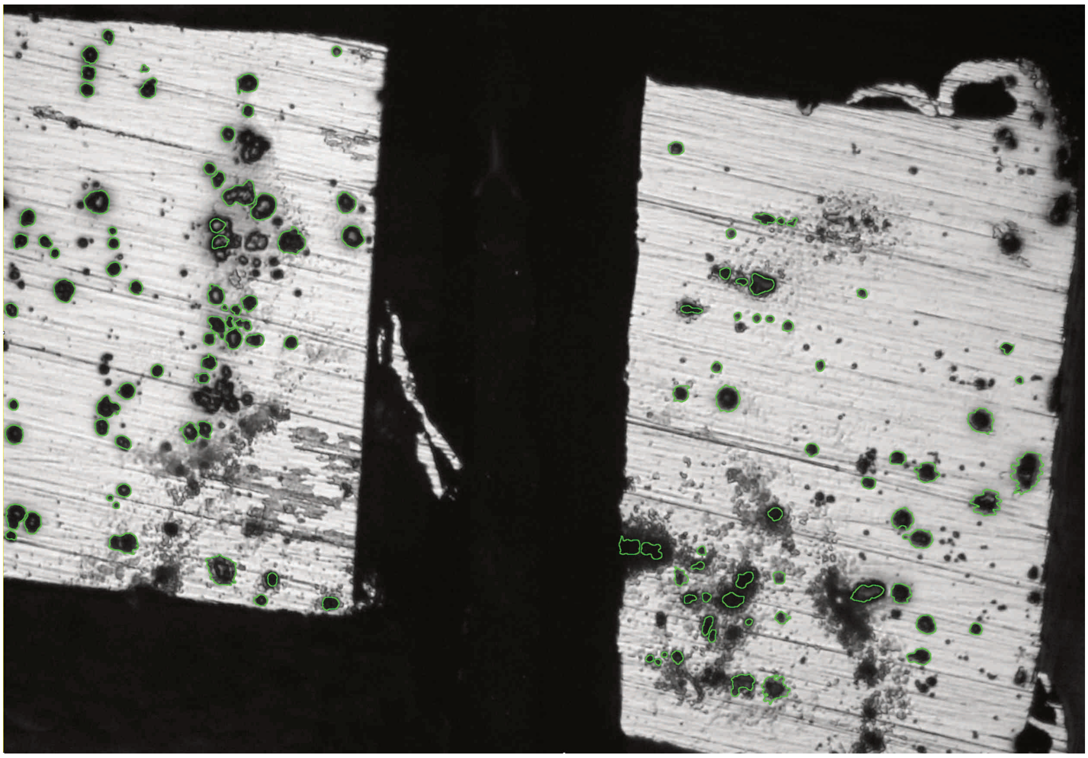

Figure S5.3. Boundaries used for the analysis of sites associated with trench activity in the sample shown in Figure 5.2.

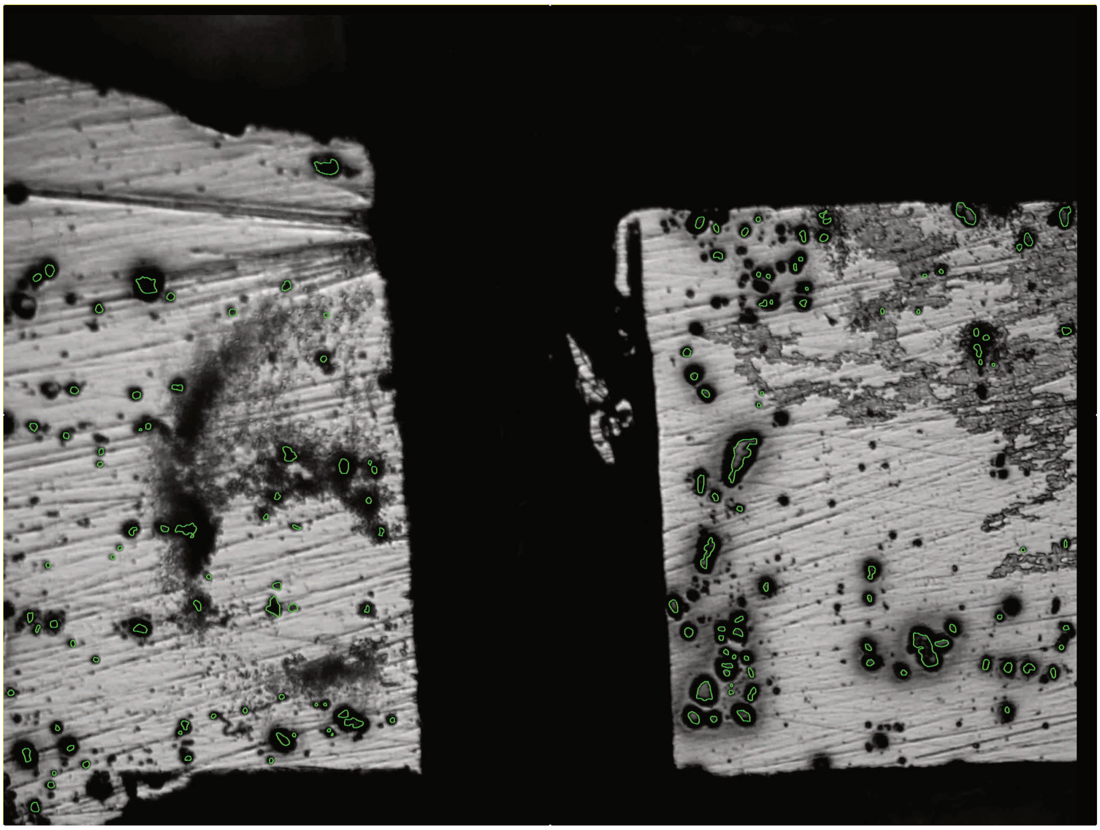

Figure S5.4. Boundaries used for the analysis of sites associated with IMP activity in the sample shown in Figure 5.4e.

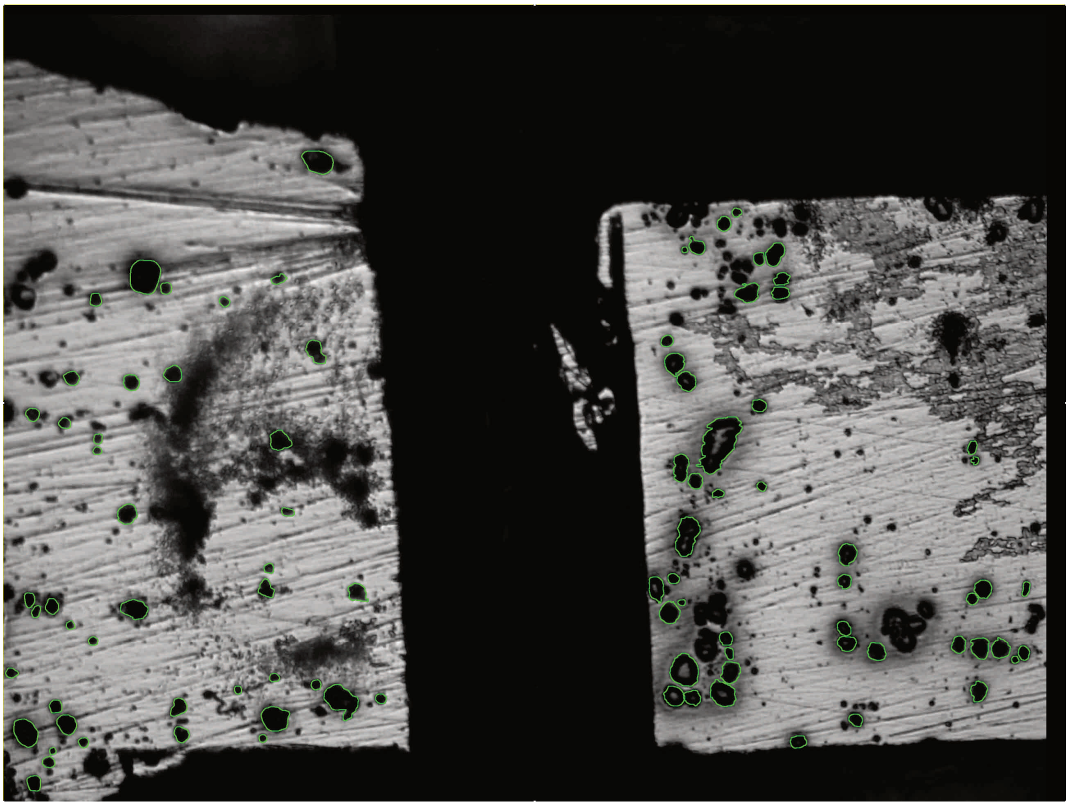

Figure S5.5. Boundaries used for the analysis of sites associated with trench activity in the sample shown in Figure 5.4e.

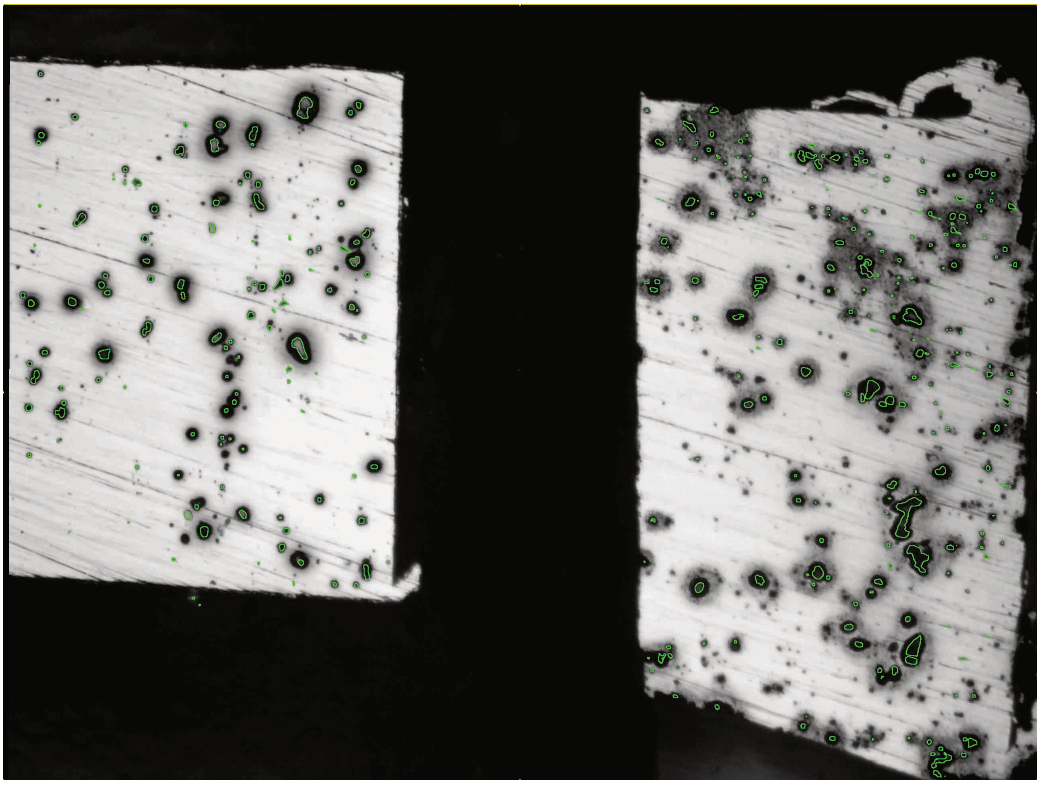

Figure S5.6. Boundaries used for the analysis of sites associated with intermetallic particle activity in the sample shown in Figure 5.4b.

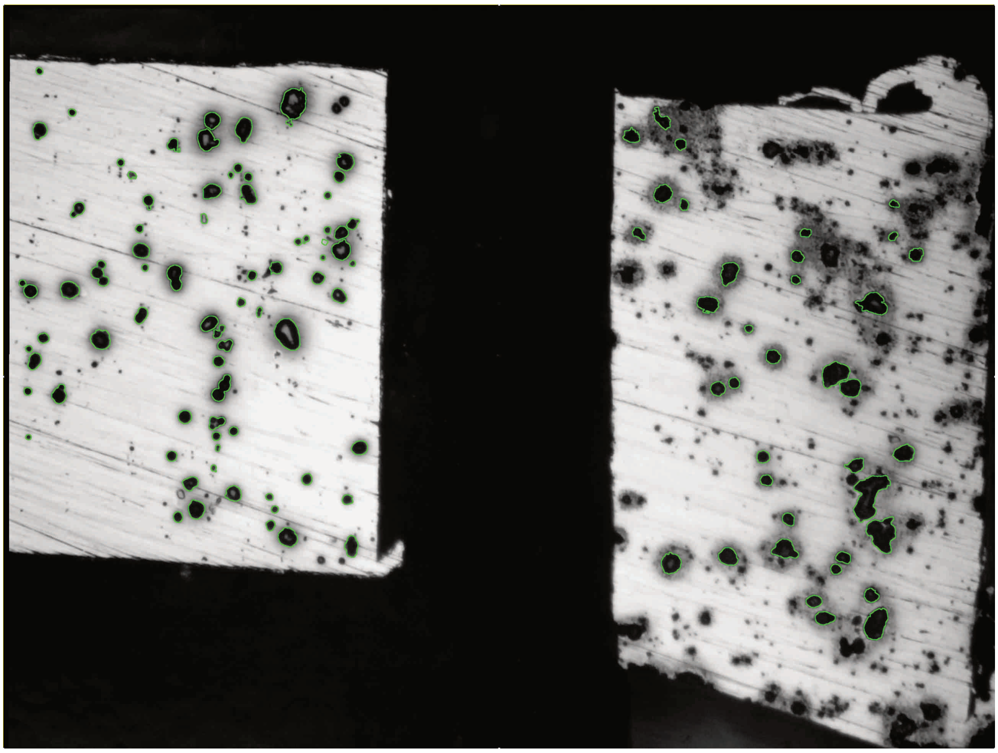

Figure S5.7. Boundaries used for the analysis of sites associated with trench activity in the sample shown in Figure 5.4b.

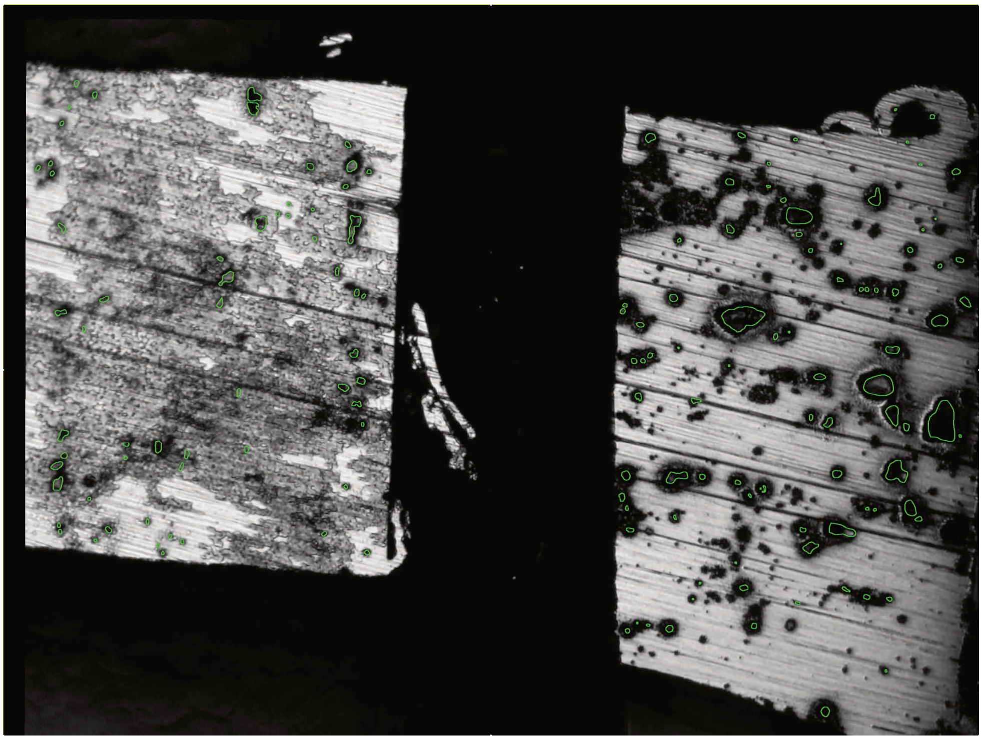

Figure S5.8. Boundaries used for the analysis of sites associated with IMP activity in the sample shown in Figure 5.4c.

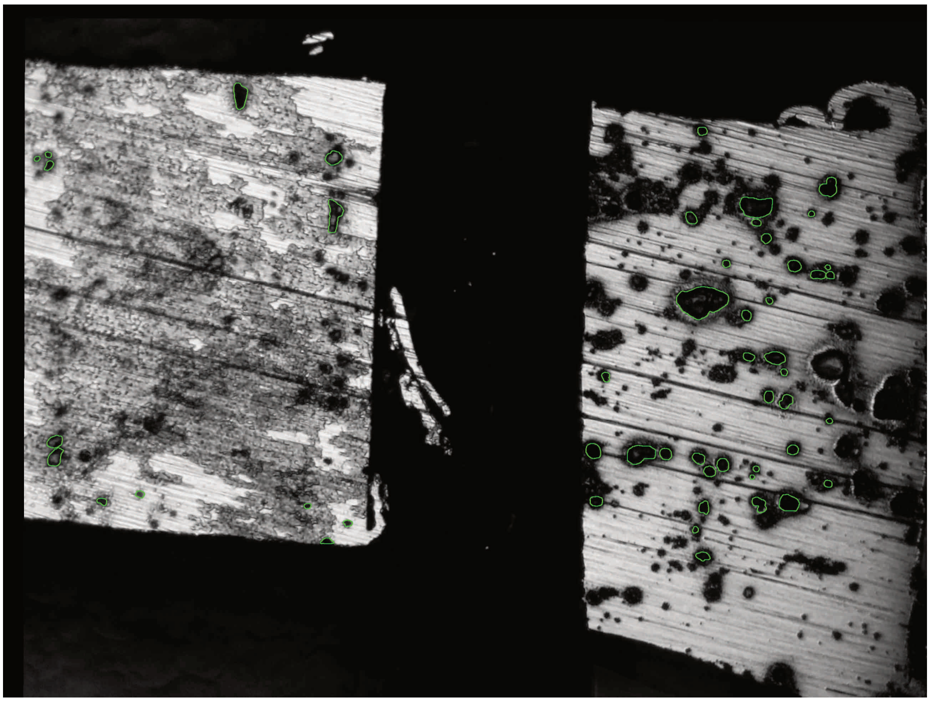

Figure S5.9. Boundaries used for the analysis of sites associated with trench activity in the sample shown in Figure 5.4c.

5.7.3. Kinetic parameters estimated from optics

5.7.3.1. Graphical estimation of kinetic parameters

In some cases, the region of interest corresponding to a local corrosion site might be subject to lighting or focus changes. This can affect the appearance of the simplified pixel activity level distribution (sPAD) plots and pose challenges on numerical estimation of the optics-based parameters. If the features associated with the t_{onset} and t_{tp} are still visible in the plot, graphical estimation of these two parameters is implemented. The features considered for t_{onset} estimation includes a period of relatively constant minAL, midAL, and maxAL which then transitions to a period of increasing activity levels. The features considered for the t_{tp} estimation include the presence of a period of relatively fast increase that transitions to a period of slower increase. The transition point is generally marked by a shoulder on the pixel activity level distribution plot. The graphically estimated values estimated using these features are validated by cross-referencing with the activity maps. Figure S5.10 shows an example of a local corrosion site with a discontinuity during the first 20 seconds of immersion due to focus-changes. The change in focus caused a pre-existing black spot to be in focus which then registered as a step discontinuity in the activity maps and the sPAD. Nonetheless, the features associated with the t_{onset} are still detectable in the sPAD thus enabling graphical estimation. The same goes for the t_{tp}. Cross-referencing with the activity maps shows that the activity on the

IMP region of interest only substantially increased after the onset and that activity around the boundary associated with trenching became substantial only after the t_{tp}. It is noted that this graphical approach is not applicable for all IMPs with discontinuity and is only used for sPADs with detectable t_{onset} and t_{tp} features.

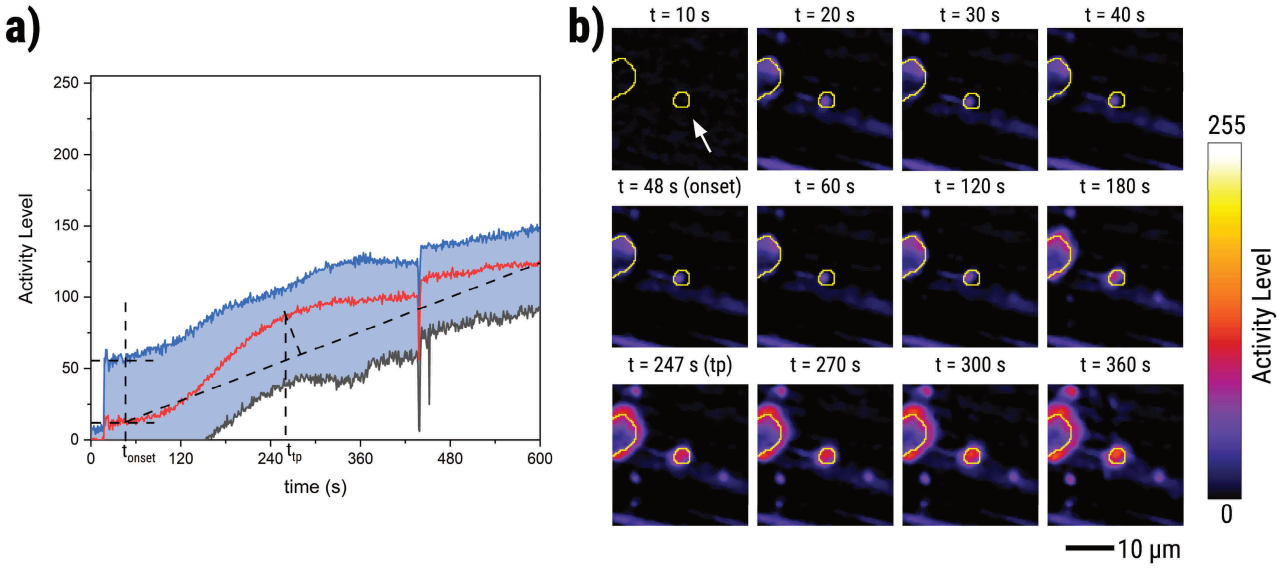

Figure S5.10. (a) Graphical estimation of the optics-based kinetic parameters from a simplified pixel activity level distribution plot with discontinuities. The values estimated from the plots are validated by cross-referencing with the **(b)** corresponding activity maps.

5.7.3.2. Rate of activity increase during stage 1

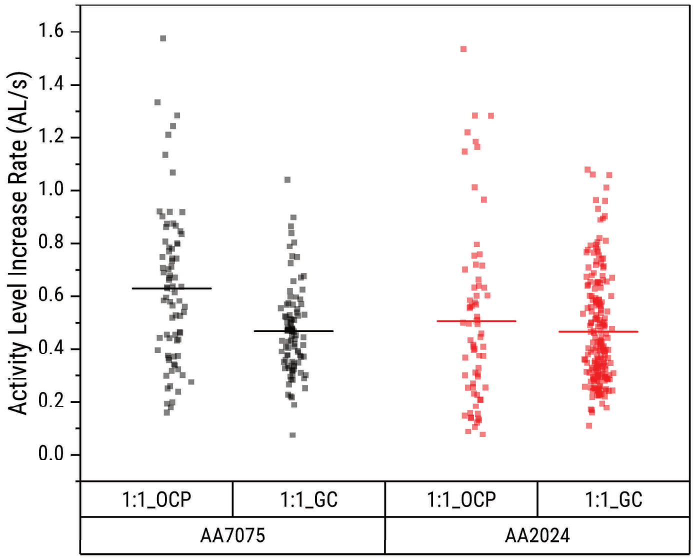

Figure S5.11. Activity level increase rate during Stage 1 estimated from the total activity level change and the duration from t_{onset} to t_{tp}. The values were obtained only from the trials shown in Figure 5.4b and Figure 5.4e due to brief focus changes in the other trials. The values show that similar to the t_{onset} and t_{tp}, the rates of change in IMP activity levels are comparable for immersion under electrically-isolated/OCP and galvanically-coupled (GC) conditions.

List of Publications

Journal publications

1. M. Mopon, A. Mol, S. J. Garcia
   Effect of delayed inhibitor supply on AA2024-T3 intermetallic activity: a local in situ analysis with reflected microscopy
   Corrosion Science, **2024**, 230, 111910

2. M. Mopon, A. Mol, S. J. Garcia
   Local re-immersion behaviour of Ce-based inhibiting layers on AA2024-T3 intermetallics: Enhanced stability through partial dealloying and prolonged exposure
   Corrosion Science, **2025**, 255, 113146

3. M. Mopon, A. Mol, S. J. Garcia
   Intermetallic particles trigger streaking corrosion in AA7075-T6
   NPJ Materials Degradation, **2025**, 9:92

4. M. Mopon, A. Mol, S. J. Garcia
   Galvanic coupling of AA7075-T6 aggravates local corrosion in AA2024-T3
   Electrochimica Acta, **2025**, 541, 147335

5. C. P. Couto, M. Mopon, P. Venkatesan, J. Ustarroz, Y. Yang, S. J. Garcia, S. T. Abrahami
   Evaluation of early-stage dissolution of spent NdFeB permanent magnet in organic acids by in-situ quantitative reflected light microscopy
   Journal of Materials Research and Technology, **in press**

Conference Contributions

1. M. Mopon, A. Mol, S. J. Garcia
   Poster presentation: Effect of delayed inhibitor supply on the local degradation and protection kinetics of IMs in AA2024-T3
   European Corrosion Congress (EuroCorr), Berlin, Germany, August 2022

2. M. Mopon, A. Mol, S. J. Garcia
   Oral presentation: Effect of delayed Ce^{3+} *supply on the local degradation and protection kinetics of IMs in AA2024-T3*
   Aluminum Surface Science and Technology (ASST), Stockholm, Sweden, May 2023

3. M. Mopon, A. Mol, S. J. Garcia
   Oral presentation: Why is it still corroding? Local corrosion triggers of AA2024-T3 after inhibition with $Ce(NO_3)_3$
   European Corrosion Congress (EuroCorr), Brussels, Belgium, August 2023

4. M. Mopon, A. Mol, S. J. Garcia
   Poster presentation: Visualizing Interactions: Analyzing inhibitor-intermetallic particle interactions with in-situ reflected light microscopy
   MaterialenNL, Arnhem, the Netherlands, December 2023

5. M. Mopon, A. Mol, S. J. Garcia
   Oral presentation: Effect of galvanic couple strength on the kinetics of local corrosion inhibition
   European Corrosion Congress (EuroCorr), Paris, France, September 2024

6. M. Mopon, A. Mol, S. J. Garcia
   Oral presentation: On the role of intermetallic particles in early-stage streaking corrosion in AA7075-T6
   European Corrosion Congress (EuroCorr), Stavanger, Norway, September 2025

Best Oral Presentation Award from the European Federation of Corrosion (EFC) at the European Corrosion Conference (EuroCorr) in 2025 for the presentation “On the role of intermetallic particles in the early-stage streaking corrosion of AA7075-T6”.

Acknowledgements

My PhD journey proved to be more than just an academic pursuit. Cliché as it may sound, it was also a journey of self-discovery filled with its fair share of good, bad, and terrible moments. Nonetheless, if given the choice, it is a journey that I would gladly take again. Not just for the experience, but also for the people who made it worthwhile. I would thus like to take this opportunity to thank them.

First and foremost, to my promotors. My heartfelt thanks go to Santiago. I reached out to you out of nowhere back in 2019 to inquire about a PhD position. A global pandemic and four years of work later, we are finally here. This journey challenged me constantly, but I count myself fortunate to have had a supervisor who gave me the push I needed to see it through. I am grateful that you saw the potential in my work, especially during the times when I struggled to see it myself. Special thanks to Arjan, for the insights and experience that you generously shared. Your kind affirmation reminded me to take pride in what I have achieved.

To Dajo. I would not have found the courage to start this journey so far from home without your support. I will always be in your debt.

To the people from ASM, Durga, Roy, Gemma, Mylene, and Tess, thank you for extending your helping hand whenever I needed it. I would especially like to thank Shanta, for helping find my footing when I arrived and for always being a friendly face around the office. You were a genuine source of comfort during my stay. Special thanks to Sybrand, who was a source of inspiration too strive for success, to be rich and famous.

To my friends and colleagues on the other side of the world. Ma’am Jem and Sir T, thank you for your support and for keeping me connected to the department. Ma’am Julie and Ma’am Marj, your guidance has been invaluable. Ate Cynthia, Audrey, and Joy, thank you for always being ready to help with the endless university paperwork. To the staff of the ERDT office, Ma’am Kath, Sir Jomar, and Ma’am Via, thank you for your assistance with all of the ERDT requirements. Jana, thank you for always being up for a catch-up. Andrew, it was comforting to have someone in the same boat.

To the extraordinary people with whom I spent the best part of the last four years, my colleagues from NovAM, the corridor, and ASM all over: Dimos, Tadgh, Jaylan, Bernadine, Adria, Yifan, Hugo, Apurva, Silvia, Mirko, Alejandro, Deniz, Tingyu, Ronan, Edward, Tomasso, Zhibin, Zhiyuan, Leith, and Orhun. Thank you for the random conversations about anything and everything under the sun. Special mention to my officemates, Vincent, Gawel, Anton, Theo, and Daniel, I have learned a lot of things from you. Kato, Greta, and Elodie, working with you on your projects was a tremendous learning experience. Special thanks to Camila and Shoshan for the opportunity to explore the application of my work in fields other than corrosion.

To the people I had the privilege of working closely with. Jingjing, thank you for helping me start my project and for sharing lessons from your own experience. Tinashe, your kindness is something that I strive to emulate. Miisa, your eye for detail and design never ceases to inspire me. Elif, you are a constant source of warmth. Riccardo, you are the embodiment of sprezzatura. Lakshmi, our random chats in the lab never failed to brighten my day.

To the friends that I made beyond the confines of the department - Jane, JV, JP, Joseph, Ice, Donald, Kevin, Ace, Roger, Shari, Evi, Elias, Ökkeş, Harris, Timo, Simone, Dennis, Leo, Melissa, Tim, Michelle, Cindy, Imelda, Alexa, and Eli, thank you for letting me experience the Netherlands in a different way. Socorro, thank you for your friendship and for introducing me to new music and salsa dancing. Eugenio, thank you for accompanying me through my ups and downs and for always being down to celebrate life. Farah, I still do not know how we became good friends and, perhaps, we never will. Nonetheless, thank you for being there for me through it all.

To Jordy, meeting you was never part of the plan, yet it changed the course of everything. You helped me become more comfortable with not being serious all the time and you opened me to new experiences. I am excited to discover what comes next.

To my family. Agie, you made me realize how nice it is to have family nearby. Ninang, thank you po for helping us a lot particularly during the difficult times with Nanay. Tatay, thank you for your understanding and for keeping it together when life tested us. May, thank you for taking care of everything. I am grateful for your consideration and for having the strength to take charge of everything.

Lastly, to Nanay. We may not have had the best relationship in recent years but I am thankful we had the chance to mend bridges before it was too late. You have always been one of my biggest inspirations in pursuing an academic career. You nurtured in me the joy of learning, even when you did not have the same opportunity to pursue your own education. Salamat po sa iyong pagtanggap, pagpapatawad, at sa mga alaalang iniwan mo.

About the Author

Marlon L. Mopon, Jr. was born in Cavite, a province in the Southern Tagalog region of the Philippines. He earned his Bachelor of Science in Chemical Engineering from the University of the Philippines Diliman in 2015. He completed his Master of Science in Chemical Engineering at the same institution in 2019, focusing on electrochemical sensor development. He began his academic career as an instructor at the UP Diliman Department of Chemical Engineering, while also contributing as project staff to a government-funded research initiative on electrochemical systems and sustainable energy technologies. In 2021, he pursued his PhD at the Delft University of Technology in the Netherlands, supported by a Faculty Development Grant from the Engineering Research and Development for Technology Program. His doctoral research was guided by Dr. Santiago J. Garcia Espallargas and Prof.dr.ir. Arjan Mol. It centered on the site-resolved analysis of local corrosion and inhibition in aerospace aluminium alloys. By integrating in situ reflected light microscopy with electrochemical techniques, his work unraveled new insights into the mechanisms of corrosion protection, with the aim of advancing active corrosion control strategies for aerospace applications.